8-2009

Optical Modeling of Schematic Eyes and the Ophthalmic Applications

Bo Tan
University of Tennessee - Knoxville

To the Graduate Council:

I am submitting herewith a dissertation written by Bo Tan entitled "Optical Modeling of Schematic Eyes and the Ophthalmic Applications." I have examined the final electronic copy of this dissertation for form and content and recommend that it be accepted in partial fulfillment of the requirements for the degree of Doctor of Philosophy, with a major in Physics.

James W. L. Lewis, Major Professor

We have read this dissertation and recommend its acceptance:

Ying-Ling Chen, Horace W. Crater, Christian Parigger, Ming Wang

Accepted for the Council:

Carolyn R. Hodges

Vice Provost and Dean of the Graduate School

(Original signatures are on file with official student records.)

To the Graduate Council:

I am submitting herewith a dissertation written by Bo Tan entitled "Optical modeling of schematic eyes and the ophthalmic applications." I have examined the final electronic copy of this dissertation for form and content and recommend that it be accepted in partial fulfillment of requirements for the degree of Doctor of Philosophy, with a major in Physics.

James W. L. Lewis, Major Professor

We have read this dissertation
and recommend its acceptance:

Ying-Ling Chen

Horace W. Crater

Christian Parigger

Ming Wang

Accepted for the Council:

Carolyn R. Hodges
Vice Provost and Dean of the Graduate School

(Original signatures are on file with original student records.)

OPTICAL MODELING OF SCHEMATIC EYES

AND THE OPHTHALMIC APPLICATIONS

A Dissertation

Presented for the

Doctor of Philosophy

Degree

The University of Tennessee, Knoxville

Bo Tan

August 2009

Acknowledgements

I would like to take this opportunity to thank all those who help me make this dissertation possible. First, thank goes to Dr. James W.L. Lewis and Dr. Ying-Ling Chen for their guidance and patience all the time in the research and the course work. What I have learned from them is not only the knowledge, the scientific research skills, and the logical thoughts, but also the rigorous scientific approach and the unremitting efforts. I would also like to express my appreciation to my committee members, Dr. Christian Parigger, Dr. Horace W. Crater, and Dr. Ming Wang for their assistance in getting this dissertation in its final form. Here I especially want to express my thankfulness to them for their help and care in my study and life since I came to UTSI. I would also like to thank my parents, my wife, all my family, and friends for their moral support through the years.

Abstract

The objectives of this dissertation are to advance and broaden the traditional average eye modeling technique by two extensions: 1) population-based and personalized eye modeling for both normal and diseased conditions, and 2) demonstration of applications of this pioneering eye modeling. The first type of representative eye modeling can be established using traditional eye modeling techniques with statistical biometric information of the targeted population. Ocular biometry parameters can be mathematically assigned according to the distribution functions and correlations between parameters. For example, the axial dimension of the eye relates to age, gender, and body height factors. With the investigation results from the studies of different population groups, population-based eye modeling can be established. The second type of eye model includes the optical components of the detailed corneal structure. Many of these structures, especially the corneal topography and wavefront aberration, are measured directly from the human eye. Therefore, the personalized eye models render the exact clinical measure and optical performance of the eye. In a sense, the whole eye, other than the identity of the individual, is quantified and stored in digital form for unlimited use for future research and industrial applications.

The presentation of this dissertation is: Chapter 1 describes the background of the research in this area, the introduction of eye anatomy, and the motivation of this dissertation work.

In Chapter 2, a comprehensive review of the contemporary techniques of measuring ocular parameters is presented and is followed by the review of literature and then the statistical analysis of the ocular biometry parameters. The goal of this chapter is to build a statistical base for population-based schematic eye modeling research. The analysis includes the investigation of the correlations between ocular parameters and ocular refraction, subject age, gender, ethnicity, and accommodation conditions.

In Chapter 3, the tools and methods that are used in our optical eye modeling are introduced. The operation of the optical program ZEMAX is discussed. The detail of the optical eye modeling procedure and method of optical optimization, which is utilized to reproduce desired clinical measurement results, are described. The validation functions, which will be used to evaluate the optimization results, are also addressed.

Chapter 4 includes the discussion of the population-based eye modeling and the personalized eye modeling. With the statistical information and the clinical measurements presented in Chapter 2 and the computation method described in Chapter 3, the two types of eye modeling technologies are demonstrated. The procedure, difficulty, and validation of eye modeling are included. The considerations of optical opacities, irregular optical surface, multiple reflection, scattering, and tear film breakup effects are discussed and the possible solutions in ZEMAX are suggested.

Chapter 5 presents eye modeling applications of the simulations of ophthalmic instrument measurements. The demonstrated simulation results are retinoscopy and photorefraction. The simulation includes both normal eye model and diseased eye model. The close conformity between the simulation results with the actual clinical measurements further validates the eye modeling technique. The ophthalmic simulation application provides the potential for medical training and instrument development.

The summary of the dissertation is given in Chapter 6.

Contents

List of Figures

List of Tables

Chapter 1 Introduction to Eye Modeling

Vision is one of the most important human senses. Eighty percent of our learning is through the visual processing of information [Murphy 1999]. In addition to the visual function, the human eye is also an open window to the chemical, physical, and physiological information of the body. Ocular responses and dynamics are accurate reflections of human cognitive processes and the brain's control strategy [Trillenberg 2004, Hung 2001, Schwartz 2004]. Examples are correlations between eye response and drowsiness [Varri 1996], schizophrenia [Hartnegg 2002, Avila 2003], autism [Neumann 2006, Rommelse 2008], bipolar behavior [Bestelmeyer 2006]. Optical techniques have also shown the capability to monitor glucose and drug concentration in the aqueous humor [Cameron 2006, Wan 2005, March 2000] and from the blood vessels on the fundus of eye, oxygen level and hypertension [Kaur 2008, Denninghoff 2003, Cardascia 2006, Sayer 2006]. Also, using the eye to monitor specific measures of astronaut health has been one area of research of the NASA manned space flight program.
[http://www.nasa.gov/centers/glenn/business/biomed_eyes.html].

The functioning of the human eyes is complex and elegant. As an optical device, the eye can be seen as an optical imaging and detection instrument. The retina of eye acts as a colored high-resolution photosensor. The operation of the two eyes as a pair provides binocular vision that enables one to determine three-dimensional location and distance and the speed of distant objects. The complex structure and relation between the eye, brain, nerves and blood flow provide rapid feedback loops for accommodation and ocular movement to complete the vision function. In this thesis, the binocular vision and nerve brain functions are not considered, and human eye modeling is performed for only the optical and imaging functions of the eye.

Elements of human eyes include the cornea, anterior chamber, iris (pupil), posterior chamber, crystalline lens, and retina and are shown in Figure 1.1. The cornea is a transparent layer of tissue of approximately 0.55 mm in thickness with refractive index slightly higher than that of water, which, in the visible region is nominally 1.333. The cornea can be seen as the extension of the sclera, the white hard part of eye that forms the oval- shaped object. It is made of the same material of sclera, but with a highly organized orientational arrangement of its fiber structure. The cornea provides approximately 2/3 (~ 43 diopters) of total focusing power of eye (~ 57 diopters). Similar to the shutter of a camera, the iris controls the size of pupil and, therefore, the amount of light entering the eye from the environmental illumination. The typical diameter of the pupil is about 1.5 mm in bright light and about *8* mm when it is dilated with drugs. The maximum diameter of pupil in the total darkness reduces with age. The good quality of vision is only present when the pupil is about 2 to 5 mm. When the environment is dark and the pupil diameter is larger than 5 mm, the aberration degrades the imaging quality. If the environment is too bright and the pupil is smaller than 2 mm, the optical diffraction reduces the imaging performance. Only a properly illuminated environment provides optimized visual performance. The crystalline lens is the transparent biconvex structure lying between the iris and the vitreous humor of the posterior chamber. It consists of a soft outer part, the cortex, and a denser inner part, the nucleus. The accommodation of the eye is the increase in thickness and convexity of the crystalline lens in response to ciliary muscle contraction in order to focus the image of near object onto the retina. The anterior and posterior chambers, which are filled with aqueous humor, a gel-like material, are divided by the lens and iris. The index of refraction of aqueous humor is about 1.336. Located at the far back, the retina works as the film of camera. From left to right in the figure, it consists of the nervous system, the photosensors (cone and rod in color), and the pigmented part. The optical axis of the

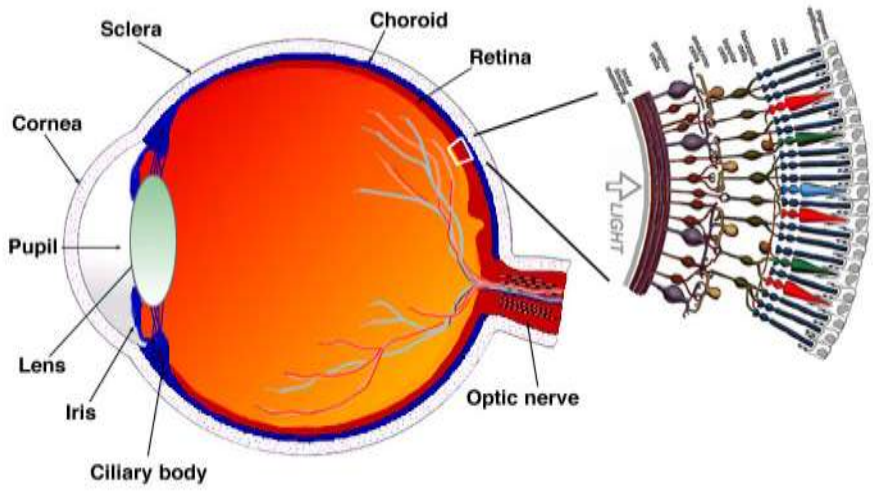

Figure 1.1 *Human eye and its optical elements. The upper side in this figure is the tempo side. The lower side is the nasal side.*

Table 1.1 *Optical parameters of typical human eye. R indicates surface radius, t is the distance to next surface, n is the index of refraction between surfaces*

Surface Radius	Distance	Refractive Index
R_1 (air to cornea) 7.8 mm	**t_1 (cornea) 0.6mm**	**1.376**
R_2 (cornea to aqueous) 6.4 mm	**t_2 (aqueous) 3.0mm**	**1.336**
R_3 (aqueous to lens) 10.1 mm	**t_3 (lens) 4.0mm**	**1.386–1.406**
R_4 (lens to vitreous) 6.1 mm	**t_4 (vitreous) 16.9mm**	**1.337**

eye is different from the visual axis due to the location of the central fovea, the most sensitive area (the central vision) on retina. The fovea is located at about five degrees temporally and two degree upward. The blind spot, where the optical nerves bounded, is located nasal side of the retina about the opposite direction to the fovea. The optical parameters of a typical human eye are listed in Table 1.1.

In the recent years, physiological optics has experienced a revolution by two synergistic forces. First, advances in technology have provided measurement instruments with escalating accuracy for the essential parameters of physiological optical system. Second, studies of the growth of the eye with reference to myopia and emmetropization have resulted to a demand for more accurate, noninvasive measurement methods. The demonstrations that the optics of the eye may be clinically altered have sped the transformation of physiological optics from an observational to a quantitative and possibly even a predictive science. The ever increasing computation capability further provides the environment for ground-breaking optical computation and simulation.

Schematic eye models in the early 20th century used spherical ocular elements and constant indexes of refraction. Later in the 1980's, aspherical ocular elements and new models of the eye's lens were incorporated to represent better the average ocular monochromatic and chromatic imaging properties of the eyes. These general eye models were valuable to evaluate optical performance, to investigate ocular properties, and to design new ophthalmic corrections, including spectacles and contact lenses. A major shortcoming was that these models were based on average ocular parameters obtained from young emmotropic adults, whereas the reality is that, for example, both monochromatic aberration and transverse chromatic aberration are known to vary widely across subjects.

Recently, high precision ophthalmic patient data has become available to characterize accurately both anterior and posterior surfaces of the cornea, ocular wavefront aberrations, and ocular element biometry. These measurements can be incorporated into the construction of an optically functional and analytical, personal-tailored, eye model. In 2006, customized eye models were developed using individual measured corneal topography, ocular biometry, and wavefront aberration from normal subjects [Navarro2006]. In the same year, our research team developed the first personalized keratoconus eye modeling and published the ophthalmic measurement simulation [Chen2006]. Customized eye modeling offers the exciting promise to assist planning of ocular surgery, such as LASIK, PRK, CK, and Intacs, and to design personalized spectacles and contact or intraocular lenses. Computational personalized eye modeling techniques allow the integrated information to be quantitatively evaluated without repetitive examination of human subjects. Simulating ocular device measurements using eye modeling could also be useful to aid medical personnel training and for evaluating ocular instrument sensitivity. The objectives of this dissertation are to advance the eye modeling technique, to extend the average eye modeling to population-based eye modeling and personalized eye modeling on normal and diseased conditions, and to demonstrate the applications of eye modeling.

The first type of representative eye modeling can be established using traditional eye modeling technique with statistical information of the targeted population. Ocular biometry parameters can be mathematically assigned according to the distribution functions and correlations between parameters. For example, the spatial length dimension of the eye relates to age, gender, and body height, etc. factors. The statistical distribution function of refractive error in many Asian countries has been shown to indicate both statistically significant myopia over a wide range and longer ocular axial lengths of subjects. Consequently, the effectiveness of any optical instrumentation that involves human eyes and this parameter would be affected when applied in different groups of people. Integration of these eye models in optical design software with any ocular instrumentation allows device sensitivity or efficiency to be evaluated with significantly fewer clinical trials.

The second method is to construct individual customized eye modeling. These eye models include the optical components of detailed corneal structure, aqueous humor, pupil, crystalline lens, vitreous humour,

and retinal surface. Many of these structures, especially the corneal topography and wavefront aberration, are measured directly from the same human eye. Therefore, the personalized eye models render the exact clinical measure and optical performance of the eye. Under specified environmental and physical conditions, the eye's optical performance change could be computationally predicted. In a sense, the whole eye, other than the identity of the individual, is reserved and stored in digital form for unlimited use for future research and industrial applications.

In the followed Chapter, I will first present a comprehensive review of the contemporary techniques of measuring ocular parameters and then perform the literatures review and the statistical analysis of the ocular biometry parameters. The goal of this work is to build a statistical base for population-based schematic eye modeling research. The analysis includes the investigation of the correlations between ocular parameters and ocular refraction, subject age, gender, ethnicity, and accommodation conditions, etc.

In chapter 3, the tools and methods that are used in our optical eye modeling are introduced. The fundamental setting and operation of the optical program, ZEMAX, are discussed. The detail of the optical eye modeling procedure and method of optical optimization, which is utilized to reproduce desired clinical measurement results, are described. The validation functions, which will be used to evaluate the optimization results, are also addressed.

Chapter 4 includes the discussion of the population-based eye modeling and the personalized eye modeling. With the statistical information summarized in Chapter 2, the computation tool described in Chapter 3, and the clinical measurements reviewed also in Chapter 2, the two types of eye modeling technologies are demonstrated. The procedure, difficulty, and validation of eye modeling are included. The considerations of optical opacities, irregular optical surface, multiple reflection, scattering, and tear film breakup effects are discussed and the possible solutions in ZEMAX are suggested.

Chapter 5 included eye modeling applications of the simulations of ophthalmic instrument measurements. The demonstrated simulation results are retinoscopy and photorefraction. The simulation includes both normal eye model and diseased eye model. The close conformity between the simulation results and the actual clinical measurements further validates the eye modeling technique. The ophthalmic simulation application provides the potential for medical training and instrument development.

If the long-term goal, the high quality, realistic eye modeling technique can be achieved, the results will expand the ocular disease knowledge base and generate new clinical treatment options. Ocular disease visual performance could be determined during different conditions. Risk factors can be better established. The technology can reduce the need for resource-intensive clinical trials. Clinical research could then spend more resources rapidly enhancing and extending the sensitivity of the devices instead of comparing necessarily limited clinical trial results.

Chapter 2 Ocular Biometry Measurements and Population Based Statistics

Throughout the 20th century, eye modeling had been limited in describing the average eyes. In these models, ocular parameters and optical characteristics were measured primarily using Caucasian male adult subjects. The recent vision research interest in UTSI, nevertheless, extends to the population-based eye modeling that illustrates ocular variations. In the past decades, a large number of studies have been performed to better understand the ocular biometry and the correlations of a wide range of factors. These ocular measurements are the foundation of the population-based eye modeling. Hundreds of recent papers were collected and are reviewed in this chapter. Specifically, the statistical distribution of ocular biometry and the correlations to subject's ocular refractive error, age, gender, and ethnic or geographic condition are examined and summarized.

2.1 MEASUREMENTS OF OCULAR BIOMETRY

The human ocular structure and elements were briefly described in the first chapter. To obtain the geometric description and optical characteristics of ocular elements, a variety of techniques are used worldwide by research groups. The most common techniques and their optical roles are described below. These techniques deliver numerical results that are essential for mathematical eye modeling. The optical differences, data presentation of these measurements, accuracies & precisions (systematic & random errors), and common commercial devices models are briefly described for these techniques.

2.1.1 Techniques for Measuring Curvature, Dimension, Thickness, or Distance of Ocular Elements

Because of the difficulty and intrusiveness of reaching the internal ocular tissues in vivo, the non-invasive reflection signals of light or sound waves from the interfacial surfaces of different ocular layers are typically used to provide important information about the ocular dimension and location. Seven types of these techniques are listed below.

1. Ophthalmic ultrasonography---- A-scan & B-scan:

Ophthalmic ultrasonography applies high-frequency sound waves thatare transmitted from a probe into the eye. As the sound waves strike intraocular structures, they are reflected back to the probe and converted into an electric signal. The signal is subsequently reconstructed as an image on a monitor, which can be used to make a dynamic evaluation of the eye or can be photographed to document pathology. The shorter the wavelength, the shallower the penetration is. However, the image resolution improves as the wavelength shortens. Given that ophthalmic examinations require little in tissue penetration (an eye is 23.5 mm long on average) and much in the tissue resolution, ultrasonic probes used for ophthalmic ultrasonography are manufactured with very high frequencies of about 10 MHz. There are two different types of ophthalmic ultrasound instruments, A-scan and B-scan, which produce 1-dimensional and 2-dimentional ocular maps, respectively.

In A-scan ultrasonography, a thin, parallel sound beam is emitted, which passes through the eye along one axis, and the echoes are represented as spikes arising from a baseline (Figure 2.1 left). The stronger the echo, the higher the spike is. The axial length (AL) and surface location of each ocular element are therefore indicated.

In B-scan ultrasonography, an oscillating sound beam is emitted, passing through the eye and imaging a slice of tissue. The resulting echoes are represented as a multitude of dots that together form an ocular cross section image on the screen (Figure 2.1 right). The stronger the echo, the brighter the dot is. The technique has a precision of approximately 0.1 mm but exhibits only moderately high intra-observer and low inter-observer reproducibility.

Ultrasonography is a somewhat invasive technique because that the ultrasound probe touches or pushes against the cornea or globe surface. It has reduced in popularity due to the commercialization of a partial-coherent optical interferometric (PCI) device for measuring axial length and calculating intraocular lens power. [Wolffsohn 2006]

Commercial devices of ophthalmic ultrasonography include DGH-5000e A-Scan unit, DGH-5100e Combination A-Scan/Pachymeter, PalmScan A2000 A-Scan, PalmScan AP2000: A-Scan & Pachymeter, EchoScan US-1800, EchoScan US-800, HF35-50 High Frequency Ultrasound, OTI-Scan 3D - 3D B & A Scan - Ophthalmic Ultrasound, Aviso A/B Ultrasound, AXIS II PR Post Refractive Ultrasound, CineScan A/B (Optional S) Ultrasound, CineScan A/B Ultrasound, Compact II Portable A/B Scan, AL-100 Ultrasound A-Scan Unit, AL-3000 Ultrasound A-Scan Unit, Accutome A-Scan Plus, Advent AB, Alcon® UltraScan®, OcuScan® RxP Ophthalmic Ultrasound System, Eye-Scan™ A-Scan, 100A+ Microscan A-Scan, 300A PacScan A-scan, 300AP PacScan A-scan / Pachymeter, A5500 A-scan, and AB5500 A/B-scan.

2. Pachymeter for cornea thickness

The pachymeter is an instrument that measures the thickness of the ocular components. Both ultrasonic and optical pachymetry are available. Ultrasonic pachymetry is more reproducible, but optical pachymetry is especially helpful in measuring the depth of corneal pathology. The ultrasound pachymeter is designed for measuring the axial length of the eye and the thickness of the cornea. Ultrasound energy is emitted from the probe tip that acts as both the transmitter and the receiver. Some of the energy is reflected back toward the probe in the form of an echo. Measurement data can be calculated based on both the time it takes the echo to travel back to the probe from the eye and the preset converted velocity (The eye dimension should be calculated by converting velocity by considering the media inside the eye. The velocity inside the media was preset.).

Commercial devices examples are Pachmate DGH 55, DGH 555, DGH-2000, ODM-1000A, etc.

3. Partial Coherence Interferometry (PCI):

PCI has been introduced as an alternative technique to measure the axial length of the eye. PCI is also referred to as optical, or ocular, coherence biometry or laser Doppler interferometry. PCI relies on a laser Doppler to measure the echo delay and intensity of infrared light reflected back from tissue interfaces. This technique have been developed for non-invasive high-precision and high-resolution biometry and tomography in ophthalmology [Fercher 1996, Fercher et al. 1993, Huang et al. 1991a, and Huang et al. 1991b]. PCI, using a dual beam version of the interferometric technique, removes any influence of longitudinal eye motions during measurement by using the cornea as a reference surface. It was used to perform axial length measurements in vivo of normal [Hitzenberger, 1991] and cataract eyes [Hitzenberger et al., 1993], as well as corneal thickness and thickness profile measurements [Hitzenberger et al., 1992, Hitzenberger et al., 1994]. This technique has been upgraded to a fully computer-controlled scanning instrument.

It has been reported that PCI is capable of measuring intraocular distances not only parallel to the visual axis, but at arbitrary angles, and of performing cross-sectional imaging of the human retina [Fercher et al., 1993, Drexler et al., 1998a, Drexler et al., 1995, Baumgartner et al., 1997]. Depending on the measured intraocular distance, precision values from 0.3 to 10μm have been reported [Drexler et al., 1997].

An example commercial device is ZEISS IOLMaster Optical Biometer.

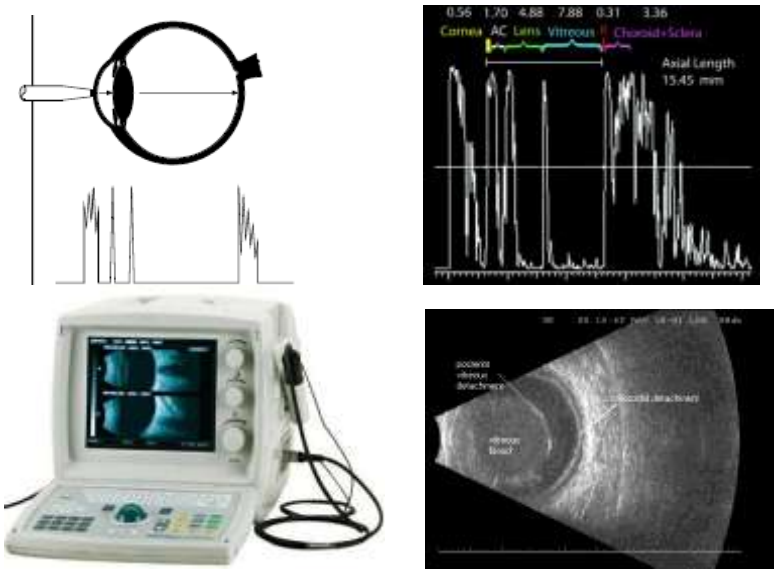

Figure 2.1 *(Top): From left to right are A-scan concept of measurement and A-scan output along ocular axis. (Bottom): B-scan device and B-scan output image.*

Figure 2.2 *Typical pachymeter and reading in front panel*

4. High-speed Optical Coherence Tomography (OCT)

Another non-invasive optical biomedical imaging technology called optical biomedical imaging technology or optical coherence tomography (OCT) has been developed in recent years. OCT is based on the PCI technique. It is similar to conventional ultrasonography, except that OCT does not require direct contact with the tissue being investigated and that it measures echo delay and intensity using infrared light reflected back from internal tissue interfaces rather than using acoustic waves. OCT is a promising method for accurate anterior segment biometry because of its high spatial resolution and noncontact nature. A wide-field horizontal cross-sectional image of the anterior segment that was generated using CAS OCT system is shown in Figure 2.3. The OCT scan provides the anterior chamber depth (*ACD*), anterior chamber width (*ACW*), and crystalline lens vault that are visible in Figure 2.3. Figure 2.4 shows an example pachymetry map obtained from rotationally scanned OCT measurement. Although the OCT technique can also be used for lens and retinal imaging, ACD data and statistics given by Goldsmith 2005 is the only paper I found. Drexler have been carried out in many studies to investigate the clinical feasibility of OCT in a clinical setting [Drexler et al. 1998a, Drexler et al. 1997a, Drexler et al. 1997b, & Drexler et al. 1998c], including suitability for intraocular lens measurements [Findl et al., 1998b, Findl et al., 1998a] and use in determination of the group refractive indices and the group dispersion of ocular media in vivo [Drexler et al., 1998b].

Commercial OCT devices include Cirrus™ HD-OCT, RTVue-100 Fourier-Domain OCT, Visante OCT, and Spectral OCT/SLO.

5. Magnetic resonance imaging (MRI):

Magnetic resonance imaging was developed from knowledge gained in the study of nuclear magnetic resonance. In its early years the technique was referred to as nuclear magnetic resonance imaging (NMRI). However, because the word "nuclear" is associated with ionizing radiation exposure, the method is generally now referred to simply as MRI. MRI uses electro-magnetic waves combined with the reception of weak radio signals to record the density or concentration of hydrogen or other nuclei in the body. MRI avoids health risks associated with ionizing radiation found in routine X-rays and CT scans but can penetrate the whole human body. Furthermore, the resolution is greater than that of traditional CT scanning. The images of an MRI are reconstructed into cross-sections of anatomy. In ophthalmology, MRI has been used to examine the whole eye and orbit with respect to space occupying lesions, soft tissue damage and extra-ocular muscle examination. It has also been used to study eye shape with refractive error and changes in the crystalline lens with accommodation. Figure 2.5 shows example data of ocular MRI.

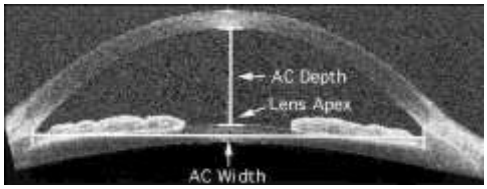

Figure 2.3 *Horizontal optical coherence tomography (OCT) section of the anterior segment after computational correction for index transitions.*

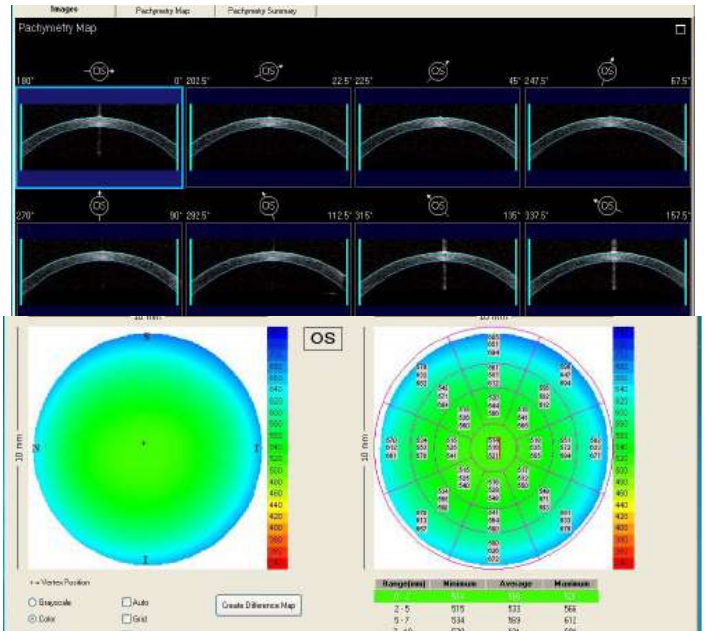

Figure 2.4 *Pachymetry map obtained from rotationally scanned OCT*

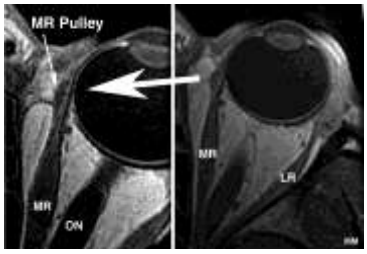

Figure 2.5 *Examples of magnetic resonance image (MRI) of a human left orbit in 2 mm thickness planes at 390 micron resolution at right, and 312 micron resolution at left.*

6. Specular microscopy

The clinical specular microscope makes it possible to observe and document the backside of human cornea of the eye, the corneal endothelial cell layer, in vivo at high magnification. The technique used in the specular microscopy is called specular reflection. Specular reflection refers to the viewing of objects that occurs when light is reflected from the interfaces of materials with different indices of refraction. This test is used to monitor the number, density, and quality of endothelial cells that line the back of the cornea. A microscope magnifies the cells thousands of times and the image is captured with a camera or video camera. The number of cells within one square millimeter are counted and recorded. The endothelium of a young, ten-year-old, healthy cornea has approximately 3,500 cells in each square millimeter. Normal aging causes the cells to gradually decrease over time. By age 60, most people have approximately 2,500 cells per square millimeter. Figure 2.6 shows an example of output image data. Corneal thickness can also be obtained by specular microscopy measurement. An example research study is [Suzuki 2005].

Commercial devices of specular microscopy include HAI CL-1000xyz Clinical Specular Microscope, Cellchek XL Specular Microscope and EM-3000 Specular Microscope.

7. Keratometer

A keratometer, also known as an ophthalmometer, is a diagnostic instrument for measuring the curvature of the anterior surface of the cornea, particularly for assessing the extent and axis of astigmatism. [Wikipedia] A keratometer measurement uses the relationship between object size (O), image size (I), the distance (d) between the reflective surface and the object, and the radius of the reflective surface (R). If three of these variables are known (or fixed), the fourth can be calculated using theequation:

$$R = 2dI / O \tag{2-1}$$

There are two distinct variants of determining R; Javal-Schiotz type keratometers have a fixed image size and are typically 'two position', whereas Bausch and Lomb type keratometers have a fixed object size and are usually “one position”.

The two-position Javal-Schiotz keratometer uses a fixed image and doubling size and adjustable object size to determine the radius of curvature of the reflective surface. It uses two self-illuminated mires (the objects), one a red square, the other a green staircase design, which are held on a circumferential track in order to maintain a fixed distance from the eye. The object size is adjusted by maneuvering the mires along this track and changing the distance between them. The reflected image is doubled through a Wollaston prism, which then allows either side of the doubled image to be aligned, and any eye movement to cancel out as both images move with the same magnitude and direction while the relative separation remains constant. A Wollaston prism uses the polarization property of light in order to split a single image into two separate, visually identical but oppositely polarized images. Once the mires are focused, the only variable remaining is object size, which is calibrated to a measurement of reflective surface radius (and sometimes dioptric power using an estimation of refractive index). This gives the curvature of the meridian along the path of the circumferential arms, the axis of which can be read from a scale around which the arms rotate. The axis can be manipulated to any axis, thereby giving a distinct advantage over a single position keratometer in cases of irregular astigmatism.

The Bausch and Lomb keratometer is a one-position keratometer that gives readings in dioptric form. The reflected rays are passed through a Scheiner disc with 4 apertures – two of which are used for the focusing of the mires at the fixed telescope focal distance, the other two for dual prism doubling. The instrument is based on the Helmholtz design which has two maneuverable prisms aligned vertically and horizontally. This creates two adjustable images in addition to the original image, one above and one to the left. By adjusting the distance between the eyepiece and the prism, the effective power of these prisms can be altered. As the distance is decreased, the effective prismatic power decreases. This decreases the image size along the respective prism alignment, moving the duplicate image closer to the original. An

increase in the eyepiece to prism distance leads to an increase in prismatic shift. Since there are two prisms, each aligned perpendicular to the other, the major and minor axis powers can be measured independently without adjusting the orientation of the instrument. In converting the measurements obtained from the corneal surface into a dioptric value, the B&L keratometer uses the general lens formula (n'-n/R) and assumes an n' of 1.3375 (compared to the actual corneal refractive index of n'=1.376). This is a fictional value, which includes an allowance for the small, yet significant, negative power of the posterior corneal surface. This allows for readout in both refractive power (dioptres) and radius of curvature (millimeters).

While it is often stated that the conventional keratometer measures the central corneal radius, the instrument utilizes pencils reflected from the area between the radii from the center of the cornea of not less than 1 mm and up to about 1.7mm. Because of the peripheral flattening it is probable that the keratometer readings are slightly longer than the vertex radius. It is difficult to generalize, but the error would probably not exceed 0.05 mm on a normal eye. [Rabbettss 2007]

Commercial keratometer devices include the MK1 Manual Keratometer, 4-In-1 TRK-1P (Auto Refractor, Keratometer, Non-Contact Tonometer and Pachymeter), Refkeratometer KW-2000

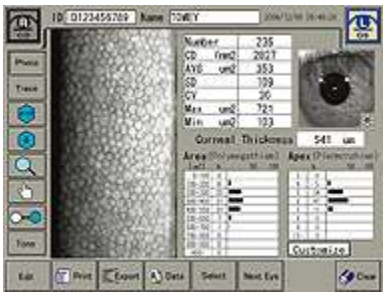

Figure 2.6 *Example output data of specular microscopy*

Figure 2.7 *Measurement of keratometry. The line points at the small reflection image of fixation point, which is irrelevant for the measurement.*

2.1.2 Techniques for Measuring Three-Dimensional Corneal Topography

Corneal topography, also known as photokeratoscopy or videokeratography, is a non-invasive medical imaging technique for mapping the surface curvature of the cornea. Since the cornea is normally responsible for some 70% of the eye's refractive power, its surface condition, especially the anterior interface that touches air, is of critical importance in determining the quality of vision. The three-dimensional topographic map is therefore a valuable aid to the examining ophthalmologist or optometrist and can assist in the diagnosis and treatment of a number of conditions, in the planning of refractive surgery such as LASIK and evaluation of its results, and in assessing the fit of contact lenses. With the development of keratoscopy, corneal topography extends the measurement range from some points a few millimeters apart that is offered by keratometry to a grid of thousands of points covering the entire cornea. The procedure is carried out in seconds, and like keratometry, no physical contact to the eye is required.

The following are the three-dimensional-corneal topographic techniques:

1. Placido disk imaging

Placido disk imaging is based on the overlay of concentric mires on the cornea. This method, also called keratoscope, permits the direct observation of illuminated mires upon the cornea and demonstrates the Placido rings. The rings are photographed as contour lines projected on the corneal epithelium. An example of raw data is shown in Figure 2.8. The cornea surface curvature modifies the light from Placido rings, and the space between the adjacent rings' images represents the shape of the local cornea surface. The closer the mires, the steeper the corneal curvature along the axis is. The wider the rings, the flatter it is. It was the first technology that was used to evaluate the shape of the cornea in conjunction with computer analysis. While systems may differ somewhat, all contain a transilluminated Placido target in the shape of a cone or disk, an imaging system containing an objective lens and camera, a video frame grabber, and a computer for image analysis. The number, position, color, and thickness of the rings vary between systems.

Placido systems are typically divided into two types. Near-target (also called small targets) systems typically allow for imaging with lower illumination and enjoy greater corneal coverage. However, they are sensitive to focusing adjustments, and facial anatomy may hinder measurement. Distant-target (large targets) systems require more illumination and are less sensitive to focusing error, but they cover less of the cornea surface area. These systems project images of illuminated keratoscope rings onto the corneal surface to produce a virtual image of the Placido disk about 4mm behind the vertex. The mire spacing directly measures the curvature of the cornea, and calculates the elevation map using a coordinate system from the curvature data. However, this requires assumptions about the corneal geometry. Elevation is generated by fitting slope data to a predefined mathematical model that may be spheric, aspheric, or a conical section. While this practice is reasonable in normal corneas, it may result in serious error in diseased eyes or eyes having undergone keratorefractive surgery.

Commercial corneal topography devices using Placido imaging principle include Humphrey® Atlas™ Corneal Topography Systems and TMS-4a Topographer

Figure 2.8 *Placido image on cornea*

2. Slit-Scanning topography

Slit-scanning technology is currently utilized by a single system, the Orbscan. The Orbscan uses a slit-scanning beam similar to parallel-piped one used in biomicroscopy and direct stereotriangulation to measure the anterior corneal surface. During the 1.5-second examination, two slit-scanning lamps project a series of 40 slit beams angled at 45 degrees to the right and left of the video axis. Twenty slits are projected from the left and twenty from the right. Proprietary software image registration attempts to minimize the influence of involuntary eye movements during data acquisition.

During calibration of this device, a reference plane (ZO) is constructed, which is situated at a known distance from the objective lens of the camera. The distance is measured from the instrument axis to the point where each of the forty slit-beams strikes the reference plane. The digital images of the slits, when projected onto a cornea, are compared with their original position at the ZO plane.

The slit beam, on striking the cornea, creates a Tyndall image which is captured by the digital camera. The instantaneous position of the leading edge ('L' ray) of the slit at the cornea is recorded in two-dimensional Cartesian co-ordinates. When the alignment is correct, the distance from the point where the instrument axis intersects the anterior surface, to the digital camera (x), and to the reference plane (z_v), is known. Figure 2.9 illustrates a slit of light, projected at 45° to the instrument axis; the 'L' ray and the 'T' ray (trailing edge) of the slit strike the cornea at points R_0 and R_1 respectively. Using the expression:

$$z_0 = z_v - b_0 - c_0 \qquad (2\text{-}2)$$

The sagittal height of R_0 is described by Equation (2-2), and with data from other locations, fitted to a low-order polynomial spline.

The typical display used for the Orbscan incorporates four images (shown in Figure 2.10): the anterior and posterior elevation maps, the curvature (axial) map, and the pachymetry map. An example is shown in the following figure. When used for screening, Tanabe et al recommend using 10 or 20 μm scales for elevation maps, which best identify abnormal corneas. [Wang 2006]

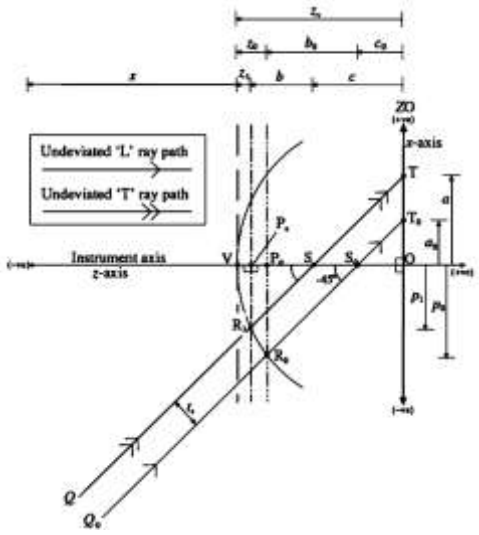

Figure 2.9 *Ray diagram of the measurement of the anterior elevation topography of a surface using a slit-scanning technique*

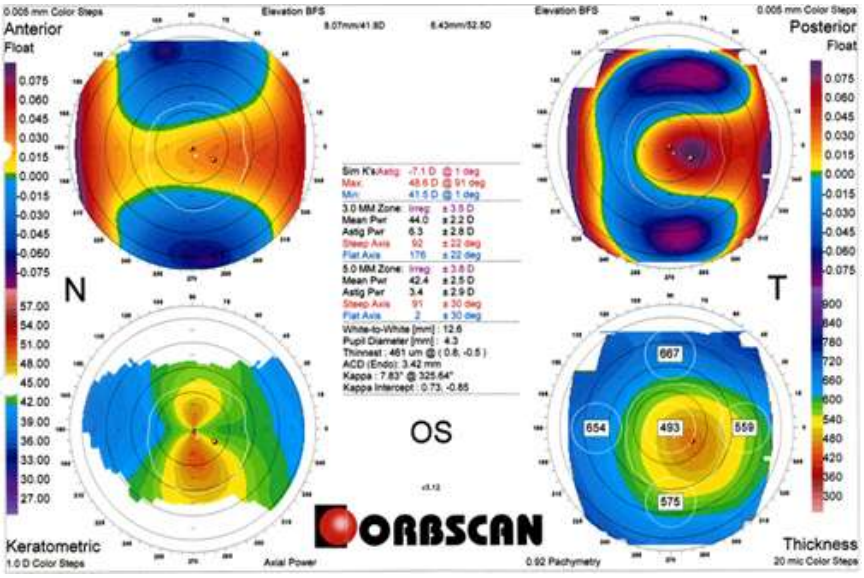

Figure 2.10 *Typical Orbscan quad map of an eye*

3. Scheimpflug imaging

The Pentacam (Oculus, Inc., Lynnwood, Wash., USA) uses a rotating Scheimpflug camera and a monochromatic slit light-source (blue LED at 475 nm) that rotate together around the optical axis of the eye. During 2 seconds, the system rotates 180° and acquires 25 images (as shown in left of Figure 2.11) that contain 500 measurement points on the front and back corneal surface and are used to draw a true elevation map. The software acquires the images as volume data so thatmulti-planar representationsallow the creation of axial and tangential maps. The patient's eye movement was constantly monitored by the system, and only measurements with less then 0.6 mm decentration were included. To better understand how the Pentacam works, we need a basic knowledge of Scheimpflug principle.

The Scheimpflug principle is a geometric rule that describes the orientation of the plane of focus of an optical system (such as a camera) when the lens plane is not parallel to the image plane. The principle is named after Austrian army captain Theodor Scheimpflug, who used it in devising a systematic method and apparatus for correcting perspective distortion in aerial photographs. Because the subject plane is not parallel to the image plane, it will be in focus only along a line where it intersects the PoF. When an oblique tangent is extended from the image plane, and another is extended from the lens plane, they meet at a point through which the PoF also passes, as illustrated in the right of Figure 2.11. With this condition, a planar subject that is not parallel to the image plane can be completely in focus.

The Pentacam provides a complete analysis of the anterior and posterior surface topography of the cornea, including curvature, tangential, and sagittal (axial) maps. The topography of the anterior and posterior surfaces of the cornea is generated from a true elevation measurement. The Scheimpflug principle allows data capture in patients with significant keratoconus and other severe irregularities, which may prevent successful Placido imaging. The anterior and posterior corneal elevation maps can be shown with various reference bodies, which can be fitted in "float" or on the corneal apex.

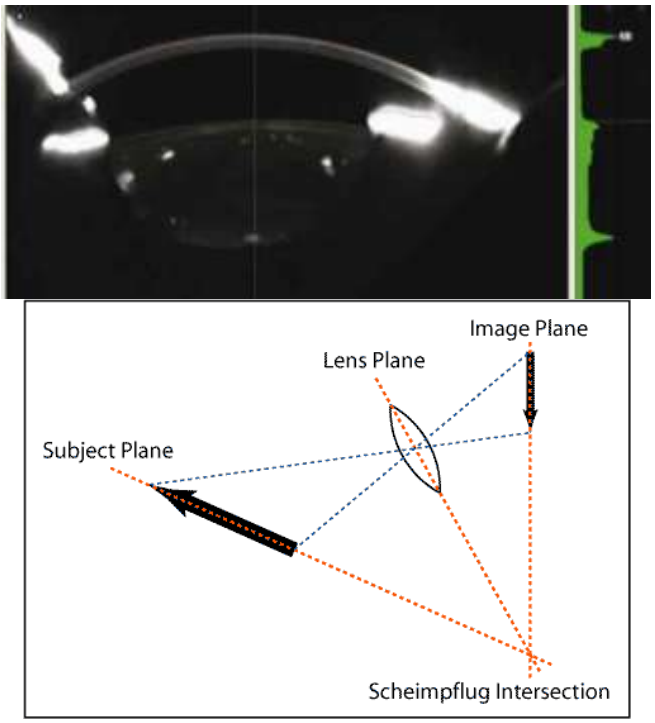

Figure 2.11 *Pentacam Scheimpflug image (left) and Scheimpflug principle (right)*

2.1.3 Techniques for Measuring Crystalline Lens Parameters: Phakometry (Purkinje Images Method)

Phako- (root word meaning lens) usually refers to the natural crystalline lens of the eye. Crystalline lens measurements are of two types: in vitro- (the technique of performing a given experiment in a controlled environment outside of a living organism) and in vivo- (the technique of performing an experiment in or on the living tissue of a whole, living organism) measurements. Ultrasound and OCT that have been introduced in 2.1.1 and Purkinje images (reflection image as shown in Figure 2.12) are the most popular in vivo methods. Though the first two methods can measure curvatures and thicknesses, they have the disadvantages of being slow and touching the cornea. Purkinje images are the sequence of reflections from the refracting surfaces of the eye. PI, PII, PIII and PIV indicate the refraction images formed at the boundary of air/cornea (or tear film), posterior cornea/aqueous, aqueous/anterior lens and posterior lens/vitreous, respectively. The Purkinje images method can measure curvatures and allows measurement while the eye is viewing a target (and can therefore monitor accommodation variations). To calculate the locations of the Purkinje images, rays are traced from an object point through the eye to the surface that creates the Purkinje image and then the rays are reflected at that surface. The reflected rays are then traced back to the cornea to find the magnification and position of the virtual image formed by the rays leaving the cornea. Using such ray-tracing the power of the reflective surfaces is Power = $(n'-n)/R$, where n and n' are refractive indexes of medias on either side of interface and R is the radius of surface curvature. On reflection, n' becomes negative and power is then $(-n-n)/R=-2n/R$. Therefore, the radius of curvature will be determined.

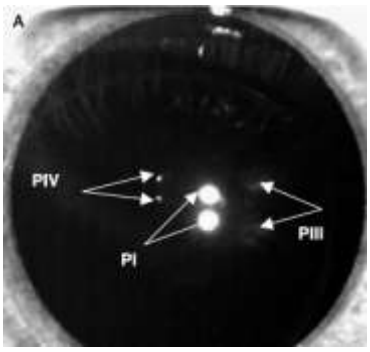

Figure 2.12 *Example photograph that shows 3 Purkinje images reflected from the anterior corneal surface (PI) and two lens surfaces (PIII and PIV).*

2.2 REVIEW OF OPTICAL PARAMETERS OF CORNEA

The cornea is the transparent front part of the eye. The refractive power of the human cornea provides approximately +43 diopters, or roughly two-thirds of the eye's total refractive power of +60 diopters. Transparency, avascularity, and immunologic privilege make the cornea a very unique tissue. It is the only tissue of a human body that has no blood supply; it obtains oxygen directly through the air. The human cornea has a diameter of about 11.5 mm and a thickness of 0.5 mm - 0.6 mm in the center and 0.6 mm - 0.8 mm at the periphery. The following will discuss the optical elements of cornea: shape (radius of curvature and asphericity) of both anterior and posterior surfaces, thickness, and refractive index.

2.2.1 Anterior Corneal Radius of Curvature (CR_1)

The anterior surface of cornea is the most contributive refractive component of human ocular optics. A collection of 40 research papers that contain measured CR_1 (in mm) data were reviewed. The results, method of measurement, number of subject, subjects' age, gender, geographic, and refractive status information are summarized in Table 2.1. The first six authors of Table 2.1 are papers that report data of scatter plot of individual measurements of young adults. Data points were extracted from these studies and plotted in Figure 2.13. Because of the overlapping symbols in the high density region near emmetropic refraction, 34 data points were unable to be extracted from the original papers. Linear regression was performed on the clearly indicated 440 data points using mean spherical refraction, K (in diopter = 1/meter), as the independent variable. This correlation can be represented by the equation, $CR_1(K) = 7.748 + 0.0155K \pm 0.264$, where the units of CR and K_1 are mm and diopter (=1/meter), respectively. The refraction correlation is weak (r^2=0.0432) but significant (p<0.0001). The average CR_1 for emmetropic eyes is 7.75 mm. The standard deviation (1 sigma) from the fitted line is 0.264 mm. One standard deviation range covers 68% of data points. This range is indicated in yellow bands in Figures 2.13 – 2.19.

Table 2.1 *Summary of 40 studies of CR_1*

Author (year)	Geographic / Ethnic	Subject no. / Eye no.	Gender	Subject age (year)	Method of measurement	Radius of corneal curvature, CR (Refractive-error, K)
Atchison 2006	Australia	121 subj. /112 OD & 9 OS	63% F	25 ± 5 yr (18 to 36)	Video-keratographic images	CR(+0.75D to -12.38D)= 0.022 K +7.77mm; n =121, r^2 = 0.048, p < 0.001
Cheung 2000	Hong Kong Chinese	63 sub./ 126 my eyes	24 F, 39 M	23±4 (18 to 39)	Topographic Modeling System (TMS-1).	flattest meridian: K=4.59 R - 39.64, r=0.51; steepest meridian: K=5.63 R - 47.35, r=0.56
Mainstone 1998	Australia	25 hyp (+2.74±1.72D)		29.9±11.4 (16 to 49)	Bausch&Lomb keratometer	CR(K=-0.37 to +6D) = 0.025K + 7.595; n=35, p=0.2609, r^2=0.038
		10 em (+.21±.26D)				
Strang 1998	Australia	57 em and hy subj		32.7±11.4 (18 to 51)	Topcon OM-4 keratometer	CR(K=-0.37 to +17.25D) = 0.04K + 7.68; n=53, p=0.009, r^2=0.128
Strang 1998	Australia, UK, USA	34 em and my subj (0 to -14D)		Young adults	All-Humphrey Auto-keratometer	CR(K=-14 to 0D) = -0.006K+7.72; n=34, r=0.84
Carney 1997	Ohio or Australia	30 em (-.25 to+.25D)	44 F, 69 M	26.4±5.9 (15 to 49)	Bausch & Lomb keratometer	CR(K=-9.88 to +0.25D) = 0.036 K + 7.762; n=113, p=0.0075, r=0.259
		30 my(-0.8 to -2D)		27.1±7.2 (22 to 52)		
		34 my (-2 to -4D)		27.7±6.4 (22 to 48)		
		19 high my (>-4D)		27±4.5 (23 to 38)		
Atchison 2008	Australia, 96+% Caucasian; K= -0.88 to +0.75D	106 subj./106 eyes	50F	18-29 yr (n=23), 30-39 yr (n=20), 40-49 yr (n=22), 50-59 yr (n=21), 60-69 yr (n=20)	Corneal topography	CR=7.66±0.26mm, n=50
			51M			CR=7.83±0.19mm, n=51
			101 mixed			Non-sgnificant slope with age, CR=7.75±0.24mm, n=101
			50F		Pentacam	CR=7.72±0.25mm, n=50
			47M			CR=7.87±0.20mm, n=47
			97 mixed			Non-significant slope with age, CR=7.79±0.24mm, n=97
Dubbelman 2006	Netherlands	114 subj/114 eyes	57F	38±14	Scheimpflug images	CR=7.72±0.23mm, n=57
			57M	39.5±15		CR=7.87±0.30mm, n=57
				39±14 (18-65)		CR(-6.88 to +3.5D)=7.84(±0.03)+0.04 (±0.01)K, r=0.29, p=0.002,n=114; CR(-1.33±2.18D) =7.79 ± 0.27 mm
Davis 2005	Ohio, US	175 subjects / eyes		(6-9) ->(11-14)	Videokerascope	CR_0=0.755±0.24; □ R ~0.17mm
		72 myopes		(6-15 yr)		CR(-1.47±1.44;≤-0.5D)=7.53±0.27mm
		370 emmetropes		(6-15 yr)		CR(0.36±0.43)=7.54±0.24mm
		201 hyperopes		(6-15 yr)		CR(1.01±0.39;≥0.75D)=7.57±0.23mm
		643 subj./643 eyes		9.9±2.4 (6-15 yr)		CR(0.31±1.12D)=7.55±0.24 mm
Logan 2005	145 W, 225 A , 3 B	373 subj./ 373 OD		19.55±2.99 yr (17–30)	IOL Master ocular biometer	7.74±0.29 (White:-1.01±2.19D); 7.77±0.24 (Asian: -1.40±2.57D)

Table 2.1, cont.

Mallen 2005	Jordan	1093 subj./ 1093 OD			Autokeratometer	CR(-0.87±1.70D)=7.71±0.30mm, CR=0.03*K+7.73mm, r=0.18, n=1093
			643F			CR(K=-0.95±1.58D)=7.67±0.31mm, n=643
			450M			CR(K=-0.74±1.84D)=7.76±0.29mm, n=450
				(17-22)		CR(K=-0.81±1.65D)=7.71±0.28mm, n=261
				(23-28)		CR(K=-1.20±1.60D)=7.72±0.31mm, n=358
				(29-34)		CR(K=-0.83±1.59D)=7.72±0.31mm, n=221
				(35-40)		CR(K=-0.44±1.88D)=7.68±0.30mm, n=253
Llorente 2004	Spain	22 hy eyes		30.3±5.2 (23-40)	Topography fit to biconic surface	CR(3.0±2.0D)=7.97 ± 0.30mm
		24 my eyes		30.5±3.8 (26-39)		CR(-3.3±2.0D)=7.86 ± 0.37mm
Kirschkamp 2004	Germany or UK	9 subj. / 9 OS	2F, 7M	(20-38 yr)	Auto-keratometer	Cycloplegia: CR=7.9±0.2 mm
						Accommodation: CR=7.9±0.2 mm
Cook 2003	UK	68 premature infants (in postmentrual age)	33F, 35M	32.9 week	Video-ophthalmo-phakometer	6.10±0.41mm (4.88-7.06mm), n=33
				36.1 week		6.43±0.24mm (5.63-6.92mm), n=44
				40 week		6.94±0.24mm (6.06-7.40mm), n=50
				44.7 week		7.21±0.28mm (6.32-7.81mm), n=47
				52.9 week		7.55±0.31mm (7.02-8.25mm), n=27
				postmenstrual age 32-53 weeks		CR= -0.0034(±0.0005)*(Week-40)^2 +0.0947(±0.0039)*(Week-40) +6.87 (±0.027) mm; K=0.24(±0.0016) *(Week -40)+0.87(±0.20)D
Gwiazda 2002	USA/ W,A,B,H	469 children/ 469 right eyes	246F, 223M	6 to 11 yr	keratometry	CR(-2.38±0.81D)=7.73±0.25mm (0°)
						CR(-2.38±0.81D)=7.59±0.24mm (90°)
Saw 2002a	Singapore /Chinese	1449 children/ 1449 OD		7-9 yr old	Autorefraction	R & K correlation to age, gender, height, weight, body-mass-index (BMI)
Saw 2002b	Singapore /Chinese	1453 children/ 1453 OD	318 M	7 yr old	Auto-keratorefractor	CR(K=-0.2±1.6D)=7.8±0.3mm, n=318
			239 M	8 yr old		CR(K=-0.5±1.7D)=7.8±0.2mm, n=239
			192 M	9 yr old		CR(K=-1.4±2.1D)=7.8±0.2mm, n=192
			313 F	7 yr old		CR(K=-0.08±1.3D)=7.7±0.2mm, n=313
			231 F	8 yr old		CR(K=-0.3±1.5D)=7.7±0.2mm, n=231
			160 F	9 yr old		CR(K=-1.1±1.8D)=7.7±0.2mm, n=160
Dubbelman 2002	Netherlands	83 subj / 83 eyes	40F, 43M	37.7±12.2 (16-62)	Scheimpflug img & Topography	CR=7.87±0.27 mm; CR=8-0.004*age, r=-0.19, p=0.09, n=83
Chang 2001	Asian	216 subj	70F, 146M	22.2±4.2 yr	Autorefractor	Larger R in eyes with longer axial length ($r = -0.22$, $p = 0.003$).
Wong 2001	Chinese in Singapore	1004 subj. /1004 OD	547F, 457M	(40-81 yr)	Autorefractor	R and K in 5 quintiles according to height, weight and BMI
Lam 1997	Chinese	60 subj.	27F, 33M	median=20 (19-24 yr)	keratometry	CR=7.80±0.24 (7.31to8.42), n=60

Table 2.1, cont.

Goss 1997	Oklahoma	34 em males	63 F, 105 M	25±4.6(21.5-44)	Bausch & Lomb keratometer or a Marco keratometer	CR(+.25±.36D)=7.77±.26mm; n=34
		71 my males		26.8±6(21.4-44)		CR(-2.87±2.14D)=7.63±0.22mm; n=71
		19 em females		25.6±4.6(21-40)		CR(+.17±.36D)=7.60±.22mm; n=19
		44 my females		25.5±4.8(21-38)		CR(-3.42±2.2D)=7.57±0.20mm; n=44
McBrien 1997	UK	14 hy subj./14 OD		29.72 (22-50 yr)		CR(+1.51±0.82D)=7.861±0.32mm, n=14
		68 em subj./68 OD		30.83 (21-61 yr)		CR(+0.10±0.25D)=7.892±0.27mm, n=68
		78 adult onset my eyes		31.04 (22-53 yr)		CR(-1.68±1.15D)=7.849±0.30mm, n=78
		47 youth onset my eyes		30.39 (21-46 yr)		CR(-3.74±2.13D)=7.847±0.33mm, n=47
		38 my onset 15-20 yr		28.77 (21-64 yr)		CR(-2.46±1.66D)=7.854±0.30mm, n=38
		166 subj				Longitudinal change
Lam 1996	Hong Kong Chinese	24 subj.	4F, 20M	19-25 yr	keratometer	OD: 7.866±0.255mm(0°); 7.660±0.286mm(90°), n=24
						OS: 7.862±0.249mm(0°); 7.648±0.278mm(90°), n=24
Lam 1994	Hong Kong Chinese	96 female subj.	96F, 124M	40-75 yr	Keratometer	CR(K=-0.29±1.93D)=7.67±0.20; n=96
		124 male subj.				CR(K=-0.28±1.99D)=7.75±0.24; n=124
Grosvenor 1994	New Zealand	194 right eyes	101 F, 93 M	18-30 yr	Auto-keratometer	CR(K=0 to +0.99D)=7.94±0.25; n=27
						CR(K=-0.01 to -1)=7.80±0.28; n=46
						CR(K=-1.01 to -2)=7.79±0.25; n=30
						CR(K=-2.01 to -3)=7.76±0.21; n=21
						CR(K=-3.01 to -4)=7.74±0.30; n=21
						CR(K=-4.01 to -5)=7.73±0.33; n=12
						CR(K=-5.01 to -6)=7.69±0.17; n=11
						CR(K=-6.01 to -7D)=7.70±0.30; n=8
Goh 1994	Hong Kong Chinese	65 female subj.	65F, 40M	19-39 yr	Keratometer	CR(K=-3.19±2.95D)=7.62±0.21; n=65
		40 male subj.				CR(K=-2.99±2.60D)=7.81±0.34; n=40
Patel 1993	UK	20 subj.		19-23 yr	Photo-Electric Keratoscope	0°: 7.71±0.43mm (7.07-8.39mm)
						90°: 7.65±0.36mm (6.94-8.13mm)
Scott 1993	New Zealand	42 em subj		17-26 yr	Auto-keratometer	CR(-0.5 to+1.5D)=7.83±0.27mm; n=42
		42 my subj				R (K=-5 to -7D)=7.70±.24mm; n=42
Garner 1992	Malay	19 em (-.25-.25D)	9 F, 10 M	9-15 yr	ophthalmometry	CR(0.01±0.05D)=7.69±0.28mm; n=19
		19 my subj(>-3D)				CR(-6.08±1.83D)=7.84±0.28mm; n=19
Bullimore 1992	UC, Berkeley	14 em subj				CR(-0.08±0.25D)=7.86±0.25mm; n=14
		14 my suj				CR(-2.18±1.05D)=7.86±0.17mm; n=14

Table 2.1, cont.

Dunne 1992	UK	80 subj.	40F		keratometer	CR(-1.52±3.86D)=7.84±1.58mm, n=40
			40M			CR(1.11±2.4D)=7.98±1.01mm, n=40
				22.0±3.3yr (n=60)		CR(-2.05±3.18D)=7.96±1.32mm, n=60
				74.6±5.6yr (n=20)		CR(0.92±2.24D)=7.77±1.19mm, n=20
Goss 1990	Japan, England, Oklahoma	my: 396 F, 415 M; hy: 237F, 238M		<16yr (n=677); ≥16yr (n=609)	keratometry	R correlation to K: r=-0.14 for males, r=-0.07 for females
Sheridan 1989	UK	21 my			keratometry	R mean=7.75mm
		23 em				R mean=7.92mm
		12 hy				R mean=7.98mm
Mcbrien 1987	UK	30 em subj		Young adults		CR(K=+0.17±0.26D)=7.96±0.28mm(0°), 7.84±0.25mm(90°); n=30
		30 my subj				CR(K=-1.29±0.75D)= 7.95 ±0.22mm (0°) 7.86±0.22 mm(90°); n=30
Lam 1991	Asian & White	65 Chinese	All male	22.8±2.4yr	keratometry	OD: CR=7.737±0.238mm(0°); 7.904±0.228mm(90°), n=64
						OS: CR=7.745±0.239mm(0°); 7.912±0.227mm(90°), n=65
					photokeratoscopy	OD: CR=7.729±0.218mm(0°); 7.865±0.212mm(90°), n=64
						OS: CR=7.721±0.230mm(0°); 7.858±0.220mm(90°), n=65
		65 Caucasian		21.2±2.6yr	keratometry	OD: CR=7.887±0.212mm(0°); 8.033±0.203mm(90°), n=63
						OS: CR=7.861±0.219mm(0°); 8.020±0.204mm(90°), n=63
					photokeratoscopy	OD: CR=7.866±0.204mm(0°); 7.985±0.213mm(90°), n=63
						OS: CR=7.824±0.231mm(0°); 7.972±0.206mm(90°), n=63
Guillon 1986	Caucasian in UK	110 subj. /220 eyes	65F, 45M	33.4±11.4 (17 to 60 yr)	keratometry	Flat: 7.856±0.254mm (7.24-8.49 mm)
						Steep: 7.692±0.256mm (7.02-8.31)
					photokeratoscopy	Flat: 7.873±0.250mm (7.14-8.54 mm)
						Steep: 7.704±0.270mm (7.03-8.86)
Edmund 1985	Denmark	40 subj. /80 eyes	21F, 19M	31.4 yr (17 to 66 yr)	photokeratoscope	0°: 7.85±0.24mm(OD); 7.86±0.25mm(OS)
						90°: 7.76±0.24mm(OD); 7.63±0.24mm(OS)

Table 2.1, cont.

Kiely 1984	Australia	98 subj. /196 eyes	44F, 54M	16-80 yr	autocollimating photokeratoscope	CR(0°)=7.79±0.26 (7.10-8.75) mm; =7.86±0.27(male); 7.70±0.24(female); =7.81±.21(16-20yr);7.86±.27(21-40yr) =7.73±.25(41-60yr);7.65±.29(61-80yr)
						CR(45°)=7.72±0.26 (7.13-8.16) mm; =7.79±0.28(male); 7.63±0.24(female); =7.74±.19(16-20yr);7.79±.22(21-40yr) 7.68±.26(41-60yr); 7.57±.29(61-80yr)
						CR(90°)=7.68±0.28 (7.06-8.66) mm; =7.75±0.28(male); 7.58±0.26(female); =7.68±.18(16-20yr);7.74±.26(21-40yr) =7.65±.28(41-60yr);7.56±.32(61-80yr)
						CR(135°)=7.72±0.26 (7.11-8.72) mm; =7.79±0.27(male); 7.62±0.25(female); =7.72±.19(16-20yr);7.79±.26(21-40yr) =7.68±.26(41-60yr);7.58±.31(61-80yr)
Alsbirk 1977	Greenland Eskimos	n=261 Females	261 F	mean 42.3 yr	Keratometer	CR(K=+0.25±1.25D)=7.68±0.24mm; CR(K-0.28D)=7.69mm(20yr); CR(+0.90D)=7.66mm(70yr)
		n=222 Males	222 M	mean 42.6 yr		CR(K=-0.07±1.34D)=7.85±0.23mm; CR(K=-0.01D)=7.84mm(20yr) ; CR(K=-0.18)=7.85mm(70yr)
W: White	A: Asian	hy: hyperopic		F: female	OD: right eye	CR: anterior cornea radius of curvature
B: Black	H:Hispanic	em: emmetropic		M: male	OS: left eye	K: refractive error (spherical equivalent)
		my: myopic		yr: year old	D: diopter	

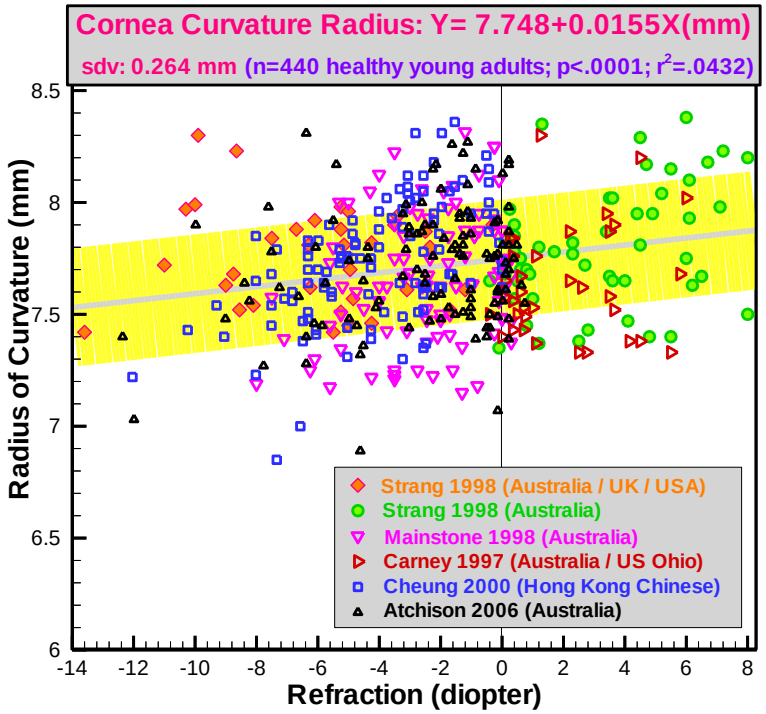

Figure 2.13 *Scatter plot and linear regression from 6 papers in Table 2.1*

Probability Distribution Function:

To illustrate the probability distribution function (PDF), the 440 data points are separated into 5 refraction groups: group 1 (-13.60D≤ K ≤-5.25D, n=88), group 2 (-5.24D≤ K ≤-2.77D, n=88), group 3 (-2.77D≤ K ≤1.27D, n=88), group 4 (-1.20D≤ K ≤0.22D, n=88), and group 5 (0.22D≤ K ≤8.00D, n=88). Figure 2.14 shows the PDF of each group. The mean CR_1 and the deviation in each refraction group are indicated in the plot. The means of the 5 normal distribution curves stay close to the linear regression line as indicated in Figure 2.14: -0.05, 0.07, 0.02, -0.01, and -0.10 mm shifts. The standard deviation in each group is reduced from 0.26 mm to ~0.23 mm when refraction region is better specified. It suggests that the linear correlation through a wide refraction range (-14D to +8D) may not be the best way to describe the refraction correlation of CR_1. Some research groups separate myopic and hyperopic groups in performing linear regression analysis since the causes of the two may be from different mechanisms [Strang 1998 a, b]. Nevertheless, only linear regression is used for the correlation fitting in all studies.

Correlation to Refractive Error:

Figure 2.15 illustrates comparisons of the representative linear regression result with the 6 studies listed on top of Table 2.1. There are 2 studies performed for hyperopic data. Strang's data [Strang 1998a] shows higher increasing rate in CR_1 as hyperopic refractive error increase. Mainstone's data [Mainstone 1998] has a very agreeable rate (slope) with the referenced gray line. This measurement of 35 samples has a nice small standard deviation (indicated by the vertical dimension of the red box). However, the CR_1 data is systematically lower for about ~0.15 mm.

Strang's myopic data [Starng 1998b] shows opposite correlation slop (increasing rate) in contrast to all other 3 studies results. Atchison reported good agreement, $Y=7.773+0.0221X$, with the reference we obtained [Atchison 2006]. Carney's data [Carney 1997] has larger myopic reducing rate, $Y=7.762+0.036X$. His measurement has larger standard deviation. Chinese data of Cheung shows an even larger decreasing rate on both steeper and flatter cornea meridians compared to other studies [Cheung 2000]. The CR_1 at emmetropic refraction (K=0) is also significantly higher than other studies. It is not clear what the responsible factor is for this discrepancy. However, this study did use a different measurement technique and analysis method that could lead to the discrepancy when compared to others. Further investigation is needed to support the race or geographic influences. The race factor will be discussed further at the end of this section.

Figure 2.16 shows the comparison of the fitted regression (grey line) with 8 additional studies. All 8 studies were performed on only adult subjects. As indicated in the Figure 2.16, multiple refraction data provide very close results on the refraction correlation (slopes) when compared to the reference. The data of Grosvenor 1994 and Scott 1993 are in especially good agreement with the reference gray line. Only Llorente 2004 has a larger distribution deviation than the reference. This may be a result from the considerably smaller number of subjects across a wider refraction range (shown in whiskers). All 7 studies have mean CR_1 values slightly higher than reference line by ~0.02 to 0.25 mm. These parallel shifts could be simply contributed from the systematic calibrations. These studies further confirm the significance of refraction correlation.

With unspecified subjects' refractions, another 8 studies reported fundamentally the same or slightly higher values than the emmetropic average of 7.748 mm as shown in Figure 2.17. Kirschkamp 2004 (UK) study reported 7.9±0.2 mm (n=9), Doubbleman 2002 (Netherlands) study had 7.87±0.27mm (n=83), Guillon 1986 (UK Caucasian) has 7.774±0.255mm (n=220), and Sheridan 1989 (UK) reported 7.75 mm, 7.92 mm, and 7.98 mm for myopia (n=21), emmetropia (n=23), and hyperopia (n=12) respectively. The vertical bars indicate the standard deviation of the data and symbols are the mean values.

Dependence on Body Height, Weight, and Body Mass Index:

Wong [Wong 2001] and Saw [Saw 2002a] gave CR_1 and K in 5 and 4 quartiles according to height, weight and BMI. Wong indicated that height and weight correlate positively with CR_1, but BMI does not

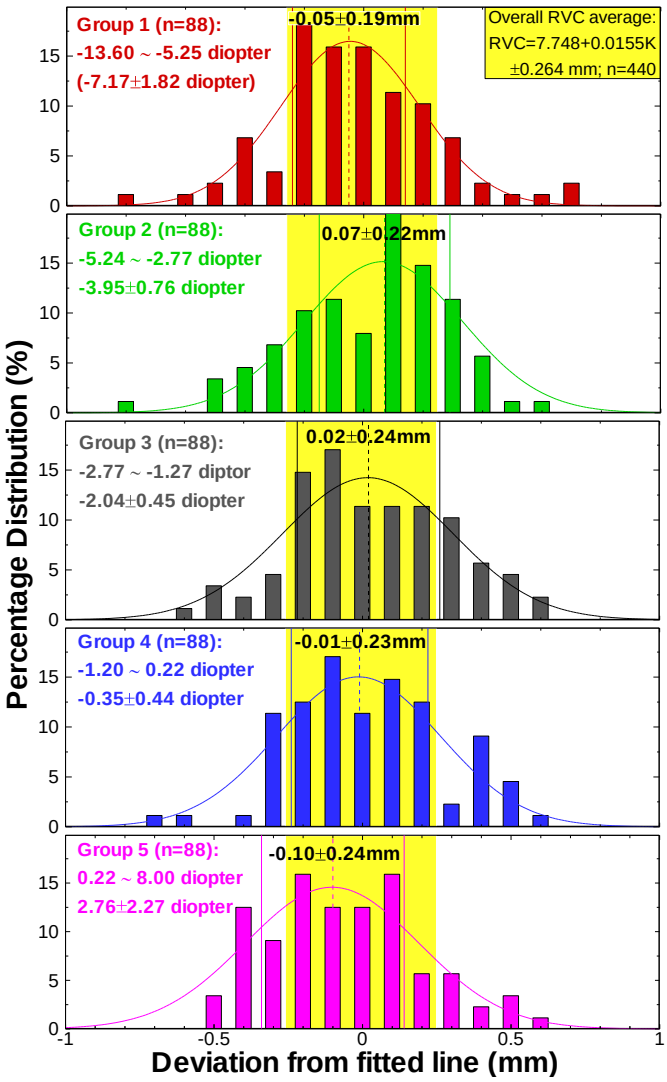

Figure 2.14 *Probability distribution functions of CR1 along the fitted line in Figure 2.13*

correlate with CR_1. [Wong 2001] The taller children are more myopic and have greater CR_1. Heavier children are also more likely to have eyes with more hyperopic refractions. Lower myopes are more likely to weigh less (p=0.008) than emmetropes, but higher myopes and hyperopes do not differ in weight from emmetropes (p=0.94, p=0.13, respectively). but the more obese (higher BMI) children are more likely to have refractions that are more hyperopic. In addition, obese girls have eyes with significantly flatter corneas (p=0.012). [Saw 2002 a]

Gender Dependence:

Gender difference of CR_1 is discussed in several of the collected papers. Males have larger CR_1 than females universally. Figure 2.18 shows the comparison of 6 studies. As the dashed lines in Figure 2.18 show, Atchison 2006 study suggests a significant mean separation of 0.12 mm along a range of refraction between the two genders' populations. Also shown in Figure 2.6, the estimate of gender separation from studies of Alsbirk [Alsbirk 1977] (Eskimos), Dunne [Dunne 1992] (UK), Lam [Lam 1994] (Hong Kong), Goh [Goh 1994] (Chinese), and Goss [Goss 1997] (US) range from 0.09 to 0.19 mm. The Dubbelman [Dubbelman 2006] study also indicates an average of 0.15 mm separation between genders, but the refractions of the 2 groups are not specified. These results suggest a common larger CR_1 measurement on males over females of about 0.14 mm. Its dependence on refraction is not clear. [Kiely 1984]. Gwiazda showed there was a gender difference, with eyes in girls having significantly steeper corneas in both meridians. In the horizontal meridian, mean corneal radius in girls' eyes was 44.0 D compared with 43.5 D in boys' ($P<0.001$), and in the vertical meridian mean corneal radius in girls' eyes was 44.8 D compared with 44.2 D in boys' ($P<0.0001$) [Gwiazda 2002]. Males had larger radii of curvature than females by a mean 0.17mm ($P<0.001$) [Atchison 2008].

Age Dependence:

Age dependence is studied in many papers. Shown in Figure 2.19 are some of these study results in comparison to the average adult reference in grey line. The Cook 2003 study shows the premature infant data in green color. The rapid development of CR_1 approaches to nearly the adult range at 1 year of age. Cook also gave the equation of the corneal radius growth rate $CR_1=-0.0034(\pm0.0005)*(Week-40)^2+0.0947(\pm0.0039)*(Week-40)+6.87(\pm0.027)$mm with the refractive growth rate $K=0.24(\pm0.0016)*(Week-40)+0.87(\pm0.20)D$ [Cook 2003]. Davis' study includes a large subject number of 643 6-15 year old US children [Davis 2005]. As shown in blue (cyan) square symbol, the average cornea radius for this younger group is about 0.2 mm lower than the average of adults. The reliability of this data point is also shown by the smaller standard deviations as indicated by the blue box. In a separate, 5-year, longitudinal study in this paper, a group of 175 children, from 6-9 year-old to 11-14 year-old period, the radius of cornea curvature increases 0.15 mm in average while the refraction correction changes a non-significant -0.5D. This indicates a growth rate of ~0.03mm per year during the age in primary school.

A study performed by Garner in 1992 on the age group, 9-15 year-old, shows larger CR_1 average numbers (orange symbols) especially for the myopic group ($n=19$). The mean of these myopic children's cornea radius of curvature appears slightly higher than adults by 0.2 mm. The myopic group of these Malay children data seems to be unlike the other refraction correlation results (slope) [Garner 1992].

For the older adults after 18, no convincing aging effect was found. Koretz examined aging of many anterior segments, and no age dependence on CR_1 was observed in adults 18-70 years old [Koretz 1989]. Another study performed by Dunne in 1992 provides also no conclusive aging effect over CR_1 (as shown in Figure 2.26, where purple, diamond symbol indicates young adult and circle symbol indicates adults in their 70th) [Dunne 1992].

Dependence on Race:

Regarding the ocular biometry dependence on race, little information was found. Most studies in our collection do not specify the ethnic conditions. In Table 2.1, the geographic location where the research was performed was listed when this ethnic condition was not specified. The ethnic or geographic condition of the subject groups are indicated in Figures 2.13, and 2.15 to 2.19 for comparison. Since the measurement and analysis methods vary across studies and small systematic errors need to be taken into account, unless the ethnic investigation is performed under the unbiased condition, it is difficult to draw conclusion. Logan examined UK Asian and White with good sample numbers n=217 & 145 (Figure 2.16). No significant difference was found [Logan 2005].

Accommodation:
It is believed and also shown by Kirschkamp that accommodation does not change anterior corneal radius. [Kirschkamp 2004]

2.2.2 Asphericity of Anterior Cornea Surface (Q_1)

In the previous section, the anterior corneal vertex radius of curvature was reviewed. Radius of curvature defines a spherical surface. However, the anterior cornea surface is aspherical as it extends toward its periphery. Therefore, a shape factor, the conic constant, Q_1, is commonly used to describe the asphericity. A collection of 18 research papers that contain measured asphericity of anterior cornea surface were reviewed. The mathematical definition of Q_1 will be given in the beginning of chapter 3. The statistical results, method of Q_1 measurement, the number and age of subjects, , gender, geographic, and refractive status information were summarized in Table 2.2.

Representative correlation to refractive error:
Three of the 18 papers include scatter plots (Q_1 *vs. K)* of individual measurements of adults [Atchison 2006, Mainstone 1998, and Carney 1997]. Data points were extracted from these studies and plotted in Figure 2.20. Atchison gives the correlation $Q_1 = -0.136-0.0002K$; $n=121$, $p=0.962$, $r^2=-0.008$, as indicated as red dashed line [Atchison 2006]. He omitted the refraction correlation and used *-0.15 (-0.148± 0.107)* in his ametropic eye modeling. In contrast, Carney (1997) obtained the significant conclusion: $Q_1=-0.402-0.032K$ ($n=105$, $r^2=0.076$, $p=0.005$), as shown in blue dashed line. The Mainstone study provides data of hyperopic eyes [Mainstone 1998]. Because of the symbol overlapping in the high density region near emmetropic refraction, 35 data points were unable to be extracted from the original papers (mainly from Carney's paper. 84/113) [Carney 1997]. Linear regression was performed on the clearly indicated 236 data points using the mean spherical refraction, *K* (in diopter = 1/meter), as the independent variable. This correlation can be represented by the equation: $Q_1 = -0.2654-0.0145K$. The statistical significance of this fitting is indicated in the p-, r-, and standard deviation values in the figure. This representative correlation and the distribution (standard deviation) are plotted in black solid line and the gray shaded band in the figure. One paper of children's data of scatter plot is also included in the same figure [Horner 2000] for presentation.

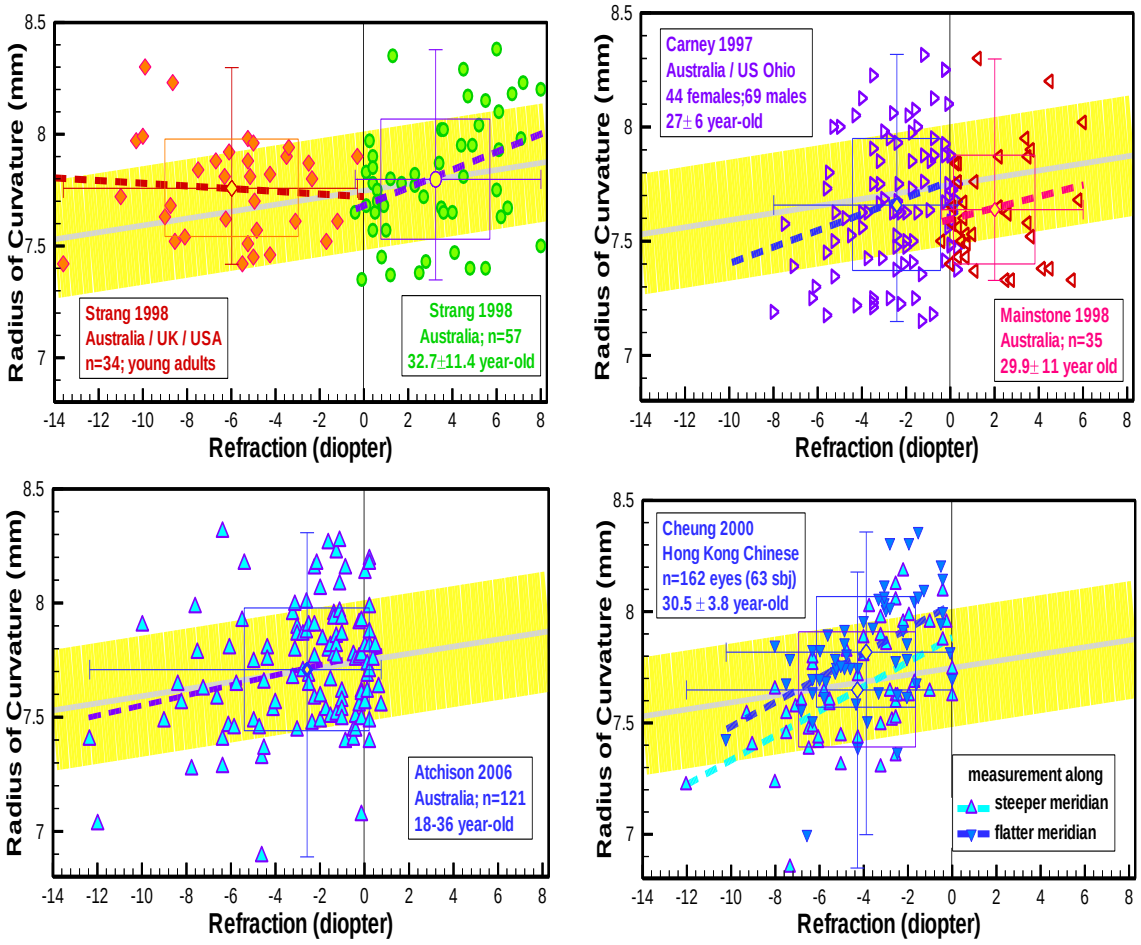

Figure 2.15 *Scatter plot comparison of linear regression result and the 6 studies in Table 2.1.*

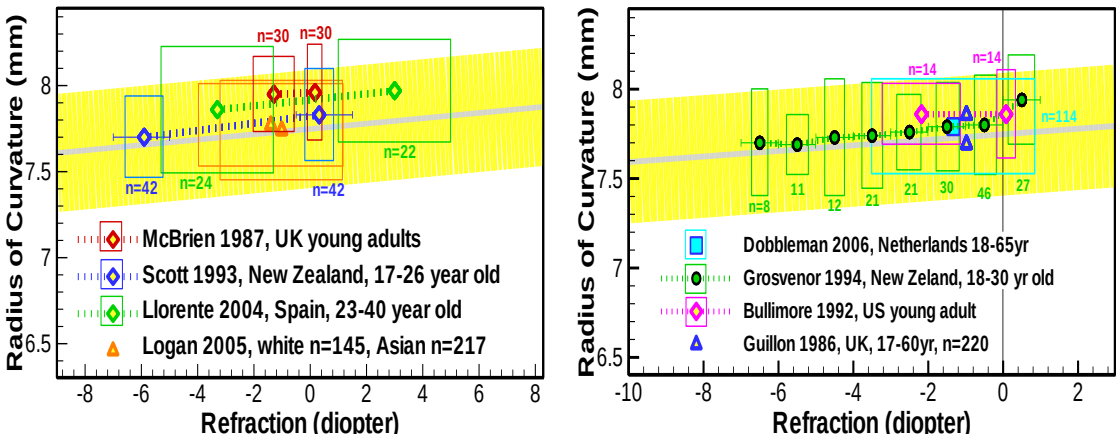

Figure 2.16 *Comparison of adult linear regression result and 6 studies. The 2 symbols of Guillon 1986 data were acquired from the steepest and flattest meridians of same subjects.*

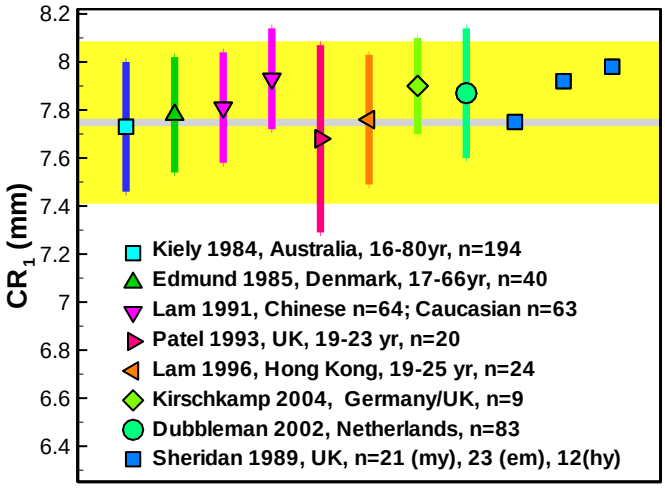

Figure 2.17 *Comparison of adult CR1 mean with 8 studies.*

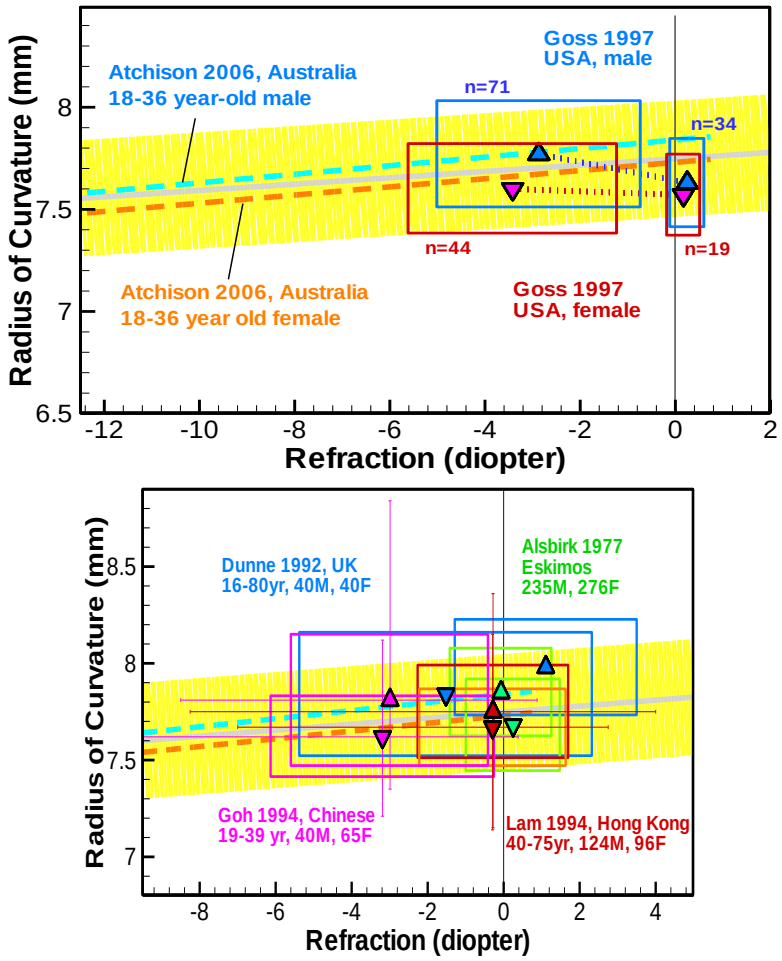

Figure 2.18 *Comparison of linear regression result and 6 studies that indicate gender difference. The delta (▲) and gradient (▼) symbols in the 5 studies indicate male and female data respectively.*

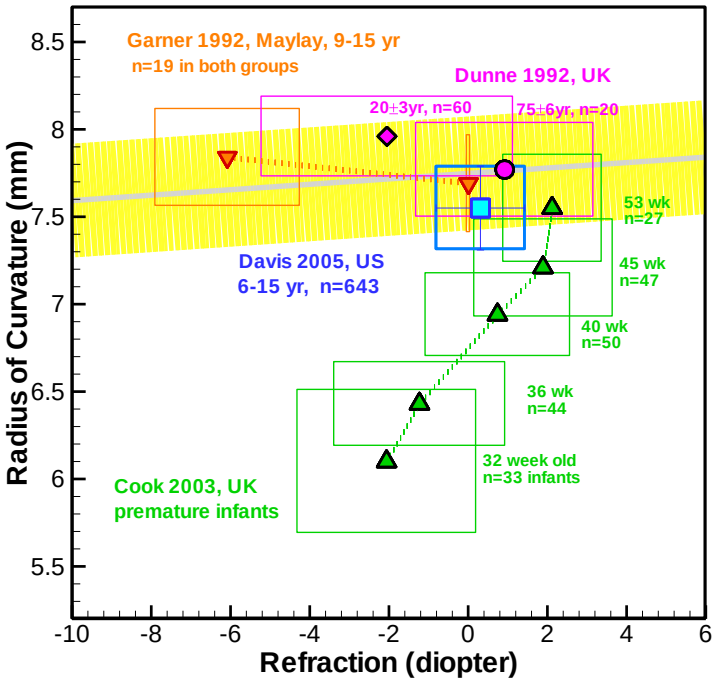

Figure 2.19 *Comparison of linear regression result of adults and 6 studies that indicate age dependence.*

Table 2.2 *Summary of 18 papers of Q_1*

Author (year)	Geographic / Ethnic	Subject no. /Eye no.	Gender	Subject age (year)	Method of test	Asphericity of cornea, Q (Refractive-error,K)
Atchison 2008	Australia (>96%) & Caucasian	106 subj./106 eyes (K=-0.88 to +0.75D)	50F	18-29(n=23), 30-39(n=20), 40-49(n=22), 50-59(n=21), 60-69(n=20)	Corneal topography	Q=-0.14±0.12, n=50
			51M			Q=-0.13±0.15, n=51
			mix			Non-sgnificant slope with age, Q=-0.132±0.137, n=101
			mix		Pentacam	Q=-0.0036+0.0038*age (adjusted r^2=0.030, n=97, p=0.045).
Atchison 2006	Australia	121 subj./112 right eyes and 9 left eyes	63% F	25 ± 5 (18–36)	Video-keratographic images	Q(+0.75D to-12.38D)=-0.136-0.0002K, n = 121, r^2 = 0.008, p = 0.962 K is spectacle mean spherical refraction
Dubbelman 2006	Netherlands	114 subj/114 eyes	57F, 57M	39±14 (18-65)	Scheimpflug images	Q=-0.24+0.003*age, r=0.38, p<0.0001, n=114

Table 2.2, cont.

Davis 2005	CA, USA	643 subj./643 eyes		9.92±2.42 yr (6-15yr) . 5-yr-longitudinal study: (6-9 yr) to (11-14yr)	Video-kerascope	Myopes (≤-0.50D, -1.47±1.44D): -0.32±0.10, n=72; 5-yr-period: ΔK=-3.72±3.33D, ΔQ=0.086±0.109, n=8
						Emmetropes (-0.50D<K<+0.75D, 0.36±0.43D): -0.35±0.10, n=370; 5-yr-period: ΔK=-0.48±0.60D, ΔQ=0.106±0.062, n=92
						Hyperopes (≥0.75D, 1.01±0.39D): -0.36±0.10, n=201; 5-yr-period: ΔK=-0.48±0.49D, ΔQ=0.098±0.077, n=75
Llorente 2004	Spain	22 hy eyes		30.3±5.2 (23-40)	Topography+ biconic fitting	Q(K=3.0±2.0D)=–0.10 ± 0.23
		24 my eyes		30.5±3.8 (26-39)		Q(K=-3.3±2.0D)=–0.20 ± 0.17
Dubbelman 2002	Netherlands	83 subj/83 eyes	40F, 43M	37.7±12.2 (16-62)	Scheimpflug images & Corneal topography	Q=-0.19±0.02; Q=-0.2+0.0003*age, r=0.02, p=0.85, n=83
Horner 2000	Indiana	48 subj		11-13 yr old at beginning of the 5-year study	EyeSys corneal topography	Q=0.0066K-0.057296, r=0.079183, n=48
Budak 1999	Houston	(≥+1D):77eye; (-2 to+1D): 56eye;(-6to-2D): 113 eyes; (<-6D): 41eyes (Total: -2.41±3.70; -20 to 6.87)		40.67±12.39 (8-71)	keratometry and CVK(ECAS, version 3.2)	Q=-0.03±0.23 (-0.90-0.82)
MainStone 1998	Australia	25 hy subj (+2.74±1.72D)		29.9±11.4 (16 to 49)	Computerized video-keratoscope	Q(K=-0.37 to +6D)=0.009K-0.35, n=35, p=0.7419, r^2=0.003
		10 em subj (+.21±.26D)				

Table 2.2, cont.

Carney 1997	Ohio or Australia	30 em (-.25 to +.25D)	44 F, 69 M	26.4±5.9 (15-49)	Bausch & Lomb keratometer	Q(K=-9.88 to +0.25D)=-0.032K-0.402, n=113, p=0.0045, r=0.275
		30 low my (0.75 to-2D)		27.1±7.2 (22-52)		
		34 mod-my (-2 to -4D)		27.7±6.4 (22-48)		
		19 high my subj (>-4D)		27±4.5 (23-38)		
Lam 1997	Hong Kong Chinese	60 subj.	27F, 33M	20 (19-24 yr)	keratometry	Q=-0.3±0.13 (-0.64to0.06), n=60
Lam 1996	Hong Kong Chinese	24 subj.	4F, 20M	(19-25 yr)	keratometer	right eyes: -0.173±0.064(horizontal); -0.130±0.089(vertical)
						left eyes: -0.180±0.056(horizontal); -0.132±0.113(vertical)
Eghbali 1995	US	41 subj.	25F, 16M	37±10 (23-61)	keratometry	Q(K=-3.6±1.5D)=-0.18±0.21
Patel 1993	UK	20 subj.		(19-23 yr)	Photo-Electric Keratoscope	Horizontal: -0.05±0.19 (-0.31-0.54), n=20
						Vertical: 0.02±0.30 (-0.31-0.24), n=20
Lam 1991	Chinese and Caucasian	65 Chinese	All male	22.8±2.4yr	Photo Electronic Keratoscope	right eyes: Q=-0.186±0.084(horizontal); -0.141±0.148(vertical), n=64
						left eyes: Q=-0.177±0.088(horizontal); -0.150±0.175(vertical), n=65
		65 Caucasian		21.2±2.6yr		right eyes: Q=-0.221±0.092(horizontal); -0.166±0.123(vertical), n=63
						left eyes: Q=-0.217±0.094(horizontal); -0.166±0.149(vertical), n=63
Guillon 1986	Causasian in UK	110 subj./220 eyes	65F, 45M	33.4±11.4 (17-60) yr	keratometry	flat meridian: Q(K=-0.98±2.36D)=-0.17±0.13 (range -0.79to0.20)
						steep meridian: Q(K=-0.98±2.36D)=-0.19±0.16 (range -0.89 to 0.16)
Edmund 1985	Denmark	40 subj. /80 eyes	21F, 19M	31.4 (17 to 66) yr	Wesley-Jessen photo-keratoscope	horizontal: -0.32±0.11 (right eye); -0.26±0.10 (left eye)
						vertical: -0.30±0.16(right eye); -0.24±0.14 (left eye)

Table 2.2, cont.

Kiely 1984	Australia	98 subj. /196 eyes	44F, 54M	16-80yr (16-20, N=19; 21-40, N=43; 41-60, N=15; 61-80, N=21)	Auto-collimating photo-keratoscope	**(horizontal):** Q=-0.21±0.13(male); -0.19±0.16 (female); total:-0.20±0.15 (-0.62-+0.13) (K=-5to+5D) **(45 degree):** Q=-0.20±0.20 (male); -0.20±0.20 (female); total:-0.20±0.20 (-0.75-+0.58) (K=-5to+5D) **(vertical):** Q=-0.20±0.24(male); -0.20±0.19(female); total:-0.20±0.22 (-1.11-+0.52) (K=-5to+5D) **(135 degree):** Q=-0.25±0.19(male);-0.24±0.24(female); total:-0.25±0.21 (-1.19-+0.39) (K=-5to+5D) **(horizontal) :** Q=-0.21±0.13(16-20yr); -0.21±0.14(21-40yr);-0.23±0.14(41-60yr); -0.16±0.17 (61-80yr) **(45 degree):** Q=-0.19±0.19(16-20yr);-0.20±0.19(21-40yr); -0.24±0.21(41-60yr); -0.19±0.23 (61-80yr) **(vertical):** Q=-0.19±0.19(16-20yr);-0.22±0.23(21-40yr); -0.21±0.15(41-60yr); -0.16±0.25 (61-80yr) **(135 degree):** Q=-0.25±0.15(16-20yr);-0.26±0.18(21-40yr); -0.22±0.17(41-60yr); -0.25±0.33 (61-80yr)

W:White	A: Asian	hy: hyperopic	F: female	OD: right eye	Q: anterior corneal asphericity
B: Black	H:Hispanic	em: emmetropic	M: male	OS: left eye	K: refracrive error (spherical equivalent)
		my: myopic	yr: year old	D: diopter	

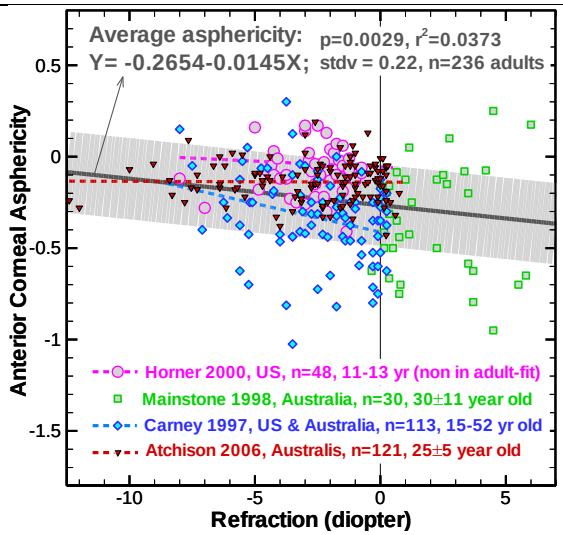

Figure 2.20 *Scatter plot of Q_1 vs. K from 4 papers. Adult data from 3 papers were used to obtain the representative regression fitting as indicated on top of the figure.*

Probability Distribution:

To acquire the probability distribution function (PDF) of Q_1, the 236 data points are separated into 4 refraction groups: group 1 (-12.40D≤ K ≤-3.50D, n=59), group 2 (-3.50D≤ K ≤-1.50D, n=59), group 3 (-1.40D≤ K ≤0.00D, n=59), and group 4 (0.00D≤ K ≤6.00D, n=59). Figure 2.21 shows the PDF of each group. The mean Q_1 and the deviation in each refraction group are indicated in the plot. The means of the 4 normal distribution curves stay close to the linear regression line show the shifts: 0.02, 0.04, 0.08, and 0.05 mm. The distribution ranges of Q_1 at high myopic and hyperopic populations are wider compared to emmetropic group. Some research groups separate myopic and hyperopic groups in performing linear regression analysis since the causes of the two may be from different mechanisms [Strang 1998 a, b]. Nevertheless, only linear regression is used for the correlation fitting in all studies. The standard deviation in each group is reduced from 0.22 mm to 0.12 – 0.19 mm when refraction region is better specified. It suggests that the linear correlation through the wide refraction range (-14D to +8D) may not be the best way to describe the refraction correlation of Q_1.

Correlation to Refractive Error:

Shown in Figures 2.22 and 2.23 are comparisons of the representative fitting with many other studies. The representative fitted line and its standard deviation are plotted in black line and gray shaded band. The majority of studies are results from adult data. The Navarro [Escudero-Sanz 1999, and Navarro 1985] emmetropic model uses $Q_{1=}$ -0.26., which is right on the fitted line (left of Figure 2.22). The standard deviation of Q_1 universally falls in the range between 0.2 and 0.3. Although the majority of these studies do not investigate the correlation of Q_1 to refraction, K, the average refractive errors are reported in a good portion of these papers and are plotted in Figure 2.22. The overall result shows the agreement of negative correlation: hyperopic eyes (marked as positive refraction) tend to have more negative Q_1 value; i.e. slightly more prolate elliptic or flatter on the peripheral. The children studies of Davis (2005) shows the similar negative refraction correlation (slope) of Q_1 as indicated in orange dotted line in the right plot. The Davis study in children includes a very significant good sample number of n=643 [Davis 2005]. Carney et al. did not report refractive errors of individual subjects, but a significant (n=105; r^2=0.076; p=0.005) and stronger correlation, $Q_1 = -0.402 - 0.032 * K$, is given [Carney 1997]. This correlation is indicated in orange dotted line on the right plot of Figure 2.22.

Correlation to Age:

As indicated in Table 2.3, Atchison [Atchison 2008] reported that anterior corneal asphericity depended on age as described by the equation Q_1=*-0.0036+0.0038*Age* (adjusted r^2=0.030, p=0.045, n=97) based on Pentacam measurement results, however, no significant age dependence was found in cornea topography measurement. Dubbelman [Dubbelman 2006 and 2002] reported that anterior corneal asphericity depended on age as described by the equations Q_1=*-0.24+0.003*Age* (n=114) and Q_1=*-0.2+0.0003*Age, r=0.02, p=0.85* (n=83) in 2006 and 2002, respectively. All three of these studies suggest that as age increases, the Q_1 value become less negative; i.e. less prolate and more circular. The two children studies in the right side of plot do not show clear evidence in comparison to other adult data. The investigation of Kiely [Kiely 1984] (Figure 2.23) shows support of this trend in trivial amplitude. The younger cornea seems to be flatter on the periphery than the older cornea.

Dependence on the ocular meridian:

Some studies measure corneal asphericity in different ocular meridians especially the vertical and horizontal. These studies results are illustrated in Figure 2.23. Except for Kiely [Kiely 1984] study, Lam ([Lam 1991], both Chinese and Caucasian), Lam [Lam 1996], Patel [Patel 1993], and Edmund [Edmund 1985] suggest that the cornea periphery is more steep in the vertical meridian than the horizontal direction.

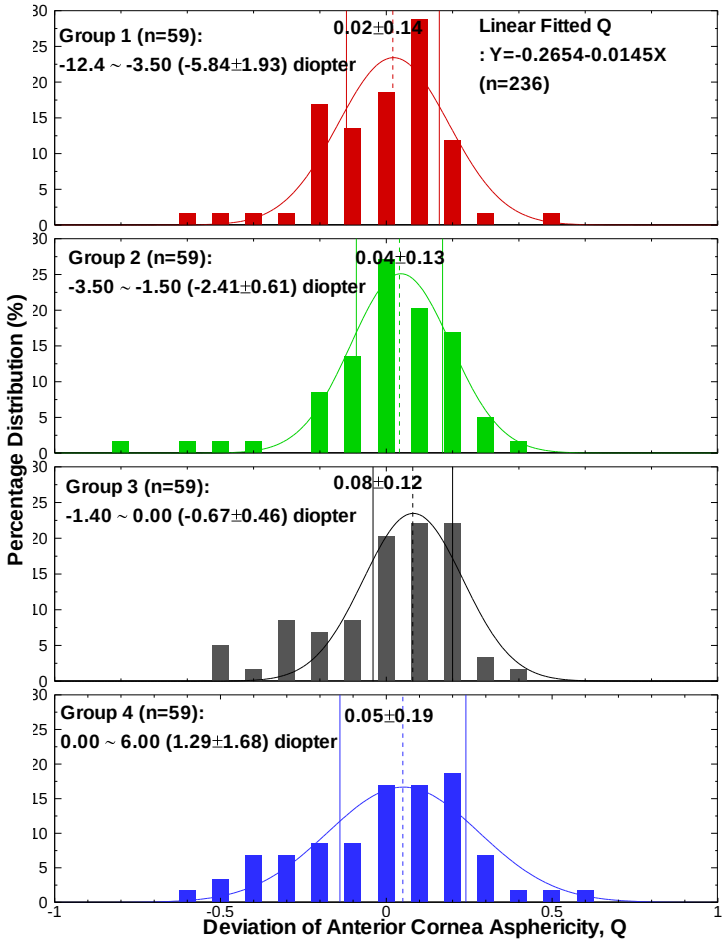

Figure 2.21 *Probability distribution functions of Q_1 along the adult fitted line in Figure 2.20*

Race dependence:
Lam [Lam 1996] is the only study that examines the difference between Chinese (n=129) and Caucasian (n=126). Chinese corneas were found to be less flat than the British Caucasian. The comparison between studies performed in different geographic areas shows no clear indication of race dependence.

Gender dependence:
There is no sufficient data for a discussion of the influence of gender. Kiely's [Kiely 1984] measurement suggests no noteworthy difference between the genders (see Table 2.2).

2.2.3 Central Corneal Thickness (CCT)

Central corneal thickness (*CCT*) is the distance between the vertexes of anterior and posterior corneal surfaces. In 2000, Doughty and Zaman [Doughty 2000] reviewed about 600 CCT studies from 1968 to 1999 and performed mete-analysis for correlations of intraocular pressure (IOP), medical procedures, and many other factors. They obtained the mean CCT of normal eyes at 0.534 mm (from 300 studies, which did not report the standard deviation) and 0.536 mm (from 230 studies, which reported the standard deviation. studies-averaged standard deviation, SD, is 0.031mm). The means obtained from 2 major types of measurements were reported as 0.530 ± 0.029 mm for slit-lamp data and 0.544 ± 0.034 mm for ultrasound measurements. However, they believe this difference may be caused by the type of individual studied (non-surgical vs. pre-surgical patients) rather than the techniques themselves. *CCT* data from 6 papers after 2000 and 2 before 2000 were collected and summarized in Table 2.3.

Correlation with Refractive error:
Pedersen in 2005 [Pedersen 2005] provided the comparison of 14 papers that study myopia correlation. Among those, 8 studies found no correlation [Liu 2000, Cho 1999, Price et al. 1999, Tanaka et al. 1996, Ehlers 1976, Hansen 1971, Martola 1968, and Blix 1880]. Among the 5 studies with the conclusion of significant correlation, 4 reported thinner CCT in myopic eyes [Touzeau et al. 2003, Srivannaboon 2002, Alsbirk 1978, and von Bahr 1956]. Only one study [Kunert et al. 2003 in India] found the thicker CCT in high myopic eyes with a large subject number of 615.

Figure 2.24 compares 5 studies and illustrates the correlation between central corneal thickness (*CCT*) and spherical equivalent refraction (*K*). The black line and gray shaded area on the background indicate the constant statistical mean at 0.536 mm and standard deviation of 0.031 mm that were reported by Doughty. The orange dashed line corresponds to the statistically significant linear fitting of data points from Chang's study (r=0.16, p=0.021) in Asain subjects [Chang 2001]. In contrast, the green dashed line indicates the result from Hosny's study in Caucasians [Hosny 2000]. Also statistically significant, Suzuki 2005 reported that the correlation between refraction and *CCT* differed between men and women. In men, refraction was negatively correlated with *CCT*, although the correlation was relatively weak (r=-0.045; p=0.018). In women, there was no correlation between refraction and *CCT*. In children study, Tong in 2004 examined 652 Singapore 9-11-year-old children and reported no significance in correlation to refraction (Figure 2.25). Overall, because of the weak correlation and contradiction between studies, there is no significant indication of *CCT* correlation in refraction.

Age dependence:
In Doughty and Zaman's review [Doughty 2000], **age-**dependence decline for 60+ year-old subjects was observed in all non-white races. They found that age did not appear to influence central thickness across the studies of Caucasian groups, but that age-related decreases were reported in non-Caucasian groups. However, in Atchison 2008's Caucasian subjects, the Pamtacam data had a significant age-related change of -0.00077 mm/year (*CCT=0.5667-0.00077*Age* adjusted r^2 = 0.051, n = 104, p = 0.011). Some other recent studies have also reported age effects [Cosar 2003, Landers 2007, Lekskul et al. 2005, Nomura 2002, Rüfer 2007, Shimmyo 2003, and Suzuki et al. 2005], while other recent studies have not found

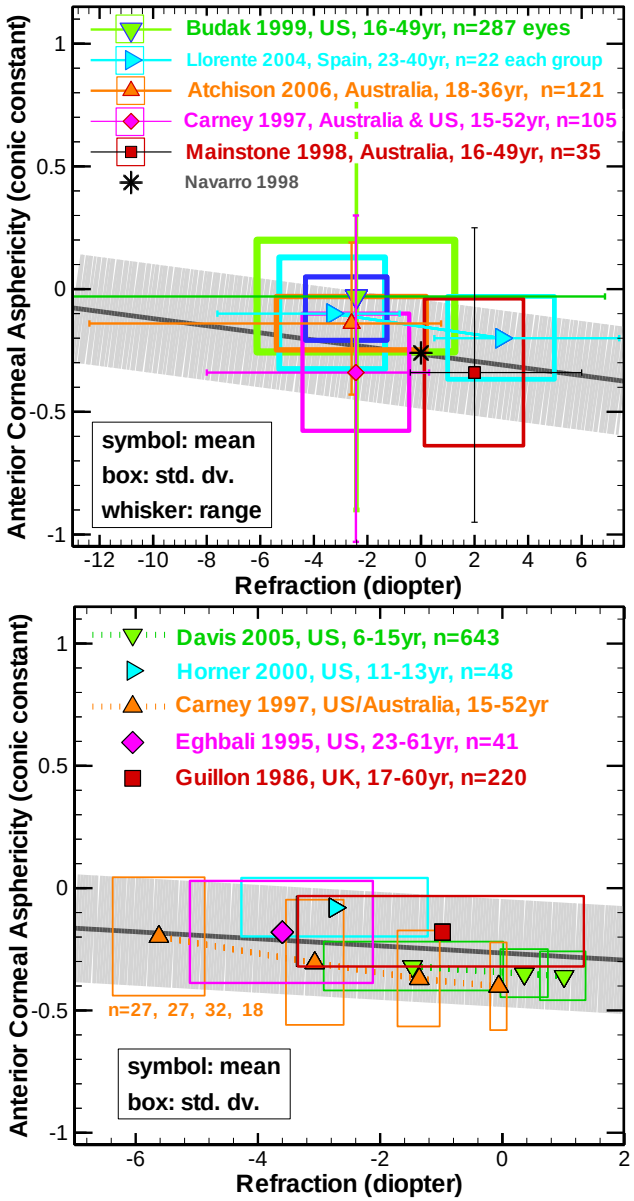

Figure 2.22 *Box-whisker plots of other published of data in comparison with the representative equation. On the top is collection of adults' data and on the bottom includes data of younger children.*

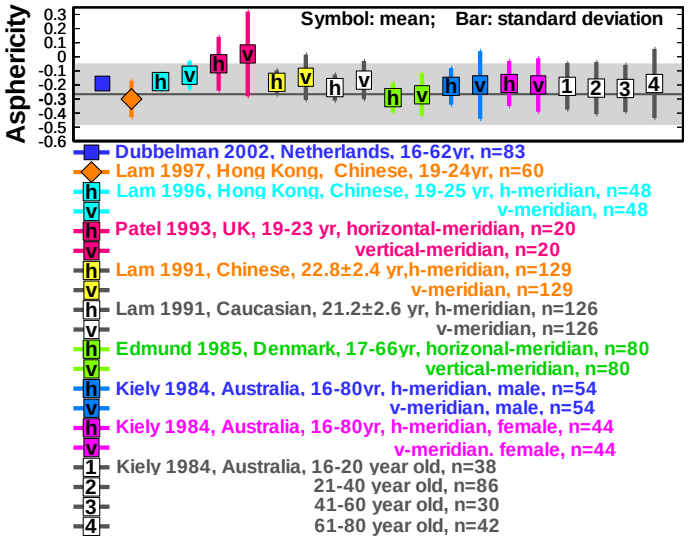

Figure 2.23 *Asphericity measurement dependence on the horizontal and vertical meridians of the eyes.*

Table 2.3 *Summary of 8 collected papers of CCT*

Author (year)	Geographic / Ethnic	Subject no. / Eye no.	Gender	Age (year)	Method of test	Central cornea thickness, CCT (Refractive-error, K)
Atchison 2008	Australian (96%) & Caucasian	106 subj./106 eyes (K=-0.88to+0.75D)	53F	18-29 (n=23), 30-39 (n=20), 40-49 (n=22), 50-59 (n=21), 60-69 (n=20)	ultrasonography	CCT=0.528±0.047mm, n=53
			51M			CCT=0.539±0.046mm, n=51
						CCT=0.5667-0.00077*age (adjusted r^2=0.051, n=104, p=0.011), CCT=0.533±0.047mm
			50F		Pentacam	CCT=0.538±0.034mm, n=50
			47M			CCT=0.543±0.036mm, n=47
						CCT=0.540±0.035mm, n=97 ; non-significant with age
Hu 2006	Chinese	30 subj./39 eyes (21 OD and 18 OS)	15F, 15M	13 (4-53)	Scheimpflug image analyzer	CCT(K=-2.70±4.71D)=0.55±0.05mm, n=21 OD; CCT(K=-1.92±4.66D)=0.54±0.05mm; n=18 OS; CCT(K=-2.33±3.29D)=0.54±0.05mm, n=39 eyes
Suzuki 2005	Japan	7313 subj.	2848M	(≥40)	Specular microscopy	CCT(K=-0.81±2.38D)=520.1±30.4μm ; n=2848 OD
			4465F			CCT(K=-0.32±1.85D)=512.8±29.0μm ; n=4465 OD
			2848M			CCT(K=-0.74±2.37D)=522.9±30.2μm; n=2848 OS
			4465F			CCT(K=-0.25±1.83D)=515.9±29.0μm ; n=4465 OS
Tong 2004	Singapore	652 subj./652 OD	103M	9 yr old	Optical low-coherence reflectometry (OLCR) pachymeter	CCT=550.7±36.8μm, n=82 Chinese; CCT=533.4±23.4μm, n=21 Non-Chinese
			106F			CCT=542.1±30.9μm, n=73 Chinese; CCT=542.1±29.6μm, n=33 Non-Chinese
			116M	10 yr old		CCT=550.0±29.6μm, n=82 Chinese; CCT=534.3±33.2μm, n=34 Non-Chinese
			109F			CCT=542.7±23.7μm, n=83 Chinese; CCT=530.3±31.9μm, n=26 Non-Chinese
			114M	11 yr old		CCT=550.1±32.4μm, n=93 Chinese; CCT=536.3±34.0μm, n=21 Non-Chinese
			104F			CCT=538.5±34.9μm, n=72 Chinese; CCT=540.8±35.1μm, n=32 Non-Chinese
Chang 2001	Asian	216 subj (K= -22 to +7D)	70F, 146M	22.2±4.2	Ultrasound pachymeter	CCT(K= -4.2±5.0D)= 538+1.001K μm, r = 0.16, p = 0.021, n=216, mean=533±29μm

Table 2.3, cont.

Hosny 2000	Spain, 211W	AL≤20mm, 21eyes		40.35±16.3 (18-78 yr) AL: Axial Length	Ultrasonic pachymeter	CCT(K=+5.45±2.43D)=554±33.1μm, n=21
		AL:20-22mm, 44eyes				CCT(K=+3.29±2.53D)=549.7±31.86μm, n=44
		AL:22-25mm,43eye				CCT(K=-2.19±2.47D)=523.9±42.68μm, n=43
		AL:25-27mm, 41eyes				CCT(K=-6.19±2.12D)=530.3±38.53μm, n=41
		AL:27-29mm, 34eyes				CCT(K=-8.97±2.92D)=528.4±37.01μm, n=34
		AL≥29mm, 28eyes				CCT(K=-19.34±3.34D)=561.8±24.68μm, n=28
Koretz 1989	US	100 subj.	68F	18-70	Optical pachymetry	CCT:OD: 0.47±0.04mm; OS: 0.47±0.04mm; age-correlation: OD: r =0.170,p=0.17; OS: r=0.184,p=0.13
			32M			CCT:OD: 0.46±0.04mm; OS: 0.47±0.04mm; age-correlation: OD: r= .555, p=.00097; OS: r=.48 1, p=.0053
						CCT:OD: 0.47±0.04mm; OS: 0.47±0.04mm age-correlation:OD: r= .298, p= .0026;OS:r = .290,p=.0034
Alsbirk 1977	Greenland Eskimos	Female: 344	344F	Female: 42 yr	Pachymeter	344 females: CCT(+0.25±1.25D)=0.526±0.029mm; 20yr: CCT(K=-0.28D)=0.529mm; 70yr: CCT(K=+0.90D)=0.521mm (female)
		Male: 294	294M	Male: 43 yr		294 males: CCT(K=-0.07±1.34D)=0.512±0.029mm; 20yr: CCT(K=-0.01D)=0.526mm; 70yr: CCT(K=-0.18D)=0.495mm

W: White	A: Asian	hy: hyperopic	F: female	OD: right eye	CCT: central cornea thickness
B: Black	H:Hispanic	em: emmetropic	M: male	OS: left eye	K: refracrive error (spherical equivalent)
		my: myopic	yr: year old		D: diopter

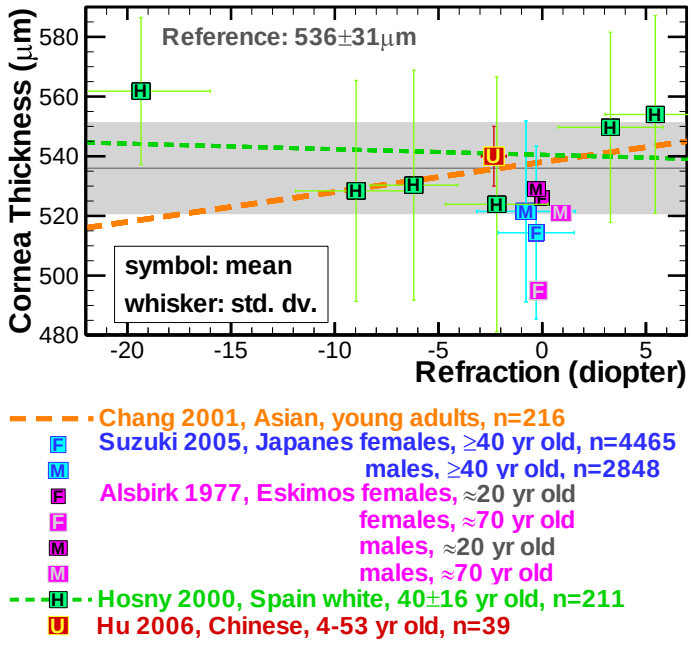

Figure 2.24 *Central corneal thicknesses, CCT, vs K*

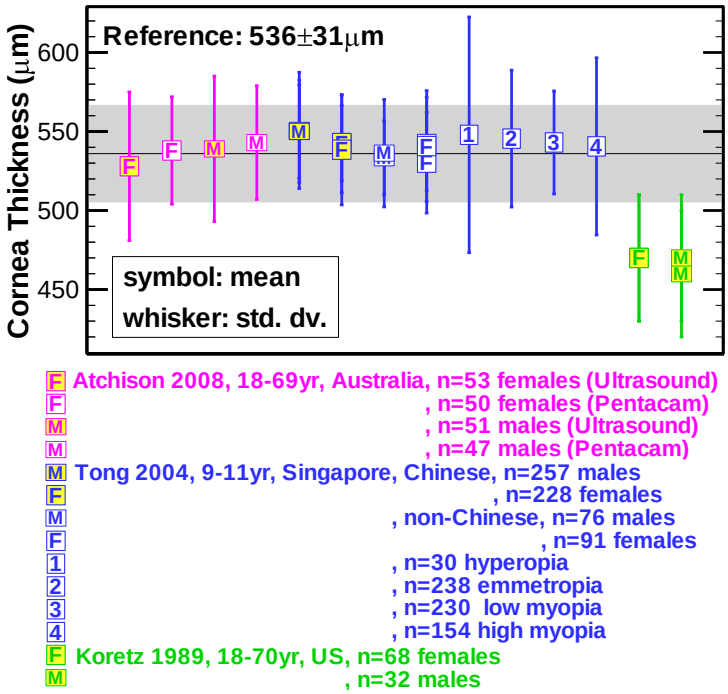

Figure 2.25 *Comparison of 3 studies of central corneal thicknesses, CCT*

them [Altinok et al. 2007, Eysteinsson et al. 2002, Khoramnia 2007, and Sanchis-Gimeno 2004). In Figure 2.24, Alsbirk's data shows the age difference at 20 and 70 year-old groups [Alsbirk 1977]. In children study, Tong 2004 (Singapore 9-11-year-old children) reported no correlation to age (Figure 2.25). They stated that when compare children and adult CCT data, the change was associated with greater difference in measured IOP [Tong 2004].

Race dependence:

Race dependence in the review of Doughty's is inconclusive [Doughty 2000]. Alsbirk's study provides a mean CCT value of 0.523 mm from a large sample of Greenland Eskimos [Alsbirk 1978]. This value is considered lower than the overall average. In the study of Dohadwala's, analysis of small numbers of Black, Asian or Native (Canadian) Americans indicate similarly low CCT values (compared to the white value of 0.552 mm) [Dohadwala 1998]. The same possible difference has not, however, been found in studies on Chinese or Hong Kong Chinese [Cho 1999] or Mongolian eyes [Foster 1998].

Dependence on gender:

Although the average CCT (0.554 mm) for **all-women** studies tends to be slightly higher than the meta-analysis-generated average (overall gender-independent average of 0.535 mm) in Doughty's review, this gender-dependence does not agree with other studies that directly compare the 2 genders in the same study. Doughty and Zammas [Doughty 2000] found no apparent gender influence across Caucasian group studies. Some recent studies with more than 500 subjects have reported males having thicker corneas than females, generally about 0.006–0.007 mm [Li 2006, Nomura et al. 2002, Shimmyo et al. 2003, and Suzuki et al., 2005]. Atshison 2008's non-significant gender differences were 0.005 and 0.011 mm for Scheimpflug and ultrasonography techniques, respectively. Others have not found gender-related differences [Altinok et al. 2007, Cosar 2003, Eysteinsson et al. 2002, Lekskul et al. 2005, Rüfer, 2005, and Rüfer et al. 2007]. Tong's children data also shows a slightly thicker cornea in males of same age (Figure 2.25).

2.2.4 Index of Refraction of Cornea (n_1)

There is no significant difference for the refractive index of the cornea between individuals. Navarro [Navarro 1985 and Escudero-Sanz 1999] determined the refractive index of cornea by fitting the experimental chromatic aberration measurement. The value of n_1= 1.3975, 1.3807, 1.37405, and 1.3668, for 365nm, 486.1nm, 656.3nm, and 1014 nm wavelength respectively from the Navarro model are accepted for modeling purpose in this dissertation.

2.2.5 Posterior Corneal Radius of Curvature (CR_2)

There is more limited number of studies in CR_2. In the table 2.4, 8 papers are summarized. Measured value is around the Navarro eye model's 6.5 mm, and the typical deviation of CR_2 is about 0.25 mm.

Correlation to refraction:

Dubbelman's paper in 2006 [Dubbelman 2006] is the only investigation of refraction correlation in my collection. His result gives the correlation, $CR_2=6.56+0.02K$ mm, r=0.19, p=0.05. However, there are a few papers that indirectly investigate the relationship between (ratio of) anterior and posterior corneal radiuses. Lowe and Clark in 1993 obtained: $CR_2=0.409+0.791CR_1$ [Lowe 1993] and Dunne in 1992 [Dunne 1992] found $CR_2=0.823CR_1$. Atchison 2008 obtained a ratio of 0.834. Dubbelman et al. [Dubbelman 2006], Edmund [Edmund 1994], Garner et al. [Garner 1997a], and Lam & Douthwaite [Lam 2000] obtained ratios between 0.83 to 0.85. Since CR_1 has a positive correlation to the refraction with

slope about +0.0155 as discussed in earlier section, this relationship suggests that CR_2 has a positive correlation around 0.0125-0.013 as well. Dubbelman's 2006 regression fitting is shown in the dashed line in Figure 2.26. The reference line (mean) and shaded area (standard deviation) in both figures are 6.5 and 0.25 mm.

Gender dependence:

Dubbelman [Dubbelman 2006] found a significant difference between male and females by 0.14 mm (Figure 2.27). Atchison [Atchison 2008] found that male radius of curvature was 0.055 mm flatter than female's mean (Figure 2.27), but this difference was not statistically significant (p=0.28). Dunne et al. [Dunne 1992] found that males had flatter corneas than females by a mean 0.08 mm (Figure 2.26), but this should be corrected by the refraction difference.

Regarding the astigmatism in the 2 genders, Dunne et al. [Dunne 1992] found significantly ($p < 0.05$) more posterior corneal toricity in males (n = 40) than in females (n = 40), but in Dubbelman [Dubbelman 2006] study, which a larger group of subjects (n = 57 in each gender) was measured, no significant difference was found.

Dependence on meridian:

As shown in the Figure 2.27, Patel [Patel 1993] and Lam [Lam 1997b] show the tendency of flatter CR_2 in horizontal than in vertical meridian. Dubbelman 2006 also obtained similar result with cylinder of 0.325mm [Dubbelman 2006].

Race dependence:

No sufficient information is obtained.

Age dependence:

Two papers reported the insignificant age dependence of CR_2. They are described as: $CR_2=6.609-0.00247*Age$ (adjusted $r^2=0.02$, n=97, p=0.16) [Atchison 2008] and $CR_2=6-0.005*Age$ (r=-0.21; p=0.06, n=83) [Dubbelman 2006]. Lam and Douthwaite [Lam 2000] also found no age significance. Overall, the correlation between CR_2 and Age is not significant in adults, though the trend is elders have smaller CR_2.

Table 2.4 *Summary of 8 papers regarding the posterior cornea radius of curvature, CR_2*

Author (year)	Geographic / Ethnic	Subject no./Eye no.	Gender	Subject age (year)	Method of measurement	Posterior radius of corneal curvature , CR_2 (Refractive-error,K) (mm)
Atchison 2008	Australian, 96% Caucasian	106 subj. /106 eyes (K=-0.88 to +0.75D)	50F	18-29(n=23), 30-39 (n=20), 40-49 (n=22), 50-59 (n=21), 60-69 (n=20)	Pentacam	CR=6.47±0.28mm, n=50
			47M			CR=6.53±0.22mm, n=47
						CR=6.609-0.00247*age (adjusted r^2=0.02, n=97, p=0.16).
Dubbelman 2006	Netherlands	114 subj /114 eyes	57F	38±14 yr	Scheimpflug images	CR=6.456±0.23mm, n=57
			57M	39.5±15 yr		CR=6.60±0.23mm, n=57
				39±14 yr (18-65 yr)		CR(-1.33±2.18D;-6.88 to +3.5D) = 6.53 ±0.25mm, CR(K)=6.56(±0.03)+0.02(±0.01)*K mm, r =0.19, p=0.05, n=114

Table 2.4, cont.

Dubbelman 2002	Netherlands	83 subj /83 eyes	40F, 43M	37.7±12.2 (16-62)	Determined by Scheimpflug images and Corneal topography	CR=6.40±0.28; CR=6.6-0.005*age, r=-0.21; p=0.06, n=83
Garner 1997	Tibetan in Nepal	120 subj.		11.16±4.28 (6-17 yr)	Ultrasonography and Phakometry (Purkinje images)	CR=6.42±0.31 (5.62 to 7.22)mm, n=120
Lam 1997a	Hong Kong Chinese	60 subj.	27F, 33M	20 (19-24 yr)	Calculated from keratometry (CR_1) & ultrasound pachometor (CCT)	CR=6.51±0.40 mm (range: 5.58 to7.27), n=60
Lam 1997b	Hong Kong Chinese	30 subj.	12F, 18M	median=20	Purkinje images	OD: 6.63±0.28mm (Horizontal); 6.38±0.25mm (Vertical), n=30
						OS: 6.65±0.27mm(Horizontal); 6.40±0.32mm(Vertical), n=30
Patel 1993	UK	20 subj.		(19-23 yr)	Calculated from Photo-Electric Keratoscope (CR_1) and ultrasonic pachometry (CCT)	Horizontal: 5.82±0.40mm (5.07-6.69mm), n=20
						Vertical: 5.80±0.42mm (5.29-6.51mm), n=20
Dunne 1992	UK	80 subj.	40F		Zeiss 110 keratometer	CR(K=-1.52±3.86D)=6.36±0.32, n=40
			40M			CR(K=1.11±2.40D)=6.44±0.25, n=40
			mix	22.0±3.3yr		CR(K=-2.05±3.18D)=6.45±0.31, n=60
			mix	74.6±5.6yr		CR(K=0.92±2.24D)=6.25±0.27, n=20
W: White	A: Asian	hy: hyperopic		F: female	OD: right eye	CR: posterior cornea radius of curvature
B: Black	H:Hispanic	em: emmetropic		M: male	OS: left eye	
		my: myopic		yr: year old	D: diopter	K: refracrive error (spherical equivalent)

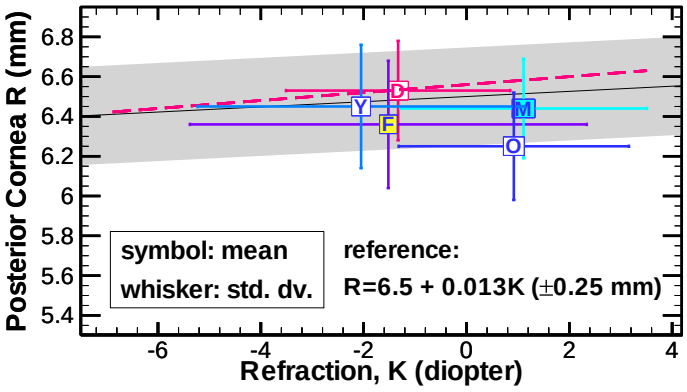

D Dubbelman 2006, Netherlands, 18-65yr, n=114
– – – fitted regression line, r=0.19, p=0.05
F Dunne 1992, UK, n=40 adult females
M n= 40 adult males
Y young adults, 22.0±3.3yr, n=60
O old adults, 74.6±5.6yr, n=20

Figure 2.26 *Comparison of 2 studies of posterior corneal radii*

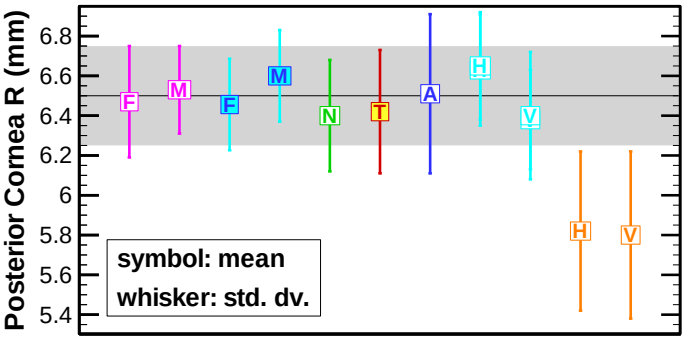

F Atchison 2008, 18-69yr, Australia, n=50 females
M , n=47 males
F Dubbleman 2006, Netherlands, 18-65yr, n=57 females
M n=57 males
N Dubbelman 2002, 16-62yr, Netherlands, n=83
T Garner 1997, 6-17yr (11.16±4.28), Tibetan in Nepal, n=120
A Lam 1997a, 19-24yr, Chinese, Hong Kong, n=60
H Lam 1997b, mean=20 yr, Chinese, horizontal, n=60
V vertical, n=60
H Patel 1993, 19-23 yr, UK, n=20, horizontal meridian
V n=20, vertical meridian

Figure 2.27 *Comparison of 7 studies of posterior corneal radii*

2.2.6 Asphericity of Posterior Cornea Surface (Q_2)

Measurements and calculated data of the asphericity of posterior cornea surface, Q2, from 4 collected papers are summarized in Table 2.5. All available data are from adults. The Navarro eye model uses 0. Dubbelman in 2003 and 2006 reported values between -0.1 and -0.6, Lam and Douthwaite [Lam 1997] estimated -0.66±0.38, and Patel et al. [Patel 1993] obtained -0.46±0.30 and -0.48±0.37 for horizontal and vertical meridians, respectively. These results are compared in the right plot of Figure 2.28. The reference line and gray shaded area in the background are -0.4 +/- 0.28.

Age dependence:

Dubbelman et al. [Dubbelman 2002 & 2006] found that posterior corneal surface asphericity is dependent upon age according to the studies performed in adults 18 to 65 year old:

$K_2 = Q_2 = -0.1 - 0.007 * Age$ (2002); r = -0.32, p = 0.003, n = 60,

$K_2 = Q_2 = -0.006 * Age$ (2006); r = -0.54, p < 0.00001, n = 114.

These results are plotted in the left of Figure 2.28.

Gender difference:

The only study of gender difference in my collection is performed by Dubbelman in 2006. No difference was found.

Table 2.5 *Summary of 4 papers about Q_2*

Author (year)	Geographic /race	Subject no. / eye no.	Gender	Age (year)	Method of measurement	Asphericity, conic constant, Q
Dubbelman 2006	Netherlands	114 subj /114 eyes	57F, 57M	39±14 (18-65)	Scheimpflug images	Q= -0.006*Age, n=114, r=-0.54, p<0.00001
Dubbelman 2002	Netherlands	83 subj / 83 eyes	40F, 43M	37.7±12.2 (16-62)	Determined by Scheimpflug images and Corneal topography	Q=-0.38±0.27; Q= -0.1 -0.007*Age, n=83, r=-0.32, p=0.003
Lam 1997	Hong Kong Chinese	60 subj.	27F, 33M	20 (19-24)	Calculated from keratometry (ACR) and ultrasound pachometer (CCT) results	Q=-0.66±0.38 (range: -1.53 to -0.10), n=60
Patel 1993	UK	20 subj.		19-23 yr	Calculated from Photo-Electric Keratoscope (ACR) & ultrasonic pachometry (CT)	Horizontal: Q=-0.48±0.30 (-0.97 to -0.31), n=20 Vertical: Q=-0.46±0.37 (-1.34 to -0.22), n=20

F: female M: male yr: year old Q: posterior cornea asphericity

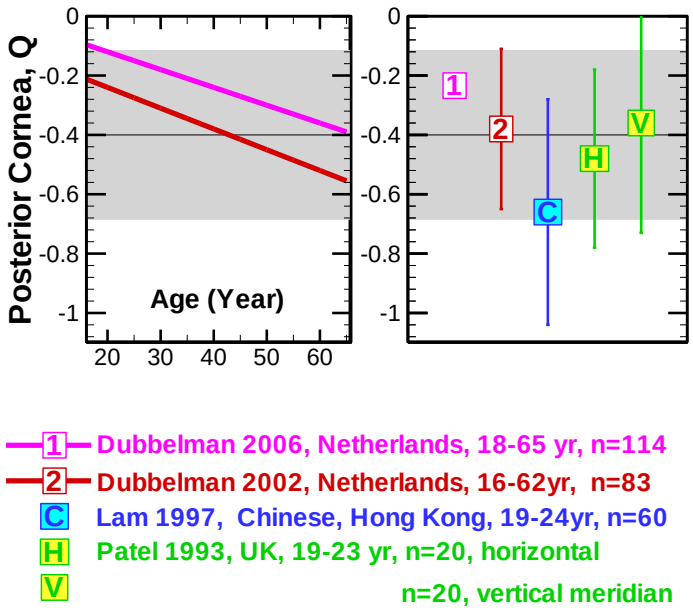

Figure 2.28 *Comparison of 4 studies of posterior corneal asphericity*

2.3 REVIEW OF PARAMETERS IN ANTERIOR, IRIS, AND POSTERIOR CHAMBERS

The anterior chamber is the fluid-filled space inside the eye between the posterior surface of the cornea (i.e. the corneal endothelium) and the iris. From the iris to the anterior lens surface is defined as the posterior chamber. Aqueous humor flows through pupil. The optical elements here include the distance, or depth, of *AC*, the refractive index of aqueous humor, and the iris stop. Because the distance is measured from the center of pupil to the vertex of lens, posterior chamber depth has been considered as zero in all eye modeling.

2.3.1 Anterior Chamber Depth (ACD) Measured from the Cornea Vertex

The Navarro eye model uses *ACD*=3.05mm. Because of the method of the measurements, the majority of the reported *ACD* in literature are actually defined by the distance including the cornea thickness. Therefore with the corneal thickness of 0.55mm in Navarro model, the 3.05 mm value will correspond to 3.6 mm in these literatures. In the collected papers, anterior chamber depth of adults is typically measured between 3.0 mm to 4.0 mm. From this point in this work, unless specified otherwise, *ACD* refers to the thickness including the cornea in this chapter. For comparison, I correct 0.55mm in those studies (in red) that report *ACD* excluding cornea thickness and provide no cornea data. These studies are performed by Hu in 2006 [Hu 2006], Mutti in 2005 [Mutti 2005], Goldsmith in 2005 [Goldsmith 2005], Shufelt in 2005 [Shufelt 2005], and Tong in 2002 [Tong 2002].

Several studies investigated the difference resulting from measurement methods [Atchison 2008, Hashemi 2005, Tong 2002, and Koretz 1989]. Discrepancies between the evaluated methods are within 0.03 to 0.15mm. Table 2.6 summarizes 36 studies of *ACD*. The adult data were plotted into 4 figures (Figures 2.29-2.32), children's data are in 2 figures (Figures 2.33-2.34) and infants' studies are plotted into Figure 2.35 for comparison.

Refractive error dependence:

The influential dependence of ACD is age and accommodation. Refractive error is believed a trivial factor of *ACD*. Atchison [Atchison 2006], Jansson [Jansson 1963], Mallen [Mallen 2005], and Goss et al. [Goss 1997] found no significance in refractive error correlation. Stenstrom [Stenstrom 1948] and Carney et al. [Carney 1997] found increase in anterior chamber depth with increase in myopia. In Figure 2.29, the myopic eyes tend to have slightly longer *ACD* compared to the emmetropic eyes and even more so than hyperopic eyes in most studies, though the correlation is not significant.

In children studies shown in Figure 2.33, Jones' US children of 3-8 year-old [Jones 2005] and Gao's Chinese children, 7-13 year-old [Gao 2002], also shown the same tendency of longer *ACD* in myopic eyes.

Gender dependence:

Adult males generally have longer *ACD* by 0.1 to 0.2 mm than females as shown in Figures 2.29 [Goss 1997], 2.30 [Shufelt 2005], 2.31 [Atchison 2008], and 2.32 [Wickremasinghe 2004, Wong 2001, and Alsbirk 1977]. Deeper ACD up to 0.18mm is also found by Cosar 2003, Eysteinsson 2005, Foster 1997, Klein 1998, and Wong 2001. Mallen 2005 is the only study that reports a longer mean *ACD* in females than males.

In children studies, about 0.1mm longer ACD in boys than girls of same age are also reported. These includes 5-8 year-old Australians [Ojaimi 2005] in Figure 2.33, 6-14 year-old in US [Zadnik 2003], and 7-9 year-old Singapore Chinese [Saw 2002b] in Figure 2.34.

Table 2.6 *Summary of 36 ACD studies*

Author (year)	Geographic /race	Subject no. / eye no.	Age (year)	Gender (F, M)	Method of test	Anterior Chamber Depth, ACD (Refractive-error, K)
Atchison 2008	Australia, >96%W	106 subj. /106 eyes K=-0.88to+0.75D	18-29 (n=23), 30-39 (n=20), 40-49 (n=22), 50-59 (n=21), 60-69 (n=20)	51F	Ultrasono-graphy	ACD=3.37±0.31mm, n=51
				51M		ACD=3.42±0.37mm, n=51
						ACD=3.857-0.0106*Age (adjusted r^2=0.196, n=102, p<0.001).
				50F	Pentacam	ACD=3.42±0.32mm, n=50
				47M		ACD=3.48±0.36mm, n=47
						ACD=3.909-0.0105*Age (adjusted r^2=0.219, n=102, p<0.001).
Bullimore 2006	USA, Ohio, 316W, 42B, 30A, 2H, 6 others	396 subj.	30.7±3.5 yr old	263F, 133M	Ultrasound	ACD(K=-3.54±1.77D)=3.64±0.29mm, n=396
Mallen 2006	UK	30 em OD	21.4±2.0	16F,14 M	IOLMaster	ACD(K=-0.07±0.23D) =3.66±0.31mm, n=30
		30 myopic OD	21.5±2.1	21F, 9M		ACD(K=-3.59±0.75D) =3.59±0.41mm, n=30;
Hu 2006	Chinese	30 subj./39 eyes (21 OD & 18 OS)	13 (4-53)	15F, 15M	Scheimpflug image analyzer	ACD(K=-2.33±3.29D)=3.81±0.27 mm, n=30
Ziylan 2006	Turkey	25 subj./50 eyes-pre	(12-24 m) pre- & full-term babies		A-Scan	ACD(K=-4.09±4.34D)=2.88±0.32mm, n=50
		35 subj./70 eyes-pre				ACD(K=1.64±0.81D)=2.77±0.28mm, n=70
		20 subj./40 eyes-full				ACD(K=1.92±0.77D)=2.87±0.37mm, n=40
Hashemi 2005	Iran	44 my subjects/ n=88 eyes	30.3±8.5 yr (19-49 yr)	25F, 19M	Orbscan	ACD(K=-5.0±2.70D(-15to-1D)) =3.67±0.31 mm, n=88
					IOLMaster	ACD(K=-5.0±2.70D(-15to-1D)) =3.79±0.30 mm, n=88
					A-Scan	ACD(K=-5.0±2.70D(-15to-1D)) =3.70±0.31 mm, n=88
Jones 2005	USA, Ohio	**my group:** 59(3yr old); 11(4yr); 15(5yr); 45(6yr);25(7yr);92(>8yr)		138F, 109M	A-Scan	ACD(K=-0.49±1.38D; ≤-0.75D) =3.68±0.2mm, n=247
		persistent hy: 12(3yr old); 5(4yr); 3(5yr); 8(6yr); 1(7yr); 14(>8yr)		23F, 20M		ACD(K=2.45±0.92D; ≥+1.0D) =3.44±0.3mm, n=43
		em group: 96(3yr old); 14(4yr); 7(5yr); 45(6yr); 3(7yr); 29(>8yr)		84F, 110M		ACD(K=0.54±0.22D; -0.25 to +1.0D) = 3.69±0.2 mm, n=194
		emmetropizing hy:21(3yr);28(4yr); 29(5yr);4(6yr);26(7yr);107 (>8yr)		135F, 118M		ACD(K=1.36±0.48D) =3.53±0.2mm, n=253

Table 2.6, cont.

Mallen 2005	Jordan	1093 subj. / 1093 right eyes			A-Scan	ACD(K=-0.87±1.70D)=3.19±0.48mm, ACD=-0.03*K+3.16mm, r=-0.12, n=1093
				643F		ACD(K=-0.95±1.58D)=3.21±0.44mm, n=643
				450M		ACD(K=-0.74±1.84D)=3.17±0.52mm, n=450
			(17-22 yr)			ACD(K=-0.81±1.65D)=3.32±0.46mm, n=261
			(23-28 yr)			ACD(K=-1.20±1.60D)=3.23±0.46mm, n=358
			(29-34 yr)			ACD(K=-0.83±1.59D)=3.14±0.48mm, n=221
			(35-40 yr)			ACD(K=-0.44±1.88D)=3.05±0.47mm, n=253
Ojaimi 2005	Australia	1726 right eyes	mean 6.7 yr old (5.5-8.4 yr)	851F, 875M	IOLMaster	ACD(K=+1.26±1.25D)=3.34±0.42mm, n=1726
		851 OD		851F		ACD(K=+1.34±1.17D)=3.28±0.29mm, n=851
		875 OD		875M		ACD(K=+1.20±0.89D)=3.39±0.30mm, n=875
		1285 OD	6 yr old			ACD(K=+1.27±1.43D)=3.32±0.36mm, n=1285
		441 OD	7 yr old			ACD(K=+1.25±0.84D)=3.32±0.21mm, n=441
	W	1112 OD	5-8 yr			ACD(K=+1.39±1D)=3.35±0.33mm, n=1112
	other ethnicity	614 OD	5-8 yr			ACD(K=+1.04±0.99D)=3.31±0.25mm, n=614
Logan 2005	UK, W	373subj. /373 right eyes	19.55±2.99 (17-30 yr)		IOLMaster	ACD(K=-1.01±2.19D)=3.62±0.32mm, n=145
	UK, Asian					ACD(K=-1.40±2.57D)=3.55±0.28mm, n=217
Goldsmith 2005	Cleveland	20 subj./40 eyes	(>18 yr old)	13F, 7M	OCT	ACD=3.54±0.323mm
Davis 2005	USA, CA	643 subj./643 eyes (1991)	9.92±2.42 (6-15 yr)		A-Scan	ACD(K=+0.31±1.12D; -5.95 to 4.23D) =3.69±0.23 mm; 2.98 to 4.56mm, n=643
		175 eyes (measured in 1991)	7.54±1.00 (6-9 yr)			ACD(K=+0.62±0.95D; -5.95 to 4.23D) = 3.64±0.21 mm; 3.04 to 4.20 mm, n=175
		175 eyes (follow-up in 1996)	12.48±1.00 (11-14 yr)			ACD(K=+0.08±1.60D; -10.21 to 3.91D) = 3.76±0.22 mm; 2.93 to 4.29 mm, n=175
Mutti 2005	USA	222 infants	3-month	118F, 104M	A-Scan	ACD(K=+2.16±1.30D)=3.31±0.27mm, n=222
			9-month			ACD(K=+1.36±1.06D)=3.58±0.35mm, n=222
			growth in 6 months			ΔACD(ΔK=-0.80±0.90D)=0.26±0.32mm, n=222

Table 2.6, cont.

Shufelt 2005	USA, LA, Latino	5588 subj. /5588 right eyes	(40-49 yr)	1304F	A-Scan	ACD(K=-0.32±1.8D)=4.04±0.3mm, n=1304
				923M		ACD(K=-0.30±1.3D)=4.16±0.31mm, n=923
			(50-59 yr)	1009F		ACD(K=-0.23±1.9D)=3.89±0.3mm, n=1009
				726M		ACD(K=0.02±1.6D)=4.02±0.31mm, n=726
			(60-69 yr)	631F		ACD(K=0.73±2.36D)=3.79±0.3mm, n=631
				441M		ACD(K=0.4±1.6D)=3.92±0.3mm, n=441
			(70-79 yr)	253F		ACD(K=1.02±2.30D)=3.72±0.3mm, n=253
				214M		ACD(K=0.6±2.5D)=3.81±.34mm, n=214
			(>=80 yr)	54F		ACD(K=0.74±2.12D)=3.64±.3mm, n=54
				33M		ACD(K=-0.3±2.6D)=3.85±0.4mm, n=33
Kirschkamp 2004	Germany or UK	9 subj./9 left eyes	(20-38 yr)	2F, 7M	A-Scan	Cycloplegia: ACD=3.6±0.2
						Accommodation=3.7±1.1D: ACD=3.4±0.2mm
Wickremasinghe 2004	Mongolian	1617 subj./1617 right eyes	(40-49 yr)	241M	A-Scan	ACD(K=+0.1±1.8D)=3.0±0.3mm, n=241
				368F		ACD(K=-0.3±1.6D)=2.9±0.3mm, n=368
			(50-59 yr)	200M		ACD(K=+0.2±0.9D)=2.9±0.3mm, n=200
				266F		ACD(K=+0.1±1.9D)=2.7±0.3mm, n=266
			(60-69 yr)	150M		ACD(K=0.0±1.5D)=2.8±0.3mm, n=150
				168F		ACD(K=-0.4±3.2D)=2.6±0.3mm, n=168
			(>70 yr)	109M		ACD(K=-0.7±3.6D)=2.7±0.3mm, n=109
				115F		ACD(K=+0.4±1.3D)=2.5±0.3mm, n=115
Zadnik 2004	USA, Ohio	194 subj. /194 right eyes	9.4±2.3 yr (6-14 yr)		A-Scan	ACD(K≈0.53±0.27D)=3.7±0.2 mm, n=194.
Rabsilber 2003	Germany	20 hy eyes ≥ +3D	62.2±12.7 yr	36 F, 24 M	IOL ocular biometer & obscan	ACD(K=-22 to +8D)=-0.035K+3.3968 mm, n=60, r^2=0.3532
		20 em eyes	26.9±3.0 yr			
		20 my eyes ≥ -6D	41.4±14.8 yr			
Cook 2003	UK	68 infants (postmenstrual age applied on the right)	32.9 weeks	33F, 35M	A-scan biometer	ACD(K=-2.06±2.27D)=1.98±0.19mm, n=54
			36.1 weeks			ACD(K=-1.23±2.17D)=2.11±0.32mm, n=52
			40 weeks			ACD(K=+0.74±1.83D)=2.25±0.19mm, n=55
			44.7 weeks			ACD(K=+1.89±1.76D)=2.43±0.23mm, n=53
			52.9 weeks			ACD(K=+2.12±1.25D)=2.80±0.25mm, n=38
			33-53W			ACD=0.04(±0.002)*(Week-40)+2.26(±0.02)mm; K=0.24(±0.0016)*(Week-40)+0.87(±0.20)D

Table 2.6, cont.

Zadnik 2003	USA: W, B, A, H, & Native American	2583 children	6 year old	1274F	A-Scan	ACD(K=0.88±0.86D)=3.51±0.26mm
			7 year old			ACD(K=0.78±1.01D)=3.49±0.25mm
			8 year old			ACD(K=0.64±1.26D)=3.57±0.24mm
			9 year old			ACD(K=0.18±1.64D)=3.61±0.23mm
			10 year old			ACD(K=-0.004±1.42D)=3.61±0.27mm
			11 year old			ACD(K=0.03±1.72D)=3.61±0.24mm
			12 year old			ACD(K=-0.16±1.55D)=3.69±0.23mm
			13 year old			ACD(K=-0.15±1.38D)=3.66±0.26mm
			14+ yr old			ACD(K=-0.46±2.18D)=3.64±0.25mm
			6 year old	1309M		ACD(K=0.81±0.87D)=3.57±0.25mm
			7 year old			ACD(K=0.72±0.95D)=3.61±0.24mm
			8 year old			ACD(K=0.53±1.11D)=3.65±0.26mm
			9 year old			ACD(K=0.37±1.14D)=3.68±0.25mm
			10 year old			ACD(K=0.34±1.25D)=3.70±0.25mm
			11 year old			ACD(K=0.18±1.57D)=3.72±0.24mm
			12 year old			ACD(K=0.32±1.50D)=3.73±0.25mm
			13 year old			ACD(K=-0.12±1.58D)=3.76±0.25mm
			14+ yr old			ACD(K=-0.11±2.78D)=3.69±0.34mm
Gao 2002	Chinese	135 subj. /270 eyes	9.6±2.3 yr (7-13 yr)	72F, 63M	A-scan	ACD(K=4.57±2.17D)=3.31±0.22 mm before & 3,66±0.17mm after cycloplegia, n=118
						ACD(K=0.11±0.47D)=3.68±0.29 mm before & 3.85±0.27mm after cycloplegia, n=38
Gao 2002	Chinese	135 subj. /270 eyes	9.6±2.3 yr (7-13 yr)	72F, 63M	A-scan	ACD(K=-2.47±1.80D)=3.76±0.30 mm before & 3.88±0.28mm after cycloplegia, n=114
Gwiazda 2002	USA: W, B, A, H	469 children / 469 right eyes	6-11 yrear old	246 F, 223 M	A-Scan	ACD(K=-2.38±0.81D)=4.0±0.2mm, n=469.
Saw 2002a	Singapore / Chinese	1449 children OD			A-Scan	ACD correlations to K, body height, weight, mass index, age, and gender
Saw 2002b	Singapore /Chinese	1453 children /1453 right eyes	7 year old	318 M	A-Scan	ACD(K=-0.2±1.6D)=3.6±0.3mm, n=318
			8 year old	239 M		ACD(K=-0.5±1.7D)=3.7±0.3mm, n=239
			9 year old	192 M		ACD(K=-1.4±2.1D)=3.6±0.3mm, n=192
			7 year old	313 F		ACD(K=-0.08±1.3D)=3.5±0.3mm, n=313
			8 year old	231 F		ACD(K=-0.3±1.5D)=3.6±0.3mm, n=231
			9 year old	160 F		ACD(K=-1.1±1.8D)=3.6±0.3mm, n=160
Tong 2002	Singapore	252 subj. /252 left eyes	9.17±1.57	110F, 142 M	A-scan	ACD(K=-3.65±1.23D)=4.42±0.23mm, n=252
					Scheimflug	ACD(K=-3.65±1.23D)=4.39±0.18mm, n=252

Table 2.6, cont.

Pennie 2001	UK	20 infants /20 right eyes	4.3±0.9 wk	10F, 10M	Through-the-eyelid ultrasonic biometry	ACD(K=+2.81±0.94D)=2.61±0.27mm, n=20
			14.0±1.9 wk			ACD(K=+2.74±1.46D)=2.94±0.31mm, n=19
			27.3±1.7wk			ACD(K=+1.91±1.31D)=3.17±0.28mm, n=18
			40.0±1.9wk			ACD(K=+1.76±1.50D)=3.33±0.30mm, n=13
			53.1±1.6 wk			ACD(K=+1.50±1.42D)=3.51±0.26mm, n=10
Wong 2001	Singapore /Chinese	1004 OD	(40-81 yr)	547F	A-Scan	ACD(K=-0.56±2.89D)=2.81±0.42mm, n=547
				457M		ACD(K=-0.40±2.41D)=2.99±0.45mm, n=457
Zadnik 1999	Ohio	554 subj. /554 right eyes	8.60±0.53		A-Scan	ACD(K=0.94±0.71D)=3.67±0.23mm, n=554
McBrien 1997	UK	14 hy OD (1st visit)	(22-50 yr)		A-Scan	ACD(K=+1.51±0.82D)=3.55±0.37 mm, n=14
		68 em OD (1st visit)	(21-61 yr)			ACD(K=+0.10±0.25D)=3.51±0.33 mm, n=68
		78 my (adult onset)	(22-53 yr)			ACD(K=-1.68±1.15)=3.69±0.44 mm, n=78
		47 my (youth onset)	(21-46 yr)			ACD(K=-3.74±2.13D)=3.76±0.48 mm, n=47
		38 my (15 to 20 yr onset)	28.77 yr (21-64 yr)			ACD(K=-2.46±1.66D)=3.67±0.49mm, n=38
Goss 1997	Oklahoma	34 em	25±4.6 yr	M	A-Scan	ACD(+0.25±0.36D)=3.86±0.28mm, n=34
		71 my	26.8±6 yr			ACD(-2.87±2.14D)=3.92±0.31mm, n=71
		19 em	25.6±5 yr	F		ACD(+0.17±0.36D)=3.72±0.32mm, n=19
		44 my	25.5±5 yr			ACD(-3.42±2.20D)=3.80±0.28mm, n=44
Garner 1997	New Zealand	11 subj. K=-1.88±1.64 D (-4.25~+0.50 D)	21.2 (18-28)		A-Scan	3.75±0.29mm at 0D stimulus
						3.73±0.29mm at 1.5D stimulus
						3.66±0.29mm at 3.5D stimulus
						3.55±0.31mm at 5.5D stimulus
						3.51±0.31mm at 8D stimulus
Scott 1993	New Zealand	42em(-.5to+1.5D)	17-26		A-Scan	ACD(K=0.32±0.52D)=3.63±0.30mm, n=42
		42 my (-5 to -7D)				ACD(K=-5.90±0.68D)=3.81±0.20mm, n=42
Cheng 1992	USA, Massachusetts	8 hy subj	>25 yr		MRI	ACD(+3.72±0.96D)=3.2±0.2mm, n=8
		6 em subj				ACD(+0.21±0.25D)=3.0±0.2mm, n=6
		7 my subj				ACD(-6.54±2.74D)=2.8±0.4mm, n=7

Table 2.6, cont.

Koretz 1989	USA	100 subj.	(18-70 yr)	68F, 32M	Optical pachymetry	ACD=-0.011*Age(±0.002)+4.11 (±0.093) mm; (r=-0.473, p=0.16*10^{-5})
					Ultrasonography	ACD=-0.011*Age(±0.002)+4.12 (±0.103) mm; (r=0.425, p=0.28*10^{-5})
					Slit-lamp Scheimpflg Photograf	ACD=-0.011*Age(±0.002)+4.14 (±0.104) mm; (r=-0.425, p=1.1*10^{-5})
Alsbirk 1977	Grrenland Eskimos	320 subj.	~43 yr old	F	Optical pachymeter and ultrasonic oculometry	ACD(K=+0.25±1.25D)=3.06±0.36mm; 20yr: ACD(K=-0.28D)=3.49mm; 70yr: ACD(K=+0.90D)=2.63mm
		279 subj.	~44 yr old	M		ACD(K=-0.07±1.34D)=3.24±0.33mm; 20yr: ACD(K=-0.01D)=3.66mm; 70yr: ACD(K=-0.18D)=2.85mm
W: White	A: Asian	hy: hyperopic	OD: right eye		F: female	ACD: anterior chamber depth
B: Black	H:Hispanic	em: emmetropic	my: myopic		M: male	K: refracrive error (spherical equivalent)

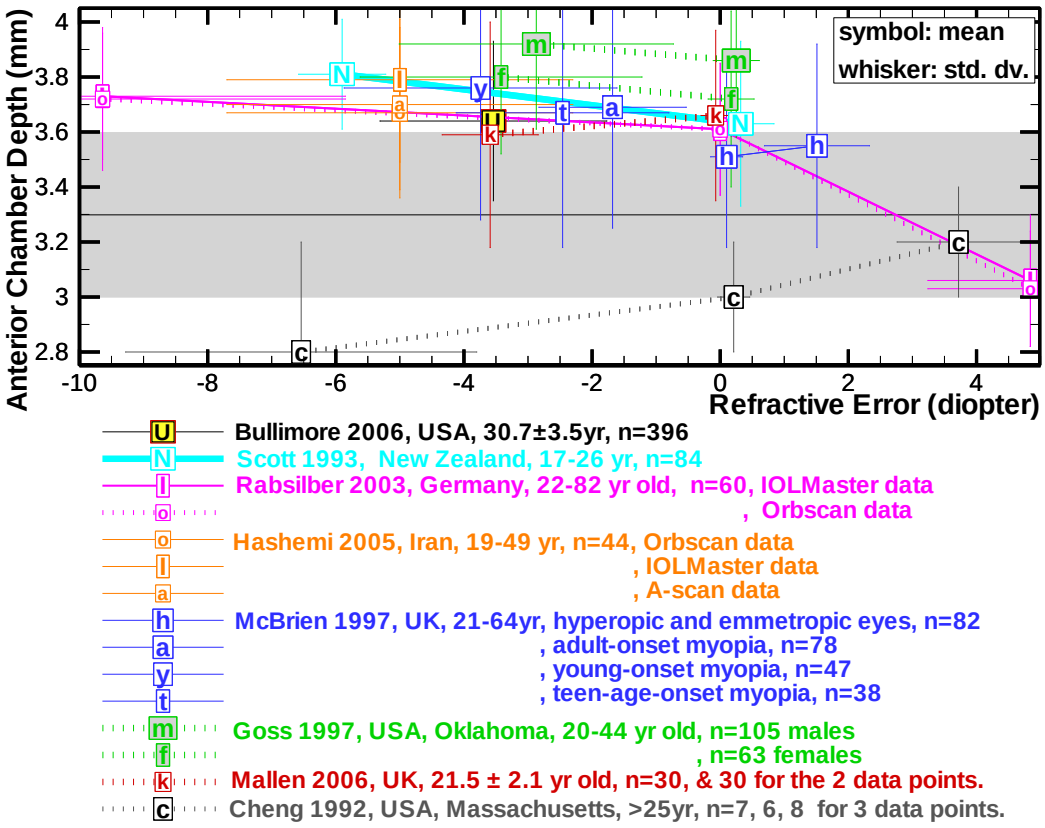

Figure 2.29 *Correlation of ACD to refractive error. (Adults data only)*

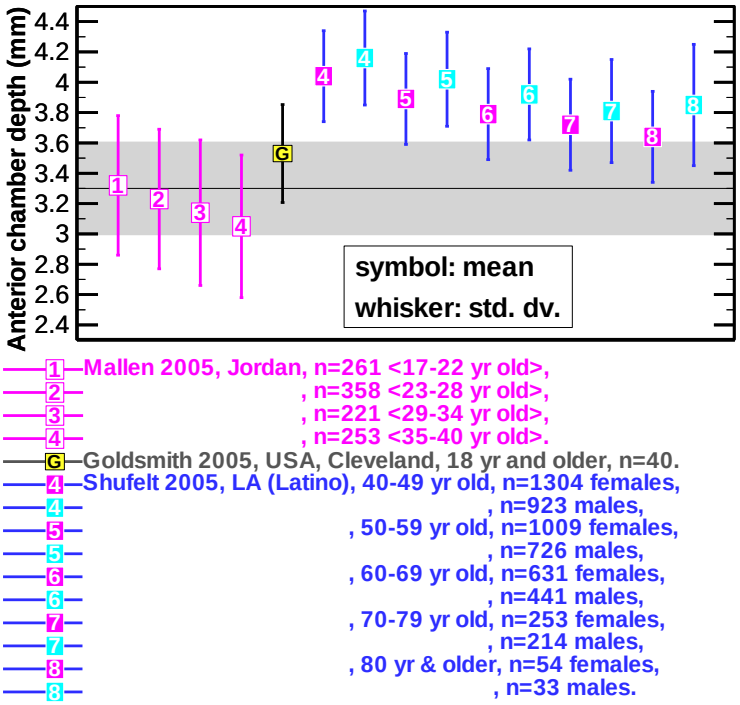

Figure 2.30 *Comparison of 3 ACD studies. (Adults data only). For comparison, data of Goldsmith and Shufelt are adjusted assuming cornea thickness of 0.55mm.*

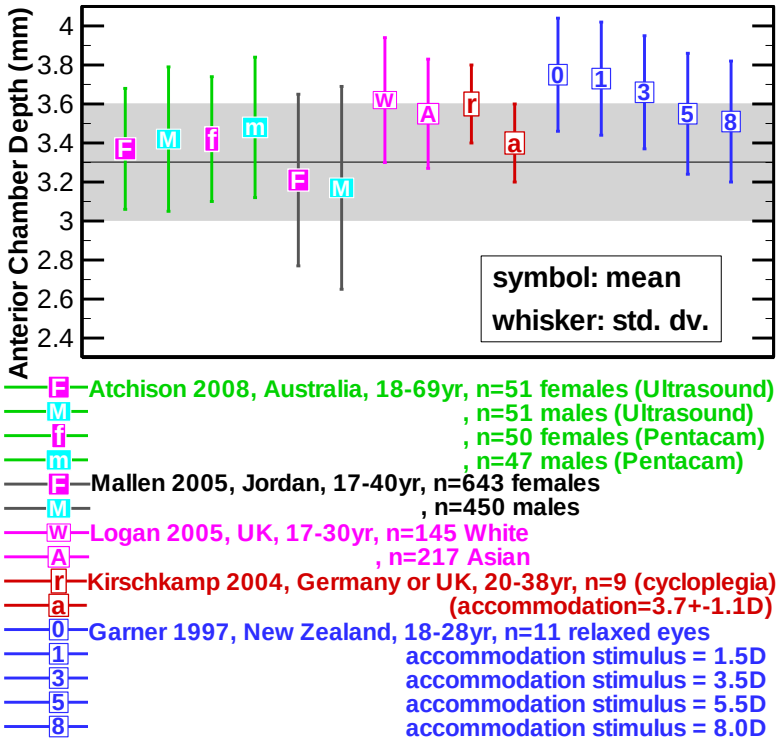

Figure 2.31 *Correlation of 5 ACD studies. (adults data only)*

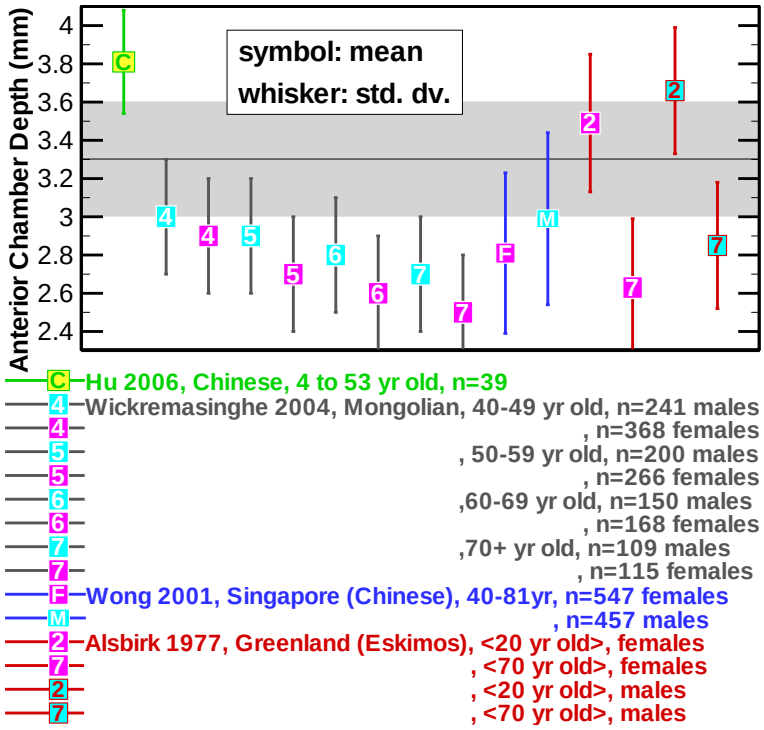

Figure 2.32 *Correlation of 4 ACD studies. (adults data only). For comparison, data of Hu is adjusted assuming cornea thickness of 0.55mm.*

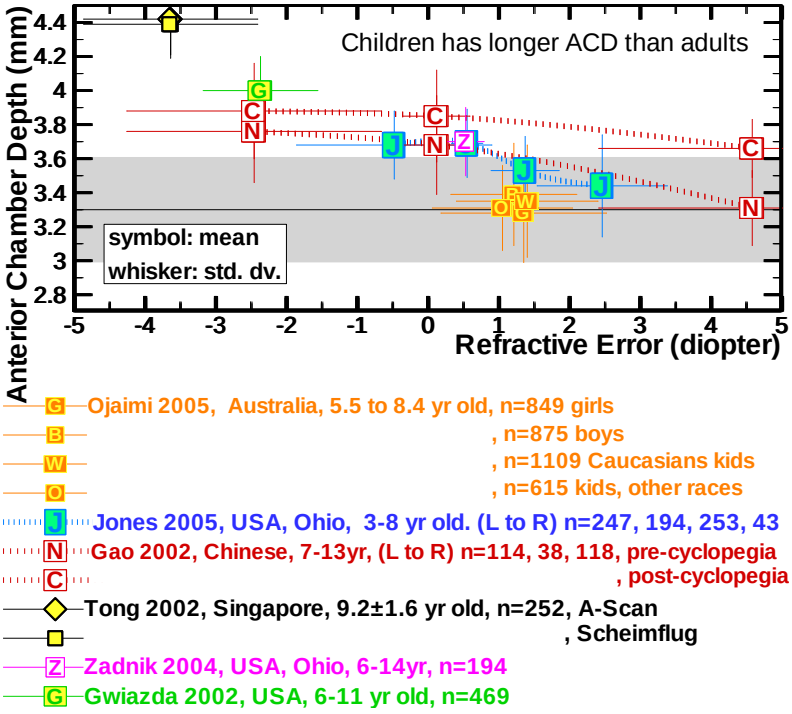

Figure 2.33 *Comparison of 6 studies of children's ACD in correspondence to refractive error. For comparison, data of Tong is adjusted assuming cornea thickness of 0.55mm.*

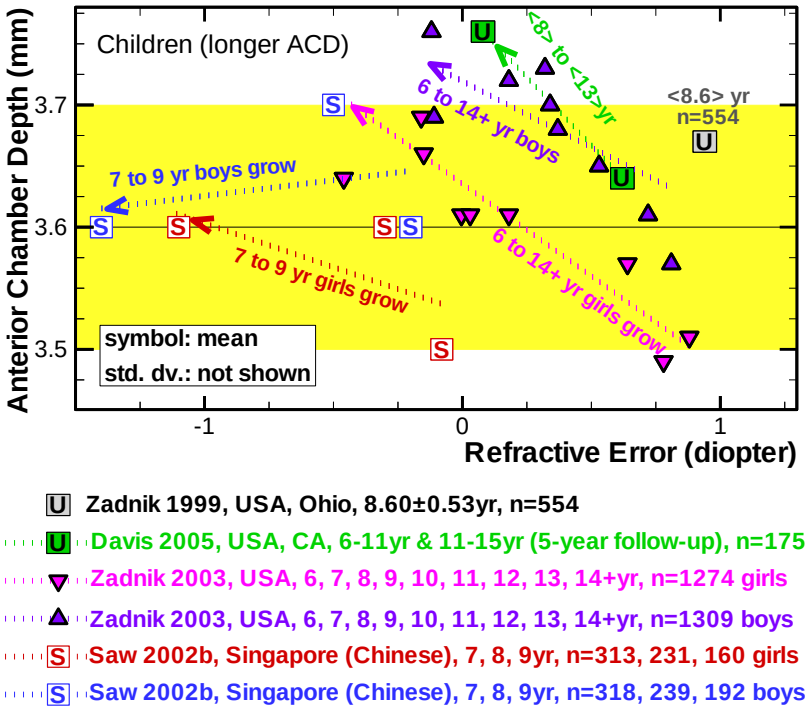

Figure 2.34 *Comparison of 4 studies of ACD in correspondence to refractive error in children data.*

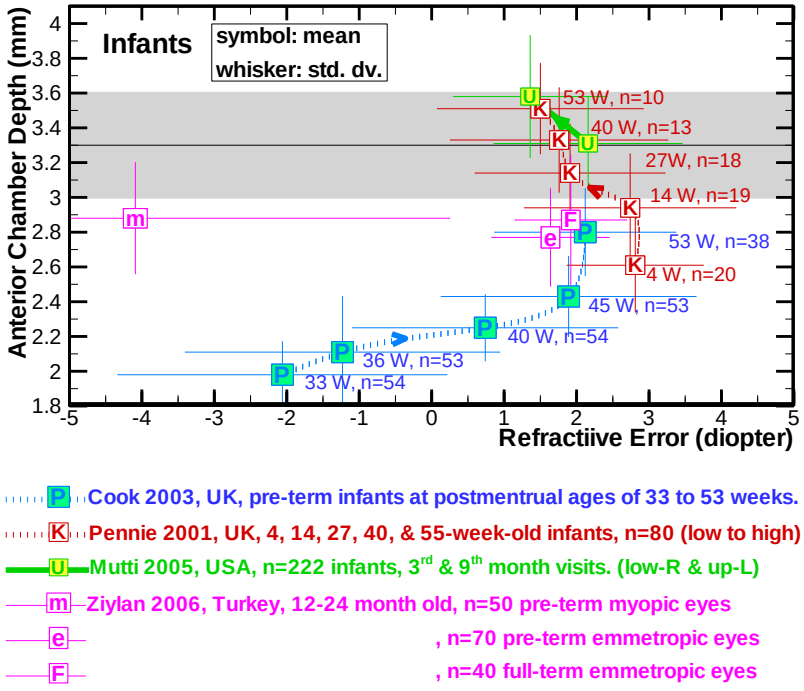

Figure 2.35 *Correlation of ACD to refractive error in infants' data. For comparison, data of Mutti is adjusted assuming cornea thickness of 0.55mm.*

Age dependence:

Age is one of the most significant factors to *ACD*'s variance. There are a lot of studies performed on this subject. In the preterm infants, measured *ACD* is smaller than 3mm (Figure 2.35) [Cook03, and Ziylan 2006]. Pre-term infants tend to be myopic and gradually develop to the same condition as full term infants, which are generally slightly hyperopic. As the eyes develop through the first year of life, *ACD* increase to the length of those of adults' and their refraction tend to be hyperopic at the early month and then gradually neutralize to emmetropic eyes [Pennie01, and Mutti05].

Compared to infants' data, children's data presents the continuous growth of *ACD* during the childhood from 6 year old to teenage [Davis 2005, Zadnik 2003, and Saw 2002b] (Figure 2.31). There seems to be a tendency to increase myopia at the same time. Jones's study provides the growth of *ACD* in 4 refractive groups of US children 6- to 15-year old (Figure 2.36) [Jones 2005].

During the young adulthood, *ACD* reaches the longest length near 3.7mm. As the age increases, *ACD* decreases in a rate about -0.1mm per decade [Atchison 2008, Dubbelman 2001, Koretz 1989]. The similar decade rate is also clearly shown in the data of Mallen [Mallen 2005] and Shufelt [Shufelt 2005] in Figure 2.31, and Wickremasinghe [Wickremasinghe 2004] and Alsbirk [Alsbirk 1997] in Figure 2.32. This shrinking phenomenon of *ACD* in adulthood is actually the effect of the lens growing pushing toward the anterior chamber. Actually, about half of the increased thickness of lens resulting from aging is contributed to the anterior chamber and the other half to the vitreous chamber [Atchison 2008, Dubbelman 2001, and Koretz 1989].

Jones' [Jones 2005] study investigated and gave age-dependent ACD for US children 6 to 15-year old. These results are plotted in Figure 2.36. These age-dependences are significant for persistent hyperopic and myopic group, but not significant for emmetropizing hyperopic group.

ACD=1.381-0.349*ln(Age)2+1.787*ln(Age) p=0.1054 (emmetropizing hyperopia);

ACD=1.817-0.265*ln(Age)2+1.441*ln(Age) (emmetropes);

ACD=1.425-0.311*ln(Age)2+1.749*ln(Age), p<0.0001 (myopia);

ACD=2.773-0.062*ln(Age)2+0.447*ln(Age), p=0.0048 (persistent hyperopia)

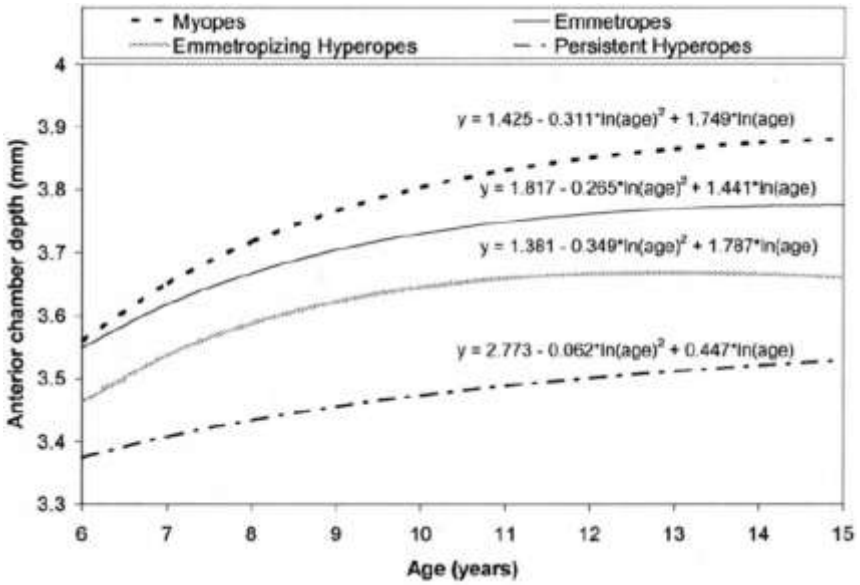

Figure 2.36 *Growth of ACD in 4 refractive groups of US children 6- to 15-year old from Jones 2005*

Ethnicity dependence:

Logan compared Caucasians and Chinese in UK (Figure 2.31) [Logan 2005]. Ojaimi compared 1109 Caucasian children with 615 other-race children of same age (5.5-8.4 year old) (Figure 2.33) [Ojaimi 2005]. In both studies, the longer *ACD* in Caucasian is not significant. However, when comparing the geographic indication of the studies, Mongolian subjects [Wickremasinghe 2004] and Chinese [Wong 2001, and Hu 2006] in Figure 2.32, and Jordan subjects [Mallen 2005] in Figure 2.30 seem to have shorter *ACD* than those obtained in European countries.

Accommodation:
Dubbelman [Dubbelman 2005] and Mallen [Mallen 2006] examined *ACD* transient changes up to 8D accommodation stimuli and obtained the decrease rate of about -0.043mm/diopter. As shown in Figure 2.31, Garner in 1997 obtained slightly smaller decrease rate with accommodation. In the same figure, Kirschkamp compared *ACD* under cycloplegia and 3.7D accommodation stimuli and reported a difference of about 0.2 mm reduction [Kirschkamp 2004]. Similar study was performed in children by Gao (Figure 2.33) without accommodation stimuli [Gao 2002]. The *ACD* reduction of 0.12 mm from cycloplegia alone is clearly shown.

Body height, weight and BMI :
Studies were performed in children. Wong [Wong 2001] and Saw [Saw 2002a] gave *ACD* and K in 5 and 4 quartiles according to height, weight and BMI. Wong indicated that height and weight correlate positively with *ACD*, but BMI does not correlate with *ACD*. Saw reported that the taller children are more myopic and have deeper *ACD* [Saw 2002a].

2.3.2 Index of Refraction of Aqueous Humor (n_2)
There is no significant difference on the refractive index of the aqueous humor between individuals. Navarro uses n_2*=1.3593, 1.3422, 1.3354,* and *1.3278*, for wavelength at 365nm, 486.1nm, 656.3nm, and 1014nm [Navarro 1985 and Escudero-Sanz 1999] in the well acknowledged Navarro eye model.

2.3.3 Iris Stop
Most of all the eye modeling researches make the iris stop centered along the optical axis. However, human iris is de-centered and the center of pupil shifts as pupil size changes. Liou model uses a decenter value of 0.5 mm to nasal [Liou 1997]. In this dissertation, I keep the pupil center on axis as most eye modeling work do.

2.4 REVIEW OF OPTICAL PARAMETERS OF LENS
The lens, also known as the crystalline lens, is a transparent, biconvex (lentil-shaped) structure in the eye that, along with the cornea, refracts light to be focused on the retina. The lens, by changing shape, functions to increase the focal power so that it can focus on objects at various distances, thus allowing a sharp real image of the object of interest to be formed on the retina. This adjustment of the lens is known as accommodation. It is similar to the focusing of a photographic camera via movement of its lenses. In humans, the refractive power of the lens in its natural environment is approximately 18 diopters, roughly one-third of the eye's total power. The accommodation capability (amplitude) of human lens can be more than 15 dioptres at young age and decreases to approximately 1 diopter at age of 50. Typically, the amplitude of 3-diopter (reciprocal of the distance of 33 cm) accommodation is required for reading.

If not specified, the lens parameters discussed in the following sections are those under relaxed (un-accommodative) condition.

2.4.1 Anterior Lens Radius (LR_1)

I collected 10 papers of anterior lens radius. No scatter point figure for LR_1 vs. K is available. Table 2.7 summarizes these studies' conditions and results. Typical relaxed value is around 10.5mm with deviation of about 1 mm. Navarro eye model uses LR_1=10.2 mm.

Refractive error correlation on lens biometry:

Very little investigations on this subject were performed in the past. In Goss' [Goss 1997] (Figure 2.37) and Dubbelman's [Dubbelman 2001] studies, no significant correlation between LR_1 and refractive error was found. In studies of Atchison [Atchison 2006], Stenstrom [Stenstrom 1948] & Goss [Goss 1997], examinations were performed on the correlation between lens power and refractive error. No significance was found by all studies. It is generally believe the independency between lens biometry and refractive error.

Gender:

Atchison pointed that males have about 0.21mm longer LR_1 than females (p=0.54) (Figure 2.38) [Atchison 2008]. Goss' study shows that for emmetropes, males have 0.48mm longer LR_1 than female and for myopes males have 0.10mm longer LR_1 than female (Figure 2.37) [Goss 1997]. These differences are insignificant.

Accommodation:

As the accommodation is induced, the curvature of anterior lens surface increases (radius decreases). Garner reported LR_1 reductions at 5 different accommodation stimulus (Figure 2.38) (Table 2.7) [Garner 1997a]. Kirschkamp 2004 reported that LR_1 reduces from 12.3±0.8mm (under cycloplegia) to 8.6±1.2mm under 3.7±1.1D accommodation (Figure 2.38) [Kirschkamp 2004]. Dubbelman reported the mean change per diopter as -0.61±0.15mm/diopter in 3mm visual zone [Dubbelman 2005].

Age:

Age is a major variable of lens biometry. Both the lens development before adulthood and the aging after adulthood are significant and studied by many groups.

Infants have smaller LR_1 than children and adults. Mutti examine infants at 3-month and 9-month visits, and obtained LR_1=7.21±0.60mm and 8.97±0.75mm respectively (Figure 2.37) [Mutti 2005]. Mutti's study provides the age dependence of children between 6 and 15 year old [Mutti 1998]. Adult data from Atchison [Atchison 2008], Dubbelman [Dubbelman 2001], and Koretz [Koretz 2001] are closely in agreement. These results also closely resemble the results of the phakometric studies of Hemenger et al. [Hemenger 1995] and Goss et al. [Goss 1997]. Brown's result is apart from the rest [Brown 1974]. These results are compared in the Figure 2.39.

2.4.2 Anterior Lens Asphericity (Q_3)

Q_3 is not a very significant parameter in ocular biometry. I found only 2 papers that discussed Q_3. Smith reported the age-related $Q_3=-0.0001429*Age^2+0.03660*Age-2.233$ [Smith 2003]. Dubbelman reported insignificant age-dependence: $Q_3+1=0.03(\pm0.04)*Age-5.4(\pm1.6)$, (r=0.08, p=0.44, n=90) [Dubbelman 2001]. Figure 2.40 illustrates the age-dependence of these 2 studies. For comparison, the Navarro eye model uses a constant of -3.1316, the Liou model uses -0.94, and the Atchison 2006 model adopts -5.

Table 2.7 *Information of 10 LR_1 papers*

Author (year)	Geographic /race	Subject no. /eye no.	Gender	Subject age (year)	Method of test	Anterior Lens Radius of Curvature, LR (Spherical equivalent power,K)
Atchison 2008	Australia (>96% W)	106 subj. /106 eyes K=-0.88 to +0.75 D	34F	18-29yr (n=23), 30-39yr (n=20), 40-49yr (n=22), 50-59yr(n=21), 60-69yr(n=20).	Purkinje images	LR=10.53±1.40mm, n=34
			32M			LR=10.32±1.41mm, n=32
						LR=12.283-0.0438*age (adjusted r^2=0.192, n=66, p<0.001).
Mutti 2005	US	222 infants	118F, 104M	3-month	Phakometer	LR(K=+2.16±1.30D)=7.21±0.60mm, n=222
				9-month		LR(K=+1.36±1.06D)=8.97±0.75mm, n=222
				growth in 6 M		ΔLR(ΔK=-0.80±0.90D)=1.79±0.61mm, n=222
Kirschkamp 2004	Germany or UK	9 subj. /9 left eyes	2F, 7M	(20 to 38 yr)	Auto-keratometer	Relaxed: LR=12.3±0.8 mm
						Accommodation=3.7±1.1D: LR=8.6±1.2mm
Dubbelman 2001	Netherlands	102 subj. /102 eyes	45F, 57M	F:36.9±13.3yr M:41.0±12.3yr	Scheimpflug image	LR=-0.057(±0.009)*Age+12.9(±0.4), r=-0.54, p<0.0001, n=102
Koretz 2001	USA	100 subj.		18–70-yr (~20 subjects per decade)	Scheimpflug photograph	LR=11.155-0.02004*Age, n=100
Mutti 1998	US(86.6%W, 11.2%A, 1.5%H, & 0.7%B)	994 subj.	451F, 543M	(6 to 15 yr)	Phakometer	LR=11.45+0.151*(Age-10)-0.021*(Age-10)^2, n=994
Goss 1997	Oklahoma	34 em males	63 F, 105 M	25±4.6 (21~44)	A-Scan	LR(+0.25±0.36D)=10.05±0.86mm; n=34M
		71 my males		26.8±6 (21~43)		LR(-2.87±2.14D)=9.88±1.16mm; n=71M
		19 em females		25.6±5 (21~38)		LR(+0.17±0.36D)=9.57±0.94mm; n=19F
		44 my females		25.5±5 (20~39)		LR(-3.42±2.20D)=9.78±1.11mm; n=44F
Garner 1997a	New Zealand	11 subj. K=-1.88±1.64D (-4.25~+0.50 D);		mean:21.2 yr (18 to 28 yr)	A-Scan	11.54±1.27mm at 0D stimulus
						10.47±0.72mm at 1.5D stimulus
						8.49±0.50mm at 3.5D stimulus
						7.51±0.30mm at 5.5D stimulus
						6.59±0.30mm at 8D stimulus
Garner 1992	New Zealand / Maylay	19 em subj (-.25~.25D)	9F, 10M	(9 to 15 yr)	Calculated with assumed Q	LR(K=+0.01±0.05D)=9.55±0.75mm; n=19
		19 my subj (>-3D)				LR(K=-6.08±1.83D)=10.68±1.00mm; n=19
Brown 1974	London, UK	100 subj.		3~82	slit-image photograph	LR=12.4±2.6mm, LR=-0.104*Age+16.815, n=100

W: White A: Asian B: Black H:Hispanic

hy: hyperopic em: emmetropic my: myopic

F: female M: male yr: year old

OD: right eye OS: left eye D: diopter

LR: anterior lens radius of curvature K: refracrive error (spherical equivalent)

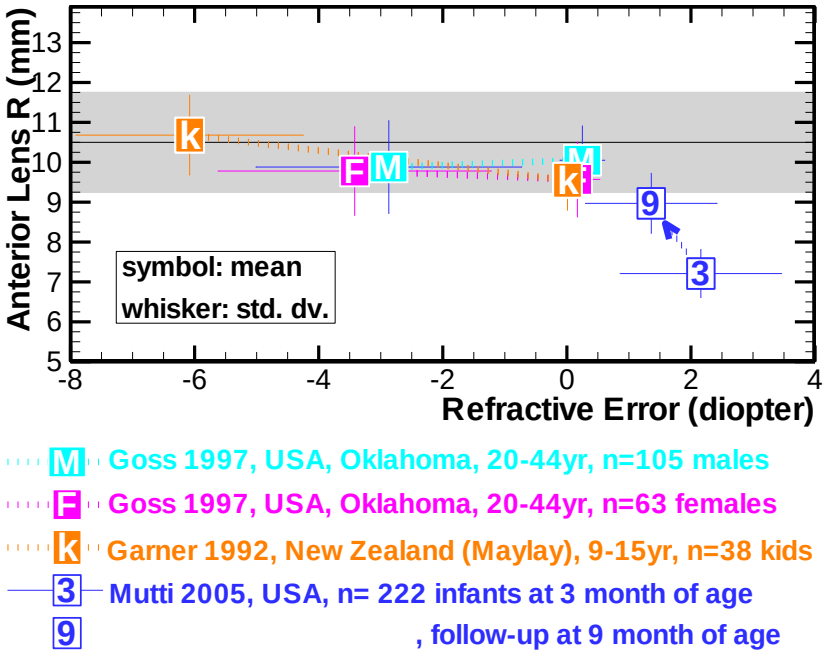

Figure 2.37 *Comparison of 3 LR_1 studies in correlation to refractive error.*

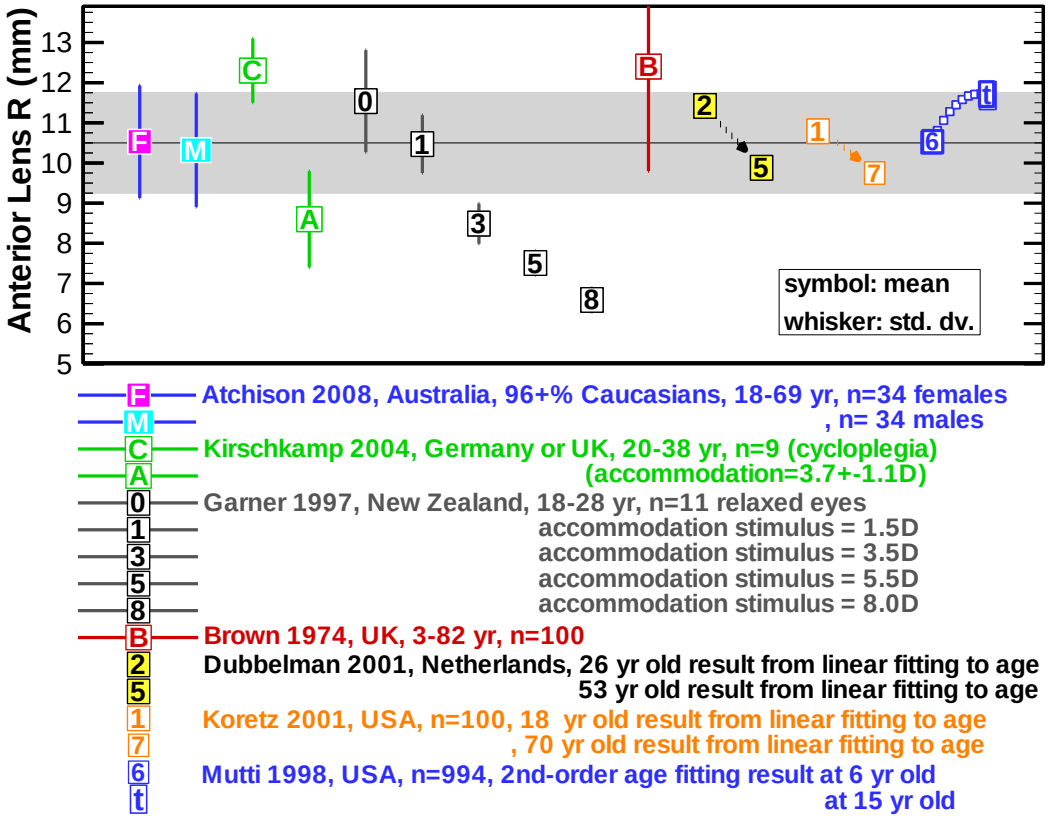

Figure 2.38 *Comparison of 7 LR_1 studies.*

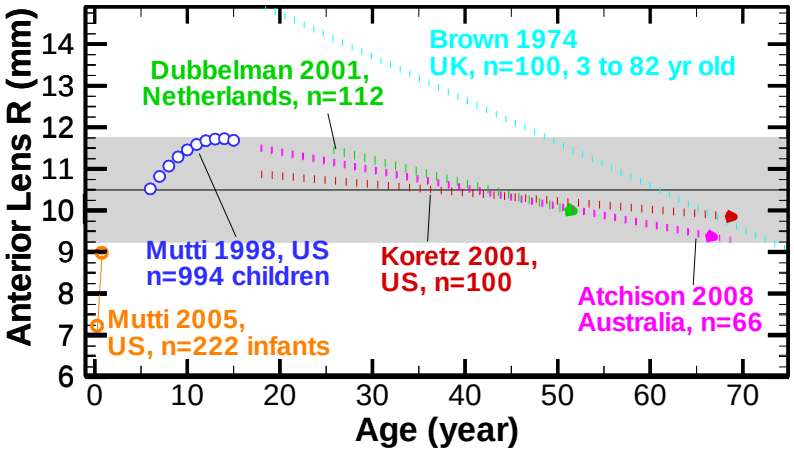

Figure 2.39 *Comparison of 6 LR_1 studies as function of age.*

Table 2.8 *Information of 2 Q_3 papers*

Author (year)	Geographic / race	subject no. /eye no.	Gender	Age (year)	Method of test	Conic constant Q (Refractive-error,K)
Smith 2003	Australia				Calculated	$Q=-0.0001429*Age^2+0.03660*Age-2.233$
Dubbelman 2001	Netherlands	102 subj. /102 eyes	45F, 57M	females 36.9±13.3 yr; males 41.0±12.3yr	Scheimpflug image	Q=0.03(±0.04)*Age-6.4(±1.6), r=0.08, p=0.44, n=90
	F: female	M: male		yr: year old		Q: anterior lens surface asphericity

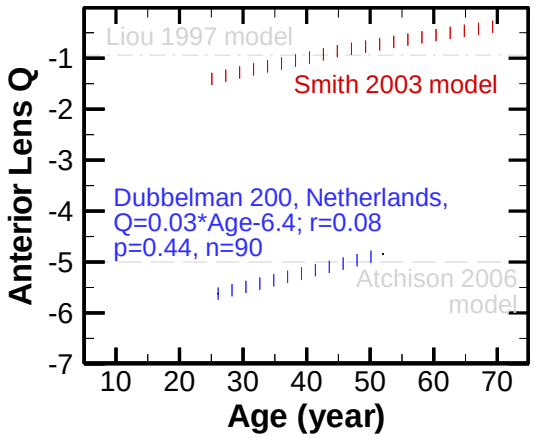

Figure 2.40 *Comparison of 7 LR_1 studies.*

2.4.3 Lens Thickness (LT)

Lens thickness is in the range of 3 to 5 mm. Navarro model uses 4.0 mm. Systematic discrepancy between instruments was investigated by Atchison in 2008, Tong in 2002, and Koretz in 1989 and typical difference up to 0.2mm were estimated. 29 papers of *LT* are collected and summarized in Table 2.9. Figures 2.41 to 2.43 show the results of these studies. Cheng reports relatively longer *LT* than other groups [Cheng 1992]. The possible reason for this longer *LT* may be because the measurement method is MRI. The similar phenomenon for axial lens (*AL*) measurement has been observed by Singh [Singh 2006].

Refractive error:
As mentioned earlier, lens biometry is believed to have little correlation with refractive error. Figure 2.41 shows the relation between the lens thickness and refraction for studies in adults and Figure 2.42 shows data of infants and children. As the results (dashed lines) of McBrien [McBrien 1997], Goss [Goss 1997], Scott [Scott 1993], Cheng [Cheng 1992], and Jones [Jones 2005] shown, no significance of this correlation has been found. Not presented in the figures, Cook [Cook 2003], Mutti [Mutti 2005], Pennie [Pennie 2001], and Ziylan [Ziylan 2006] also obtained the insignificant conclusion.

Accommodation:
Lens thickness increases as the accommodation increases. Garner reported *LT* changes at 5 different accommodation stimuli (Figure 2.41) [Garner 1997a]. Kirschkamp reported a 0.2mm increase in lens thickness from cycloplegia to the 3.7±1.1D accommodation (Figure 2.43) [Kirschkamp 2004]. Dubbelman's study obtained the lens thickness increasing rate as +0.375mm/diopter [Dubbelman 2005]. In a children's study, Gao's research presents 0.1~0.25mm decrease of *LT* with cyclopegia (Figure 2.42) [Gao 2002].

Age dependence:
Measured and reported in many studies [Cook 2003, Ziylan 2006, Mutti 2005, and Pennie 2001], infants' lenses are thicker compared to children. During childhood before 15 years of age, human lens tends to reduce in thickness [Zadnik 2003, Saw 2002a, and Mutti 1998]. After 20-years old, thickness of lens continues to increase [Atchison 2008, Koretz 1989, Shufelt 2005, Alsbirk 1997, Mallen 2005, and Wickremasinghe 2004]. Age dependence of lens thickness is illustrated in Figure 2.44. For comparison, Figure 2.45 shows the age development of LT in 4 refractive groups of US children 6- to 15-year old from Jones' study [Jones 2005].

Jones' [Jones 2005] study investigated and gave age-dependent LT for US children 6 to 15-year old. These results are plotted in Figure 2.45. These age-dependences are significant for persistent hyperopic group, but not significant for myopic, and emmetropizing hyperopic groups.

Age<=9.5 years LT=3.778-0.036*Age;
Age>9.5 years LT=3.363-0.007*Age, p=0.5221 (emmetropizing hyperopia);
Age<=9.5 years LT=3.799-0.041*Age;
Age>9.5 years LT=3.352+0.006*Age (emmetropes);
Age<=9.5 years LT=3.841-0.046*Age;
Age>9.5 years LT=3.389+0.002*Age, p=0.1827 (myopia);
Age<=9.5 years LT=3.746-0.026*Age;
Age>9.5 years *LT=3.428+0.007*Age*, p=0.0954 (persistent hyperopia)

Table 2.9 *Summary of 29 LT papers*

Author (year)	Geographic /race	Subject no. /eye no.	Subject Age (year)	Gender	Method of test	Lens Thickness, LT (Refractive-error, K)
Atchison 2008	Australia, 96%W	106 subj. /106 eyes K= -0.88 to +0.75D	18-29(n=23), 30-39(n=20), 40-49(n=22), 50-59(n=21), 60-69(n=20)	51F	Ultrasono-graphy	LT=4.13±0.40mm, n=51
				51M		LT=4.19±0.47mm, n=51
						LT=3.1267+0.02351*age (adjusted r^2=0.63, n=102, p<0.001).
Ziylan 2006	Turkey	25 subj./50 eyes	(12-24month) pre-term children		A-Scan	LT(K=-4.09±4.34D)=3.95±0.21mm, n=50
		35 subj./70 eyes				LT(K=1.64±0.81D)=3.94±0.22mm, n=70
		20 subj./40 eyes				LT(K=1.92±0.77D)=3.92±0.25mm, n=40
Jones 2005	Ohio	**my group:** 59(3yr old); 11(4yr); 15(5yr); 45(6yr); 25(7yr); 92(>8yr)		138F, 109M	A-Scan	LT(K=-0.49±1.38D; ≤-0.75D) =3.5±0.2mm, n=247
		hy group: 12(3yr old); 5(4yr); 3(5yr); 8(6yr); 1(7yr); 14(>8yr)		23F, 20M		LT(K=2.45±0.92D; ≥+1.0D stable) =3.55±0.2mm, n=43
		em group: 96(3yr old); 14(4yr); 7(5yr); 45(6yr); 3(7yr); 29(>8yr)		84F, 110M		LT(K=0.54±0.22D; -0.25to+1.0D stable) =3.47±0.1mm, n=194
		emmetropizing hy: 21(3yr old); 28(4yr); 29(5yr); 4(6yr); 26(7yr); 107(>8yr)		135F, 118M		LT(K=1.36±0.48D)=3.54±0.2mm, n=253
Mallen 2005	Jordan	1093 subj. / 1093 right eyes			A-Scan	LT(K=-0.87±1.70D)=3.85±0.45mm, LT=0.03*K+3.88mm, r=0.12, n=1093
				643F		LT(K=-0.95±1.58D)=3.83±0.41mm, n=643
				450M		LT(K=-0.74±1.84D)=3.89±0.50mm, n=450
			(17-22yr)			LT(K=-0.81±1.65D)=3.71±0.38mm, n=261
			(23-28yr)			LT(K=-1.20±1.60D)=3.76±0.38mm, n=358
			(29-34yr)			LT(K=-0.83±1.59D)=3.89±0.45mm, n=221
			(35-40yr)			LT(K=-0.44±1.88D)=4.10±0.50mm, n=253
Mutti 2005	US	222 infants	3-month visit	118F, 104M	A-Scan	LT(K=+2.16±1.30D)=3.92±0.17mm, n=222
			9-month visit			LT(K=+1.36±1.06D)=3.86±0.18mm, n=222
			6-month change			ΔLT(ΔK=-0.80±0.90D)=-0.05±0.19mm, n=222

Table 2.9, cont.

Shufelt 2005	LA, Latino	5588 subj. /5588 right eyes	(40-49 yr)	1304F	A-Scan	LT(K=-0.32±1.8D)=4.22±0.63mm, n=1304
				923M		LT(K=-0.30±1.3D)=4.2±0.7mm, n=923
			(50-59 yr)	1009F		LT(K=-0.23±1.9D)=4.37±0.46mm, n=1009
				726M		LT(K=0.02±1.6D)=4.4±0.6mm, n=726
			(60-69 yr)	631F		LT(K=0.73±2.36D)=4.49±0.5mm, n=631
				441M		LT(K=0.4±1.6D)=4.6±0.6mm, n=441
			(70-79 yr)	253F		LT(K=1.02±2.30D)=4.63±0.51mm, n=253
				214M		LT(K=0.6±2.5D)=4.7±0.6mm, n=214
			(≥80 yr)	54F		LT(K=0.74±2.12D)=4.72±0.471mm, n=54
				33M		LT(K=-0.3±2.6D)=4.6±0.4mm, n=33
Kirschkamp 2004	Germany or UK	9 subj. /9 left eyes	(20-38 yr)	2F, 7M	Auto-keratometer	Relaxed: LT=3.7±0.1
						Accommodation: LT=3.9±0.1 (accommodation=3.7±1.1D)
Wickremasinghe 2004	Mongolian	1617 subj. /1617 right eyes	(40-49)	241M	A-Scan	LT(K=+0.1±1.8D)=4.2±0.3mm, n=241
				368F		LT(K=-0.3±1.6D)=4.1±0.3mm, n=368
			(50-59)	200M		LT(K=+0.2±0.9D)=4.4±0.3mm, n=200
				266F		LT(K=+0.1±1.9D)=4.4±0.3mm, n=266
			(60-69)	150M		LT(K=0.0±1.5D)=4.5±0.4mm, n=150
				168F		LT(K=-0.4±3.2D)=4.7±0.9mm, n=168
			(≥70 yr)	109M		LT(K=-0.7±3.6D)=4.6±0.5mm, n=109
				115F		LT(K=+0.4±1.3D)=4.7±0.9mm, n=115
Zadnik 2004	Ohio	194 subj. /194 right eyes	9.4±2.3 (6-14)		A-Scan	LT(K=0.52±0.26D vertical/0.55±0.26D horizontal)=3.5±0.1, n=194.
Cook 2003	UK	68 infants	32.9 weeks	33F, 35M	A-scan biometer	LT(K=-2.06±2.27D)=3.84±0.22mm, n=54
			36.1 weeks			LT(K=-1.23±2.17D)=3.93±0.18mm, n=52
			40 weeks			LT(K=+0.74±1.83D)=3.98±0.19mm, n=55
			44.7 weeks			LT(K=+1.89±1.76D)=3.98±0.22mm, n=53
			52.9 weeks			LT(K=+2.12±1.25D)=3.96±0.21mm, n=38
			33-53 weeks postmenstrual			LT= .0056(±.0018)*(Week-40)+3.93(±.018)mm; K=0.24(±.0016)*(Week-40)+0.87(±0.20)D

Table 2.9, cont.

Zadnik 2003	USA: W, B, A, H, & Native American	2583 children	6 year old	1274F	A-Scan	LT(K=0.88±0.86D)=3.54±0.15mm
			7 year old			LT(K=0.78±1.01D)=3.52±0.16mm
			8 year old			LT(K=0.64±1.26D)=3.47±0.15mm
			9 year old			LT(K=0.18±1.64D)=3.44±0.17mm
			10 year old			LT(K=-0.004±1.42D)=3.41±0.17mm
			11 year old			LT(K=0.03±1.72D)=3.45±0.17mm
			12 year old			LT(K=-0.16±1.55D)=3.41±0.16mm
			13 year old			LT(K=-0.15±1.38D)=3.45±0.18mm
			14+ year old			LT(K=-0.46±2.18D)=3.43±0.20mm
			6 year old	1309M		LT(K=0.81±0.87D)=3.53±0.17mm
			7 year old			LT(K=0.72±0.95D)=3.52±0.15mm
			8 year old			LT(K=0.53±1.11D)=3.46±0.16mm
			9 year old			LT(K=0.37±1.14D)=3.44±0.17mm
			10 year old			LT(K=0.34±1.25D)=3.43±0.18mm
			11 year old			LT(K=0.18±1.57D)=3.43±0.17mm
			12 year old			LT(K=0.32±1.50D)=3.39±0.17mm
			13 year old			LT(K=-0.12±1.58D)=3.44±0.18mm
			14+ year old			LT(K=-0.11±2.78D)=3.52±0.22mm
Gao 2002	Chinese	135 subj. /270 eyes	9.6±2.3 (7-13)	72F, 63M	A-scan	LT(K=4.57±2.17D)=3.72±0.22 mm before & 3.46±0.26mm, after cycloplegia. n=118
						LT(K=0.11±0.47D)=3.57±0.19mm before & 3.44±0.15mm, after cycloplegia. n=38
						LT(K=-2.47±1.80D)=3.49±0.24mm before & 3.40±0.18mm, after cycloplegia. n=114
Gwiazda 2002	US, B, W, H, A	469 children / 469 right eyes	6 to 11 year old	246 F, 223 M	A-Scan	LT(K=-2.38±0.81D)=3.4±0.2mm, n=469.
Saw 2002a	Singapore /Chinese	1449 children /1449 right eyes			A-Scan	LT correlations to K, body height, weight, mass index, age, and gender
Saw 2002b	Singapore, Chinese	1453 children /1453 right eyes	7 year old	318 M	A-Scan	LT(K=-0.2±1.6D)=3.5±0.2mm, n=318
			8 year old	239 M		LT(K=-0.5±1.7D)=3.5±0.2mm, n=239
			9 year old	192 M		LT(K=-1.4±2.1D)=3.4±0.2mm, n=192
			7 year old	313 F		LT(K=-0.08±1.3D)=3.5±0.2mm, n=313
			8 year old	231 F		LT(K=-0.3±1.5D)=3.5±0.2mm, n=231
			9 year old	160 F		LT(K=-1.1±1.8D)=3.4±0.2mm, n=160
Tong 2002	Singapore	252 subj. /252 left eyes	9.17±1.57	110F, 142 M	A-scan	LT(K=-3.65±1.23D)=3.41±0.16mm, n=252
					Scheimflug	LT(K=-3.65±1.23D)=3.21±0.16mm, n=252
Pennie 2001	UK	20 infants /20 right eyes	4.3±0.9 week	10F, 10M	Throughthee yelid ultrasonic biometry	LT(K=+2.81±0.94D)=3.70±0.22mm, n=20
			14.0±1.9 week			LT(K=+2.74±1.46D)=3.65±0.25mm, n=19
			27.3±1.7 week			LT(K=+1.91±1.31D)=3.63±0.23mm, n=18
			40.0±1.9 week			LT(K=+1.76±1.50D)=3.58±0.24mm, n=13
			53.1±1.6 week			LT(K=+1.50±1.42D)=3.65±0.14mm, n=10

Table 2.9, cont.

Wong 2001	Singapore /Chinese	1004 subj. / 1004 OD	(40-81 yr)	547F	A-Scan	LT(K=-0.56±2.89D)=4.78±0.47mm, n=547
				457M		LT(K=-0.40±2.41D)=4.73±0.47mm, n=457
Zadnik 1999	Ohio	554 subj. /554 OD	8.60±0.53 yr		A-Scan	LT(K=0.94±0.71D)=3.46±0.16mm, n=554
Mutti 1998	USA 86.6%W, 11.2%A, 1.5%H, 0.7%B	994 subj.	(6 to 15 yr)	451F, 543M	Ultrasono--graphy	LT=3.428-0.0111*(Age-10)+0.0055*(Age-10)^2-0.0005*(Age-10)^3, n=994
McBrien 1997	UK	14 hy OD	29.72 (22-50)		A-Scan	LT(K=+1.51±0.82D)=3.91±0.52mm, n=14
		68 em OD	30.83 (21-61)			LT(K=+0.10±0.25D)=3.96±0.41mm, n=68
		78 adult onset my OD	31.04 (22-53)			LT(K=-1.68±1.15)D)=3.88±0.44mm, n=78
		47 youth onset my OD	30.39 (21-46)			LT(K=-3.74±2.13D)=3.91±0.48mm, n=47
		38 15-20y-onset my OD	28.77 (21-64)			LT(K=-2.46±1.66D)=3.98±0.55mm, n=38
Goss 1997	USA, Oklahoma	34 em males	25±4.6 (21~44)	63 F, 105 M	A-Scan	LT(+0.25±0.36D)=3.63±0.25mm; n=34M
		71 my males	26.8±6 (21~43)			LT(-2.87±2.14D)=3.62±0.24mm; n=71M
		19 em females	25.6±5 (21~38)			LT(+0.17±0.36D)=3.69±0.31mm; n=19F
		44 my females	25.5±5 (20~39)			LT(-3.42±2.20D)=3.66±0.23mm; n=44F
Garner 1997	New Zealand	11 subj. K=-1.88±1.64 D (-4.25 to +0.5D)	21.2 (18-28 yr)		A-Scan	3.54±0.17mm at 0D accommodative stimulus
						3.53±0.17mm at 1.5D accommodative stimulus
						3.62±0.17mm at 3.5D accommodative stimulus
						3.76±0.22mm at 5.5D accommodative stimulus
						3.82±0.22mm at 8D accommodative stimulus
Koretz 1989	US	100 subj.	(18-70)	68F, 32M	Ultrasono-graphy	LT= 0.013(±0.002) *Age+3.460 (±0.080)mm, r=0.611, p=0.95*10^{-6})
					slit-lamp Scheimpflug photography	LT= 0.013(±0.002) *Age+3.460 (±0.080)mm, r=0.611, p=0.95*10^{-6})
Scott 1993	New Zealand	42 em (-0.5 to +1.5D)	(17-26 yr)		A-Scan	LT(K=0.32±0.52D)=3.62±0.23mm; n=42
		42 my (-5 to -7D)				LT(K=-5.90±0.68D)=3.58±0.23mm; n=42
Cheng 1992	Massachu setts	8 hy subj	>25 yr		MRI	LT(+3.72±0.96D)=4.8±0.6mm; n=8
		6 em subj				LT(+0.21±0.25D)=5.0±0.7mm; n=6
		7 my subj				LT(-6.54±2.74D)=4.8±0.2mm; n=7

Table 2.9, cont.

Alsbirk 1977	Grrenland Eskimos	326 subj.	~43 yr old	F	Ultrasonic oculometry	LT(K=+0.25±1.25D)=4.37±0.28mm; 20yr: LT(K=-0.28D)=3.85mm; 70yr: LT(K=+0.90D)=4.90mm
		279 subj.	~44 yr old	M		LT(K=-0.07±1.34D)=4.36±0.27mm; 20yr: LT(K=-0.01D)=3.76mm; 70yr: LT(K=-0.18D)=4.93mm

A: Asian	W: White	hy: hyperopic	F: female	OD: right eye	LT: lens thickness
B: Black		em: emmetropic	M: male	OS: left eye	K: refracrive error (spherical equivalent)
H:Hispanic		my: myopic	yr: year old	D: diopter	

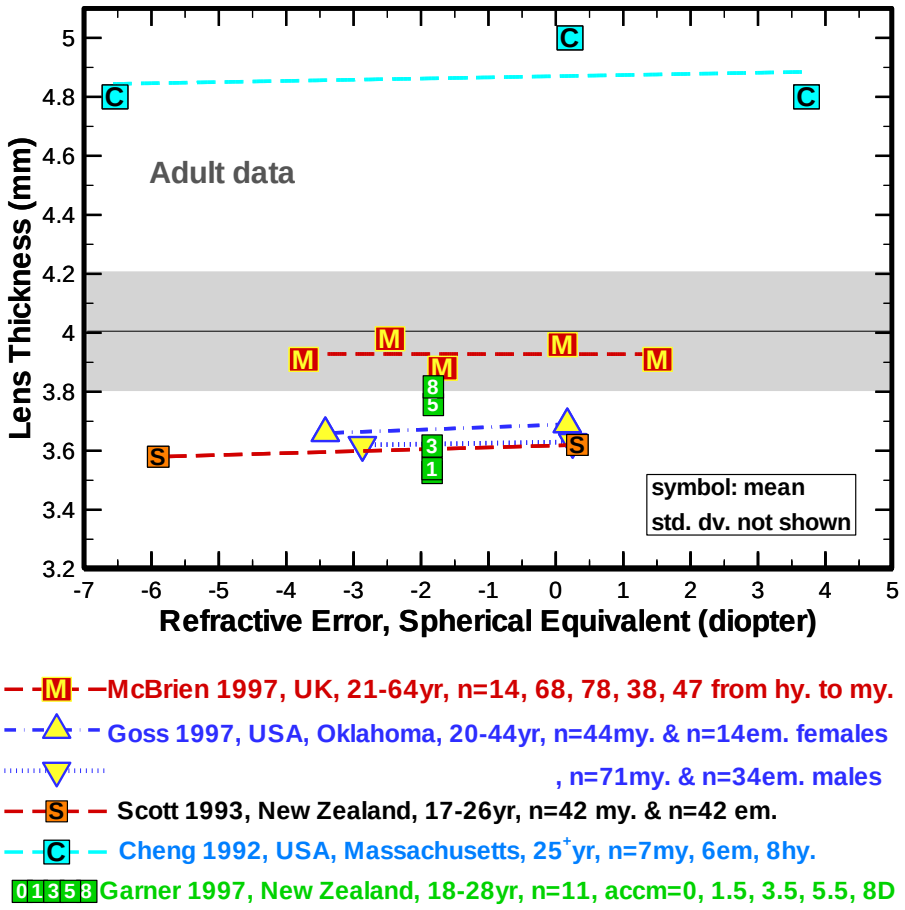

Figure 2.41 *Comparison of 5 studies: LT vs. K in adults*

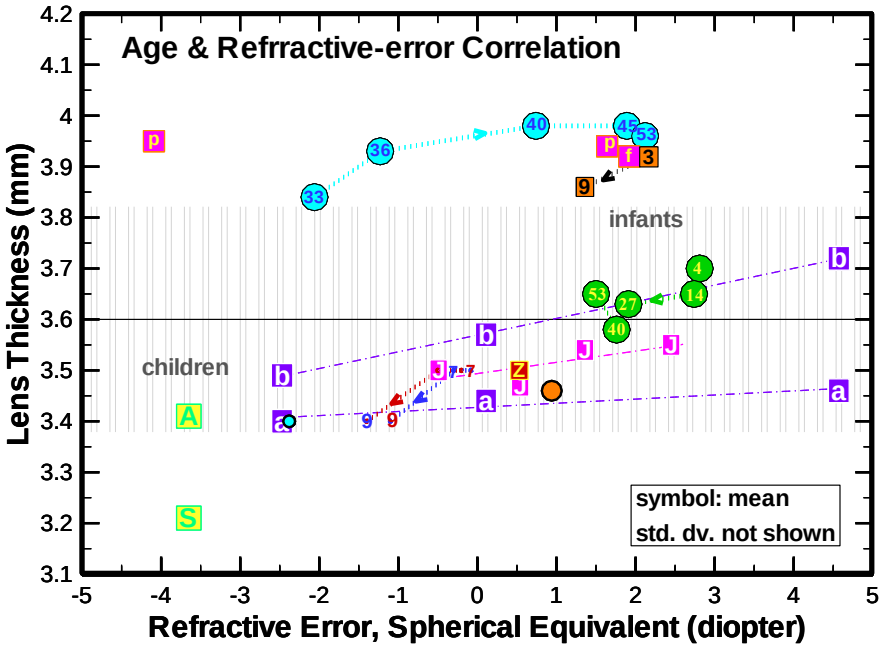

Cook 2003; UK, postmentrual age=33, 36, 40, 45, 53 weeks. n=68

Pennie 2001, UK, infants, age=4, 14, 27, 40, 53 weeks, n=20

Mutti 2005, US, infants at 3 and 9 month, n=222

Ziylan 2006, Turkey, 12-24 months pre-term & full-term children

Jones 2005, USA, Ohio, 3-8yr children, n=737

Gao 2002, 7-13yr, Chinese, 7-13yr, n=270, before cycloplegia

, after cycloplegia

Gwiazda 2002, USA, 6-11yr, n=469

Saw 2002, Singapore(Chinese), 7yr (n=313) & 9yr(n=160) girls

, 7yr(n=318) & 9yr(n=192) boys

Zadnik 2004, USA, Ohio, 6-14yr, n=194

Tong 2002, Singapore, 9.17±1.57yr, n=252, AScan

, Scheimflug

Zadnik 1999, USA, Ohio, 8.60±0.53yr, n=554

Figure 2.42 *Comparison of 11 studies: LT vs. K in infants and children*

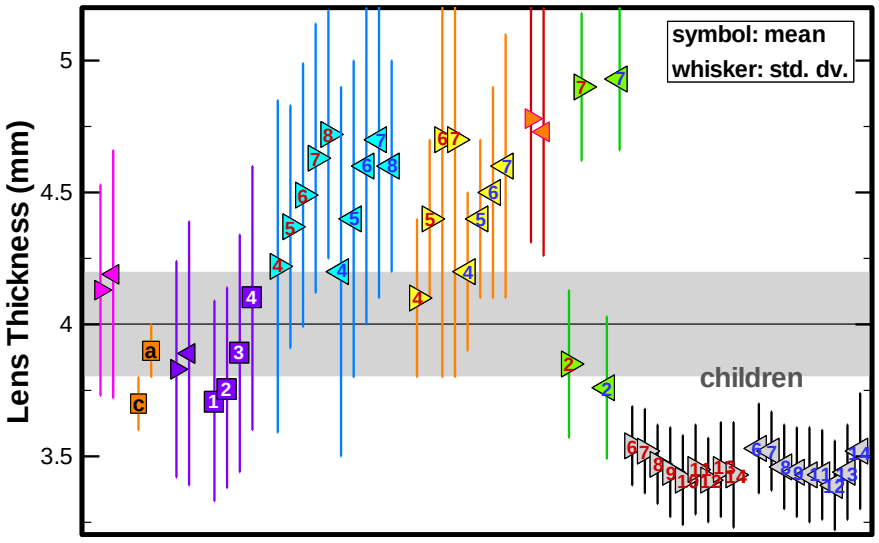

Atchison 2008, Australia, 96+% Caucasians, 18-69yr, n=51 females
, n=51 males
Kirschkamp 2004, Germany / UK, 20-38yr, 20-38yr, n=9, cycloplegia
, accommodative 3.7±1.1D
Mallen 2005, Jordan, 17-40yr, n=643 females
, n=450 males
, n=261(17-22yr), 385(23-28yr), 221(29-34yr), 253(35-40yr)
Shufelt 2005, USA/Latino, 40's, 50's, 60's, 70's, 80+yr, 3251 females
, 2337 males
Wickremasinghe 2004, Mongolian, 40's, 50's, 60's, 70+yr, 970 females
, 700 males
Wong 2001, Singapore/Chinese, 40-81yr, n=547 females
, n=457 males
Alsbirk 1977, Greenland, Eskimos, 20yr & 70yr females
, 20 yr & 70yr males
Zadnik 2003, USA, 6, 7, 8, 9, 10, 11, 12, 13, 14+yr, n=1274 girls
, n=1309 boys

Figure 2.43 *Comparison of 8 LT studies*

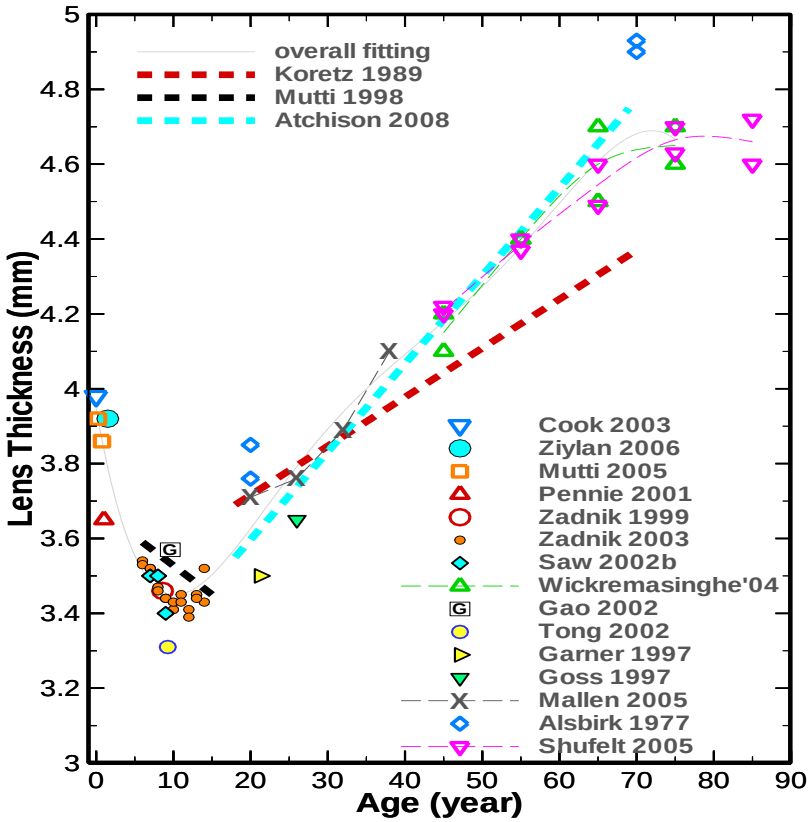

Figure 2.44 *Comparison of age-dependence in 18 LT studies*

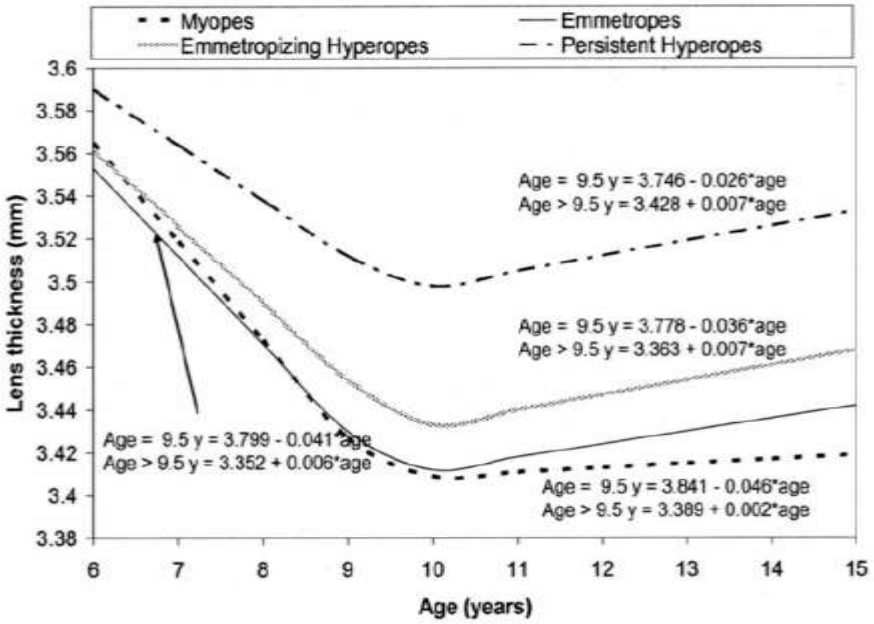

Figure 2.45 *Development of LT in 4 refractive groups of US children 6- to 15-year old from Jones 2005*

Gender dependence:

There is no significance in gender correlation in all the studies. In Goss's study (Figure 2.41) [Goss 1997] and Wong (Figure 2.43) [Wong 2001], females have slightly larger *LT* than males. Atchison's [Atchison 2008] and Mallen's [Mallen 2005] studies show slightly larger *LT* in males (Figure 2.43). In the same figure, Shufelt [Shufelt 2005], Wickremasinghe [Wickremasinghe 2004], and Alsbirk [Alsbirk 1977] show no difference between genders,

In children's studies, Saw's [Saw 2002b] study shows boys had same *LT* with same aged girls (Figure 2.42). Zadnik's study also shows that gender factor does not significantly affect LT [Zadnik 2003] (Figure 2.43).

Body height, weight, and BMI:

Wong [Wong 2001] and Saw [Saw 2002a] gave *LT* and *K* in 5 and 4 quartiles according to height, weight and BMI. Wong indicated that height and weight correlate negatively with *LT*, but BMI does not correlate with *LT* [Wong 2001]. Saw found that the taller children are more myopic and have thinner *LT*. [Saw 2002 a]

2.4.4 Refractive Index of Crystalline Lens (n_3)

The human lens has gradient refractive index, and the Liou and Brennan eye model [Liou 1997] uses a gradient index to mimic the measured data.

For simplification, an 'equivalent' constant index is often used instead of the actual gradient index. Navarro 1985 model uses 1.42 for relaxed eye. The model also describes the index as a function of accommodation.

Atchison 2008 study described lens equivalent refractive index as a function of age with Purkinje imagery and applied the parameter in the 4-surface eye model. There is a significant trend: n_3=1.4506-0.00035*Age (adjusted r^2 = 0.21, n = 102, p<0.001) [Atchison 2008]. In comparison, Dubbelman 2001 study obtained n_3=1.441-0.00038*Age.

Jones study investigated and gave age-dependent crystalline lens index for US children 6 to 15-year old [Jones 2005].

$n_3=0.162*Age^{-2}+1.427$ (persistent emmetropia);

$n_3=0.222*Age^{-2}+1.429$, p=0.4645 (Persistent hyperopia);

$n_3=0.079*Age^{-2}+1.428$, p=0.2563 (myopia);

$n_3=0.121*Age^{-2}+1.429$, p=0.6064 (Emmetropizing hyperopia).

These results are plotted in Figure 2.46. However, these age-dependences are not significant.

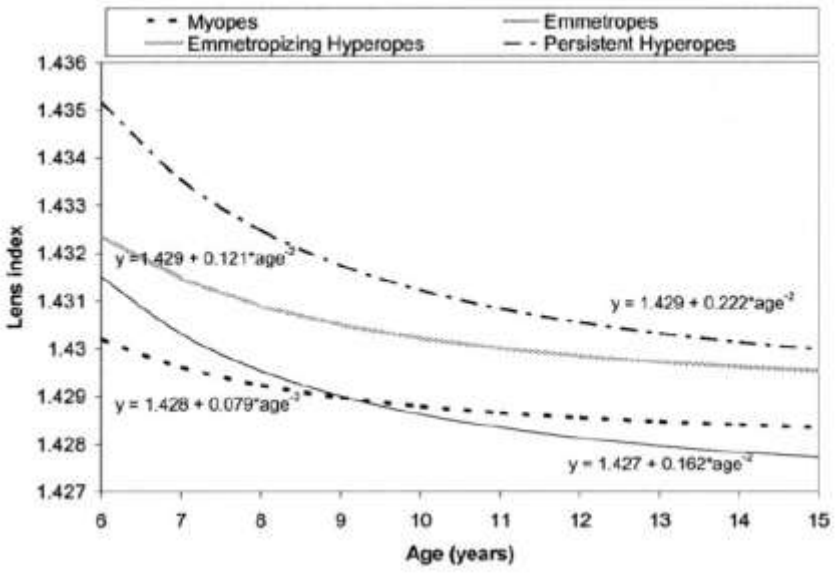

Figure 2.46 *Development of n_3 in 4 refractive groups of US children 6- to 15-year old from Jones 2005*

2.4.5 Posterior Lens Radius of Curvature (LR_2)

I collected 10 papers concerning the posterior lens radius. No scatter point figure for LR_2 vs. K is available. Table 2.10 summarizes these papers. The measured LR_2 are in the range from 5 to 8 mm. Navarro model uses 6.0 mm.

Refractive error correlation:

As described earlier and as the studies of Goss [Goss 1997] (Figure 2.47) and Dubbelman [Dubbelman 2001] found, there is no significant correlation between posterior crystalline lens radius and refractive error.

Age:

As shown in Figure 2.49, Mutti 2005 provides infant's data at 3 and 9 months of age. The Mutti 1998 data describe the growth of the lens from 6 to 15 years of age. Adult's data are also compared in the Figure 2.49. Atchison 2008 fitting result is insignificant (p=0.30) [Atchison 2008].Dubbelman obtained significant regression: $LR_2=-0.017(\pm0.008)*Age+6.5(\pm0.3)$, r=-0.34, p=0.03, n=102 (LR_2 vs. Age scatterpoint figure is available) [Dubbelman 2001]. Koretz 2001 and Brown 1974 data are larger (flatter surface) compared to others.

Gender:

Atchison study obtained that females have about 0.18mm longer LR_2 than males [Atchison 2008] (Figure 2.48). However, the difference is not significant (p=0.39). In the Goss 1997 study, male emmetropes has 0.25mm longer LR_2 than females emmetropes and male myopes have 0.27mm longer LR_2 than female myopes [Goss 1997] (Figure 2.47).

Accommodation:

Accommodation increases the curvatures (reduces the radius) of both anterior and posterior lens surfaces. Doubbelman 2005 reported the mean change per diopter on LR_2 as -0.13±0.06mm/diopter in the 3mm

visual zone. Garner reported LR_2 at 5 different accommodation stimulus. The result shows similar reduction [Garner 1997_change] (Figure 2.48. Kirschkamp reported that 3.7±1.1D accommodation reduced LR_2 from 6.1±0.2mm, under cycloplegia, to 5.3±0.2mm [Kirschkamp 2004]. The use of cycloplegia always relaxes the leans more than the natural relaxation status. This is observed in both the anterior and posterior surface and the lens thickness.

Table 2.10 *Information of 10 LR_2 papers*

Author (year)	Geographic /race	Subject no. /eye no.	Gender	Subject Age (year)	Method of test	Posterior Lens Radius of curvature LR (Spherical equivalent power, K)
Atchison 2008	Australia, 96% W	106 subj. /106 eyes K=-0.88to+0.75D	34F 32M	18-29 yr (n=23), 30-39 yr (n=20), 40-49 yr (n=22), 50-59 yr (n=21), 60-69 yr (n=20)	Purkinje images	LR=6.95±0.91mm, n=34 LR=6.77±0.78mm, n=32 LR=7.1857-0.0076*Age (adjusted r^2=0.0012, n=66, p=0.30), LR=6.86±0.85mm.
Mutti 2005	US	222 infants	118F, 104M	3-month old 9-month old	Phakometer	LR(K=+2.16±1.30D)=4.68±0.31mm, n=222 LR(K=+1.36±1.06D)=5.21±0.36mm, n=222 Growth in 6 monthes: ΔLR(ΔK=-0.80±0.90D) =0.53±0.33mm, n=222
Kirschkamp 2004	Germany or UK	9 subj. / 9 left eyes	2F, 7M	(20 to 38 yr)	Auto-keratometer	LR=6.1±0.2 (Relaxed) LR=5.3±0.2 (Accommodation=3.7±1.1D)
Dubbelman 2001	Netherlands	102 subj. /102 eyes	45F, 57M	F:36.9±13.3 yr M:41.±12.3yr	Scheimpflug image	LR=-0.017(±0.008)*Age+6.5(±0.3), r=-0.34, p=0.03, n=102
Koretz 2001	USA	100 subj.		18–70 yr	Scheimpflug photograph	LR=8.267-0.02025*Age, n=100
Mutti 1998	US:0.7%B, 86.6%W, 11.2% A, 1.5%H.	994 subj.	451F, 543M	(6 to 15 yr)	Phakometer	LR=6.236+0.063*(Age-10)+0.004*(Age-10)^2, n=994
Goss 1997	USA, Oklahoma	34 em males 71 my males 19 em females 44 my females	63 F, 105 M	25±4.6 (21-44) 26.8±6 (21-43) 25.6±5 (21-38) 25.5±5 (20-39)	A-Scan	LR(+0.25±0.36D)=5.93±0.43mm; n=34M LR(-2.87±2.14D)=6.10±0.59mm; n=71M LR(+0.17±0.36D)=5.68±0.50mm; n=19F LR(-3.42±2.20D)=5.83±0.57mm; n=44F
Garner 1997	New Zealand	11 subj. K= -1.88±1.64D (range: -4.25 to +0.50D)		21.2 yr (18-28 yr)	A-Scan	LR=6.62±0.94mm at 0D stimulus LR=6.29±0.61mm at 1.5D stimulus LR=6.03±0.46mm at 3.5D stimulus LR=5.77±0.38mm at 5.5D stimulus LR=5.28±0.38mm at 8D stimulus
Garner 1992	New Zealand, Maylay	19 em subj (-.25~.25D) 19 my subj (>-3D)	9 F, 10 M	(9 to 15 yr)	Calculated with assumed Q	LR(K=+0.01±0.05D)=5.74±0.45mm; n=19 LR(K=-6.08±1.83D)=6.40±0.59mm; n=19
Brown 1974	London, UK	100 subj.		(3-82 yr)	slit-image photograph	LR=8.1±1.6mm, LR=-0.015*Age+8.719, n=100

W: White A: Asian hy: hyperopic F: female OD: right eye LR: Posterior lens radius of curvature

B: Black H:Hispanic em: emmetropic M: male OS: left eye K: refracrive error (spherical equivalent)

my: myopic yr: year old D: diopter

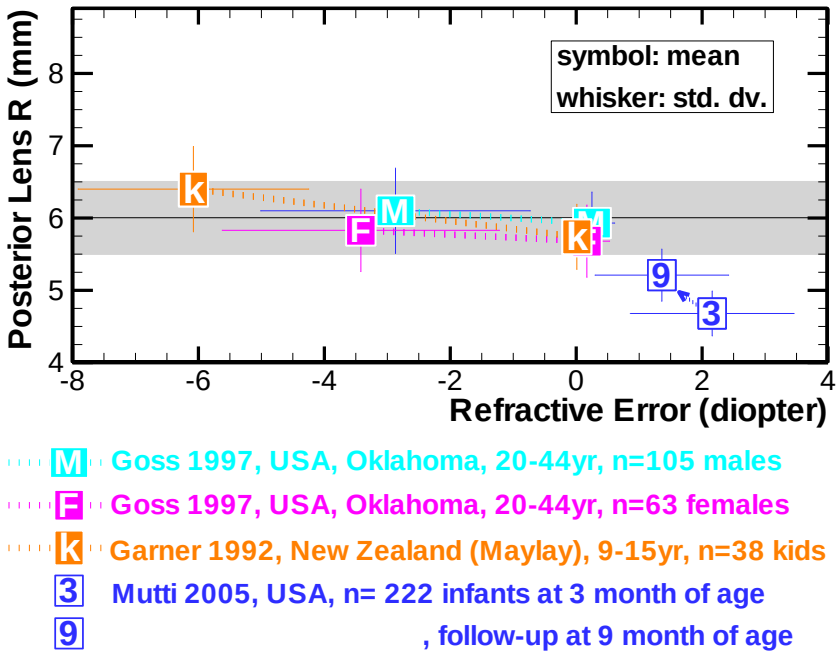

Figure 2.47 *Comparison of age-dependence in 18 LT studies (1)*

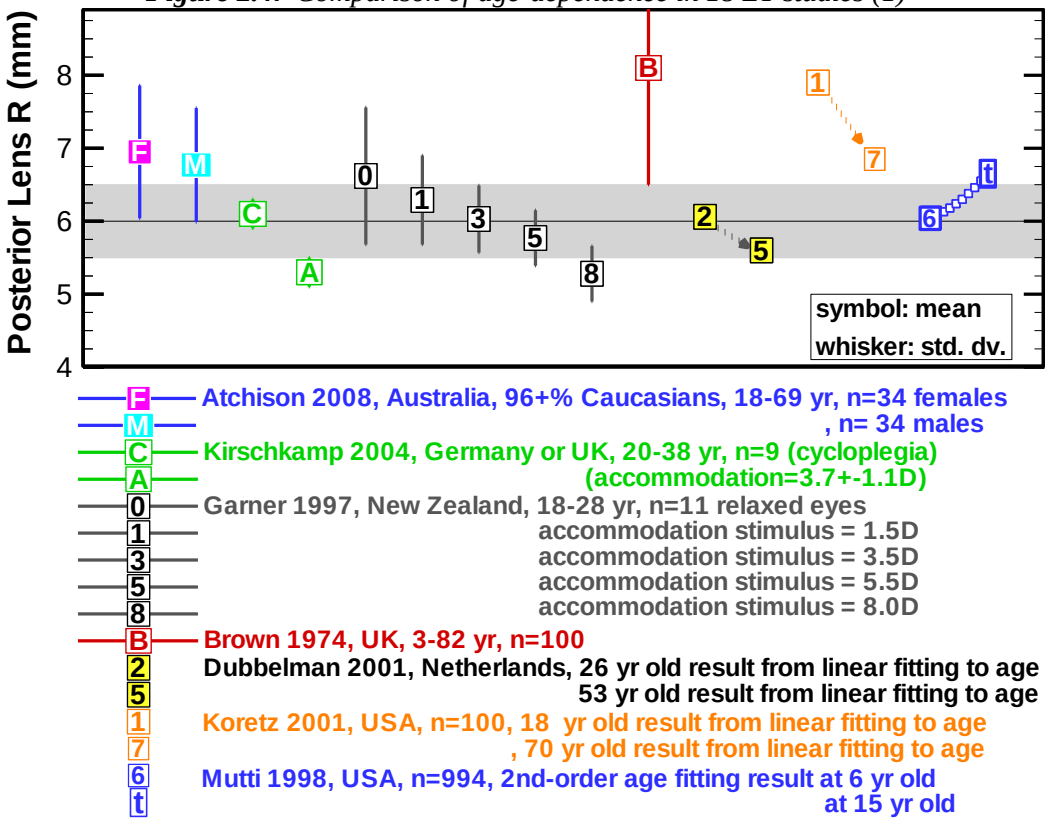

Figure 2.48 *Comparison of age-dependence in 18 LT studies (2)*

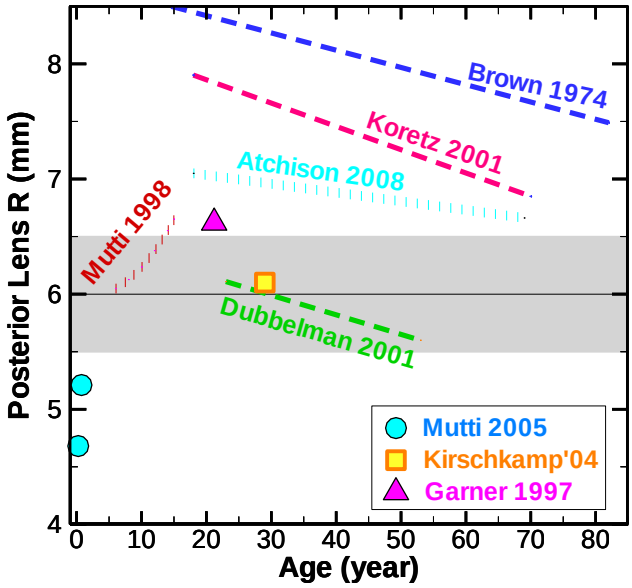

Figure 2.49 *Comparison of age-dependence in 18 LT studies (3)*

2.4.6 Posterior Lens Asphericity (Q_4)

I found only 2 papers that discussed Q_4. Smith's study in 2003 reported Q_4=*-0.000008929 *Age^2+0.002863 *Age+0.9402* [Smith 2003]. Dubbelman reported insignificant correlation: $K_4=Q_4+1=0.07(\pm0.06)*Age-5(\pm2)$, r=0.20, p=0.21, n=41 [Dubbelman 2001]. As references, the values used by Liou model, Navarro model, and Atichson model are indicated in Figure 2.50 with the 2 results.

Table 2.11 *Information of 2 Q_4 papers*

Author (year)	Geographic /race	Subject no. /eye no.	Gender	Age (year)	Method of measurement	Asphericity, conic constant, Q
Smith 2003	Australia				(calculated)	Q=-0.000008929*Age^2+0.002863*Age+0.9402
Dubbelman 2001	Netherlands	102 subj. /102 eyes	45F, 57M	females 36.9±13.3; males 41.0±12.3yr	Scheimpflug image	Q=0.07(±0.06)*Age-6(±2), r=0.20, p=0.21, n=41
	F: female	M: male		yr: year old		Q: posterior lens surface asphericity

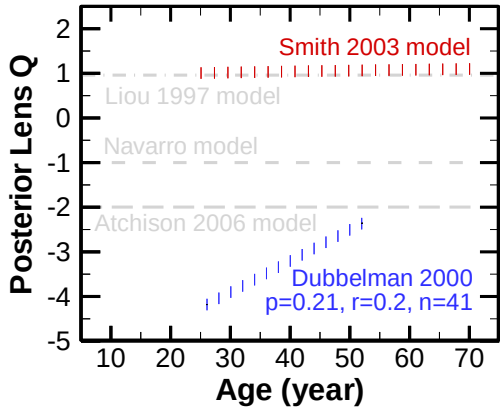

Figure 2.50 *Comparison of age-dependence in Q_4 studies*

2.4.7 Tilt of Lens

Lenses of eyes are considerably tilted about the vertical axis, with their axes usually being directly temporally into object space. Using MRI images, Atchison et al. [Atchison 2005] found that tilt was not significantly affected by refraction, and that the horizontal component of the mean tilt was significantly different from zero at -4.0±2.4°. The negative sign is used to match the convention used by the optical design program (Zemax), and means that the axis is directly temporally into object space. The method of MRI measurement, in which the orientation of the lens was important in determining the alignment of the eye [Atchison et al. 2004] meant that no estimate of the lens tilt about the horizontal axis could be made, and hence I have set this to zero.

2.4.8 Decenter of Lens

I have not collected any paper about the lens decenter. Atchison 2006 eye model assumes that the lens centre coincides with the line of sight. Because the light-of-sight doesn't coincide with the optical axis, this requires horizontal decentration of the anterior and posterior surfaces of equal amounts but in opposite directions by 1.8cos(4°)=0.125562mm, with the front surface temporal decentration having a positive sign to match the convention of the optical design program.

2.4.9 Diameter of Lens

In Atchison's study [Atchison 2006], lens diameters were measured in the axial transverse section for 84 subjects with MRI images. There is no significant trend for the group, with the regression equation being $D_L(\text{mm}) = 9.012\text{-}0.030K$ (adj.r^2=0.017, p=0.114). The mean diameter for all subjects is 9.08±0.41 mm, with a range of 7.8-9.9 mm. Males have greater diameters (9.18±0.42 mm) than females (9.01±0.38 mm), but the difference is not quite significant. Although not used in their raytracing, a useful diameter to use for modeling the unaccommodated lens is $D_L(\text{mm}) = 9.1$

The results for Atchison group are slightly smaller, but not significantly, than the 9.18±0.30 mm (range 8.6-9.9 mm) obtained by Strenk et al. [Strenk 1999] in a group of 25 subjects across the age range 22-83 years. They found that lens diameter did not change significantly with age for unaccommodated eyes.

2.5 REVIEW OF OCULAR AXIAL LENGTH (*AL*):

56 papers of *AL* are collected. Table 2.12 includes 14 papers with scatter data points. All are adult data. Table 2.13 contains additional 22 papers of adults. Table 2.14 further comprises 20 papers of children and infants. The subjects in these studies are all in ocular health. Axial dimensions human eyes are usually measured with ultrasonography, partial coherence interferometry and magnetic resonance imaging. Typical human eye length ranges from 2 to 3 cm. It has been shown universally that *AL* has strong correlation to refractive error. Linear fitting is generally used for their correlation. For a specified refractive error, the statistical distribution deviation is about 0.5 mm to 1.0 mm.

Different measurement tools produce systematic discrepancies. For example, Singh 2006 study investigated the difference between Magnetic Resonance Imaging (MRI) and partial coherence interferometry (PCI) [Singh 2006]. Among the 14 eyes measured, the MRI determined longer lengths than those determined by PCI (mean difference, 0.41 mm). In Atchison 2008 comparison, MRI reported about 0.1mm longer axial length compared to ultrasonography data. Bullimore 2006 obtained 0.18mm longer measurement in IOLMaster than the Ultrasonography.

Table 2.12 *Summary of 14 ocular axial length studies, which provide scatter data points.*

Author (year)	Geographic /race	Subject no. /eye no.	Gender	Age (year)	Method of measurement	Ocular Axial-Length, AL (Spherical equivalent power,K)
Atchison 2006	Australia	121 subj./ 112 OD & 9 OS	63% F	25 ± 5 yr (18–36 yr)	A-scan	AL(K=+0.75D to-12.38D)=-0.298K +23.70, n = 119, r^2 = 0.570, p < 0.001
Singh 2006	UK	7subj./14 eyes	4F, 3M	(24 to 38 yr)	MRI, PCI	14 data points, (AL, K), are available.
Chui 2005	Chinese	60 subj	28F, 32M	(20 to 29 yr)	A-Scan	Scatter pionts (K, 1/AL) are reported, K=1.57/AL-66.6 diopter, n=60
Gray 2005	UK	20 hy subj		Young adults	IOL ocular biometer	AL(K=-7.25 to +6.50D)=-0.37K+23.29, n=24, r^2=0.5665
		20 em subj				
		20 my subj				
Mallen 2005	Jordan	1093 subj./ 1093 right eyes		(17-40 yr)	A-Sacn	AL(K=-0.87±1.70D)=23.13±1.00mm, AL=-0.30*K+22.87mm, r=-0.52, n=1093
Chau 2004	China	33 subj./33 eyes	17F, 16M	mean 21 yr (19 to 42 yr)	A-Scan	AL(K=-12.75to+1.00D)=-0.49K+23.42, n=33, p<0.005, r=-0.91
Llorente 2004	Spain	22hy eyes		30.3±5.2 yr (23-40 yr)	IOL ocular biometer; (average of 3-5 scans)	AL(K=+0.5 to +7.4D)=-0.10K+22.9, n=22, p=0.25, r=-0.26
		24my eyes		30.5±3.8 yr (26-39 yr)		AL(K=-7.6 to -0.8D)=-0.38K+24.2, n=24, p=0.001, r=0.57
Atchison 2004	Australia, 74 W, 14A	22 em eyes		(18 to 36 yr)	MRI	AL(K=-12 to +0.75D)=-0.35K+23.31, n=87, p<0.001, r^2=0.53
		66 my eyes				
Rabsilber 2003	Germany	20 hy eyes ≥ +3D	36 F, 24 M	62.2±12.7 yr	IOL ocular biometer	AL(K=-22 to +8)=-0.3663K+23.779, n=60, r=0.94 (ACD measured with IOL ocular biometer and Orbscan)
		20 em eyes		26.9±3.0 yr		
		20 my eyes ≥ -6D		41.4±14.8 yr		
Mainstone 1998	Australia	25 hy subj(+2.7±1.7D)		29.9±11.4 yr (16 to 49 yr)	Bio-pen hand-held biometric ruler	AL(K=-0.37 to +6)=-0.384K+23.533, n=35, p=0.001, r^2=0.567
		10em subj(+.21±.26D)				
Strang 1998 (hy-study)	Australia	57 em and hy subj		32.7±11.4 yr (18 to 51 yr old)	Mentor Biopen XL biometric ruler	AL(K=-0.37 to +8.00)=-0.34K+23.50, n=53, r^2=0.61
Strang 1998	Australia, UK or USA	34 em and my (0 to -14D)		Young adults	A-Scan	AL(K=-14 to 0D)= AL(K=0)-22.267K /(60+K), n=34, r=0.84; AL(K=0)=24.0D
Carney 1997	Ohio or Australia	30 em(-0.25 to +0.25D)	44 F, 69 M	26±5.9 (15~49)	Bio-pen hand-held biometric ruler	AL(K=-10 to +0.25D)=-0.29K+23.061, n=113, p=0.0001, r=0.603
		30 low my (0.75 to -2D)		27±7.2 (22~52)		
		34 mod-my (-2 to -4D)		28±6.4 (22~48)		
		19 high my (worse-4D)		27±4.5 (23~38)		

Table 2.12, cont.

Hirzenberger 1991	Austria	7 subj. / 7 eyes			A-scan & Laser doppler interferometry	7 subjects' refraction and axial length measured by A-scan and LDI
W: White	A: Asian	hy: hyperopic		F: female	OD: right eye	AL: ocular axial length
B: Black	H:Hispanic	em: emmetropic		M: male	OS: left eye	K: refracrive error (spherical equivalent)
		my: myopic		yr: year old	D: diopter	

Table 2.13 *Information of 22 AL papers of adults*

Author (year)	Geographic /race	Subject no. /eye no.	Gender	Age (year)	Method of test	Ocular Axial-Length, AL (Spherical equivalent power,K)
Atchison 2008	Australia: >96%W	106 subj./106 eyes K=-0.88 to +0.75D	51F	18-29 yr (n=23), 30-39 yr (n=20), 40-49 yr (n=22), 50-59 yr (n=21), 60-69 yr (n=20)	Ultrasono-graphy	AL=23.17±0.77mm, n=51
			51M			AL=23.79±0.55mm, n=51
						AL(Age)=22.984+0.0113*Age , Age=18-69 yr (adjusted r^2=0.04, n=102, p=0.02)
Bullimore 2006	Ohio, 316W, 2H, 42B, 30A, 6 others	396 subj.	263F, 133M	30.7±3.5	Ultrasound & IOLMaster	AL(K=-3.54±1.77D)=24.46±1.05 mm, n=396 (ultrasound); AL(K=-3.54±1.77D)=24.62±1.06 mm, n=355 (IOLMaster)
Mallen 2006	UK	30 em subj. /30 right eyes	16F, 14M	21.4±2.0 yr	IOLMaster	AL(K=-0.07±0.23D)=23.25±0.66mm, n=30; AL changes=2D: 0.014±0.019mm; 4D: 0.026±0.021mm; 6D: 0.037±0.027mm
		30 my subj. /30 right eyes	21F, 9M	21.5±2.1 yr		AL(K=-3.59±0.75D)=25.39±1.03mm, n=30; AL changes=2D:0.019±0.020mm; 4D:0.037±0.026mm; 6D:0.058±0.037mm
Mallen 2005	Jordan	1093 subj. / 1093 right eyes		(17-40 yr)	A-Scan	AL(K=-0.87±1.70D)=23.13±1.00mm, AL=-0.30*K+22.87mm, r=-0.52, n=1093
			643F			AL(K=-0.95±1.58D)=22.99±0.97mm, n=643
			450M			AL(K=-0.74±1.84D)=23.33±1.02mm, n=450
				(17-22 yr)		AL(K=-0.81±1.65D)=23.08±1.01mm, n=261
				(23-28 yr)		AL(K=-1.20±1.60D)=23.18±0.96mm, n=358
				(29-34 yr)		AL(K=-0.83±1.59D)=23.15±1.08mm, n=221
				(35-40 yr)		AL(K=-0.44±1.88D)=23.10±1.00mm, n=253
Pedersen 2005	Denmark	105 subj. /105 eyes	30F, 18M	37±8.8 yr (18-55 yr)	Optical low-coherence reflectometry (OLCR) pachymeter	AL(K<-6D)=26.52±1.265mm, n=48
			29F, 28M	36±8.6 yr (18-55 yr)		AL(K=0to+1.5D)=23.52±0.775mm, n=57

Table 2.13, cont.

Logan 2005	UK, White	373subj. /373 right eyes		19.55±2.99 yr (17-30 yr)	IOLMaster	AL(K=-1.01±2.19D)=23.91±1.18mm, n=145
	UK, Asian					AL(K=-1.40±2.57D)=24.09±1.24mm, n=217
Gudmundsdottir 2005	Iceland White	757 subj. /757 right eyes	419F, 338M	(55-64)	A-Scan	AL(K=0.68D)=23.56±1.08mm, n=306
				(65-74)		AL(K=1.55D)=23.40±1.01mm, n=280
				(>=75)		AL(K=1.42D)=23.23±1.27mm, n=171
Shufelt 2005	LA/Latino	5588 subj. /5588 right eyes	1304F	(40-49)	A-Scan	AL(K=-0.32±1.8D)=23.2±1.1mm, n=1304
			923M			AL(K=-0.30±1.3D)=23.7±1.0mm, n=923
			1009F	(50-59)		AL(K=-0.23±1.9D)=23.2±0.9mm, n=1009
			726M			AL(K=0.02±1.6D)=23.6±0.8mm, n=726
			631F	(60-69)		AL(K=0.73±2.36D)=23.1±1.0mm, n=631
			441M			AL(K=0.4±1.6D)=23.6±0.9mm, n=441
			253F	(70-79)		AL(K=1.02±2.30D)=23.1±0.9mm, n=253
			214M			AL(K=0.6±2.5D)=23.5±0.9mm, n=214
			54F	(>=80)		AL(K=0.74±2.12D)=22.9±0.9mm, n=54
			33M			AL(K=-0.3±2.6D)=23.7±0.9mm, n=33
Wickremasinghe 2004	Mongolian	1617 subj. /1617 right eyes	241M	(40-49)	A-Scan	AL(K=+0.1±1.8D)=23.4±1.3mm, n=241
			368F			AL(K=-0.3±1.6D)=23.0±1.3mm, n=368
			200M	(50-59)		AL(K=+0.2±0.9D)=23.3±0.8mm, n=200
			266F			AL(K=+0.1±1.9D)=23.1±1.1mm, n=266
			150M	(60-69)		AL(K=0.0±1.5D)=23.5±1.0mm, n=150
			168F			AL(K=-0.4±3.2D)=23.2±1.1mm, n=168
			109M	(>70 year old)		AL(K=-0.7±3.6D)=23.6±0.9mm, n=109
			115F			AL(K=+0.4±1.3D)=23.1±1.2mm, n=115
Wong 2001	Singapore /Chinese	1004 subj. /1004 right eyes	547F	(40-81 yr)	A-Scan	AL(K=-0.56±2.89D)=22.98±1.16mm, n=547
			457M			AL(K=-0.40±2.41D)=23.54±1.10mm, n=457
Chang 2001	Asian	216 subj	70F, 146M	22.2±4.2 yr	A-Scan	AL(K=-4.17±5.03D)=25.2±2.0mm, n=216.
Hosny 2000	Spain, 211W	AL<=20mm, 21eyes		40.35±16.3 yr (18-78 yr)	Ultrasonic pachymeter	K=+5.45±2.43D
		AL=20-22mm,44eyes				K=+3.29±2.53D
		AL=22-24mm,43eyes				K=-2.19±2.47D
		AL=25-27mm,41eyes				K=-6.19±2.12D
		AL=27-29mm,34eyes				K=-8.97±2.92D
		AL>=29mm, 28eyes				K=-19.34±3.34D

Table 2.13, cont.

McBrien 1997	UK	14 hy subj./14 OD		29.72 (22-50)	A-Scan	AL(K=+1.51±0.82D)=23.26±/0.97mm, n=14
		68 em subj./68 OD		30.83 (21-61)		AL(K=+0.10±0.25D)=23.69±0.66mm, n=68
		78 adult onset my OD		31.04 (22-53)		AL(K=-1.68±1.15D)=24.71±1.06mm, n=78
		47 youth onset my OD		30.39 (21-46)		AL(K=-3.74±2.13(SD)D)=25.47±1.17mm, (47)
		38my(15-20yr-onset) OD		28.77 (21-64)		AL(K=-2.46±1.66D)=24.89±0.181.11mm, n=38
Goss 1997	Oklahoma	34 em males	63 F, 105 M	25±4.6 (21~44)	A-Scan	AL(+0.25±0.36D)=23.82±.72mm; n=34M
		71 my males		26.8±6 (21~43)		AL(-2.87±2.14D)=24.67±1.02mm; n=71M
		19 em females		25.6±5 (21~38)		AL(+0.17±0.36D)=23.24±.78mm; n=19F
		44 my females		25.5±5 (20~39)		AL(-3.42±2.20D)=24.31±0.85mm; n=44F
Grosvenor 1994	New Zealand	194 subj. /194 eyes	101 F, 93 M	18-30 yrs	A-Scan	AL(K= -13.32 to +7.91 D)≈ 23.5-0.36K
Scott 1993	New Zealand	42 em (-0.5 to +1.5D)		17~26 yr	A-Scan	AL(K=0.32±0.52D)=23.36±0.78mm; n=42
		42 my (-5 to -7D)				AL (K=-5.90±0.68D)=25.31±0.68mm; n=42
Cheng 1992	US Massachusetts	8 hy subj		>25 yr	MRI	AL(K+3.72±0.96D)=22.3±1.1mm; n=8
		6 em subj				AL(K=+0.21±0.25D)=23.0±1.2mm; n=6
		7 my subj				AL(K=-6.54±2.74D)=24.5±1.6mm; n=7
Dunne 1992	UK	80 subj.	40F		A-Scan	AL(K=-1.52±3.86D)=24.47±1.58mm, n=40
			40M			AL(K=1.11±2.40D)=24.96±1.01mm, n=40
				22.0±3.3 yr		AL(K=-2.05±3.18D)=24.99±1.32mm, n=60
				74.6±5.6 yr		AL(K=0.92±2.24D)=23.91±1.19mm, n=20
Bullimore 1992	UC, Berkeley	14 em subj				AL(K=-0.08±0.25D)=24.25±0.69mm; n=14
		14 my suj				AL(K=-2.18±1.05D)=25.49±0.94mm; n=14
Koretz 1989	US	100 subj.	68F	18-70	Ultrasonography	AL=23.43±0.76mm, n=68
			32M			AL=24.08±0.81mm, n=32
						AL=23.64±0.83mm, n=100
Mcbrien 1987	UK	30 em subj		Young adults		AL(K=+0.17±0.26D)=23.76±0.65mm; n=30
		30 my subj				AL(K=-1.29±0.75D)=24.58±0.87mm; n=30
Alsbirk 1977	Greenland Eskimos	261 subj.	F	mean ~ 43 yr	Ultrasonic oculometry	Total: AL(K=+0.25±1.25D)=23.00±0.87mm; 20yr: AL(K=-0.28D)=23.17mm; 70yr: AL(K=+0.90D)=22.83mm
		279 subj.	M	mean ~ 44 yr		Total: AL(K=-0.07±1.34D)=23.71±0.88mm; 20yr: AL(K=-0.01D)=23.69mm; 70yr: AL(K=-0.18D)=23.73mm

Table 2.13, cont.

H:Hispanic		hy: hyperopic	F: female	D: diopter	AL: ocular axial length
B: Black	W: White	em: emmetropic	M: male	yr: year old	K: refracrive error (spherical equivalent)
A: Asian		my: myopic	OD: right eye	OS: left eye	

Table 2.14 *Information of 20 AL papers of children and infant*

Author (year)	Geographic /race	Subject no. /eye no.	Gender	Age (year)	Method of test	Ocular Axial-Length, AL (Spherical equivalent power, K)
Ziylan 2006	Turkey	25 subj./50 eyes		(12-24month) pre-term children	A-Scan	AL(K=-4.09±4.34D)=21.65±1.55mm, n=50
		35 subj./70 eyes				AL(K=1.64±0.81D)=20.30±0.66mm, n=70
		20 subj./40 eyes				AL(K=1.92±0.77D)=20.37±0.58mm, n=40
Cook 2003	UK	68 premature infants	33F, 35M	30-45 weeks post-menstrual	A-scan biometer	AL=0.16(±0.004)*(Week-40)+16.66(±0.04)mm
Mutti 2005	US	222 infants	118F, 104M	3-month visit	A-Scan	AL(K=+2.16±1.30D)=19.03±0.58mm, n=222
				9-month visit		AL(K=+1.36±1.06D)=20.23±0.64mm, n=222
				6-month change		ΔAL(ΔK=-0.80±0.90D)=1.20±0.51mm, n=222
Pennie 2001	UK	20 infants (20 OD)	10F, 10M	4.3±0.9 week	Through-the-eyelid ultrasonic biometry	AL(K=+2.81±0.94D)=17.71±0.41mm, n=20
				14.0±1.9 week		AL(K=+2.74±1.46D)=18.69±0.67mm, n=19
				27.3±1.7 week		AL(K=+1.91±1.31D)=19.77±0.75mm, n=18
				40.0±1.9 week		AL(K=+1.76±1.50D)=20.16±0.90mm, n=13
				53.1±1.6 week		AL(K=+1.50±1.42D)=20.41±0.87mm, n=10
Jones 2005	Ohio	**my group:** 59(3yr old); 11(4yr); 15(5yr); 45(6yr);25(7yr);92(>8yr)		138F, 109M	A-Scan	AL(K=-0.49±1.38D; ≤-0.75D) =23.05±0.9mm, n=247
		hy group 1: 12(3yr old); 5(4yr); 3(5yr); 8(6yr); 1(7yr); 14(>8yr)		23F, 20M		Persistent hy: AL(K=2.45±0.92D; >=+1.0D always)=21.91±0.9mm, n=43
		em group: 96(3yr old); 14(4yr); 7(5yr); 45(6yr); 3(7yr); 29(>8yr)		84F, 110M		AL(K=0.54±0.22D; -0.25to+1.0D always) =22.93±0.7mm, n=194
		hy 2: 21(3yr old); 28(4yr);29(5yr); 4(6yr); 26(7yr); 107(>8yr)		135F, 118M		Emmetropizing hy: AL(K=1.36±0.48D)=22.30±0.6mm, n=253
Ojaimi 2005	Australia	1726 OD	mixed	6.7 (5.5-8.4)	IOLMaster	AL(K=+1.26±1.25D)=22.61±0.83mm, n=1716
		844 OD	F	5-8 yr		AL(K=+1.34±1.17D) = 22.32±0.58mm, n=844
		872 OD	M	5-8 yr		AL(K=+1.20±0.89D)=22.89±0.59mm, n=872
		1278 OD	mixed	6 year old		AL(K=+1.27±1.43D)=22.58±0.71mm, n=1278
		438 OD	mixed	7 year old		AL(K=+1.25±0.84D)=22.67±0.63mm, n=438
		1105 white	mixed	5-8 yr		AL(K=+1.39±1.00D)=22.57±0.66mm, n=1105
		611 other	mixed	5-8 yr		AL(K=+1.04±0.99D)=22.68±0.74mm,

		ethnicities				n=611

Table 2.14, cont.

Davis 2005	CA	643 subj. / 643 eyes (measured in 1991)	mixed	9.92±2.42 yr (6-15 yr)	A-Scan	AL(K=+0.31±1.12(range:-5.95 to 4.23)D) =23.07±0.85(20.80~26.38)mm, n=643
		175 out of 643 (1991)	mixed	7.54±1.00 yr (6-9 yr)		AL(K=+0.62±0.95(range:-5.95 to 4.23)D) =22.80±0.71(20.87~24.94)mm, n=175
		175 out of 643 (follow-up in 1996)	mixed	12.48±1.00 yr (11-14 yr)		AL(K=+0.08±1.60(range:-10.21 to 3.91)D) =23.38±0.85(21.62~26.01)mm, n=175
Selovic 2005	Croatia	1600 subj.	800F, 800M	(>=8)	A-Scan	AL vs Height & Weight in different age groups
Saw 2004	Singapore /Chinese	1204 children / 1204 OD	592F, 612M	(10-12)	Biometry ultrasound	AL(K=-1.56±2.18D)=23.92±1.10mm, n=1204
Zadnik 2004	Ohio	194 subj. /194 OD		9.4±2.3 yr (6-14 yr)	A-Scan	AL(K=0.5±0.3D)=22.9±0.7, n=194; AL=20.189+1.258*ln(Age), <10.5 yr; AL=21.353+0.759*ln(Age), >10.5 yr
Zadnik 2003	USA: W, B, A, H, & Native American	2583 children	1274F	6 year old	A-Scan	AL(K=0.88±0.86D)=22.33±0.66
				7 year old		AL(K=0.78±1.01D)=22.49±0.76
				8 year old		AL(K=0.64±1.26D)=22.65±0.84
				9 year old		AL(K=0.18±1.64D)=23.02±0.85
				10 year old		AL(K=-0.004±1.42D)=23.07±0.85
				11 year old		AL(K=0.03±1.72D)=23.13±0.86
				12 year old		AL(K=-0.16±1.55D)=23.27±0.87
				13 year old		AL(K=-0.15±1.38D)=23.34±0.91
				14+ year old		AL(K=-0.46±2.18D)=23.48±1.05
			1309M	6 year old		AL(K=0.81±0.87D)=22.82±0.56
				7 year old		AL(K=0.72±0.95D)=22.94±0.63
				8 year old		AL(K=0.53±1.11D)=23.14±0.81
				9 year old		AL(K=0.37±1.14D)=23.40±0.70
				10 year old		AL(K=0.34±1.25D)=23.43±0.80
				11 year old		AL(K=0.18±1.57D)=23.54±0.84
				12 year old		AL(K=0.32±1.50D)=23.55±0.86
				13 year old		AL(K=-0.12±1.58D)=23.76±0.84
				14+ year old		AL(K=-0.11±2.78D)=23.69±1.17
Gao 2002	Chinese	135 subj./270 eyes	72F, 63M	9.6±2.3 (7-13)	A-scan	AL(K=4.57±2.17D)=21.64±1.09mm, n=118
						AL(K=0.11±0.47D)=23.54±0.88mm, n=38
						AL(K=-2.47±1.80D) =24.44±1.06mm, n=114
Edwards 2002	Hong Kong	133 subjects	61M, 72F	9.17 (7–10.5)	A-scan	AL(-2.92±0.99D)=24.44±0.77mm; n=133

Table 2.14, cont.

Gwiazda 2002	USA; 469 subj. (OD)	17 OD	M	6-7 year old	A-Scan	AL(K=-2.12±0.65D)=23.73±0.40mm, n=17
		38 OD	M	8 year old		AL(K=-2.14±0.83D)=24.31±0.62mm, n=38
		58 OD	M	9 year old		AL(K=-2.49±0.85D)=24.31±0.61mm, n=58
		70 OD	M	10 year old		AL(K=-2.37±0.72D)=24.45±0.71mm, n=70
		40 OD	M	11 year old		AL(K=-2.41±0.79D)=24.62±0.64mm, n=40
		25 OD	F	6-7 yrear old		AL(K=-2.40±0.87D)=23.56±0.69mm, n=25
		45 OD	F	8 year old		AL(K=-2.11±0.74D)=23.90±0.58mm, n=45
		53 OD	F	9 year old		AL(K=-2.58±0.81D)=23.92±0.64mm, n=53
		64 OD	F	10 year old		AL(K=-2.42±0.89D)=24.02±0.79mm, n=64
		59 OD	F	11 year old		AL(K=-2.42±0.80D)=23.97±0.70mm, n=11
		42 OD	mixed	6-7 yrear old		AL(K=-2.29±0.79D)=23.63±0.59mm, n=42
		83 OD	mixed	8 year old		AL(K=-2.13±0.78D)=24.09±0.63mm, n=83
		111 OD	mixed	9 year old		AL(K=-2.54±0.83D)=24.12±0.65mm,n=111
		134 OD	mixed	10 year old		AL(K=-2.39±0.80D)=24.24±0.78mm,n=134
		99 OD	mixed	11 year old		AL(K=-2.42±0.79D)=24.23±0.75mm, n=99
	Black, B	122 OD	mixed	6-11 yrar old		AL(K=-2.47±0.77D)=24.11±0.68mm,n=122
	Asian, A	35 OD	mixed	6-11 yrar old		AL(K=-2.56±0.74D)=24.29±0.64mm, n=35
	Hispanic ,H	68 OD	mixed	6-11 yrar old		AL(K=-2.23±0.81D)=24.21±0.75mm,n=68
	Mixed	27 OD	mixed	6-11 yrar old		AL(K=-2.50±0.90D)=24.21±0.58mm,n=27
	White,W	217 OD	mixed	6-11 yrar old		AL(K=-2.32±0.82D)=24.08±0.75mm,n=217
Saw 2002a	Singapore /Chinese	1449 children / 1449 right eyes			A-Scan	Correlations to body height, weight, mass index, age, and gender
Saw 2002b	Singapore /Chinese	1453 children/1453 right eyes	318 M	7 year old	A-Scan	AL(K=-0.2±1.6D)=23.4±0.9mm, n=318
			239 M	8 year old		AL(K=-0.5±1.7D)=23.7±0.8mm, n=239
			192 M	9 year old		AL(K=-1.4±2.1D)=24.2±0.9mm, n=192
			313 F	7 year old		AL(K=-0.08±1.3D)=22.8±0.8mm, n=313
			231 F	8 year old		AL(K=-0.3±1.5D)=23.2±0.8mm, n=231
			160 F	9 year old		AL(K=-1.1±1.8D)=23.4±1.0mm, n=160
Zadnik 1999	Ohio, USA	554 subj. /554 right eyes		8.60±0.53 yr	A-Scan	AL(K=0.94±0.71D)=22.83±0.70mm, n=554
Lam 1999	Hong Kong, China	142 subj. / 142 right eyes	75F, 67M	(6-17 yr)	A-Scan	AL(K=-1.14±1.53D)=23.40±1.01mm, (1991)
				(6-17 yr)		AL(K=-1.33±1.66D)=23.97±1.02mm, (1991)
				(8-19 yr)		AL(K=-1.83±2.04D)=23.91±1.22mm, (1993)
				(8-19 yr)		AL(K=-1.90±1.94D)=24.51±1.07mm, (1993)
Mutti 1998	US: 0.7%B, 86.6% W, 11.2% A, 1.5% H.	994 subj.	451F, 543M	(6 to 15 yr)	Ultrasono-graphy	AL=23.08+0.133*(Age-10)-0.011*(Age-10)^2, n=994

Table 2.14, cont.

Garner 1992	New Zealand /Maylay	19 em subj (-.25~.25D)	9 F, 10 M	(9 to 15 yr)	A-Scan	AL(K=+0.01±0.05D)=23.16±0.72mm; n=19
		19 my subj (>-3D)				AL(K=-6.08±1.83D)=26.00±1.43mm; n=19

A: Asian	W: White	hy: hyperopic	F: female	OD: right eye	AL: ocular axial length
B: Black	H:Hispanic	em: emmetropic	M: male	OS: left eye	K: refracrive error (spherical equivalent)
		my: myopic	yr: year old	D: diopter	

Representative regression fitting and the distribution function:

Table 2.12 summarizes 14 recent publications that contain measurement data of ocular axial length (*AL*) and the corresponding spherical equivalent refractive errors, K. The *AL-K* correlation findings with fitted lines from measured data points and the reported significance of the fitting in each study are indicated. As indicated in the table, subjects in these studies are primarily young adults with unbiased gender selection in various races. All the 14 listed studies provide the scatter points, which are illustrated in Figure 2.51. 622 of the total claimed 659 data points were distinguishable from 12 papers. The missing 37 data points are majorly overlapped in the high density area in the original publications (17 of 113 in [Carney 1997], 4 of 60 in [Rabsilber 2003], 4 of 88 in [Atchison 2004], 4 of 60 in [Chui 2005], and 8 of 121 in [Atchison 2006]). In Figure 2.51, the black line corresponds to the linear regression fitting line of all 622 data points. The gray shaded area represents a standard deviation of ±0.91 mm, which covers 74.4% data points.

The probability distribution functions of axial length, along the fitted regression line are shown in Figure 2.52. In this figure, I sort the subjects into five groups according to their refractive errors. They are group 1 (-21.22D≤K≤-5.60D, n=125), group 2 (-5.60D≤K≤-2.54D, n=125), group 3 (-2.54D≤K≤-0.83D, n=124), group 4 (-0.77D≤K≤0.26D, n=124), and group 5 (0.26D≤K≤17.25D, n=124). The centers of the 5 normal distribution curves stay closely (-0.12, 0.08, 0.09, -0.08, and -0.10 m\m away) to the fitted mean, *AL= -0.36K+23.61 mm*.

Correlation to refractive error:

Other than the 14 studies in Table 2.12, *AL* correlation to refractive error investigation is also presented in abundant papers. Figure 2.53 includes 11 studies in young adults. Figure 2.54 further contains 12 studies of adults and one in children. Most of these results show great correspondence to the representative regression line.

In children's studies, Jones [Jones 2005], Saw [Saw 2002b], Gao [Gao 2002], Garner [Garner 1992], show that children 3 year old to 15 year old have the refractive error correlation similar to adults results with the same or slightly sharper fitting slope.

Gender dependence:

The difference of *AL* between male and female subjects is approximate 0.5mm in all reports with specified gender of subjects. In the Atchison 2008 study, males had greater lengths than females by a mean of 0.62 mm ($p<0.001$). [Atchison 2008]. Atchison gave numbers for detailed eye dimensions of each component in 2006 [Atchison 2006]. Since there is strong significant dependence of *AL* upon refraction, the regression equations for males and females are given separately as $AL = 24.04-0.314K$ ($r^2 = 0.632$) and $AL = 23.46-0.303K$ ($r^2 = 0.618$). Goss' study that is performed in US [Goss 1997] and Wong's study in Singarpore Chinese [Wong 2001] also obtained about 0.5mm longer *AL* in males (Figure 2.54). In the same figure, Chau's study of Chinese subjects study obtained a much smaller excess in

males than females, after corrected to refraction [Chau 2004]. On the other hand, UK study of Dunne report a much higher *AL* in male groups over females after refraction correction [Dunne 1992]. In general, 0.5 mm is a good estimation. 6 more gender correlation studies results are plotted in Figure 2.57 for comparison. Similar conclusions were drawn.

In children studies, girls also have shorter *AL* than boys. Shown in Figure 2.56 is Saw's study in Chinese children of age 7-9, boys have 0.63mm longer *AL* compared to girls [Saw 2002b]. In Figure 2.55, both 6-to 14 year old boys in Zadnik study [Zadnik 2003] and 6-11 year old boys in Gwiazda study [Gwiazda 2002] have about 0.5mm longer *AL* than girls in the control groups of same ages.

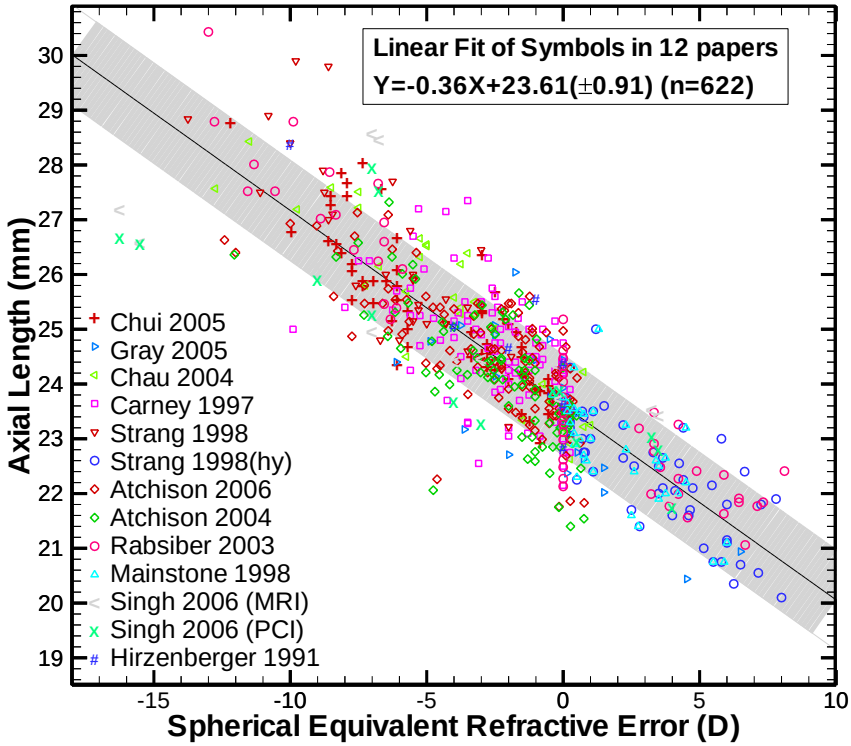

Figure 2.51 *Reproduction of data points from 12 papers in the above table*

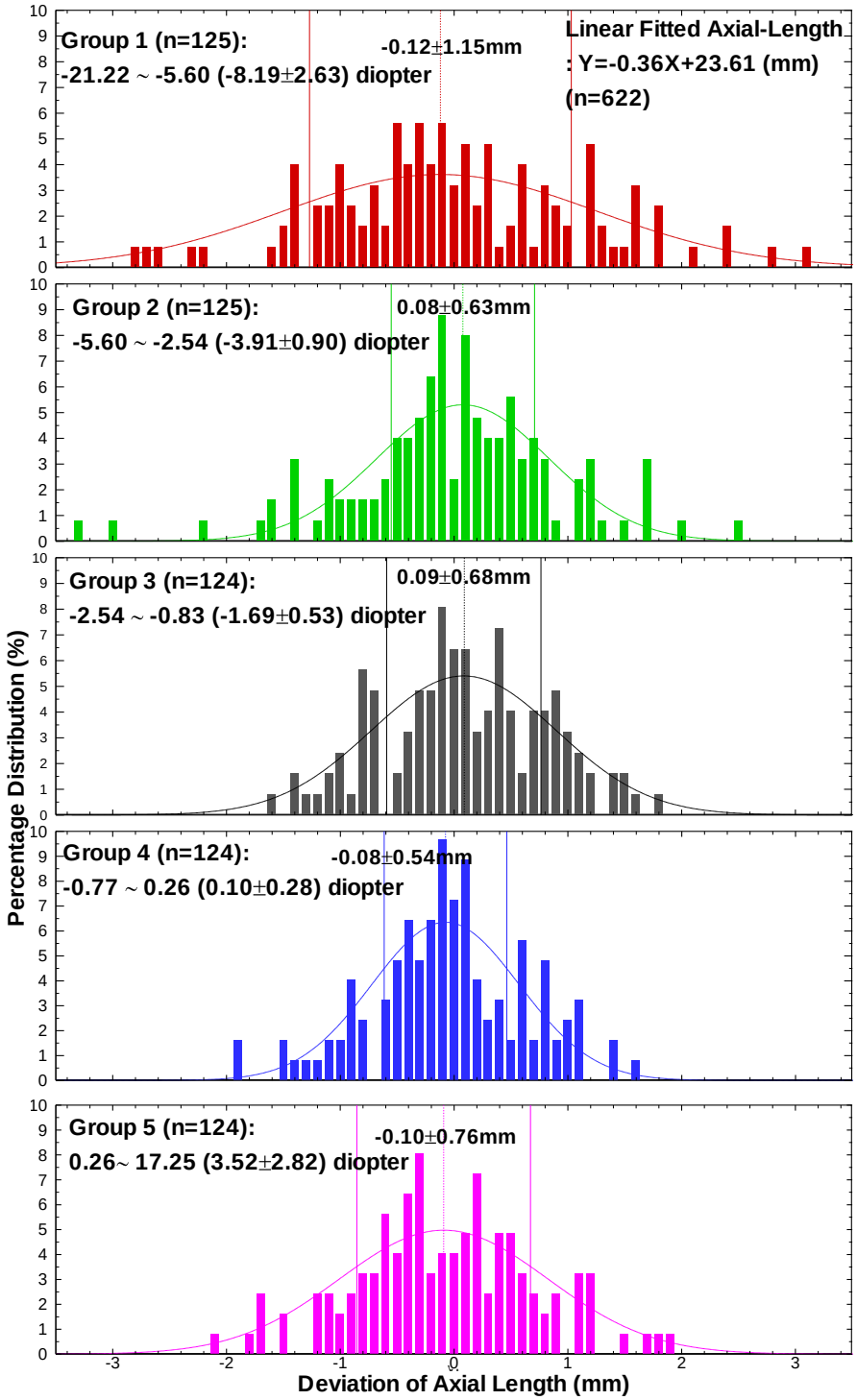

Figure 2.52 *Probability distribution functions of eye length along the fitted line in Figure 2.51*

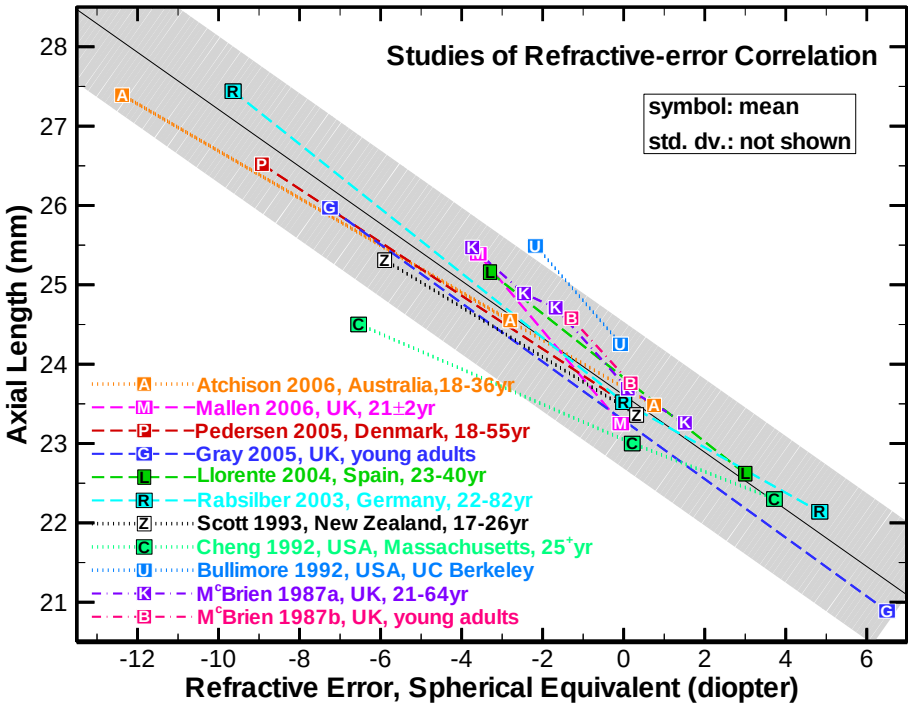

Figure 2.53 *Refractive error correspondence of AL in 11 papers that performed in young adults*

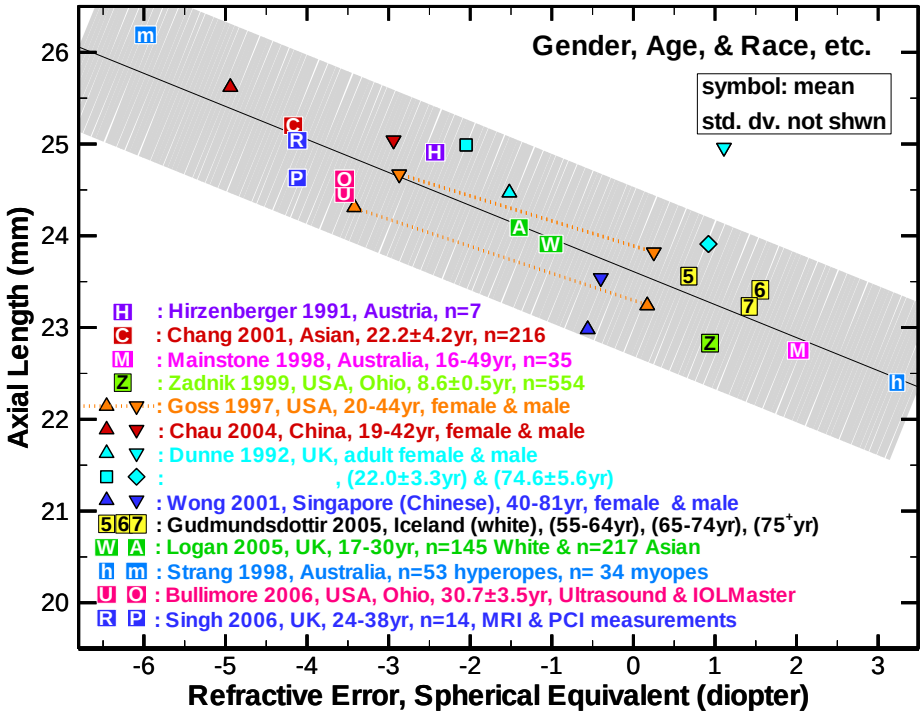

Figure Adult data

Figure 2.54 *Refractive error correspondence of AL in 12 papers that performed in adults and one study [Zadnik 1999] in children*

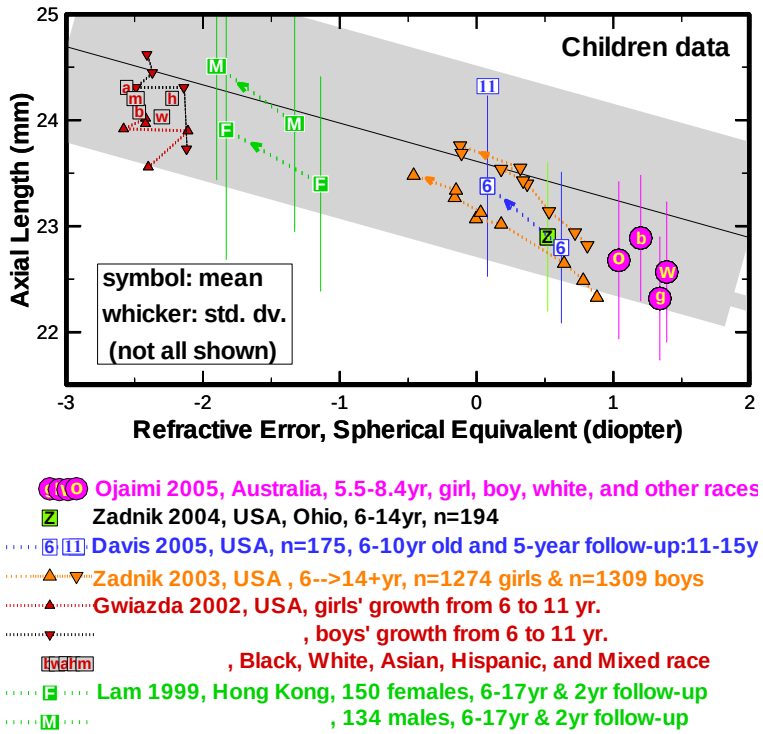

Figure 2.55 *Refractive error correspondence of AL in 6 papers that performed in children*

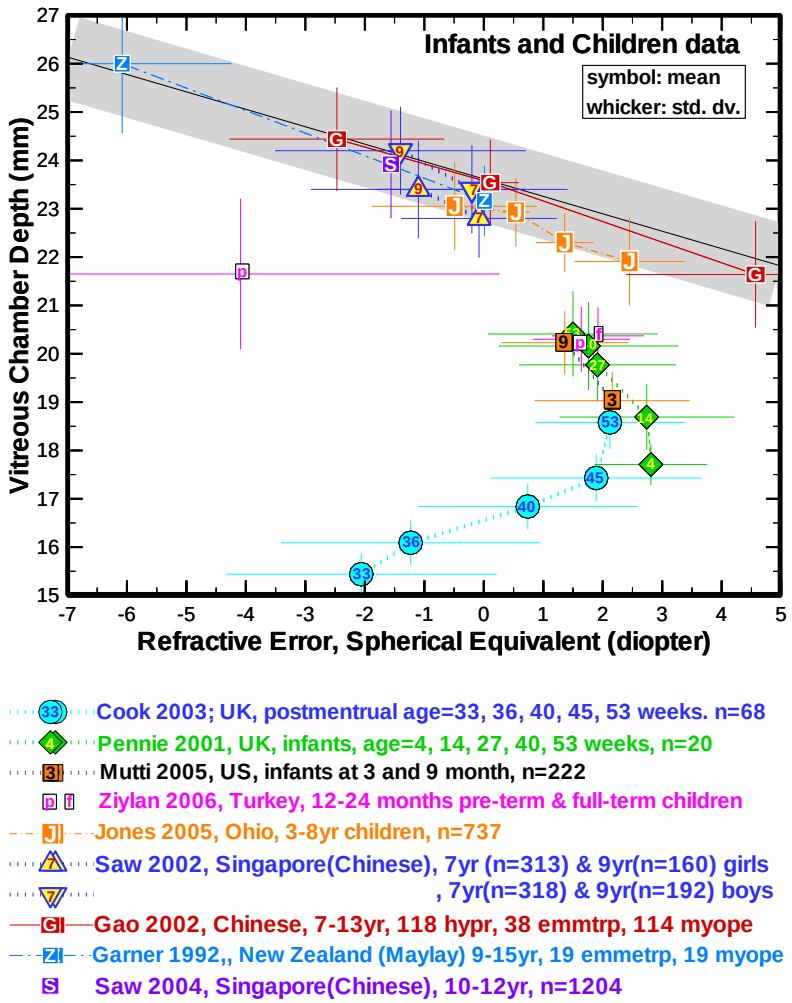

Figure 2.56 *Refractive error correspondence of AL in 9 papers that performed in infants and children. The reference regression line in the background is the representative fitting line of adults.*

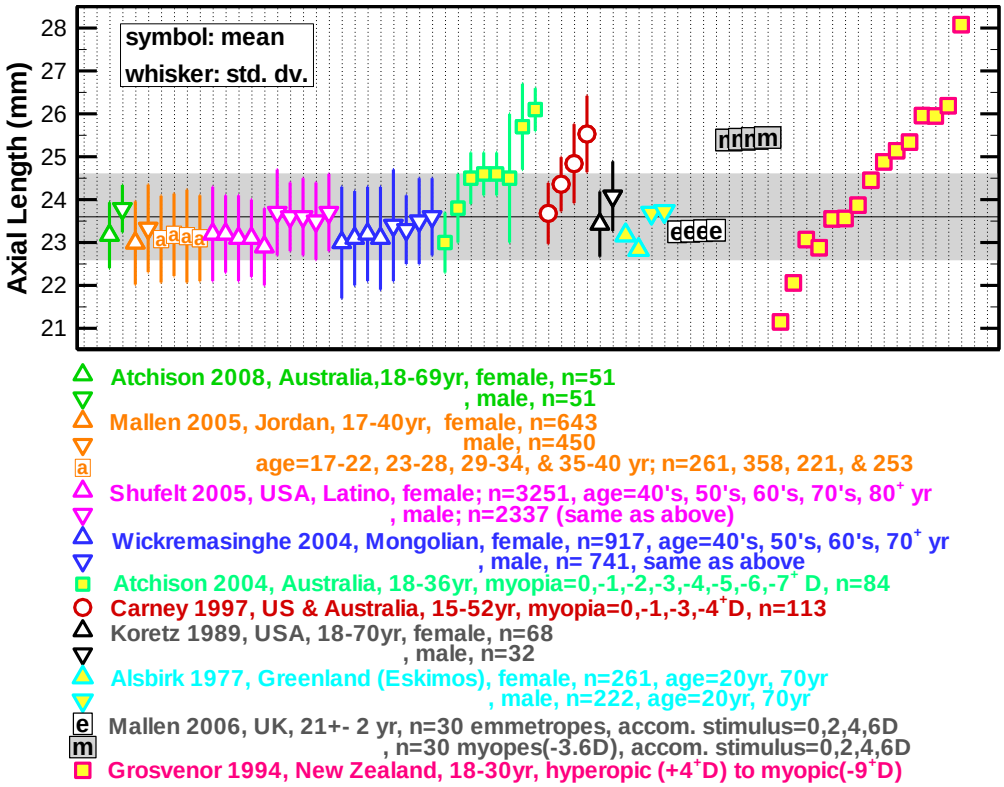

Figure 2.57 *Mean plus deviation of adults AL in 10 studies*

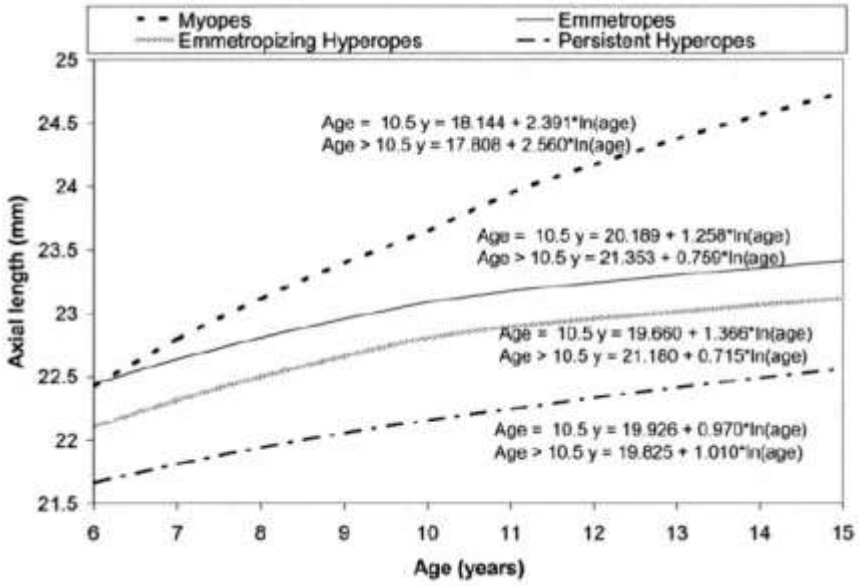

Figure 2.58 *Development of AL in 4 refractive groups of US children 6- to 15-year old from Jones 2005*

Ethnicity:

Among the collected data, adjusted for age and gender, Asian data from 11 papers lie along with the representative fitting line except the data from Chau [Chau 2004] (19-43 year-old Chinese, *AL* is measured 0.4mm longer), Mallen [Mallen 2005] (17-40 year-old Jordan, 0.6mm shorter *AL*), Wong [Wong 2001] (40-81 year-old Singapore Chinese, 0.4mm shorter AL) and Wickremasinghe [Wickremasinghe 2004] (>40 year-old Mongolian, 0.3mm shorter AL).

European subjects fit well with the regression fitting and distribution band while they have a little longer *AL* in McBrien's 2 papers [McBrien 1987 and 1997] and Llorente's paper [Llorente 2004].

Considering the variety of ethnicity in US, we are not surprised to observe the large distribution range of American subjects' data.

Adjusted for age and gender, Oceanian subjects fit well with the regression fitting line, except Scott reports shorter *AL* (about 0.4mm) found in 42 myopes from New Zealand [Scott 1993].

Accommodation effect:

Mallen gave *AL* transient changes at 2D, 4D and 6D accommodation stimuli. [Mallen 2006] Mallen also discussed that the action of accommodation may induce errors in the measurement of axial length obtained from the IOLMaster. To calculate axial length from the optical path length, the IOLMaster uses an average refractive index for the eye, and therefore may be susceptible to an overestimation of up to 0.02 mm in axial length for an eye accommodating to a 10-D stimulus when compared with PCI methods that use individual refractive indices for the ocular components. The insignificant increases of *AL* due to accommodation are shown in Figure 2.57.

Gao's research in 2002 shows no significant difference in *AL* measurements with and without cycloplegia [Gao 2002].

Age dependence:

Ocular axial length growths rapidly during the infancy and approaches the size of adults' eyes in early childhood. After 18 year old, axial length remains practically the same through the age.

Figure 2.56 illustrates 4 studies of axial length during the first 24 months after birth. Cook's [Cook 2003] data show the fast development of *AL* in premature infants. At 53rd weeks, the eye length has reaches typical normal infants' eye size. At the same time, the refractive errors of these babies also shift from myopia to hyperopia, the typical refractive status of infants. Pennie's [Pennie 2001] study provides information of healthy infants from 4 weeks to 53 weeks old. Mutti's [Mutti 2005] data shows longitudinal study of infants' eye length at the 3rd and 9th month visits. These data describe well the eye development during the first year of life. Ziylan's [Ziylan 2006] data further compares a myopic pre-term baby group with a pre-term and a full-term baby group of babies that are with normal hyperopic eye sights.

In the same figure, 5 studies of children subjects are exemplified. All the studied groups of Chinese, Maylay, and US children from 3 to 15 year old in these studies reported axial length means that are very close to adults regression fitted line. Another 6 studies are compared in Figure 2.55. From earlier childhood to about 17 year old, *AL* increase barely 0.5 mm. Zadnik's data (Figure 2.54) further shows the 8 year old group of children in the US has mean *AL* values only about 0.4mm shorter than the adult mean in our regression reference line [Zadnik 1999]. Illustrated in Figure 2.58 is the Jones' study result of the development of *AL* in 4 refractive groups of US children 6- to 15-year old [Jones 2005].

Aging of *AL* in adults is investigated in many studies. As shown in Figure 2.57, Mallen compared *AL* of Jordanians age 17 to 40 year-old [Mallen 2005], Shufelt studied Latino 40 to 80 year-old [Shufelt 2005], Wickremasinghe examined Mongolian 40 to 70 year-old [Wickremasinghe 2004], and Alsbirk measured Eskimos 20 and 70 year old groups, no age correlation is found [Alsbirk 1977].

Jones' [Jones 2005] study investigated and gave age-dependent AL for US children 6 to 15-year old. These results are plotted in Figure 2.58. These age-dependences are significant for persistent hyperopic, and myopicgroups, but not significant for emmetropizing hyperopic group.

Age<=10.5 years AL=19.660+1.366*ln(Age);
Age>10.5 years AL=21.180+0.715*ln(Age), p=0.2231 (emmetropizing hyperopia);
Age<=10.5 years AL=21.1899+1.258*ln(Age);
Age>10.5 years AL=21.353+0.759*ln(Age) (emmetropes);
Age<=10.5 years AL=18.144+2.391*ln(Age);
Age>10.5 years AL=17.808+2.560*ln(Age), p<0.0001 (myopia);
Age<=10.5 years AL=19.926+0.970*ln(Age);
Age>10.5 years AL=19.825+1.010*ln(Age), p=0.0273 (persistent hyperopia)

Other factors:
Wong [Wong 2001] and Saw [Saw 2002a] gave *AL* and *K* in 5 and 4 quartiles according to height, weight and BMI. Wong indicated that height and weight correlate positively with *AL*, but BMI does not correlate with *AL*. [Wong 2001] Saw's study found that the taller children are more myopic and have longer *AL* [Saw 2002 a].

Selovic gave *AL* vs Height, *AL* vs Weight in different age groups for >=8yr children. [Selovic 2005]

2.6. VITREOUS CHAMBER AND RETINA

2.6.1 Vitreous Chamber Depth (VCD)

Vitreous chamber describes the space between lens and retina. Vitreous chamber depth (*VCD*) is equal to the total ocular axial length, *AL*, minuses anterior segment length. 20 papers of *VCD* are collected and summarized in Table 2.15.

Refractive error correlation:
As described in the previous sections, each portion of the anterior segment length (the central corneal thickness, anterior chamber depth, and the lens thickness) has been investigated in a large number of research studies and believed to have no refractive error correlation. The vitreous chamber depth is, therefore, considered correlates to refractive error in the same manner as the axial length that is discussed in the last section (2.5). Hence, I use the same slope and standard deviation of AL fitted regression line as reference, in the Figures 2.51: *VCD= -0.36K+16.15 (±0.91) mm.*

Figure 2.59 includes 3 refraction correlation studies on adult subjects. McBrien's study in UK [McBrien 1997], Goss' study in the US [Goss 1997], and Scott's study in New Zealand [Scott 1993] show good agreement with the regression line. Children data in both Figure 2.59 and Figure 2.60 also present close conformity with the regression.

Gender:
The male with longer mean *VCD* than the female by 0.5 mm is found by many research groups with good statistic significance. This is shown in Figure 2.61 [Atchison 2008, Mallen 2005, Shufelt 2005, Wong 2001, Koretz 1989, and Alsbirk 1997] and Figure 2.59 [Goss 1997]. Wickremasinghe study [Wickremasinghe 2004] is the only exception that shows Mongolian males and females with about the same VCD mean.

Table 2.15 *Information 24 studies about VCD vs. K*

Author (year)	Geographic /race	Subject no. /eye no.	Age (year)	Gender	Method of measurement	Vitreous Chamber Depth, VCD (Refractive-error, K)
Atchison 2008	Australia, 96%W	106 subj. /106 eyes K=-0.88 to +0.75D	18-29(n=23), 30-39(n=20), 40-49(n=22), 50-59(n=21), 60-69(n=20)	51F	Ultrasono-graphy	VCD=15.67±0.72mm, n=51
				51M		VCD=16.18±0.59mm, n=51
						VCD=15.99-0.0016*Age (adjusted r^2=0.00, n=102, p=0.70).
Mallen 2005	Jordan	1093 subj. / 1093 right eyes	17-40 year old		A-Scan	VCD(K=-0.87±1.70D)=16.04±0.97mm, VCD=-0.28*K+15.80mm, r=-0.48
		643 OD	(17-40)	643F		VCD(K=-0.95±1.58D)=15.93±0.91mm
		450 OD	(17-40)	450M		VCD(K=-0.74±1.84D)=16.20±1.03mm
		261 OD	(17-22)			VCD(K=-0.81±1.65D)=15.99±0.92mm
		358 OD	(23-28)			VCD(K=-1.20±1.60D)=16.12±0.94mm
		221 OD	(29-34)			VCD(K=-0.83±1.59D)=16.10±1.05mm
		253 OD	(35-40)			VCD(K=-0.44±1.88D)=15.94±0.99mm
Shufelt 2005	USA, Latino	5588 subj. /5588 right eyes	(40-49)	1304F	A-Scan	VCD(K=-0.32±1.8D)=14.98±1.2mm
				923M		VCD(K=-0.30±1.3D)=15.3±1.1mm
			(50-59)	1009F		VCD(K=-0.23±1.9D)=14.92±1.0mm
				726M		VCD(K=0.02±1.6D)=15.2±0.9mm
			(60-69)	631F		VCD(K=0.73±2.36D)=14.8±1.03mm
				441M		VCD(K=0.4±1.6D)=15±0.9mm
			(70-79)	253F		VCD(K=1.02±2.30D)=14.7±1.02mm
				214M		VCD(K=0.6±2.5D)=15.0±1.04mm
			(>=80)	54F		VCD(K=0.74±2.12D)=14.6±0.88mm
				33M		VCD(K=-0.3±2.6D)=15.4±0.9mm
Kirschkamp 2004	Germany or UK	9 subj./ 9 left eyes	(20-38)	2F, 7M	Auto-keratometer	Relaxed: VCD=16.3±0.4 mm
						Accommodation(3.7±1.1D): VCD=16.3±0.4 mm
Wickrema-Singhe 2004	Mongolian	1617 subj. /1617 right eyes	(40-49)	241M	A-Scan	VCD(K=+0.1±1.8D)=15.9±1.1mm, n=241
				368F		VCD(K=-0.3±1.6D)=15.9±1.3mm, n=368
			(50-59)	200M		VCD(K=+0.2±0.9D)=15.8±0.7mm, n=200
				266F		VCD(K=+0.1±1.9D)=15.9±1.1mm, n=266
			(60-69)	150M		VCD(K=0.0±1.5D)=15.9±0.8mm, n=150
				168F		VCD(K=-0.4±3.2D)=16.0±1.1mm, n=168
			(>70)	109M		VCD(K=-0.7±3.6D)=16.1±0.9mm, n=109
				115F		VCD(K=+0.4±1.3D)=15.9±0.9mm, n=115
Wong 2001	Singapore /Chinese	1004 subj. /1004 right eyes	(40-81)	547F	A-Scan	VCD(K=-0.56±2.89D)=15.39±1.09mm, n=547
				457M		VCD(K=-0.40±2.41D)=15.82±1.08mm, n=457

Table 2.15, cont.

McBrien 1997	UK	14 hy subj./14 OD	29.72 (22-50)		A-Scan	VCD(K=+1.51±0.82D)=15.81±1.05mm
		68 em subj./68 OD	30.83 (21-61)			VCD(K=+0.10±0.25D)=16.23±0.66mm
		78 adult onset my OD	31.04 (22-53)			VCD(K=-1.68±1.15D)=17.14±1.06mm
		47 youth onset my OD	30.39 (21-46)			VCD(K=-3.74±2.13D)=17.80±1.10mm
		38my(15-20yr-onset)OD	28.77 (21-64)			VCD(K=-2.46±1.66D)=17.24±1.17mm
Goss 1997	Oklahoma	34 em males	25±4.6 (21~44)	63 F, 105 M	A-Scan	VCD(+0.25±0.36D)=16.33±0.62mm; n=34M
		71 my males	26.8±6 (21~43)			VCD(-2.87±2.14D)=17.13±0.94mm; n=71M
		19 em females	25.6±5 (21~38)			VCD(+0.17±0.36D)=15.83±0.64mm; n=19F
		44 my females	25.5±5 (20~39)			VCD(-3.42±2.20D)=16.85±0.77mm; n=44F
Garner 1997	New Zealand	11 subj. K=-1.88±1.64D (range: -4.25 to +0.50D)	21.2 yr (18-28 yr)		A-Scan	VCD=16.66±0.91mm at 0D stimulus
						VCD=16.67±0.90mm at 1.5D stimulus
						VCD=16.68±0.91mm at 3.5D stimulus
						VCD=16.64±0.89mm at 5.5D stimulus
						VCD=16.62±0.89mm at 8D stimulus
Scott 1993	New Zealand	42 em (-0.5 to +1.5D)	(17-26 yr)		A-Scan	VCD(K=0.32±0.52D)=16.12±0.72mm; n=42
		42 my (-5 to -7D)				VCD(K=-5.90±0.68D)=17.93±0.66mm; n=42
Koretz 1989	US	100 subj.	(18-70 yr)	68F	Ultrasono-graphy	VCD=15.81±0.68mm, n=68
				32M		VCD=16.34±0.75mm, n=32
						VCD=15.98±0.75mm, n=100
Alsbirk 1977	Greenland Eskimos	261 subj.	mean ~ 43 yr	F	Ultrasonic oculometry	VCD(K=+0.25±1.25D)=15.57±0.79mm; 20yr: VCD(K=-0.28D)=15.83mm; 70yr: VCD(K=+0.90D)=15.30mm
		279 subj.	mean ~ 44 yr	M		VCD(K=-0.07±1.34D)=16.11±0.81mm; 20yr: VCD(K=-0.01D)=16.28mm; 70yr: ACD(K=-0.18D)=15.94mm
Jones 2005	USA, Ohio	**my group:** 59(3yr old); 11(4yr); 15(5yr); 45(6yr);25(7yr);92(>8yr)		138F, 109M	A-Scan	VCD(K=-0.49±1.38D; ≤-0.75D) =15.87±0.9mm, n=247
		hy group 1: 12(3yr old); 5(4yr); 3(5yr); 8(6yr); 1(7yr); 14(>8yr)		23F, 20M		VCD(K=2.45±0.92D; >=+1.0D stable) =14.93±0.8mm, n=43
		em group: 96(3yr old); 14(4yr); 7(5yr); 45(6yr); 3(7yr); 29(>8yr)		84F, 110M		VCD(K=0.54±0.22D; -0.25to+1.0D stable) =15.77±0.7mm, n=194
		emmetropizing hy: 21(3yr);28(4yr); 29(5yr); 4(6yr); 26(7yr); 107(>8yr)		135F, 118M		VCD(K=1.36±0.48D)=15.24±0.6mm, n=253

Table 2.15, cont.

Mutti 2005	USA	222 infants	3-month old	118F, 104M	A-Scan	VCD(K=+2.16±1.30D)=12.35±0.51mm, n=222
			9-month old			VCD(K=+1.36±1.06D)=13.34±0.56mm, n=222
						growth in 6 month period: ΔVCD(ΔK=-0.80±0.90D)=0.99±0.40mm, n=222
Davis 2005	USA, CA	643 subj. /643 eyes (1991)	9.92±2.42 (6-15 yr)		A-Scan	VCD(K=+0.31±1.12(-5.95~4.23)D) =15.94±0.82(13.86~19.23)mm, n=643
		175 subj. (measured in 1991)	7.54±1.00 (6-9 yr)			VCD(K=+0.62±0.95(-5.95~4.23)D) =15.68±0.73(13.97~17.92)mm, n=175
		175 subjects (follow-up in 1996)	12.48±1.00 (11-14 yr)			VCD(K=+0.08±1.60(-10.21~3.91)D) =16.17±0.83(14.53~18.80)mm, n=175
Garner 2004	Nepal /Asian	897 children / 897 left eyes	(3-18 yr)		A-Scan	VCD grows 0.072 and 0.165mm /yr for non-myopic (>-0.5D) and myopic (<=-0.5D) group, respectively.
Zadnik 2004	USA, Ohio	194 subj. /194 right eyes	9.4±2.3 yr (6-14 yr)		A-Scan	VCD(K≈0.53±0.26D)=15.8±0.7mm
Zadnik 2003	USA: B, A, W, H, & Native American	2583 children	6 year old	1274F	A-Scan	VCD(K=0.88±0.86D)=15.28±0.66mm,
			7 year old			VCD(K=0.78±1.01D)=15.48±0.73mm
			8 year old			VCD(K=0.64±1.26D)=15.61±0.80mm
			9 year old			VCD(K=0.18±1.64D)=15.97±0.84mm
			10 year old			VCD(K=-0.004±1.42D)=16.05±0.81mm
			11 year old			VCD(K=0.03±1.72D)=16.06±0.87mm
			12 year old			VCD(K=-0.16±1.55D)=16.18±0.86mm
			13 year old			VCD(K=-0.15±1.38D)=16.22±0.91mm
			14+ year old			VCD(K=-0.46±2.18D)=16.41±1.04mm
			6 year old	1309M		VCD(K=0.81±0.87D)=15.72±0.57mm
			7 year old			VCD(K=0.72±0.95D)=15.81±0.64mm
			8 year old			VCD(K=0.53±1.11D)=16.03±0.79mm
			9 year old			VCD(K=0.37±1.14D)=16.28±0.69mm
			10 year old			VCD(K=0.34±1.25D)=16.30±0.78mm
			11 year old			VCD(K=0.18±1.57D)=16.39±0.83mm
			12 year old			VCD(K=0.32±1.50D)=16.44±0.85mm
			13 year old			VCD(K=-0.12±1.58D)=16.56±0.82mm
			14+ year old			VCD(K=-0.11±2.78D)=16.48±1.14mm
Gao 2002	Chinese	135 subj. /270 eyes	9.6±2.3 yr (7-13 yr)	72F, 63M	A-scan	VCD(K=4.57±2.17D)=14.62±1.09 mm before & =14.54±1.09mm after cycloplegia, n=118
						VCD(K=0.11±0.47D)=16.32±0.79mm before & =16.24±0.79mm after cycloplegia, n=38
						VCD(K=-2.47±1.80D)=17.18±1.04mm before & =17.14±1.04mm after cycloplegia, n=114

Table 2.15, cont.

Gwiazda 2002	USA: W, B, A, H	469 children /469 right eyes	6-7 year old 8 year old 9 year old 10 year old 11 year old	246 F, 223 M	A-Scan	VCD(K=-2.38±0.81D)=16.8±0.7mm, n=469. Age, gender and ethnicity dependence report.
Saw 2002a	Singapore /Chinese	1449 children /1449 right eyes			A-Scan	VCD correlation of K, body height, weight and mass index
Saw 2002b	Singapore /Chinese	1453 children /1453 right eyes	7 year old 8 year old 9 year old 7 year old 8 year old 9 year old	318 M 239 M 192 M 313 F 231 F 160 F	A-Scan	VCD(K=-0.2±1.6D)=16.3±0.9mm VCD(K=-0.5±1.7D)=16.6±0.8mm VCD(K=-1.4±2.1D)=17.0±0.9mm VCD(K=-0.08±1.3D)=15.8±0.8mm VCD(K=-0.3±1.5D)=16.1±0.8mm VCD(K=-1.1±1.8D)=16.4±0.9mm
Zadnik 1999	USA, Ohio	554 subj. /554 right eyes	8.60±0.53 yr		A-Scan	VCD(K=0.94±0.71D)=15.70±0.69mm
Lam 1 999	Hong Kong, China	142 subj. / 142 OD	(6-17 yr) (6-17 yr) (8-19 yr) (8-19 yr)	75F 67M 75F 67M	A-Scan	VCD(K=-1.14±1.53D)=16.34±0.96mm, (1991) VCD(K=-1.33±1.66D)=16.85±0.96mm, (1991) VCD(K=-1.83±2.04D)=16.80±1.15mm, (1993) VCD(K=-1.90±1.94D)=17.33±1.04mm, (1993)
W: White B: Black	A: Asian H:Hispanic	hy: hyperopic em: emmetropic my: myopic	F: female M: male yr: year old		OD: right eye OS: left eye D: diopter	VCD: vitreous chamber depth K: refracrive error (spherical equivalent)

In children, boys also have about 0.5mm longer VCD than girls (6-17 year old Chinese from Lam's study [Lam 1999] in Figure 2.59 and Zadnik 2003 US, 6-14 year old American from Zadnik's study [Zadnik 2003], and Saw 2002b Chinese, 7-9 year old Chinese from Saw's study [Saw 2002b] in Figure 2.60).

Age:

In the last section, I described that ocular length growths rapidly during the infancy and approaches the size of adults' eyes in early childhood. After 18-year old, eye length remains practically the same through the age although some studies show a slight increase with age. The major ocular element that is affected by aging in adulthood is the lens. After 20 year old, the thickness of lens (*LT*) increases with age by growing additional tissue on both anterior and posterior surfaces resulting to the decreases of both anterior chamber depth (*ACD*) and the vitreous chamber depth (*VCD*). This concept is described with aging rates of *ACD* and Anterior segment length (*ASL=ACD+ LT*, lens thickness) in non-refraction specific groups of Dubbelman's study [Dubbelman 2001] as -0.010 and +0.024mm/year, in Koretz's study [Koretz 1989] as -0.011 and +0.021 mm/year, in Allouch's study [Allouch 2005] as -0.016 and +0.021 mm/year, and in Atchison 2008 as -0.010 and +0.0235 mm/year. Another 3 studies show that the increase of lens thickness with age pushes only toward the anterior chamber but not the vitreous chamber. These results are Wojciechowski with -0.021 and +0.018 mm/year [Wojciechowski 2003], Shufelt with -0.011 and +0.010mm/year [Shufelt 2005], and Koretz with -0.022 and +0.019 mm/year [Koretz 2004].

In the infancy, Mutti's study provides the typical *VCD* of 12-13.5 mm in 3- and 9-months old babies (Figure 2.59) [Mutti 2005].

Jones gave age dependence of US children from 6 to 15 year old [Jones 2005] (Figure 2.62). Because of the strong *VCD* correlation with refractive error, the age dependence needs to be corrected by refractive error. Jones 2005 study simply presents the age-dependence at 4 refractive groups as shown in the Figure 2.62.

The increase of *VCD* in childhood is also shown in the 4 studies in Figure 2.60. Notice that the refractive error is shifted from hyperopic to myopic at the same time the *VCD* increases with age. The same observation is also obtained in Lam's study in Figure 2.59 [Lam 1999].

In adults, Atchison attended the regression fit of decreasing *VCD* with ultrasonography data: *VCD=15.99-0.0016*Age* (adjusted r^2 = 0.00, p = 0.70) [Atchison 2008]. As the statistical p value indicates, there is no significance on this age dependence.

Mallen's study in Jordanians [Mallen 2005] and Wickremasinghe's study in Mongolians [Wickremasinghe 2004] also obtained "insignificant" conclusion (Figure 2.61). However, Shufelt's data in Latinos [Shufelt 2005], Alsbirk's in Eskimos [Alsbirk 1977], as shown in the same figure, obtained clearly decreasing *VCD* with age. Opposite to this indication, Garner's study reported that *VCD* increasing with the rate 0.072mm/yr and 0.165mm/yr for emmetropic and hyperopic group (>-0.5D) and myopic group (<=-0.5D), respectively [Garner 2004].

Ethnicity:

Among the collected data, adjusted for age and gender, Asian data lie along with the dashed fitting line except the data from Wong 01 (40-81 year-old Singapore Chinese, 0.6mm shorter *VCD*) and Wickremasinghe 04 (>40 year-old Mongolian, 0.4mm shorter AL).

Considering the variety of ethnicity in US, we are not surprised to observe the large distribution range of American subjects' data. Latino in US [Shufelt 2005] showed >0.8mm shorter *VCD* from the fitting line.

Adjusted for age and gender, Oceanian subjects [Scott 1993] have shorter *VCD* (about 0.4mm) found in 42 myopes from New Zealand.

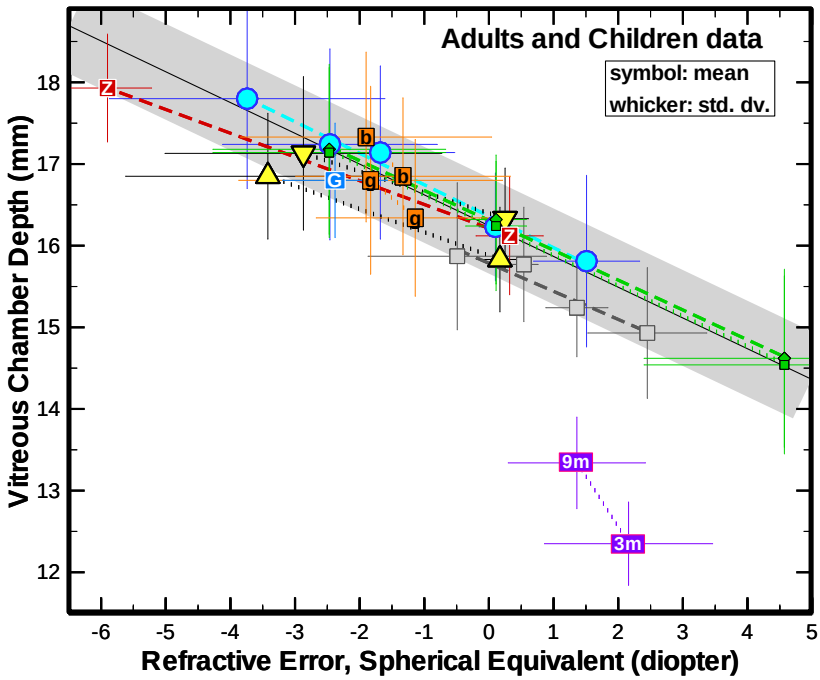

M^cBrien 1997, UK, 21-64yr, n=245

Goss 1997, USA, Oklahoma, 20-44yr, n=63 females

, n=105 males

Scott 1993, New Zealand, 17-26yr, n=84

Jones 2005, USA, Ohio, 3-8yr-old children, n=737

Mutti 2005, USA, infants at 3 and 9 month (follow-up) , n=222

Gao 2002, Chinese, 7-13yr, n=270, before cycloplegia

, after cycloplegia

Lam 1999, Hong Kong, Chinese, 6-17yr & 2yr-follow-up, n=75 girls

, n=67 boys

Gwiazda 2002, USA, 6-11yr, n=469

Figure 2.59 *Comparisons of 8 studies of vitreous chamber depth*

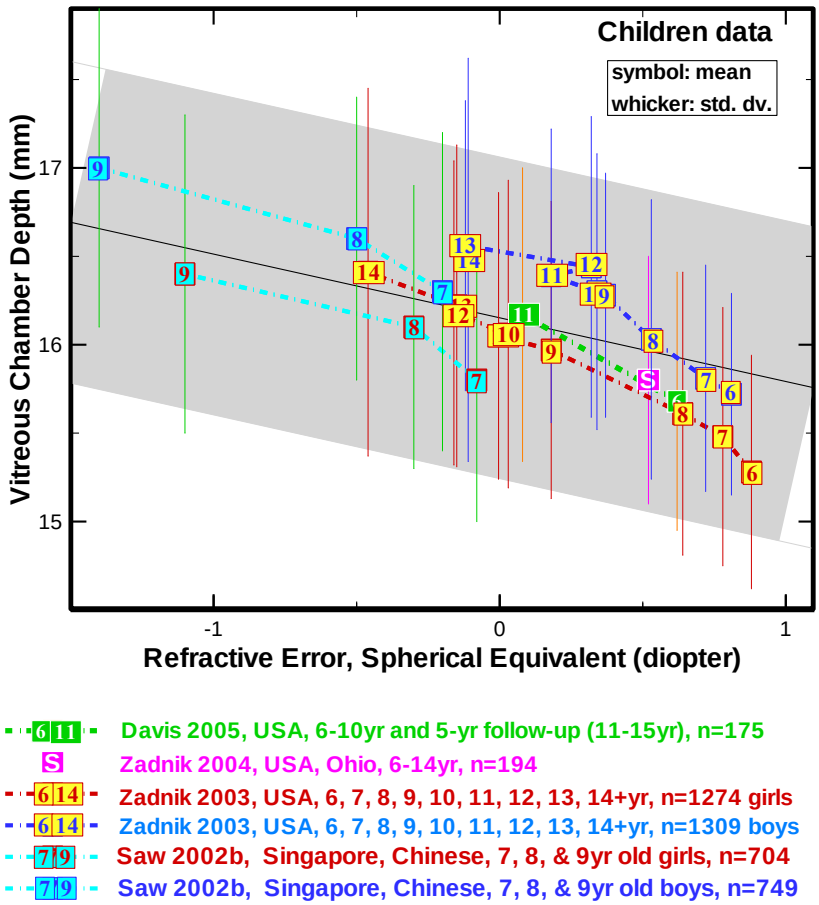

Figure 2.60 *VCD vs. K in children*

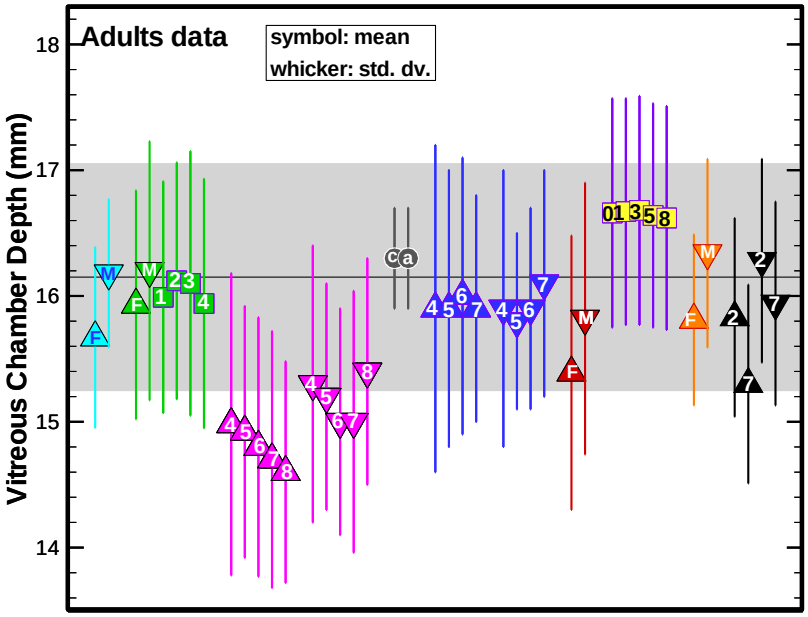

Atchison 2008, Australia, 96+% white, 18-69yr, n=51female & 51males
Mallen 2005, Jordan, 17-40yr, n=643 females & n=450 males
, age=17-22yr, 23-28yr, 29-34yr, 35-40yr, total n=1093
Shufelt 2005, USA (Latino), 40's, 50's, 60's, 70's, 80+yr, 3251 females
, 2337 males
Kirschkamp 2004, Germany/UK, 20-38yr, cyclplg & 4D accomm. n=9
Wickremasinghe 2004, Mongolian, 40's, 50's, 60's, 70+yr, 970 females
, 700 males
Wong 2001, Singapore/Chinese, 40-81yr, n=547 females & 457 males
Garner 1997, New Zealand, 18-28yr, accom. stmlu=0, 1.5, 3.5, 5.5, 8D
Koretz 1989, USA, 18-70yr, n=68 females & n=32 males
Alsbirk 1977, Greenland, Eskimos, 20yr & 70yr females
, 20 yr & 70yr males

Figure 2.61 *VCD vs. K in adults*

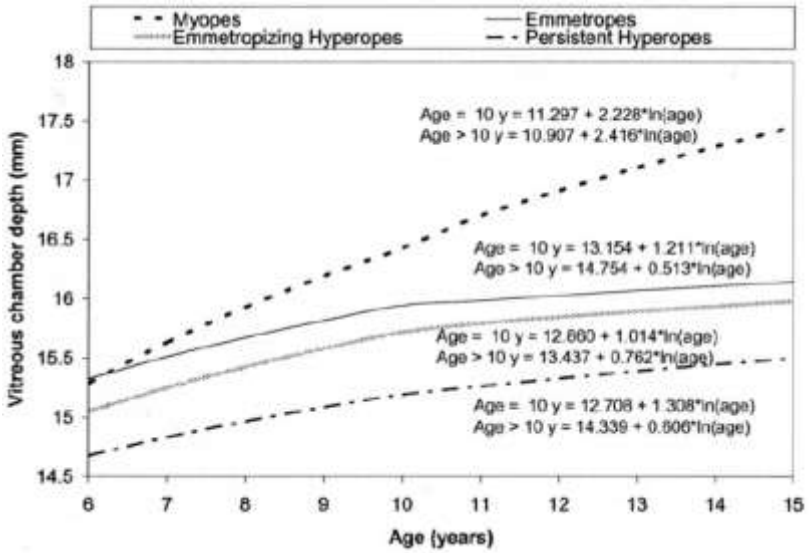

Figure 2.62 *Age-dependence of VCD in US children. Figure is adopted from Jones 2005.*

Accommodation:
In a UK study performed by Garner in 1997, no *VCD* correlation with accommodation was found [Garner 1997b]. This can be clearly seen in Figure 2.61. The standard deviation of each mean value is far larger than the difference from accommodation.

Kirschkamp's study shows that cycloplegia has no observable effect on *VCD* (Figure 2.61) [Kirschkamp 2004]. The same conclusion is also obtained by the Chinese children study of Gao [Gao 2002] (Figure 2.59).

Other factors:
Wong [Wong 2001] and Saw [Saw 2002a] gave *VCD* and *K* in 5 and 4 quartiles according to height, weight and BMI. And Wong indicated that height and weight correlate positively with *VCD*, but BMI does not correlate with *VCD* [Wong 2001]. Saw 2002a concluded that taller children are more myopic and have longer *VCD* [Saw 2002a].

2.6.2 Refractive Index of Vitreous Humor (n_{VC})

There is no significant difference for the index of refraction of the vitreous humor. The typical number used in literature is n_{VC} =1.336 at wavelength of 555 nm. The values of n_{AC}=*1.3565, 1.3407, 1.3341*, and *1.3273*, for wavelength at 365nm, 486.1nm, 656.3nm, and 1014nm from Navarro model [Navarro 1985 and the extended model in Escudero-Sanz 1999] are used for the eye modeling work in this dissertation.

2.6.3 Retina

Lotmar eye model used 12.3 mm as the retina radius of curvature [Lotmar 1971]. Navarro and co-worker uses 12.0 mm as the radius of curvature of retina in the wide angle emmetropic eye model [Escudero-Sanz 1999] and obtained good aberration agreement with real human eyes. Atchison's study [Atchison 2006] (2005 originally) provides more detailed retinal surface description, in radius of curvature, R_R and conic constant, Q_R, as functions of spherical refractive error, *K*. The refractive error can be applied from 0 to -12 diopters. He also provided the description of retinal decentration and tilt. Like most of the eye

modeling work, I adopt only a constant R_R = 12.0 mm and don't apply these decenter and tilt conditions in this dissertation.

2.7 CHALLENGE AND POTENTIAL POPULATION-BASED EYE MODELNG

Our original purpose of performing the ocular biometry statistics is to propose population-based eye modeling. In this population-based eye modeling, we expect to include the dependence of ocular biometry on refractive error and also consider the factors of age, gender, ethnicity and physical condition. We planned to accomplish this work in one chapter. However, as we collect more and more ocular biometry measurement results from all over the world and also perform certain statistical analysis, we found two challenges, regarding which we will have to only show the idea and direction of this review work and leave this topic for our future research. The first reason we can not finish the analysis in one chapter is that we will have to collect more data to perform convincing statistical analysis. The proposed topic is population-based eye modeling so sufficient data number is the foundation we can draw solid conclusion and eliminate the bias in some experiments caused by methods, instruments, subjects' characters, and other factors. The second challenge is that we will need to perform meta-analysis if we want to isolate each subject's character factor and the significance of that dependence. Though the above two difficulties have prevent us from claim solid population-based models, our methodologies in collecting data, executing regression, and narrowing down the distribution function by isolating the factors are promising. It is worth pursuing our work and extending it into a thesis.

Chapter 3 Optical Eye Modeling

3.1 EYE MODELING USING CONTEMPORARY OPTICAL DESIGN SOFTWARE

Traditional schematic eye models are generic in the sense that they represent average anatomic and optical properties of adult eyes. This type of model is used to understand the optics and vision of the human eye and to design common visual optics. However, an individual eye can be very different from any models. All of the generic models are highly symmetric. They have ideal rotationally symmetric, centered, and aligned surfaces, whereas real eyes show degrees of irregularities with no well-defined optical or symmetry axes. Among the current published generic eye models, the wide-angle Navarro model, based on anatomical data, has been demonstrated to produce on-axis image quality as well as off-axis aberrations that are well aligned with human measurements [Escudero-Sanz 1999]. After evaluating many published eye models in my earlier work [Chen 2003], this model has been selected and used as the base model in majority of the recent CLA eye modeling research work.

The wide-angle Navarro model was built by incorporating published conic constant anatomical values into the Gullstrand-Le Grand spherical surfaces [Le Grand 1956] and by updating the values of the anterior radius and refractive index of the cornea using more recent anatomical data. Other refractive indices in Ref. [Le Grand 1956] were preserved for the standard D-line, 589.3 nm wavelength. Refractive indices for other wavelengths were estimated, departing from experimental data of chromatic dispersions, and adjusting experimental values of longitudinal chromatic aberration (Ref. [Navarro 1985] for details).

Most of current generic eye modeling research requires the assistance of optical design software such as ZEMAX, Code V, and OSLO for both the construction of models and the extension to applications in optical engineering. I have been using ZEMAX for the eye modeling procedure and this dissertation research work is utilized with only this program. ZEMAX is a program that assists the design of optical systems by providing optical modeling and analysis that is based on the ray tracing technology. The optical parameters of an eye model or an optical system are entered in a spread sheet format. Table 3.1 shows the lens data editor in ZEMAX with input parameters of Navarro eye model. The rows describe, from top to bottom, the object (OBJ), the surfaces of cornea (surfaces 1 and 2), pupil (STO; aperture stop), crystalline lens (surfaces 4, 5), and the imaging surface of retina (surface IMA).

The first column "Surf: Type" shows a selected surface type from ZEMAX. The most commonly used optical surface is an aspherical surface named "Standard Surface". Standard surface required 2 specified parameters: radius and conic constant. ZEMAX treats planes as a special case of the sphere (i.e. a sphere with infinite radius of curvature). The surface is centered on the "current" optical axis, with the vertex located at the "current" Z-axis position. The "sag" or z-value of the standard surface is given by

$$z = \frac{cr^2}{1+\sqrt{1-1(1+Q)c^2r^2}}, \qquad (3\text{-}1)$$

where c is the curvature (the reciprocal of the radius), r is the radial coordinate in the lens unit and Q is the conic constant. The radius of the surface vertex curvature is entered in the second column, "Radius", in mm. The conic constant, Q, is assigned at the sixth column. The conic constant of less than -1 describes a hyperbolas surface, -1 describes parabolas, between -1 and 0 is ellipses, 0 defines spheres, and greater than 0 depicts an oblate ellipsoids. As shown in Figure 3.1, the colored lines illustrate the anterior corneal surfaces for different conic constants with the same cornea radius of curvature, R =7.72 mm. Shown on the right is the zoom-in area of 5 mm (corneal radius direction) by 2.5 mm (thickness in z-direction).The effect of conic constant is more observable at the periphery of cornea. Although the human corneal surface extends about 5.5 mm in radius, the most effective visual zone falls inside the center 2mm of radius due to the limitation of the pupil stop. Although the conic constant doesn't seem to cause much variation inside 2 mm visual zone, in general it produces significant spherical aberration (SA) and impacts the imaging quality appreciably.

The third column “Thickness” expresses the distance from the vertex of the present surface to the vertex of the next surface in mm. The fourth column “Glass” is the refractive index data of the material between the current surface and the next surface. For each “glass” name, the glass name entered must be in one of the currently loaded glass catalogs. The parameters of the refractive index should have been added to that glass catalog. If the optical computation considers multiple wavelengths, the data should include dispersion information over the spectral range. The fifth column “Semi-Diameter” (diameter/2) describes the aperture size of each surface. Columns after the sixth describe the decentering of the apex and the tilting parameters of the surface. Since all the surfaces in Navarro model are centered and symmetric to the optical axis as well as most optical system, they are not shown in Table 3.1.

After the data input in the lens data editor, analysis tools of ZEMAX can be used to illustrate the result. Figure 3.2 shows a typical 3-D layout of an eye model in ZEMAX. With an eye model constructed in ZEMAX, light-rays can be traced from the object space (OBJ) sequentially through system to the image plane (IMA), i.e. the retina, in Snell Law. Optical analysis, including point spread function (PSF), wavefront aberration (WFA), Spot diagram, etc. are available in ZEMAX for examining the optical performance. With specified merit functions, ZEMAX uses a mathematical algorithm to perform the Optical Optimization iteration until the specified target criteria are met. The following sections describe these optical optimizations in the approach to the application to real human eyes.

The step-by-step general eye modelling procedures is described in Appendix A. In ZEMAX website [Tocci 2007], and there is also the step-by-step procedure of modelling Liou 1997 model [Liou 1997], which uses gradient refractive index for lens. In addition, a forward, a backward, and a non-sequential eye model module can be downloaded in website [Watkins 2007].

After an eye model is constructed, validation is required. This is normally done by comparing the optical performance of the model with real human eyes. In general optical system design, analysis is performed on the aberrations and final result is examined with Spot Diagram (SPD), Point Spread function (PSF), and Modulation Transfer function (MTF). Agreement with mean ocular aberrations confirms the final general eye model.

Table 3.1 *Ocular parameters input of Navarro Eye Model in lens editor of ZEMAX*

Surf:Type		Radius	Thickness	Glass	Semi-Diameter		Conic
OBJ	Standard	Infinity	Infinity		0.000000		0.000000
1*	Standard	7.720000	0.550000	CORNEA_NAVARRO	5.000000	U	-0.260000
2*	Standard	6.500000	3.050000	AQUEOUS_NAVARRO	5.000000	U	0.000000
STO*	Standard	Infinity	0.000000	AQUEOUS_NAVARRO	3.500000	U	0.000000
4*	Standard	10.200000	4.000000	LENS_NAVARRO	5.000000	U	-3.131600
5*	Standard	-6.000000	16.320300	VITREOUS_NAVARRO	5.000000	U	-1.000000
IMA*	Standard	-12.000000	-	VITREOUS_NAVARRO	12.000000	U	0.000000

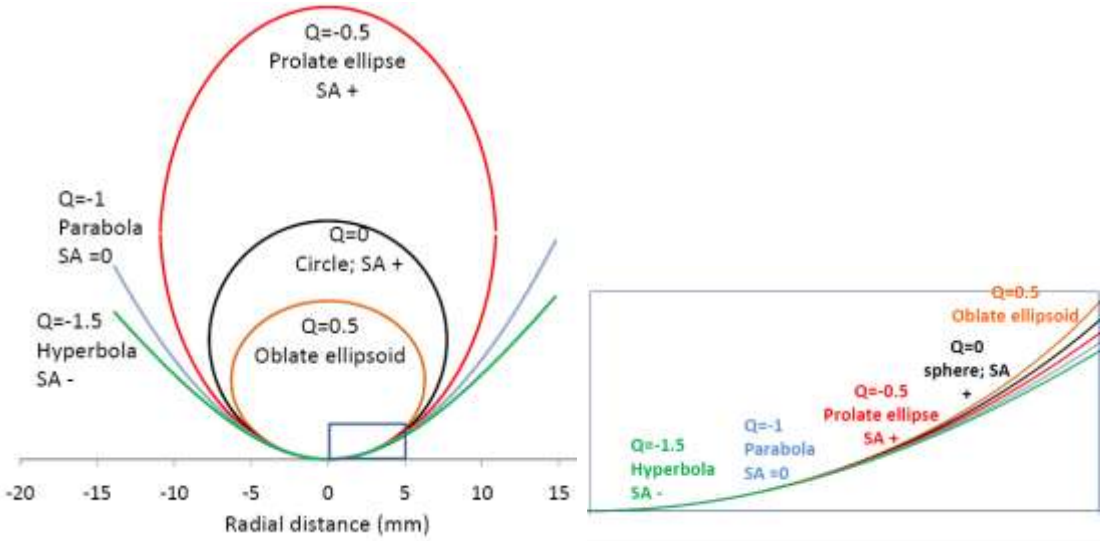

Figure 3.1 *(Left): Anterior corneal surface diagram of different conic constants with same cornea curvature of radius=7.72 mm. (Right): The zoom-in block, 5 mm radius by 2.5 mm thick, as indicated in the left picture.*

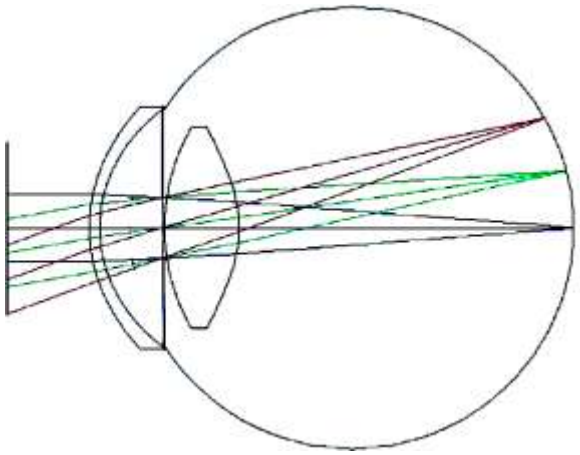

Figure 3.2 *A 3-D layout of eye model in ZEMAX program. The left most plane surface is a dummy surface for illustration, which is not included in Table 3.1.*

3.2 OPTICAL OPTIMIZATION

For more specific or customized eye modeling, ocular parameters require to be mathematically tailored in order to better describe the properties of the target eye. “Optical optimization” is the iteration algorithm that takes a starting optical design layout and changes the parameters in steps to approach the specified targets. The starting layout should have a suitable number of optical surfaces of appropriate types, since optimization can change only the values of the parameters, but not the number or types of surfaces. Optimization requires three steps:

1) Construct a reasonable initial layout so that rays can be traced from the object plane to the image surface;
2) Specify the free variables to be “optimized” and the corresponding tolerances to prevent unrealistic results or convergence to local minima;
3) Define the merit functions that describe the ultimate goals at the end of iteration.

A “reasonable” system is a rather loose concept. Although there are exceptions, poorly conceived initial layouts are not likely to be transformed into ideal outcomes by the optimization algorithm.

The variables of iteration, for the optimization algorithm to be able to make any progress, are specified next. Since optics is very precise (distances of micrometers can make a big difference), we need to closely determine the values of all our variables at each step of the optimization. The selection of variables is very important for optimization. In the eye modeling, I assigned variables on different ocular components at different modeling stages.

After the variables are assigned, suitable metrics are used as the indicators of progress of optical optimization. These metrics are defined as the merit functions. A merit function is a numerical representation of how closely the optimization result meets a specified set of goals. Usually, different merit functions will lead to different final optimization results. On the other hand, the final values of merit functions after optimization are indicators to evaluate the success of eye modeling. So the optimization and selection of merit functions are the most important process in eye modeling procedure as well as validation.

The optimization feature provided by ZEMAX is quite powerful. ZEMAX uses either an actively damped least squares or an orthogonal descent algorithm. The algorithms are capable of optimizing a merit function composed of weighted target values; these target values are named "operands". ZEMAX has several different default merit functions that will be described in a subsequent section. For the majority of application, the optical optimization is performed to achieve optimal imaging quality. The default merit functions include attempts to minimal optical aberration or smallest focus spot (point spread function).

In eye modeling applications, the goals of optimizations are to produce the realistic human eye with the personal clinically measured or validated ocular measurements. These specific merit functions are assigned using the Merit Function Editor in ZAMAX. If the clinical measured wavefront aberration (WFA) map is available for an eye, the personalized eye modeling will aim to reproduce the exactly measure on the modeled eye. Since the clinical measured WFA data is typically expressed in Zernike polynomials coefficients, the merit function at the final optimization mean to produce wavefront of the exact series of Zernike coefficients. The ZEMAX operand, ZERN, which designates the intended set of Zernike coefficients of the target wavefront would be used for this purpose. However, when the wavefront data are not obtained from the patient, the most common clinical eye examinee record, the sphero-cylindrical refraction prescription for contact lens or spectacles and the visual acuity (VA), would be my targets of optimizations. These optimization goals and their optical relevancies are described below in this section. In the following section 3.3, the merit functions to be used to approach these clinical measures will be addressed.

3.2.1 Wavefront Aberration (WFA), Zernike Polynomials, and Root Mean Square (RMS) WFA

Wavefront aberration (WFA):

Wavefront aberration is a popular way of evaluating monochromatic performance of the human eyes in the recent years. A wavefront (WF) specifies a surface of a constant optical path (OP) from the light source. For example, a point source produces a sequence of wavefronts of spherical surfaces. The aberration of WF is defined as the optical path difference (OPD) between the real wavefront and an ideal wavefront. For an ideal relaxed eye, the retinal image surface conjugates to the object plane at infinity. For a point source located at infinity, the image should be formed right on the retinal surface, and the ideal wavefront emerges as a plane-wave at the exit pupil. As shown in Figure 3.3, WFA of an eye can be measured clinically by projecting a laser beam onto retina to form a diffusive point source. The rays from this point source travel through the ocular elements and exit the cornea. The 2-dimensional wavefront at the exit pupil is measured and compared with the ideal wavefront of a plane-wave. The wavefront aberration is generally expressed in a unit polar coordinate as $W(\rho, \theta)$, where $\rho = r/r_{max}$ is the normalized distance from the centre of exit pupil and θ is the azimuth angle. Wavefront aberration is usually presented in μm or wavelength, λ, and is often assigned to be zero at the center point, i.e. $W(\rho=0)=0$. It is comprehensible to describe WFA in wavelength since the destructive interference occurs when $W(\rho, \theta) > \lambda/2$.

Zernike coefficients:

Zernike polynomial functions are normally used to describe the 2-dimensional *WFA* function. Zernike polynomial functions, $\{Z_n^m\}$, represent a completely orthonormal set of functions that can be used to describe any 2 dimensional functions in a normalized polar coordinate. The mathematic form of Zernike function is

$$Z_n^m(\rho,\theta) = \left\{ \begin{array}{l} N_n^m R_n^{|m|}(\rho)\cos(m\theta), \text{ for } m \geq 0 \\ N_n^m R_n^{|m|}(\rho)\sin(|m|\theta), \text{ for } m < 0 \end{array} \right\},$$

where

$$R_n^{|m|}(\rho) = \sum_{s=0}^{(n-|m|)/2} \frac{(-1)^s (n-s)!}{s![0.5(n+|m|-s)]![0.5(n-|m|-s)]!} \rho^{n-2s},$$

and N_n^m is the corresponding normalization constant. The indexes, n and m ($=-n,-n+2,\ldots.+n$) , in Zernike function indicate the highest power of normalized radius and the frequency of azimuthal angle respectively. These polynomials have an orthogonal basis set in the polar coordinates over the interior of the unit circle. Their characteristic is that the average value of each polynomial (other than the zero-order term) is zero over the unit circle and each term minimizes the RMS wavefront error to the order of that term. 2-dimensional maps of Zernike functions are plotted in the Figure 3.4. The following table gives the first 28 Zernike functions. The aberration names and number 0 to 20+ in Figure 3.4 and Table 3.2 were announced as standard by Optical Society of America (OSA) in 1999 to present human eye aberrations [Thibos 2002]. The same system was also adopted by the American National Standards Institute in 2004 [American National Standards Institute 2004]. It is very important to point out that although the names (terminology) of Zernike polynomial aberrations, as indicated in the Table 3.2, appear to be identical to the names used in Seidel aberrations, they do not imply the same aberrations. For example, coma and astigmatism in Seidel system are aberrations caused by the off-axis field angle. They exist even when the

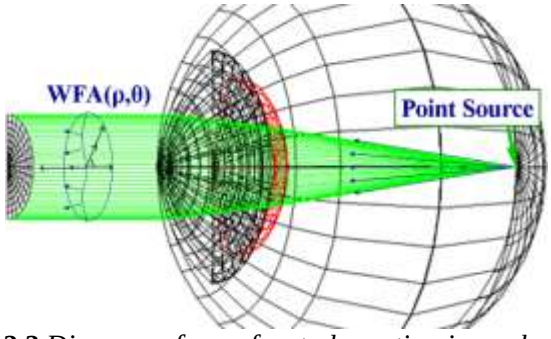

Figure 3.3 *Diagram of wavefront aberration in ocular system*

optical system is rotationally symmetric. The coma and astigmatism in the wavefront system present the rotational asymmetry of the system.

The wavefront aberration, $W(\rho,\theta)$ of human eye is expressed as the superposition of Zernike functions, $\{Z_n^m\}$, weighted with the set of Zernike coefficients, $\{C_n^m\}$.

$$W(\rho,\theta)=\sum_{n=0}^{k}\sum_{\substack{m=-n\\ n-|m|=even}}^{n} C_n^m Z_n^m(\rho,\theta)$$

Therefore, the set of coefficients, $\{C_n^m\}$, represent the 2-dimmensional *WFA* of an eye. Typically, the zero-order (n=0; m=0) and first-order (n=1; m=+1, -1) coefficients present the coordinate shift in z-direction and the tilt along z-axis. The three coefficients in second order (n=2; m=-2, 0, +2) Zernike (C_2^{-2}, C_2^0, C_2^{+2}) correspond to the ocular defocus and astigmatism. They relate mathematically to the clinical prescription of refractive error, which can be corrected by typical eye glasses and contact lens. I will address the refractive error further in the followed section.

Higher-order Zernike coefficients describe more complex asymmetry and radius dependence of eyes which cannot be corrected with regular eye glasses or contact lens. Although high-order aberration is normally trivial and not required to be corrected in majority population, the values can increase and become significant to impair the vision. In abnormalities such as keratoconus eyes or post-laser surgeries (radial keratotomy, photorefractive keratectomy and automated lamellar keratoplasty, etc.) where the high-order terms are significant, the impaired vision can't be corrected by the typical spectacles or contact lens.

<u>*RMS WFA*</u>:

The departure of the real wavefront from the ideal wavefront indicates the degree of ocular irregularity. Therefore, the root-mean-square wavefront aberration, RMS WFA, is frequently used to rate the abnormality. In general, the larger the RMS value is, the worse the abnormality is. Because of the orthonormal nature of Zernike polynomials, $\{Z_n^m\}$, the RMS integration over the pupil area returns to a simple form: $RMS\_WFA=\sqrt{\frac{\iint W(\rho,\theta)^2\,\rho d\theta d\rho}{\iint \rho d\theta d\rho}}=\sqrt{\sum_n\sum_m {C_n^m}^2}$. Notice that from the right most expression, the amplitude of each Zernike coefficient contributes a positive amount to the quantity of *RMS WFA*. As a consequence, most of literature addresses *RMS WFA* for each *n*-order (and ignore *m*). Usually, the zero, first, and second order terms (n=0, 1, and 2) are ignored. Only total high-order *RMS WFA* ($n \geq 3$) is used in general to indicate the ocular irregularity.

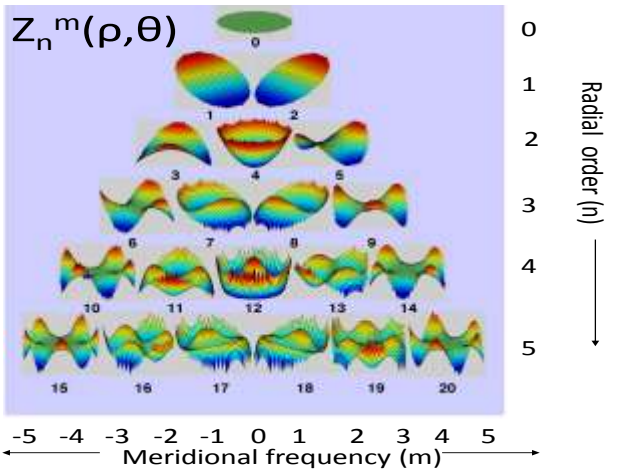

Figure 3.4 *Zernike expansions showing the first 5 radial order modes using the Optical Society of America (OSA) recommended notation.*

Table 3.2 *Zernike polynomial function*

#	Z_n^m	ab.	Characteristic	Polar presentation
0	Z_0^0	N/A	Piston	*1*
1	Z_1^{-1}		Vertical tilt	$2\rho \sin(\theta)$
2	Z_1^1		Horizontal tilt	$2\rho \cos(\theta)$
3	Z_2^{-2}	low order aber.	Oblique astigmatism	$\sqrt{6}\,\rho^2 \sin(2\theta)$
4	Z_2^0		Defocus	$\sqrt{3}\,(2\rho^2-1)$
5	Z_2^2		With-/against-the-rule astigmatism	$\sqrt{6}\,\rho^2 \cos(2\theta)$
6	Z_3^{-3}	high order aber.	Oblique trefoil	$\sqrt{8}\,\rho^3 \sin(3\theta)$
7	Z_3^{-1}		Vertical coma	$\sqrt{8}\,(3\rho^3-2\rho) \sin(\theta)$
8	Z_3^1		Horizontal coma	$\sqrt{8}\,(3\rho^3-2\rho) \cos(\theta)$
9	Z_3^3		Horizontal trefoil	$\sqrt{8}\,\rho^3 \cos(3\theta)$
10	Z_4^{-4}		Oblique quatrefoil	$\sqrt{10}\,\rho^4 \sin(4\theta)$
11	Z_4^{-2}		Oblique secondary	$\sqrt{10}\,(4\rho^4-3\rho^2) \sin(2\theta)$
12	Z_4^0		Spherical aberration	$\sqrt{5}\,(6\rho^4-6\rho^2+1)$
13	Z_4^2		With/against rule secondary astigmatism	$\sqrt{10}\,(4\rho^4-3\rho^2) \cos(2\theta)$
14	Z_4^4		Quatrefoil	$\sqrt{10}\,\rho^4 \cos(4\theta)$
15	Z_5^{-5}			$\sqrt{12}\,\rho^5 \sin(5\theta)$
16	Z_5^{-3}			$\sqrt{12}\,(5\rho^5-4\rho^3) \sin(3\theta)$
17	Z_5^{-1}		Secondary vertical coma	$\sqrt{12}\,(10\rho^5-12\rho^3+3\rho) \sin(\theta)$
18	Z_5^1		Secondary horizontal coma	$\sqrt{12}\,(10\rho^5-12\rho^3+3\rho) \cos(\theta)$
19	Z_5^3			$\sqrt{12}\,(5\rho^5-4\rho^3) \cos(3\theta)$
20	Z_5^5			$\sqrt{12}\,\rho^5 \cos(5\theta)$
21	Z_6^{-6}			$\sqrt{14}\,\rho^6 \sin(6\theta)$
22	Z_6^{-4}			$\sqrt{14}\,(6\rho^6-5\rho^4) \sin(4\theta)$
23	Z_6^{-2}			$\sqrt{14}\,(15\rho^6-20\rho^4+6\rho^2) \sin(2\theta)$
24	Z_6^0		Secondary spherical	$\sqrt{7}\,(20\rho6-30\rho4+12\rho^2-1)$
25	Z_6^2			$\sqrt{14}\,(15\rho^6-20\rho^4+6\rho^2) \cos(2\theta)$
26	Z_6^4			$\sqrt{14}\,(6\rho^6-5\rho^4) \cos(4\theta)$
27	Z_6^6			$\sqrt{14}\,\rho^6 \cos(6\theta)$

3.2.2 Refractive Errors and Sphero-Cylindrical Refraction Prescription

The most general cause for the poor optical performance of the naked eyes in the population is the refractive errors. For a good eye without refractive error (named emmetropia), at fully relaxed condition when no lens accommodation is present, the image of distant objects would be sharply focused on the retina surface. For healthy eyes with refractive errors (called ametropia), light rays from the distant objects are also focused into sharp point. However, the focused point falls either in front (near-sightedness; also called myopia) or behind (far-sightedness; also called hyperopia) the retina surface. In another word, a myopic eye either has too powerful a cornea and/or lens or too long an axial length as described in Chapter 2. To correct the vision, a negative lens is applied to reduce the total focusing power. On the other hand, a hyperopic eye has either under-powered optics elements or too short an axial length and requires a positive lens to correct the vision. These two types of defocus are rotationally symmetric in the eyes and these refractive errors are called spherical. If the defocus is not rotationally symmetrical due to the more "foot-ball-shaped" eye optics, the ocular power is typically described by the maximum and minimum defocus values along two perpendicular meridians. This is the condition of astigmatism. Astigmatism could be caused by one or more of the optical surfaces of the eye being toroidal, tilted, or displaced from the axis. The power difference of the two defocus values is called the cylindrical refractive error. The prescription of spherical, cylindrical (error), and axis of defocus are given to patients after a common eye examination in (S, C, X) form. S describes the needed correction on one of the major meridians, which is specified with the third number, the angle of X (viewed by the clinician, counter-clockwise from the +X-axis of the X-Y coordinate). The sum of S and C describes the required correction power in the perpendicular meridian. For an eye without cylindrical refractive error, the C and X terms will be both zero. All of the three types of refractive errors can be corrected with common eye glasses, contact lens, or laser cornea surgery. Generally speaking, these corrections are to balance the defocus or to remove of low-order aberration. In the wavefront aberration section, I mentioned that the three 2^{nd}-order wavefront aberration coefficients represent the sphero-cylindrical refractive error. The interchange of these low order aberrations, (C_2^{-2}, C_2^{0}, C_2^{+2}), to (S, C, X) is given in many literature [Schwiegerling 1995, and Porter 2006].

In the eye modeling work, I generally insert a virtual lens with the prescribed sphero-cylindrical refraction correction (clinically determined best correction) to the anterior cornea location of the eye model and then run the iteration to approach a normal eye condition where the retina surface is conjugate to the infinity. In such manner, as the ideal virtual lens is removed after the optimization, the final model eye would represent an eye with the appropriate clinical refractive error.

3.2.3 Visual Acuity (VA) and the Best-Corrected Visual Acuity (BCVA)

There are different ways to evaluate the optical quality of an eye. Visual acuity is one of the most common measures used in a comprehensive eye examination. Visual acuity describes the acuteness or "sharpness" of vision; that is the ability to perceive small details. However, visual acuity is a subjective measure. The loss or diminishment of VA can be caused by not only optical factors such as refractive errors and cataracts but also neural factors such as damages on the retina due to glaucoma, diabetic retinopathy, or macular degeneration.

Distance visual acuity is normally measured using an eye chart. Various forms of eye charts are in use today. The most familiar is the Snellen letter chart. Snellen acuity is given in terms of a Snellen fraction S, which is defined as the ratio of the greatest distance at which subject can just read a given line on the chart and the greatest distance a "normal" observer can just read the same line. Typical testing distances for the Snellen letter chart are 20 feet in the U.S. and 6 meters in European countries. If a subject can read a line at 20 feet and the "normal" observer can see the same line at 40 feet, then the subject has 20/40

Snellen acuity. Visual acuity is sometimes specified in terms of LogMAR acuity to give a continuous number for acuity. LogMAR, *LA*, and Snellen acuity are related by $LA = \log_{10}\left(\frac{1}{S}\right)$.

Near visual acuity is usually assessed with a reading card to evaluate a subject's ability to accommodate. A common near acuity card is the Rosenbaum card. This card is designed for testing at 14 inches of distance. Jaeger scores (nominated J1, J2…) are often used to describe near acuity. Table 3.3 compares Jaeger values, equivalent Snellen distance acuities, and point sizes for Times New Roman font. Newsprint is typically between 10- and 14-point or between J7 and J10.

The equivalent visual acuity means the spatial resolution of the testing characters are identical. Figure 3.5 shows the designed symbols in different tests with same spatial resolution. The 20/20 visual acuity represents the vision that can resolve the spatial resolution of 1 minute (1/60 degree) in the object space. Take the Snellen letter E for example; each black and/or each white space in the letter has a unit width of 1 minute of spatial resolution. Hence, the letter E itself occupies a length of 5 minutes for the 20/20 vision no matter what distance (20 feet or the reading distance of ~14 inches) is used for testing. The resolution of 1 minute is also corresponds to roughly the size of the photoreceptor in human eyes.

The term of "best-corrected visual acuity (*BCVA*)" is the visual acuity of an eye with the best glasses or contact lens correction. In optical language, the 2nd-order aberration (or refractive error) is eliminated. If no neural factors are involved, the optical aberrations, namely the high-order wavefront aberrations, are responsible for this finite focus resolution.

In the optical eye modeling, the *VA* measurement data provides the upper limit of acceptable spatial resolution to be achieved. It means that after correcting/eliminating the 2nd-order aberrations, the focus spot size on the retina of the final eye model has to be equal or smaller than the spatial resolution that corresponds to the measured *BCVA*.

Optical performance of a system can be evaluated from geometric optics or wave optics point of view. In ZEMAX as well as most optical engineering, the following are some common analysis.

Spot Diagrams

The spot diagram shows the positions of the rays hitting the image plane through straight forward sequential rays tracing in an optical system. The spot diagram does not necessarily indicate the distribution of irradiance in the image since the plot does not show any weighting of the rays unless the pupil is uniformly illuminated, and the rays are uniformly distributed within the pupil. In the ideal optical system, all rays from a point source in the object plane meet in one single point in the image plane. This is not the case with the existence of aberrations.

Quantitative spot size analysis is done by tracing enough rays from a specified point on the object plane to the image plane. Each ray is considered to carry a weight proportional to the area it represents in the aperture of the system. The spot size can be statistically calculated as the **root-mean-square spot radius** with respect to either the Chief Ray or the Centroid. This evaluation is purely geometric. As one may expect, this spot size is relevant to the *VA* that is described earlier.

Point Spread Function (PSF)

The point spread function (PSF) is related to the wavefront aberration through a Fourier transform [Atchison 2000]. Similar to the Spot Diagram, the PSF is the resulting luminance distribution in the image surface of a point source of light. In other words, it is the image of a point source. The appearance of the PSF depends on diffraction, defocus, aberration, scatter and the shape and size of the aperture stop. For an ideal optical system without aberrations (a diffraction-limited system) and a circular aperture stop, the PSF is the Airy disk, the Fourier transform of the pupil. Its 1-dimentional section follows a Bessel function of the first kind of order 1. If the optical system has aberrations, the PSF is broader and the peak is lowered, relative to the diffraction limited case, and is typically not rotationally symmetric any more.

The ratio of the peak intensity of PSF to the peak in the ideal case is defined as the **Strehl Ratio (SR)**. A near perfect system with SR $\geq$0.8 is considered near diffraction-limited system. To compare to *VA* resolution in human eyes, the full width at half maximum **(FWHM) of the PSF** is appropriate.

Table 3.2 *Comparison of LogMar and Snellen presentations of distance visual acuity*

LogMAR, LA	Snellen (English)	Snellen S	Snellen (Metric)
–0.3	20/10	2.00	6/3
–0.2	20/12.5	1.61	6/3.75
–0.1	20/16	1.25	6/4.75
0.0	**20/20**	**1.00**	**6/6**
0.1	20/25	0.80	6/7.5
0.2	20/32	0.63	6/9.5
0.3	20/40	0.50	6/12
0.4	20/50	0.40	6/15
0.5	20/63	0.32	6/19
0.6	20/80	0.25	6/24
0.7	20/100	0.20	6/30

Table 3.3 *Comparison of Jaeger, Snellen presentations, and print size of rear visual acuity*

Jaeger	Snellen	Point
J1+	20/20	3
J1	20/25	4
J2	20/30	5
J3	20/40	6
J5	20/50	8
J7	20/70	10
J10	20/100	14

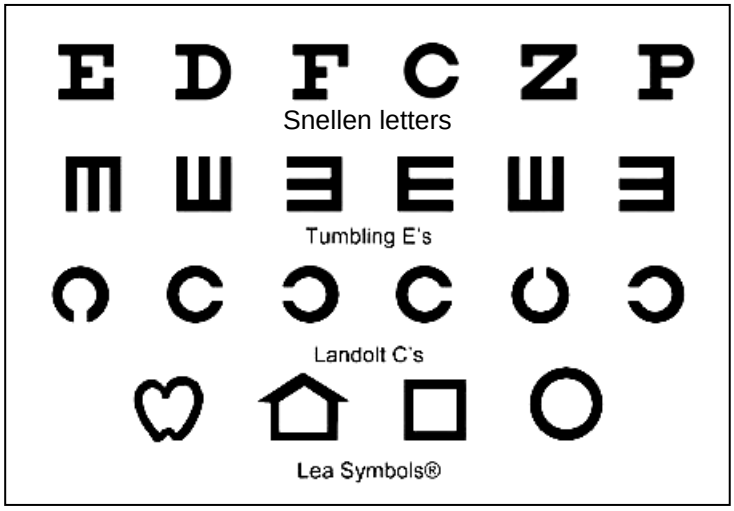

Figure 3.5 *Characters used in different visual acuity tests.*

3.3 MERIT FUNCTION: THE OPTICAL QUALITY METRIC IN ZEMAX

I have discussed the importance of optics optimization in our eye modeling technique, especially for the personalized eye modeling work. When the optimization is performed, merit functions, which specify the endpoint of the optimization, and boundary constrains need to be assigned. The merit function is a numerical representation of how closely an optical system meets a specified set of goals. ZEMAX utilizes a collection of operands which individually represent different constraints or goals for the optimization. Operands represent goals such as image quality, focal length, magnification, and many others, including WFA.

In the ZEMAX merit function editor, one can assign many operands and their corresponding constrains and targets. The merit function is defined to be the square root of the weighted sum of the squares of the difference between the actual and target values of each assigned operand. The merit function is ideal when it equals to zero. The optimization algorithm will attempt to make the value of this function as small as possible. The easiest way to define a merit function is to select the Tools, Default Merit Function option on the Merit Function Editor menu bar. A dialog box will appear which allows selection of options for the default merit function. In this section, I first describe the default merit function and the consideration for eye modeling. Then I address some user defined merit functions that I used in the eye modeling work.

3.3.1 Default Merit Functions in ZEMAX

ZEMAX default optimization is used to improve the performance of wide-ranging optical systems. Generally, it intends for the final optical system to produce the best imaging quality. The default merit functions are designed to approach the minimum focus size or the spot radius in spot diagram (SPD i.e. the approach in geometric optics) or the minimum aberration or Root Mean Square wavefront aberration (RMS WFA i.e. the approach in wave optics). Shown in Figure 3.6 is the dialog box of the default merit function. The default merit function is constructed using four key choices: 1). the optimization type, 2). data type, 3). reference point, and 4). integration method. These choices are described in Tables 3.4 to 3.6.

1. Optimization type: In eye modeling, I use only RMS instead of the peak-to-valley (PTV) because of the weakness of PTV. The PTV approach only looks at two points, the highest and lowest, and ignores all that lie between. Important issues such as roughness are totally ignored while a very small high or low point are exaggerated totally out of proportion to their significance. RMS greatly improves on the PTV method since it takes into account areas on the optic that may vary when compared to the optic's general surface characteristics.

2. Data type: WFA or SPD:

The numerical value of the merit function is physically significant when using RMS as the optimization type. If the merit function is RMS-Wavefront-Centroid, then the numerical value of the merit function is the RMS wavefront error in the unit of waves (λ). If the merit function is RMS-Spot Radius-Chief, then a value of 0.145 means the RMS spot radius is 0.145 lens units. If the lens units were millimeters, this would correspond to a focus radius of 145 micrometers RMS. If more than one field or wavelength is defined, then the merit function numerical value is the weighted average of the RMS values for the various fields and wavelengths.

Note that optimization using the RMS spot radius merit function will in general yield an optimum design different from the RMS wavefront merit function. The basic reason is that ray aberrations are proportional to the derivative of the wave aberrations. Therefore, it is unreasonable to expect that the minimum of one corresponds to the minimum of the other. A general rule is to use wavefront error if the

system is close to diffraction limited (say a PTV wavefront error of less than two waves). Otherwise, use the spot radius.

In the eye modeling work, a typical focus size is larger than 2 micron for green light (555nm). This is derived by 1.22*λ*f/d, where f is equivalent focal length of the eye (17mm) and d is the pupil diameter (~6mm). So usually, I use SPD first to run optimization. Then at the end of the optimization, if I can get the system close to diffraction limit, I will change to WFA and do another "fine-tune" optimization to get the desired system performance.

3. Reference point: Centroid or Chief Ray:
Generally speaking, the merit functions with the centroid as a reference are superior to those that reference to the chief ray. Most diffraction-based performance measures, such as MTF or encircled energy, improve when the RMS wavefront error referenced to the centroid decreases. However, it is always the best to re-optimize a final design with the various merit functions to verify which one provides the best performance for the system being designed. For example, the RMS wavefront centroid reference often yields better low frequency MTF response but worse medial frequency response, than does the RMS chief ray reference optimization does.

As indicated in Table 3.6, piston, x-tilt, and y-tilt don't degrade the image quality, which is my optimization target in most eye modeling cases. Therefore, I usually use centroid as reference point. However, it will be safe to re-optimize with reference to chief ray and make sure the centroid reference point give the better result.

4. Integration methods: There are two different pupil integration methods to construct the merit function: Gaussian quadrature (GQ) and rectangular array (RA). The integration normally can be approximated by: $\int_a^b f(x)dx \approx \sum_{i=0}^{N} w_i f(x_i)$

Gaussian quadrature approximates integrals with this equation, but grid points {xi} are equally spaced and weights {wi} are chosen craftily. Actually, Gaussian quadrature is a class of integration techniques, and each one is best suited for a different type of integral. The GQ algorithm is greatly superior for almost all cases of practical interest. The GQ algorithm uses a carefully selected and weighted ray set to accurately compute the RMS or PTV error over the entrance pupil (strictly speaking, the PTV algorithm is not a GQ algorithm, but it is very similar). The weighting for all rays is applied according to the weights set on the wavelength and field data dialog boxes, any pupil apodization function, and by the GQ merit function algorithm. For RMS merit functions, the weighting and ray set selection used is based on a method described in Forbes' paper [Forbes 1988]. For the PTV merit functions, the ray set is based on solutions to the Chebyshev polynomials [described in Numerical Recipes, Cambridge University Press (1989)]. GQ is much, much more accurate than any other known method, and requires fewer rays. There GQ provides us greater speed and greater accuracy at the same time. The GQ algorithm requires specification of the number of "Rings" and the number of "Arms". The only drawback to GQ is that the algorithm assumes the pupil is a circle, or more generally, an ellipse. For non-elliptical pupils, GQ does not work accurately. For example, if there are surface apertures in the optical system that vignette enough rays to alter the effective shape of the pupil significantly, GQ should not be used. One notable exception is when using circular pupils with modest central obscurations, such as a Newtonian telescope. Modest central obscurations do not usually affect the RMS significantly because the aberrations tend to be smaller in the central zone of the pupil. Note also that GQ works fine when used with vignetting factors, since the ray pattern is redistributed from a circle to an ellipse.

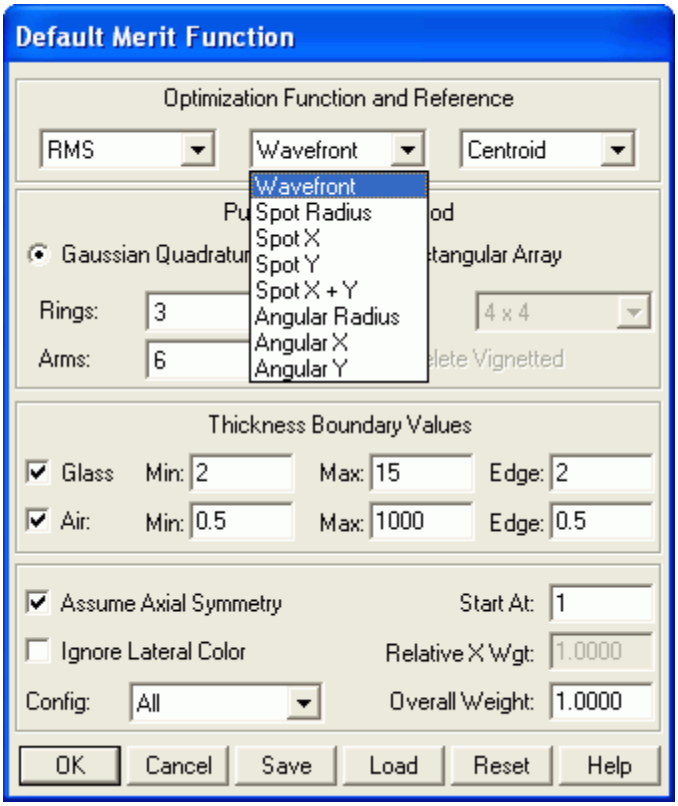

Figure 3.6 *Default merit function dialog box*

Table 3.4 *Zemax default Optimization types*

Name	Description
RMS	RMS is an abbreviation for Root-Mean-Square. This type is by far the most commonly used. The RMS is the square root of the average value of the squares of all the individual errors.
PTV	PTV is an abbreviation for Peak-To-Valley. There are rare cases where the RMS is not as important as the maximum extent of the aberrations. For example, if all the rays need to land within a circular region on a detector or fiber. In these cases, the PTV may be a better indicator of performance. This merit function type attempts to minimize the PTV extent of the errors.

Table 3.5 *Optimization data*

Name	Description
Wavefront	Wavefront is the aberration measured in waves.
Spot Radius	The radial extent of the transverse ray aberrations in image space.
Spot X	The x extent of the transverse ray aberrations in image space.
Spot Y	The y extent of the transverse ray aberrations in image space.
Spot X and Y	Both the x and y extent of the transverse ray aberrations in image space. The x and y components are considered separately, and both are optimized together. This is similar to Spot Radius, except the signs of the aberrations are retained, which yields better derivatives. Note that in computing the radius of an aberration, the sign information is lost.
Angular Radius	The radial extent of the angular aberrations in image space. Intended for afocal systems.
Angular X	The x extent of the angular ray aberrations in image space. Intended for afocal systems.
Angular Y	The y extent of the angular ray aberrations in image space. Intended for afocal systems.

Table 3.6 *Optimization reference point*

Name	Description
Centroid	The RMS or PTV computation of the data is referenced to the centroid of all the data coming from that field point. Centroid reference is generally preferred, especially for wavefront optimization. For wavefront optimization, reference to the centroid subtracts out the mean wavefront over the entire pupil, x-tilt, and y-tilt, none of which degrade image quality. Centroid reference also yields more meaningful results when coma is present, since coma shifts the image centroid away from the chief ray location.
Chief	The RMS or PTV computation of the data is referenced to the chief ray at the primary wavelength. For wavefront optimization, reference to the chief ray subtracts out the mean wavefront over the entire pupil, but not x-tilt or y-tilt. Note the exact point at which the OPD is defined to be zero is arbitrary; this is the reason the chief ray reference subtracts out the mean wavefront.
Unreferenced	This option is only available if the data is wavefront. If the wavefront is unreferenced, then the OPD data with respect to the chief ray is used without subtracting the mean wavefront or tilt.

The RA algorithm traces a grid of rays through the pupil. The "Grid" size determines the number of rays traced. The advantage to the RA algorithm is the ability to accurately account for the effects of vignetting in the merit function. This is useful in systems such as obscured telescopes and camera lenses which intentionally clip troublesome rays. The disadvantage to the RA algorithm is speed and accuracy. Usually, more rays are required to achieve a given degree of accuracy than the GQ algorithm.

To summarize the above discussion about GQ and RA, I use GQ for most optimization as long as the surface apertures are not clipped. However, once the apertures are clipped and appear not to be an ellipse shape, RA is required. When choosing RA, many more rays are required to achieve same level of accuracy than the GQ method.

Boundary constraints: Boundary constraints may be automatically generated and included in the default merit function by checking "on" the air and/or glass boundary values. If selected, then MNCG, MXCG, and MNEG operands will be added to the merit function to constrain the minimum center thickness, maximum center thickness, and minimum edge thickness for glass surfaces, respectively.

When I optimize the base eye model to construct a general ametropic eye model or general KC model, constraints for vitreous chamber depth and cylindrical axis were set. To set limit of VCD, MNCT (minimum center thickness) and MXCT (maximum center thickness) on the posterior lens surface were set to 13mm and 19mm, respectively. (These 2 values were obtained from VCD section in chapter 2.) When optimizing cylindrical axis, ZeMax can give some value like 365 degree, which does not make sense at all. So a constraint operand was set to limit the cylindrical axis between 0 to 180 degrees. Also, to prevent the optimization result from falling into a local peak or valley, I would make cylindrical axis scan the region of 0 to 180 degree in step of 5 or even smaller degrees

The default merit function is easy to set up, numerically efficient, and suitable for a large number of optimization problems. Actually, in all general ametropic eye modeling and general KC modeling, I used ZeMax default merit function with constrains about VCD and cylindrical axis. However, most optical designs require extensions or modifications to the default as the design progresses. ZEMAX offers significant flexibility in the definition of the merit function, as described in the following section. I will show how to use the operands provided by ZEMAX to refine the merit functions we need in for personalized eye modeling.

3.3.2 Defining Merit Functions for a Point Object in ZEMAX

In 2004, Thibos and co-workers select and define a total of 33 optical quality metrics and then evaluate their accuracy and precision for determining the refraction of human eyes [Thibos 2004]. The mathematic forms of the 33 optical quality metrics can be used as the merit functions to optimize eye models. According to the result of the accuracy and precision analysis of these metrics, I chose the Strehl ratio in space domain (SRX) as the best merit function for our early stages of eye modeling where the target is the subjective refraction. Here, I will show how to define SRX in ZEMAX and perform optimization.

To edit the merit function, first we should select Editors/Merit Function from the main menu bar. The insert and delete keys are used to add new operands or delete old ones on the list. The current merit function value and the value of each operand can be updated by selecting Tools/Update. Operands are set by typing the name in the first column and then filling in the remaining data fields. There are multiple fields that may be required to define an operand. The fields are called Int1 and Int2 for the two integer values and Data1 through Data6 for up to 6 double precision values. Not all of the operands use all of the fields provided.

Many of the operands use Data1 through Data4 for the normalized field and pupil coordinates values, Hx, Hy, Px, and Py. Note that ZEMAX does not check to see if the specified Hx, Hy, Px, and Py coordinates are within the unit circle. For example a pupil coordinate of (1, 1) is actually outside the entrance pupil, but no error message will be reported when tracing these rays unless the rays cannot physically be traced.

The target is the desired value of the specified parameter. The difference between the target and the value of the operand is squared, and summed over all operands to yield the merit function. The value of the target and the operand itself is unimportant in optimization; only the difference between the two is of concern. The larger the difference is, the greater the contribution to the merit function would be.

The weight is the relative importance of that parameter. The weight can be any number, positive or negative. However, the optimizer will act somewhat differently if the weight is negative, zero, or positive.

The merit function is defined as:

$$MF^2 = \frac{\sum W_i (V_i - T_i)^2}{\sum W_i},$$

where W is the absolute value of the weight of the operand, V is the current value, T is the target value, and the subscript i indicates the operand number (row number in the spreadsheet). The sum index "i" is normally over all operands in the merit function, however the merit function listing feature sums the user defined and default operands separately. The weight can be any number, positive or negative. However, the optimizer will act somewhat differently if the weight is negative, zero, or positive.

When the weight is negative, the operand will be treated as a Lagrangian multiplier. The Lagrangian multipliers force the optimization algorithm to find a solution which exactly meets the specified constraint, regardless of the effect on the other operands. This is sometimes useful to exactly meet an optimization target, such as focal length or magnification. In some respects, this is similar to a weight of "infinity", however it is implemented in a way that is numerically more stable.

When the weight is zero, the optimization algorithm calculates but ignores the operand. This is very useful for computing a result that does not have a specific target, but might be used elsewhere in the merit function; or if the value is used as a check or monitored parameter.

If the weight is greater than zero, then the operand will be treated as an "aberration" to be minimized along with the merit function.

The operand used to define SRX is “STRH” in ZEMAX. This operand computes the Strehl Ratio using the Huygen’s PSF computation. The parameters are:

Samp: The pupil sampling, where 1 yields 32 x 32 and 2 yields 64 x 64 etc. The sampling is assumed to be the same for both pupil and image.

Wave: The wavelength number to be used for optimization (use 0 for polychromatic).

Field: The field number to be used for optimization.

Pol?: Set to 0 to ignore polarization and 1 to consider it.

All Conf?: Set to 0 to use the current configuration (defined by the last CONF operand preceding this operand), and 1 to sum over all configurations.

I choose Huygen’s PSF instead of FFT PSF. That is because Huygens PSF is more general and accurate with fewer assumptions. The FFT PSF computes the intensity of the diffraction image formed by the optical system for a single point source in the field. The intensity is computed on an imaginary plane which is centered on and lies perpendicular to the incident chief ray at the reference wavelength. The reference wavelength is the primary wavelength for polychromatic computations or the wavelength being used for monochromatic calculations. Because the imaginary plane lies normal to the chief ray and not the image surface, the FFT PSF computes overly optimistic (a smaller PSF) results when the chief ray angle of incidence is not zero. This is often the case for systems with tilted image surfaces, wide angle systems, systems with aberrated exit pupils, or systems far from the telecentric condition. The other main assumption the FFT method makes is that the image surface lies in the far field of the optical beam. This means the computed PSF is only accurate if the image surface is fairly close to the geometric focus for all rays; or put another way, that the transverse ray aberrations are not too large. There is no hard and fast limit, however, if the transverse aberrations exceed a few hundred wavelengths, the computation is likely not accurate. Note that even systems with very little wavefront aberration can have large transverse ray

aberrations; one such example is a cylinder lens which only focuses rays along one direction. In this case, the transverse aberrations along the unfocused direction will be on the order of the beam diameter. The Huygens PSF method may provide more accurate results in these cases as well. For most lenses, a less important assumption is that scalar diffraction theory applies. The vectorial nature of the light is not accounted for. This is significant in systems that are very fast, around F/1.5 (in air) or faster. The scalar theory predicts overly optimistic (a smaller PSF) results when the F/# is very fast. For systems where the chief ray is nearly normal (less than perhaps 20 degrees), the exit pupil aberrations are negligible, and the transverse ray aberrations are reasonable, then the FFT PSF is accurate and generally much faster than the Huygens PSF method. When in doubt, both PSF methods should be employed for comparison. A solid understanding on the part of the user of these assumptions and the method of computation is essential to recognize cases where the accuracy may be compromised.

Now let us look at the detailed discussion about Huygens PSF. The purpose of using Huygens PSF is to compute the diffraction PSF using direct integration of Huygens wavelets method. The Strehl ratio is also computed. Table 3.7 shows the basic setting needed for calculating Huygens PSF.

To compute the Huygens PSF, a grid of rays is launched through the optical system, and each ray represents a particular amplitude and phase wavelet. The diffraction intensity at any point on the image surface is the complex sum of all these wavelets, squared. The PSF is computed this way for every point on the image grid.

The Image Delta value determines the point spacing of the image space grid. If a value of zero is specified, a default grid spacing is used. The default Image Delta is given by $\Delta = \frac{2\lambda F}{\sqrt{n}}$, where n is the number of points in the image space grid, is the longest wavelength used in the calculation, and F is the working *F/#*. The exact value of the image Delta size is not critical as long as the entire width of the PSF is included within the range of n * (Image Delta).

Unlike the FFT PSF, ZEMAX computes the Huygens PSF on an imaginary plane tangent to the image surface at the chief ray intercept. Note the imaginary plane is normal to the normal of the surface, not the chief ray. Therefore, the Huygens PSF accounts for any local tilt in the image surface caused by either the image surface slope, the chief ray incidence angle, or both.

The Huygens method accounts for the evolving shape of the diffraction image as the beam propagates along the image surface. This is an important effect if the image surface is tilted with respect to the incoming beam. Another advantage to the Huygens PSF method is that any grid size and spacing may be selected by the user. This allows direct comparison between PSF's from two different lenses, even if the F/#'s or wavelengths are different.

The only disadvantage of the Huygens PSF is speed. Direct integration is slow when compared to the FFT method. The computation time depends upon the pupil grid size squared times the image grid size squared, times the number of wavelengths. ZEMAX accounts for any symmetry the system has. The Huygens PSF automatically uses all available processors for maximum speed on multiple CPU computers.

Table 3.7 *Huygens PSF settings*

Item	Description
Pupil Sampling	Selects the size of the grid of rays to trace to perform the computation. Higher sampling densities yield more accurate results at the expense of longer computation times.
Image Sampling	The size of the grid of points on which to compute the diffraction image intensity. This number, combined with the image delta, determine the size of the area displayed.
Image Delta	The distance in micrometers between points in the image grid. Use zero for the default grid spacing.
Rotation	Rotation specifies how the surface plots are rotated; either 0, 90, 180, or 270 degrees.
Wavelength	The wavelength number to be used in the calculation.
Field	The field number for which the calculation should be performed.
Type	Select linear (intensity), or logarithmic (intensity). The logarithmic scaling can range from 1 to 5 decades. Also available are real amplitude, imaginary amplitude, and phase in degrees.
Configuration	Select "All" to perform a coherent sum of the PSF at each wavelength across all configurations, or select the "Current" or any single configuration. Note this is a coherent sum for the same wavelength in each configuration, followed by an incoherent sum of the resulting PSF's for different wavelengths. For this reason, each defined wavelength must be the same in all configurations. Wavelength and configuration weights may be used but the wavelength values must be identical. This coherent sum also assumes that the image surface is located in the identical position in all configurations. If "All" is selected, and both focal and afocal mode configurations are defined, the Configuration setting will automatically be reset to "Current".
Normalize	If checked, the peak intensity will be normalized to unity. Otherwise, the peak intensity is normalized to the peak of the unaberrated PSF (the Strehl ratio).
Show As	Choose surface plot, contour map, grey scale, or false color map as the display option. The True Color option creates an RGB color representation of the PSF by converting the wavelengths to the closest RGB equivalent and summing over all wavelengths. The accuracy of the True Color presentation is limited by the RGB method of rendering color on a computer display; and it is not possible to exactly represent monochromatic colors. The True Color option cannot be used if the Type is real, imaginary, or phase.
Use Polarization	If checked, polarization is considered.
Use Centroid	If checked, the plot will be centered on the geometric image centroid. If unchecked, the plot will be centered on the chief ray.

3.3.3 Defining Merit Functions for a Grating Object in ZEMAX

Grid: Operand(s): contrast

This section is a brief description of defining merit function for a grating object in ZEMAX. Although I didn't use this Operand in the eye modeling and simulations work in this dissertation, it is useful in our future work. In visual science, the concept is often used for contrast analysis. Using a grating object, in comparing the precision for predicting defocus and astigmatism, Thibos and co-workers found that 2 metrics were ranked on the top of 25 of accuracy and precision [Thibos 2004]. The two are SRMTF (Strehl ratio computed in frequency domain (MTF method)) and SROTF (Strehl ratio computed in frequency domain (OTF method)). From the straight-forward equations given in this paper, SRMTF and SROTF can be calculated and so assigned as merit functions. Because there is no predefined ZEMAX optimization operand of SRMTF or SROTF, we need to define our own operands. This can be done with the feature of user defined operand provided by ZEMAX. Using SRMTF as an example, I will show how to define the operand. From the equation of SRMTF, we require to calculate the integration of MTF about frequencies along 2 meridians. MTF is a predefined function in ZEMAX. So the key is to define the operand through a macro, which will perform the integration. After the macro is defined, we will call this macro and import the macro calculation result into the merit function. This task is done by the operand "ZPLM", which is used for optimizing numerical results computed in ZPL macros.

If the ZPL macro language is sufficient to perform the required computations, then the operand ZPLM may be used to call a ZPL macro from within the merit function. The macro performs the required computations, and returns the result using the ZPL OPTRETURN keyword. ZPLM is easy to use. The Mac# and Data values are used to specify the macro number and data field number, respectively. The macro number is used to indicate which ZPL macro should be executed, while the data field number indicates which value computed by the macro should be optimized. The macro number must be an integer between 0 and 99. If the Mac# value is 17, for example, then the macro to be executed must be named ZPL17.ZPL. The macro name must always use a two digit representation of the macro number. If the macro number was 6, then the macro to be executed would be ZPL06.ZPL. The ZPL macro file must reside in the default directory for ZPL macros. The data field number may be any number between 0 and 50, inclusive. This number refers to a position in a global array associated with the lens in memory. During execution of the macro, the macro keyword OPTRETURN specifies which data field number stores the results of the macro calculation. There are 51 different data fields, so that a single macro call can be used to optimize up to 51 different values simultaneously. For example, suppose you needed a macro which computed the total length of the lens from surface 1 to the image surface (this is in effect a user-defined version of the TOTR operand). The macro might look like this:

```
n = NSUR()
x = 0
FOR i = 1, n, 1
x = x + THIC(i)
NEXT
OPTRETURN 0, x
```

Note the use of the OPTRETURN keyword. This keyword stores the resulting value for "x" in the global array position 0. Suppose this macro was named ZPL15.ZPL. To optimize the resulting value for x, the ZPLM merit function operand would be added to the Merit Function Editor, with Mac# = 15 and Data = 0. After updating the merit function, the "value" would be the same as that returned by TOTR, and it can be optimized in the same way. ZPLM also permits the use of the data in the Merit Function Editor columns. These data fields can be read by the ZPL macro using the PVHX, PVHY, PVPX, and PVPY ZPL functions, respectively. "PV" is a mnemonic for "Pass Value". There is one very important thing to know about the data field number: If it is zero, then the macro is executed and the value from OPTRETURN 0 is returned. However, if the data field number is not zero, then the macro is not executed,

but any previous value stored from an earlier call to the macro is used instead. The advantage to this convention is substantial. If the macro computes many values, all of which need to be optimized, the macro only needs to be called once, yet multiple ZPLM operands can access the data. This is much more efficient than calling the macro multiple times.

For example, suppose a macro named ZPL11.ZPL computes three values, all of which require optimization.

In the macro, the values are stored using OPTRETURN:

OPTRETURN 0, x
OPTRETURN 1, y
OPTRETURN 2, z

Then three ZPLM operands in the merit function can extract the data and perform the optimization with a single call to the macro:

ZPLM 11 0
ZPLM 11 1
ZPLM 11 2

The macro ZPL11.ZPL is only called during the evaluation of the ZPLM 11 0 operand. Note the data columns can only be used if the Int2 value is zero, since only in this case is the macro evaluated.

The merit function is always evaluated using a temporary copy of the lens. After evaluation of the merit function, the copy of the lens, and any changes made to the lens, are discarded. For this reason, no changes should be made to the lens data from within the macro called by the ZPLM operand. These changes are not retained and may interfere with the computation of operands following the ZPLM operand in the same merit function evaluation. ZEMAX does not restore the lens being evaluated to the state it was in prior to the evaluation of the ZPLM specified macro. If however the macro is intentionally used to alter the lens data prior to evaluation of subsequent operands, two macros should be executed. The first should modify the data as required, and the second should restore the data to the original condition. Both macros can be listed in the merit function editor, with the intervening operands executing on the altered lens data.

ZPLM should not be used in the middle of a default merit function, but should instead be placed either prior to or after the portion of the merit function that ZEMAX defined by default.

3.3.4 Defining Merit Functions to Approach Clinical WFA Report in ZEMAX

When performing optimization for the personalized eye models to achieve the clinically measured wavefront, I must determine where to assign the free iteration variables. Since the cornea surfaces are defined by clinical topography of the patient, the lens parameters will be where I set the variables. One way of doing so is to assign the type of the anterior lens surface as "**Zernike standard sag"** in the ZEMAX lens data editor. The "Zernike Standard Sag" surface is defined by the same set of polynomial parameters as selecting the "Even Aspheric surface" (which supports planes, spheres, conics, and polynomial aspheres) plus additional aspheric terms that are defined by the Zernike Standard coefficients. The surface sag includes the standard aspherical surface (first term), polynomial surface (second term) and Zernike surface (third term) as: $z = \frac{cr^2}{1+\sqrt{1-(1+k)c^2r^2}} + \sum_{i=1}^{8} \alpha_i r^{2i} + \sum_{i=1}^{N} A_i Z_i(\rho,\varphi)$, where N is the number of Zernike coefficients in the series, A_i is the coefficient on the i^{th} Zernike Standard polynomial, r is the radial ray coordinate in lens units, ρ is the normalized radial ray coordinate, and φ is the angular ray coordinate. These ZEMAX input parameters are described in the 2 tables below. As the first table shows, the Zernike terms are allowed to be decentered from the conic and aspherical terms using parameters number 9 and 10. All the coefficients A_i must be entered in the same units as defined for the lens units, typically in millimeter or inch. The coefficients $\{\alpha_i\}$ have no unit. If the "Extrapolate" flag is set to 0, the

Zernike terms are ignored outside of the normalization radius. If the "Extrapolate" flag is set to 1, then the Zernike terms will be considered no matter where the ray lands on the surface; even if the ray lands beyond the normalization radius.

Note that the “Zernike Standard Sag” surface describes surface deformations, not wavefront error directly. **“Zernike Standard Phase”** surface is another option in ZEMAX. It may be more convenient to set Zernike coefficient data in terms of waves of optical path difference (OPD), as measured by an interferometer.

The "Number of terms" specifies the maximum Zernike polynomial term to be used in calculating the surface sag. This number is provided to speed the ray tracing calculation; terms beyond this number are ignored. Zernike polynomials are orthogonal over the unit circle, and so the normalization radius should be set to the radius over which the coefficient data was normalized. Zernike polynomials tend to diverge quite rapidly beyond the normalization radius, and so care should be taken that rays do not strike the surface beyond this radius. Although the ray tracing algorithm may work, the data may be inaccurate. The extrapolate flag may be set to zero to ignore the Zernike terms for rays that land outside the normalization radius.

Next, I should set the Zernike coefficients as free variables for iteration in optimization. The merit function will be defined by the operand “ZERN”, which will make sure the optimized result represent the exactly same wavefront from the measurement. The description of “ZERN” is as follows:

The parameters are:

Term: The Zernike term number (1 - 37 for fringe, 1 - 231 for standard or annular).

Wave: The wavelength number.

Samp: The pupil sampling, where 1 yields 32 x 32, 2 yields 64 x 64 etc.

Field: The field number.

Type: The Zernike type (0 for fringe, 1 for standard, 2 for annular).

Epsilon: The obscuration ratio (for annular coefficients only).

The **Term** value, if negative or zero, may also be used to return other data from the Zernike fitting as follows:

-8: Peak to Valley OPD (to centroid)
-7: Peak to Valley OPD (to chief)
-6: RMS to zero reference (unused by ZEMAX)
-5: RMS to chief ray
-4: RMS to centroid
-3: Variance
-2: Strehl Ratio
-1: RMS fit error
0: Maximum single point fit error

Note that if we use multiple ZERN operands which only differ in the **Term** value, they should be placed on adjacent lines in the editor so ZEMAX only does the fitting once; otherwise, the computation is slower. After the merit functions are set, optimization can be performed.

Table 3.8 *Parameter definitions for Zernike standard sag surfaces*

Parameter 0	Parameters 1-8	Parameter 9	Parameter 10
Extrapolate	α_1 - α_8	Zernike decenter X in lens units	Zernike decenter Y in lens units

Table 3.9 *Extra data definitions for Zernike standard sag surfaces*

Extra Data Number	Description
1	Number of terms.
2	Normalization radius. Coordinates are normalized by this value.
3 - 233	Coefficients on Zernike polynomials 1 - 231, respectively, in lens units.

Chapter 4 Population-Based and Personalized Eye Modeling

In Chapter 2, the ocular biometry measurement and statistics were reviewed. The general eye modeling and optical eye modeling tools of optimization were introduced and described in Chapter 3. In this chapter, more specific eye modeling will be considered. First, the population-based modeling of specified types of eyes including the ametropic eyes, the accommodative eyes, ageing eyes, and eyes that demonstrate degrees of specific disease will be discussed. Following this, customized eye modeling using clinical data is discussed in 4.2. The difficulties and possible solutions to achieve even more realistic eye modeling are addressed in section 4.3. In the last section, additional considerations of diseased eye modeling are given.

4.1 POPULATION-BASED EYE MODELING

In the past century, tens of eye models were published, ranging from simplistic representations of eyes that consist of a single refracting surface to complex models with thousands surfaces. Many models use gradient index crystalline lens, some with multiple shells, but most have a homogeneous lens. Regardless of these important details, most of these models are constructed with the average ocular biometry of young adults. This section discusses eye modeling in more specific populations.

4.1.1 Ametropic Eye Modeling

Ametropic eyes are eyes with sphero-cylindrical refractive errors and are discussed in Chapter 3. In my M.S. thesis [Tan 2005], I constructed 3 types of ametropic eye models according to the possible causes of the defocus: mismatches of the cornea curvature, the lens power, and the axial length. Based on the well accepted Navarro Eye Model [Navarro 1985], the axial type of ametropic eye model is constructed by varying only the posterior axial length (Model I). The pure refractive type of ametropic eye model depends only on the variable of corneal surface curvature (Model II). The pure index ametropic eye model varies only the virtual power of near pupil and lens position (Model III). Since then, I have changed the use of merit function slightly to obtain the ametropic eye models. The modeling procedures of the three ametropic eye models are summarized as the following:

Model I --- The only adjustable parameter in this modeling is the vitreous chamber thickness. This thickness value is optimized to approach the desired spherical refractive error. To do so, a virtual Gaussian thin lens is placed in front of the optical model eye. The power of the thin lens is set to be the compensation of the defocus. For example, a clinically near-sighted eye of -5.5 diopter is an over-powered eye of +5.5 diopter from emmetropia. The compensation virtual lens is, therefore, -5.5 diopter. Before the optimization, in the lens editor in ZEMAX, the vitreous body thickness is set to be the only variable in the base Navarro model. In my M.S. thesis, I used the default RMS WFA as the merit function to optimize VCD alone. Based on my previous investigation and comparison of the results, I now use the maximization of the Strehl Ratio as the merit function for a finely-tuned optimization following the first optimization. As discussed in Chapter 3, the minimal difference between SRX and the diffraction limited case of "1" will be approached in the iteration. The same merit function is used for the optimizations in constructing models B and C. All the iterations are run under paraxial eye condition (i.e. small pupil diameter) because the Navarro model eye is emmetropic only under the paraxial condition. With a larger pupil diameter and the resulting aberrations, the refractive error of the Navarro model eye will not be zero. For example, in a 3-mm-pupil Navarro eye, a small refractive error of -0.18 diopter (slightly near-sighted) is present. Therefore, in my eye modeling that uses the Navarro model as the emmetropic standard, the refractive result of final model is always determined under the paraxial assumption.

Model II --- The vertex curvature radius of anterior cornea surface is set to be the only variable to provide the result refractive error. Curvature contributions in the posterior cornea and the two lens surfaces were omitted because they provide very small refractive influence compared to the front cornea surface. For example, the influence of the posterior cornea surface is only about 10% of the anterior surface. According to the ocular biometry studies in Chapter 2, the lens parameters have very little to do with refractive error. Therefore, with the single variable of curvature of the first surface of the Navarro eye, the refractive ametropic eye is obtained by similar optimization process as it is done in model A.
Model III --- The single adjustable parameter in this model is an extra virtual thin lens that is specified with a uniform power at the location of pupil. Similar to the process in Model A, the power of virtual thin lens is varied to approach the desired conjugate point of the retina and to obtain the corresponding ametropic condition.

One thing to be noted in this ametropic eye modeling is the role played by the conic constants in these models. The conic surface is the standard surface type in ZEMAX and is also the most commonly used surface type in today's eye modeling community to produce the adequate asphericity of human eye elements. Unless additional parameters or the user-defined surface(s) are introduced in the modeling, the conic constants and the radius on surfaces of cornea and lens are the parameters that determine the final high-order aberrations of these models. Although the conic constants will not change the results of refractive error in paraxial region, they affect the resulting spherical aberration significantly. From the discussion in Chapter 2, the conic constant of the anterior cornea varies significantly from one person to another, and the reported values are also very different between studies. Even when examining a single eye, the Q number is rarely the same in the temporal, nasal, upper and lower quarters of the eyes. From the spherical aberration measurements among populations, the corresponding Q value tends to be near -1.0 for infants and toddlers and tends to increase toward zero with age. It has been shown in my M.S. thesis [Tan 2005] that the deviation of the cornea surface from Q = 0 to Q = -1.0 is observable only near the periphery of cornea. Surprisingly, this 'small' deviation results in a significant difference in the spherical aberration of the eye up to several diopters in the periphery vision in a darkened environment. The conic constant, Q, in the anterior cornea surface of Navarro model is -0.26 for adult. The validation of this model as described in the paper makes sure that the final model provides the result spherical aberration that is equivalent to the clinically measured values in Navarro's study. In my ametropic eye models A, B, and C, the final spherical aberrations were not examined or validated since the statistical data in Chapter 2 do not provide evidence of aberrations on the refraction dependence.

In 2006, Atchison published the optical models for myopic eyes [Atchison 2006] according to the analysis of statistical relevance obtained from the subjects and studies majorly of his research group. Table 4.1 compares the refraction dependence of Atchison's myopic eye model, the conclusion I obtained from the review in Chapter 2, and the emmetropic eye model of Navarro's [Isabel Escudero-Sanz 1999] (N). Not included in the table is the information regarding the decenters of the pupil and the lens, the tilt of the lens, and the fovea location that are used in the models. These parameters concerning ocular asymmetry introduce astigmatism, coma, and irregular aberrations, and therefore have important effect upon optical performance. The significance of using these parameters depends on the types of applications.

After putting together an eye model, validations to optical performance of various types of aberrations are the next step to ensure that the model preserves the integrity of required characteristics. Because many parameters, especially the conic constants, are not confidently assigned, they can be set as variables within a given reasonable ranges for iteration to approach the target aberrations.

Table 4.1 *Comparison of ocular parameters in Atchison myopic eye model, the statistical finding in Chapter 2, and the emmetropic Navarro model.*

Ocular parameter	Model	Emmetropic condition (K=0)	Refractive error,(K) dependence
Anterior Corneal Radius of Curvature (CR_1):	Atchison	7.77 mm	+0.022 mm/diopter
	Tan	7.75 mm	+0.016 mm/diopter
	Navarro	7.72 mm	X
Asphericity of anterior cornea surface (Q_1):	Atchison	-0.15	Not significant
	Tan	-0.2654	-0.0145 /diopter
	Navarro	-0.26	X
Central corneal thickness (CCT):	Atchison	0.55 mm	Not significant
	Tan	0.536 mm	Not significant
	Navarro	0.55 mm	
Index of refraction of cornea, n_1	Atchison	use Navarro's	
	Tan	use Navarro's	
	Navarro	1.3975,1.3807,1.37405,1.3668, for □ = 365,486.1,656.3,1014nm	
Posterior Corneal Radius (CR_2):	Atchison	6.40 mm	Not significant
	Tan	6.50 mm	+0.013 mm/diopter
	Navarro	6.50 mm	X
Asphericity of posterior cornea surface (Q_2):	Atchison	-0.275	Not significant
	Tan	-0.4	Not enough info
	Navarro	0	X
Anterior chamber depth (ACD)	Atchison	3.15 mm	Not significant
	Tan	Adopt Navarro's	Not significant
	Navarro	3.05 mm	X
Index of refraction of aqueous humor: n_2	Atchison	use Navarro's	
	Tan	use Navarro's	
	Navarro	1.3593,1.3422,1.3354,1.3278, for□ = 365, 486.1,656.3,1014nm.	
Anterior lens radius (LR_1):	Atchison	11.48 mm	Not significant
	Tan	10.50 mm	Not significant
	Navarro	10.20 mm	X
Anterior lens asphericity (Q_3):	Atchison	-5	Not significant
	Tan	use Navarro's	No info
	Navarro	-3.1316	X
Lens thickness (LT):	Atchison	3.6 mm	Not significant
	Tan	Adopt Navarro's	Not significant
	Navarro	4.0 mm	X
Refractive index of crystalline lens: n_3	Atchison	Gradient index	
	Tan	use Navarro's	
	Navarro	1.4492,1.4263,1.4175,1.4097, for □ = 365,486.1,656.3, 1014nm	

Table 4.1, cont.

Posterior lens radius (LR_2)	Atchison	-5.9 mm	Not significant
	Tan	use Navarro's	Not significant
	Navarro	-6.0 mm	X
Posterior lens asphericity (Q_4):	Atchison	-2	Omit; Not significant
	Tan	use Navarro's	Not significant
	Navarro	-1	X
Vitreous chamber depth (VCD):	Atchison	16.28 mm	-0.299 mm / diopter
	Tan	16.15 mm	-0.36 mm/ diopter
	Navarro	16.32 mm	X
Refractive index of vitreous humor (n_4):	Atchison	use Navarro's	
	Tan	use Navarro's	
	Navarro	1.3565,1.3407,1.3341,1.3273, for □ =365,486.1, 656.3,1014nm.	
Radius of retina curvature (RR):	Atchison	Use Navarro's	X
	Tan	use Navarro's	X
	Navarro	-12 mm	X

4.1.2 Accommodative Eye Modeling

Most schematic eyes are emmetropic, relaxed, adult eyes. Under accommodation demand for close vision, the ciliary muscles holding the crystalline lens tighten, thereby causing the lens to become more rounded. The thickness and curvatures on both surfaces of lens increase. As described in Chapter 2, the lens biometry is fundamentally independent of refractive error. However, other than accommodation dependence, they are also significantly related to age. With increase in age in adulthood, the lens becomes thicker, more curved in its relaxed state, and its refractive index distribution changes. Therefore, the modeling of accommodative eye should be under some assumption of a more confined age range.

In the history of eye modeling, a few accommodative models exist. Gullstrand No. 1 [Gullstrand 1909] is constructed at about 10.9 diopter accommodation. Gullstrand-Emsley [Emsley 1952] and Le Grand [Le Grand 1980] full schematic eyes are in accommodated forms of 8.6 and 7.1 diopters respectively. The Navarro model eye is "adaptive" in the sense of its variability of lens parameters (the thickness and both radius of curvatures and conic constants on both surfaces) and the anterior chamber and vitreous depths. In this popular eye model, these ocular parameters are given as functions of accommodation level. The four accommodative eye models are summarized in tables in the appendix A3 of Atchison and Smith book in 2000 [Atchison 2000].

4.1.3 Modeling with Ocular Growing & Aging Consideration

Age is another important factor of ocular biometry. The ocular dimension increases significantly during the first year of life. At the same time, the ocular refraction develops from mild hyperopia to emmetropia. From one year old to adulthood, ocular dimensions continue to grow with a much reduced rate and with time become constant. After adulthood, the dimension of eye ball and the outer shape remain invariable. Regarding the lens development, infants have steeper anterior lens surface. With growth, it becomes flatter until maturation. While aging, the anterior lens surface will become steeper again. Similarly to the change of anterior lens radius when people are aging, the posterior lens surface becomes steeper and steeper. The thickness of lens continues to increase with a varying rate through life. Infants have shorter VCD. As the growth, VCD increases and then decreases in older age.

Although many studies have investigated the correlation between the ocular biometric parameters and age as reviewed in Chapter 2, to my knowledge, no age-dependent eye model has been published. In Chapter 2, I have given an inclusive statistical study of age effect in ocular biometry. Basically, we can separate the data into three age groups: infants, from new born to about 12 month-old, children, from about 1 year-old to about 16 year-old, and adults, from about 16 years-old to older age. Here, I will summarize the age-dependent parameters for potential modeling work. Similar to the accommodative and the ametropic eye modeling, validation of the models are required via optical optimization and proper selections of free variables necessary to achieve the targeted ocular optics.

Infants (0~1 year-old):

***CR_1*:** Infants' CR_1 grows rapidly at a rate ~0.1mm per week and approaches to nearly adult altitude at 1 year of age. And the result also indicates a growth rate of ~0.03mm per year during the age in primary school. To the older adults after 18, no convincing aging effect was found.

***ACD*:**Compared with other age groups (between 3 to 4mm), infants obviously have shorter *ACD*. Immature eyes of infants have shorter ACD and grow quickly in the first year. The mixed-model linear regression equation of the first year life of the infants is: $ACD=2.619+0.018*Week$ r^2=0.78. [Pennie 2001].

LR_1: Infants obviously have smaller LR_1 than adults. Mutti [Mutti 2005] gave infants' LR_1 at 7.21±0.60mm and 8.97±0.75mm for 3-month and 9-month visits, respectively.

LR_2: Infants obviously have smaller LR_2 than adults. Mutti [Mutti 2005] gave infants' LR_2 at 4.68±0.31mm and 5.21±0.36mm for 3-month and 9-month visits, respectively.

LT: Lens thickness of infants appears to be within the range between 3.5mm and 4mm [Cook 2003, Mutti 2005, Pennie 2001, and Ziylan 2006].

Children (1~16 year-old):

ACD: Children subjects show comparable *ACD* with adults [Davis 2005, Gao 2002, Jones 2005, and Gwiazda 2002]. *ACD* is decreasing. Jones [Jones 2005] gave age dependence: *ACD=1.817-0.265*ln(age)2+1.441*ln(age)* (persistent emmetropia); *ACD=2.773-0.062*ln(age)2+0.447*ln(age)*, p=0.0048 (Persistent hyperopia); *ACD=1.425-0.311*ln(age)2+1.749*ln(age)*, p<0.0001 (myopia); *ACD=1.381-0.349*ln(age)2+1.787*ln(age)*, p=0.1054 (Emmetropizing hyperopia) [Jones 2005].

LT: Jones (2005) gave age dependence: Age≤9.5yr, *LT=3.799-0.041*Age*, Age>9.5yr, *LT=3.352+0.006*Age* (persistent emmetropia); Age≤9.5yr, *LT= 3.746-0.026*Age*, Age>9.5yr, *LT=3.428+0.007*Age*, p=0.0954 (Persistent hyperopia); Age≤9.5yr, *LT= 3.841-0.046*Age*, Age>9.5yr, *LT=3.389+0.002*Age*, p=0.1827 (Myopia); Age≤9.5yr, *LT= 3.778-0.036*Age*, Age>9.5yr, *LT=3.363+0.007*Age*, p=0.5221 (Emmetropizing hyperopia) [Jones 2005].

VCD: Jones (2005) gave age dependence: Age≤10yr, *VCD=13.154+1.211*ln(Age)*, Age>10yr, *VCD=14.754+0.513*ln(Age)* (persistent emmetropia); Age≤10yr, *VCD=12.860+1.014*ln(Age)*, Age>10yr, *VCD=13.437+0.762*ln(Age)*, p=0.0743 (Persistent hyperopia); Age≤10yr, *VCD=11.297+2.228*ln(Age)*, Age>10yr, *VCD=10.907+2.416*ln(Age)*, p<0.0001 (Myopia); Age≤10yr, *VCD=12.708+1.308*ln(Age)*, Age>10yr, *VCD=14.339+0.606*ln(Age)*, p=0.3867 (Emmetropizing hyperopia) [Jones 2005].

Adults (>16 year-old):

Q_1: Atchison [Atchison 2008] reported that anterior corneal asphericity depended on age as described by the equation Q_1*=-0.0036+0.0038*Age* (adjusted r^2=0.030, n=97, p=0.045) based on Pentacam measurement results. However, no significant age dependence was found in cornea topography measurement. Dubbelman [Dubbelman 2006 and 2002] reported that anterior corneal asphericity depended on age as described by the equations Q_1*=-0.24+0.003*Age* (n=114) and Q_1*=-0.2+0.0003*Age*, r=0.02, p=0.85 (n=83) in 2006 and 2002, respectively. So we can conclude that there is no significant and strong correlation between Q_1 and age.

ACD: Although ACD does not change significantly for young adult, it does with aging. There are significant age trends observed with ultrasonography and the Pentacam instruments: ultrasonography *ACD=3.857-0.0106*age* (adjusted r^2 = 0.196, n = 102, p<0.001); Pentacam *ACD=3.909-0.0105*age* (adjusted r^2 = 0.219, n = 97, p<0.001). [Atchison 2008]

LR_1: Atchison gave age dependence LR_1*=12.283-0.0438*Age* (adjusted r^2=0.192, n=66, p<0.001) [Atchison 2008]. Dubbelman gave LR_1*=-0.057(±0.009)*Age+12.9(±0.4)*, r=-0.54, P<0.0001, n=102 [Dubbelman 2001]. Koretz gave LR_1*=11.155-0.02004*Age*, n=100 [Koretz 2001]. Mutti gave LR_1*=11.45+0.151*(Age-10)-0.021*(Age-10)*^{2}, n=994 [Mutti 1998]. Brown gave that LR_1*=12.4±2.6mm*, LR_1*=-0.104*Age+16.815*, n=100 [Brown 1974].

n_3: Jones [Jones 2005] gave age dependence: crystalline lens index, n_3*:=0.162*Age*$^{-2}$*+1.427* (persistent emmetropia); n_3*=0.222*Age*$^{-2}$*+1.429*, p=0.4645 (Persistent hyperopia); n_3*:=0.079*Age*$^{-2}$*+1.428*, p=0.2563 (myopia); n_3*:=0.121*Age*$^{-2}$*+1.429*, p=0.6064 (Emmetropizing hyperopia). Lens equivalent refractive index was found with Purkinje imagery and the 4-surface eye model to be a function of age. There is a significant trend: *CLI=1.4506-0.00035*age* (adjusted r^2 = 0.21, n = 102, p<0.001). [Atchison 2008] In summary, the refractive index of crystalline lens decreased slowly when aging, though not significantly.

LR_2: Atchison gave the age dependence LR_2*=7.1857-0.0076*age* (adjusted r^2=0.0012, n=66, p=0.30) [Atchison 2008]. Dubbelman gave LR_2*=-0.017(±0.008)*Age+6.5(±0.3)*, r=-0.34, p=0.03, n=102 [Dubbelman 2001]. Koretz gave LR_2*=8.267-0.02025*Age*, n=100 [Koretz 2001]. Mutti gave LR_2*=6.236+0.063*(Age-10)+0.004*(Age-10)*^{2}, n=994 [Mutti 1998]. Brown gave that LR_2*=8.1±1.6mm*, LR_2*=-0.015*Age+8.719*, n=100 [Brown 1974].

LT: The anterior segment is the front third of the eye that includes the structures in front of the vitreous humour: the cornea, iris, ciliary body, and lens. A significant correlation found between anterior segment depth and age (*ASD=0.0237*Age+6.653*, r^2=0.164) and reflects the possibility that thickening of crystalline lens following aging because ACD decreases with aging. This result is similar to that of Alsbirk (1977) [Goh 1994]. Alsbirk gave the age difference at 20 and 70 year-old groups: 20yr: *LT(K=-0.28D)=3.85mm*; 70yr: *LT(K=+0.90D)=4.90mm* (female) and 20yr: *LT(K=-0.01D)=3.76mm*; 70yr: *LT(K=-0.18D)=4.93mm* (male) [Alsbirk 1977]. The slope of the linear regression equation for the first year life of the infants is *LT=3.684−0.002*Week* [Pennie 2001]. There is a significant trend found with ultrasonography: *LT=3.1267+0.02351*Age* (adjusted r^2 = 0.63, n = 102, p<0.001) [Atchison 2008]. The subjects in Shufelt, Wickremasinghe, and Wong's reports were older than 40 years old and they showed a increasing LT with aging. [Shufelt 2005, Wickremasinghe 2004, and Wong 2001]. *LT* is found to increase with aging. This was quantitatively expressed as *LT= 0.013 *Age+3.46mm* by Koretz and coworker [Koretz 1989].

VCD: Garner reported that VCD increasing with the rate 0.072mm/yr and 0.165mm/yr for emmetropic and hyperopic group (>-0.5D) and myopic group (<=-0.5D), respectively (Garner 2004). The regression fit with ultrasonography has a non-significant slope: *VCD=15.99-0.0016*Age* (adjusted r^2 = 0.00, p = 0.70) [Atchison 2008]. Lam gave *VCD=a*Age+b*, for >40 year-old subjects. [Lam 1994]

4.1.4 General Keratoconus Models

KC is a degenerative non-inflammatory disorder of the eye for which structural changes occur within the cornea that result in thinning of the cornea and change to a more conical shape than its normal gradual curve. KC can cause substantial distortion of vision, with multiple images, streaking and sensitivity to light all often reported by the patients. KC is the most common dystrophy of the cornea and affects around one person in a thousand. It seems to occur in populations throughout the world, although some ethnic groups experience a greater prevalence than others. It is typically diagnosed in the patient's adolescent years and presents as a more severe state in the twenties and thirties. KC is a little-understood disease with an uncertain cause, and its progression following diagnosis is unpredictable. If both eyes are affected, the deterioration in vision can affect the patient's ability to drive a car or read normal print. In most cases, special corrective lenses are effective enough to allow the patient to continue to drive legally and likewise function more normally. Further progression of the disease may require surgery including transplantation of the cornea. However, despite its uncertainties, KC can be successfully managed with a variety of clinical and surgical techniques to lessen significantly the impairment to the patient's quality of life.

One purpose of KC modeling is to study and understand the influence of the properties of the KC cone(s) on the optical performance of human eyes. With the general KC eye models, the effects and visual impacts of different parameters of KC cone, such as the cone location, volume, and shape, were investigated. The research results of this subject have been published in the online journal, Journal of Vision in 2008 [Tan 2008]. In the general KC eye modeling in this paper, the anterior cornea surface is assumed to be the only affected ocular element. The diseased condition of cornea is engineered on the Navarro healthy adult model. Although the thickness of cornea and the posterior surface are also influenced by this disease, they are ignored in the pioneer modeling because of the relatively weak optical impact owing to the smaller refractive index difference on the interface. The optical influence of irregular posterior surface was estimated 10–20% of the anterior influence due to the smaller refractive index difference.

The corneal topography of patients can be measured clinically as described in Chapter 2. The elevation maps of anterior corneal surface can be exported from the ophthalmic devices and used for mathematical analysis. This is described in Appendix B for one of the most common topography device, the Humphrey. The similar method was used by Schwiegerling et al. to examine the resulting KC cone from the topographical map [Schwiegerling 1995]. The height maps from 56 KC eyes were decomposed into Zernike polynomials. Then the parabolic ($C_2^0 Z_2^0$) and the cylindrical ($C_2^{+2} Z_2^{+2}$ and $C_2^{-2} Z_2^{-2}$) components were eliminated to yield a residual height map [Schwiegerling 1997, and Schwiegerling 1995]. Corneas with normal refractive errors appear to have relatively flat residual maps. In contrast, a KC cornea's residual map reveals more significant high-order Zernike terms, which represent the irregular surface of the KC cone. After the cones' surfaces were obtained, they were fitted to two-dimensional Gaussian surfaces to define the sizes and positions of the assumed right elliptical cones. This allows an accurate optical KC cornea model to be constructed based on the 5 cone parameters, (x_o, y_o, σ_x, σ_y, h_o), from the Gaussian expression, $f(x,y) = h_0 \exp -\{\frac{(x-x_0)^2}{2\sigma_x^2} + \frac{(y-y_0)^2}{2\sigma_y^2}\}$, where h_o is the peak height of the cone, (x_o, y_o) is the cone's center location with respect to the visual axis, and (σ_x, σ_y) are the corresponding dimensions where the height drops to $e^{1/2}$ of the cone's peak height. The full width at half

maximum of a Gaussian function is equal to 2.35σ. The 56 clinically diagnosed KC corneas' residual height maps were processed and each parameter's statistical distribution was reported [Schwiegerling 1997].

The 5-parameter elliptical Gaussian elevation is a simple assumption on KC cone structure. Although many KC cones have more complex shapes, the Gaussian surface fits well to a very good portion of KC cases. The more particular and complex cones that are not well modeled in this general KC cone modeling include significant asymmetric cones and cones with multiple peaks. These complex shapes can be mathematically modeled by adopting more shape parameters. Here we use the least number of parameters to enable the study on the comprehension of the optical influences of (a) cone location that requires at least 2 variables, (x_o, y_o), (b) cone shape that needs no less than 2 variables, (σ_x, σ_y), and (c) cone dimension that requires at least one additional variable, (h_o).

To corroborate the KC statistics of Schwiegerling's 56 eyes, 15 additional KC topography maps from the Wang Vision Institute at Nashville, TN, were examined. These 15 KC cases include two cases with steepest corneal curvature less than 45 diopter, nine cases between 45 and 52 diopter, and four greater than 52 diopter. The statistical distributions of the five cone parameters from measurement and reported data were then adopted to model various KC cone dimensions and locations.

Four degrees of KC cones (mild, moderate, advanced, and severe) are created based on the statistical distribution of measured cone volumes. The volume enclosed by the two-dimensional Gaussian surface is given by $V = 2\pi h_0 \sigma_x \sigma_y$. The shape-correlated eccentricity e of the cross-sectional ellipse of semi-major and minor axis, a and b, respectively, is $e = \sqrt{1 - \frac{b^2}{a^2}}$. The eccentricity always lies between $0 \leq e \leq 1$. An eccentricy e=0 corresponds to a circular cone, and as e increases the cone becomes more elliptical. The synthetic anterior KC corneal surface is generated by superimposing the Gaussian surface onto a normal corneal surface of the emmetropic eye model [Escudero-Sanz 1999]. The importing of user-defined surface to ZEMAX is described in Appendix B.

Subsequent to the construction of the general KC models, three-dimensional ray tracing on KC eye models was performed to determine the resulting optical imaging quality. The spherical equivalent (SE), cylinder, together with residual high-order ocular aberrations, are examined and related to each separated variable.

Determination of the subsequent refractive error is achieved using optimization in ZEMAX. Similarly to the step in general ametropic eye model construction, a Gaussian thin lens with three variables, spherical equivalent, cylindrical power, and astigmatic axis, is placed in front of the optical model eye. These three values are set to be the iteration variables in the ray-tracing program to achieve optimized optical performance. It is noted that the wavefront aberration maps of KC patients are very irregular and that the high-order Zernike coefficients, including the $m \neq 0$ terms, are pronounced. Because of this, the simplified Zernike derivation methods ("Paraxial curvature matching" discussed in Chapter 3) [Atchison 2004, and Dorsch 1998] that use only the ρ^2- Zernike terms do not provide adequate results for KC cases. We find that the optimization method provides stable, converged results that are significantly different from the Zernike-derived prediction. The iteration is carefully examined over the 180-deg meridians to prevent convergence of local minimum. In addition to the sphero-cylindrical prescription, the residual RMS wavefront aberration provides the measure of the high-order ocular aberration that causes the higher level of difficulty for the KC patient.

In the study and the published paper, the cone shape, protruding height and extent, and distance from the visual zone are independently investigated for how they influence the patient vision. This study demonstrates a novel and contemporary research application using the general population-based eye modeling technique.

4.2 CUSTOMIZED EYE MODELING

In the recent years, high precision ophthalmic patient data have become available to characterize accurately both anterior and posterior surfaces of the cornea, ocular wavefront aberrations, and ocular element biometry. These measurements can be incorporated into the construction of an optically functional and analytical, personal-tailored, eye model. In contrast to the general eye modeling in section 4.1, this section describes the construction of personalized eye models, which are based on the clinical measurement of individual human eye. The computer-based technical implementation of the optical components is described as well as the methods for calculations and optimizations in ZEMAX. In 2004, Navarro published the first construction of 19 personalized eye models of healthy eyes with the optical design software, CodeV [Navarro 2004]. I used very similar methods and procedures. The basic concept of personalized eye modeling is demonstrated in Figure 4.1. The personalized patient data may include all or, in most cases, some of the modeling parameters, which include refractive index and ocular geometric data, and some info that evaluate the optical performance such as the total wavefront aberration, the refractive error measurement and the visual acuity. It is almost guaranteed that a generic eye model is needed as the base model, which provides a draft functioning model with complete set of mean optical parameters. For an adult eye, I generally use the emmetropic Navarro model of 1985. Navarro model has a constant refractive index lens and is used here in the un-accommodated state. It was based on the Gullstrand-LeGrand model with a constant effective refractive index for the lens but incorporating experimental average asphericities (conic constants) of the refractive surfaces. The radius of the anterior surface of the cornea was updated using published data of the mean shape of the cornea. In addition, the dispersions of the refractive indexes were adjusted to fit the longitudinal chromatic aberration. This model varies continuously with accommodation and reproduced remarkably well the overall average optical performance (aberrations, polychromatic MTF and PSF) of the eye both on-axis and off-axis. Its total refractive power is +60.4 D.

As shown in the figure, the first step of modeling is the substitution of the optical and geometric parameters with the clinically measured data. If we have the geographic information of the patient, many ocular parameters can be modified according to the patient's age, gender, and geographic characteristics, as described in Chapter 2. Like most research groups that perform eye modeling, I generally assume that the refractive indices are constants among individuals and are equal to those of the generic model used. However, with the published research results of the age dependence of refractive indices in Chapter 2, it is feasible to adapt age-corrected refractive indices as well as many other age dependent parameters. The clinically obtained geometric data of the patient's eye will remain invariable parameters throughout the modeling process. One potentially important aspect is the dependence of the result on the initial generic model used, because the final personalized model will necessarily depend on those parameters of the initial model that are not changed (iterated) during the optimization process.

The replacement of the thicknesses of ocular elements obtained from the ultrasound biometry is straight forward. The corneal topography substitution requires some description. The corneal topographic data exported from the clinical instrument requires mathematic process of interpolation and extrapolation to obtain a sufficient area, namely a 10 mm diameter, of anterior corneal map. The corneal map obtained in the clinic often contains missing data points due to the interference of eye lids and eye lashes. C^{++} is used to create a ZEMAX-readable grid sag from this corneal map. The C^{++} code is included in the Appendix D. Before the insertion of the user-defined surface, the grid sag surface should be selected in the anterior corneal surface in the lens-data-editor of the draft model. The importing of user-defined topographic surface to the ZEMAX file is described in Appendix B.

After the step 1, an initial personalized eye model is formed. The 2nd step is the validation of this model through the optical optimization to approach the expected optical performance of the patient vision. As mentioned in last chapter, the most commonly acquired clinical eye data that indicates the vision quality is the refractive errors and the visual acuity (*VA*). As discussed in section 3.2.3, *VA* clinical

measurement gives a minimum requirement for the focus size of retinal blur (i.e. the size of the point spread function (PSF)). Refractive error is the 2^{nd}-order aberration that corresponds to the 3 variables related to sphero-cylindrical refraction prescription (detailed in section 3.2.2). In the recent years, wavefront aberration map (WA), the so-called fingerprint of the eye, is available. WA provides not only the 2^{nd}-order aberration, it also provides high-order aberration information up to 6^{th} or 7^{th}-order. In this optimization process, these clinical vision assessments are the targeted merit functions. Variables will be assigned in the initial personalized model for iteration to obtain the optical quality target values given by the merit function. If the WA map is obtained from the patient eye, it would be assigned as the merit function in the final optimization.

Optimization for refractive error: When a refractive error condition is on demand, the optimization will be tailored to reach the exact prescription. An ideal Gaussian thin lens with three parameters, the spherical equivalent power, the cylindrical power, and the astigmatic axis, which represent the refractive error correction, is inserted in front of the cornea surface of the optical eye model. With such a correction in place, we expect that the typical optical optimization such as the use of default merit function in ZEMAX will bring the final system to the optimized image quality, which means that the point source at infinity will be focused right on the retinal surface. Because we demand three numbers, three free variables should be assigned before the optimization. Typically, I perform this task in two separate optimizations. Because the ocular axis length is found universally to depend on the spherical refractive error (the spherical equivalence, SE) and the dependence is very strong, I perform the first optimization by assigning only one variable on the axial length, or more specifically, the vitreous chamber depth (VCD). The merit function is the demand for exact spherical equivalence. In the second optimization, the cylindrical power will be achieved by adding a virtual Gaussian thin lens with three free variables, spherical equivalent, cylindrical power, and astigmatic axis, powers along in front of anterior lens surface. Lens and cornea are the two possible sources of cylindrical error. I place this thin lens on the crystalline lens because the cornea biometry is clinically determined and, therefore, is invariable. Axial length remains constant during this stage of optimization. After the iteration, the three variables are optimized to minimize the merit function.

One important factor that deserves much attention in the refractive error determination is the pupil diameter. With the presence of aberration, the refractive error varies with the pupil size. A typical example is the existence of (positive and negative) spherical aberration that induces (myopic and hyperopic) refractive error in the periphery. As the pupil size increases (such as in the night time), the eye tends to be more myopic (or hyperopic) in average over the visual zone. For this reason, when I perform the optimization for refractive error, I need to determine a reasonable pupil size that is about the condition for typical reading situation. I normally use a 3-mm pupil aperture. When the pupil diameter is set as 3.0 mm, the entrance pupil will be approximately 3.33 mm due to the magnification from the anterior chamber and cornea. In clinical language, the pupil size is the "pupil appearance", which is actually the entrance pupil in the optical system, not the physical aperture size. After the 2-step optimization, the virtual correction lens in front of the cornea should be removed to achieve the personalized eye model.

Optimization for wavefront aberration: If the wavefront data are available, the second optimization for cylindrical refractive error is not required. At the beginning of the optimization, the type of the anterior lens surface should be selected to the "Zernike standard sag", and the Zernike coefficients will be assigned as free variables for iteration. In this step, the merit function will be changed from SRX to Zernike coefficients. The optimization target is to approach the measured WF aberration, which is reported in Zernike polynomial format. The merit function will require the optimization operand "ZERN", which has been addressed in Chapter 3. The parameters will be set as Term=1, 2..in the order of Zernike coefficients in ZEMAX, Wave=1 (only one wavelength used in each of our calculations), Samp=2 (pupil sampling=64*64), field=1 (only one field set in our calculations), and Type=1 (Zernike standard coefficient), and Zernike coefficients of the clinical WFA will be input at the column of the

"target" values and the weight of each coefficient will be set equally. Figure 4.2 shows the comparison of the measured WF and the final WF after optimization in one of my test run. The result demonstrates a successfully conducted personalized eye model, which has the exactly same anterior cornea map as well as the WF aberration as the individual subject.

Tolerance analysis: The above proposed method bears intrinsic uncertainties in the sense that the whole lens geometry is unknown initially. The geometry is then adjusted to fit the observed (measured) optical performance with the sole constraint that the result is as close as possible to the initial base model. This is basically an optical design problem, in which it is essential to perform a tolerance analysis to determine how critical the optimized values for the different variables are for the prediction of the total wave aberration of the eye. Navarro has developed the following procedure for this particular optical design problem. Once the optimization algorithm finds the minimum of the merit function, he obtained one-dimensional plots of this merit function vs. each variable (like surface curvature, conic constant, decentrations, and tip/tilt angle in Navarro's study) around the optimal (minimum) value. Here, we perform a similar procedure ---- once the optimization algorithm finds the minimum of the merit function, we obtain plots of this merit function vs. varied RMS for each order of Zernike coefficients of anterior lens around the optimal (minimum) value. From these plots, we can see which order is the most significant and dominate (the smallest tolerance).

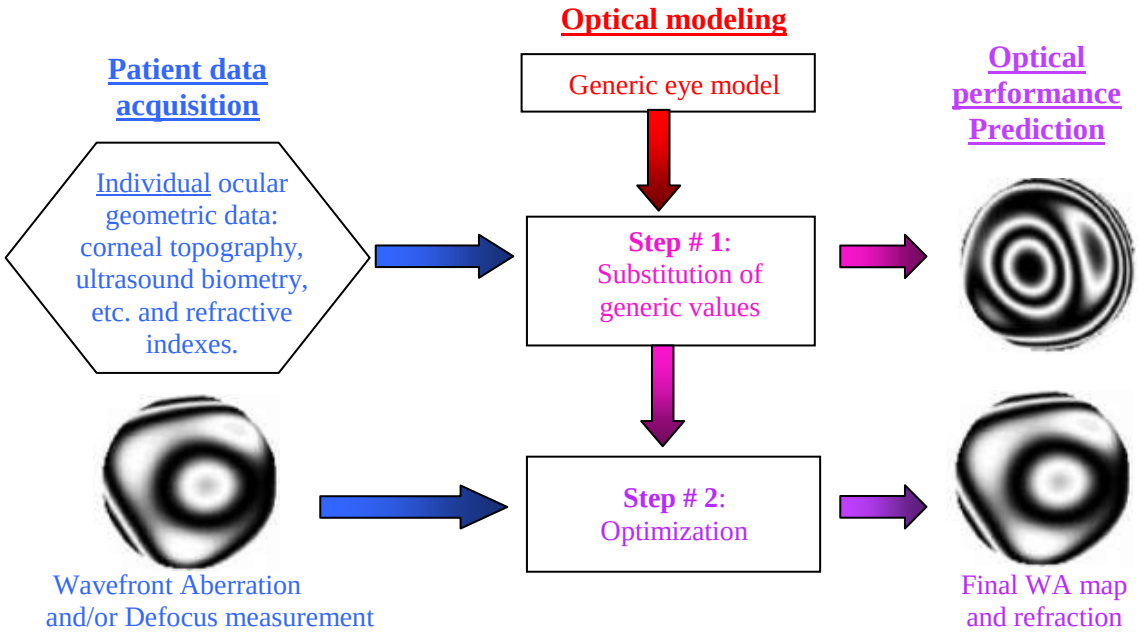

Figure 4.1 *Schematic diagram of the personalized eye modeling method*

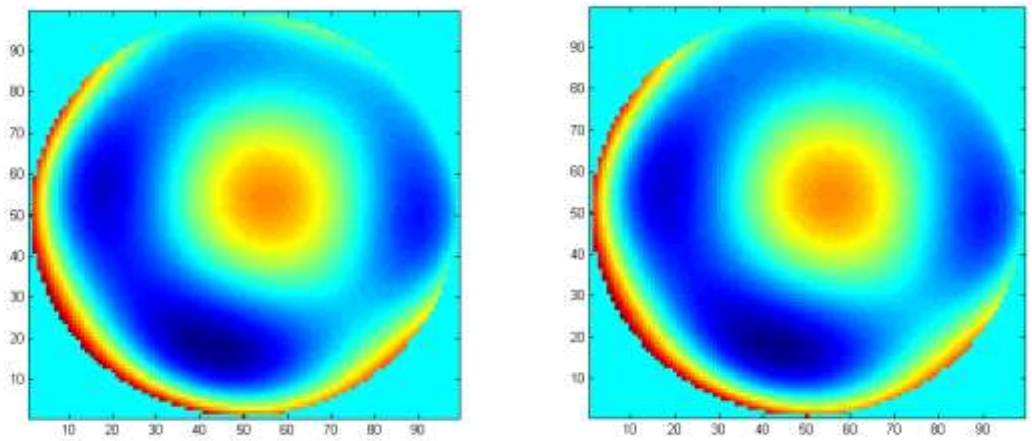

Figure 4.2 *Comparison of measured and reproduced WF aberration*

4.3 OTHER MODELING DIFFICULTIES

In the previous sections, we have discussed the construction of population based eye models and the personalized eye modeling. However, we must be advised that there are further difficulties that we have overlooked in these modeling. In this section, I will provide my considerations and suggestions for these problems.

4.3.1 Tear Film Influence:

To my knowledge, the tear film has not been included or discussed in any acknowledged schematic eye models. Although the typical tear film is very thin (3 to 40μm) compared to the cornea thickness (greater than 500μm), vision image quality as well as the ophthalmic measurements can be influenced significantly by the tear film condition. The tear film quality is determined by its structure, composition, and thickness. The pre-ocular tear film is essentially a stratified incompressible shear thinning fluid and consists of a basal mucus (sticky) layer, covered by an aqueous (watery) layer, which is turn covered by an extremely thin lipid (oily) surface layer (as shown in figure 4.3). It possesses a free surface; is secreted by the lacrimal gland; is lost via evaporation and drainage at the lacrimal ducts at the nasal side; and will eventually break-up in the absence of blinking. The tear film break-up-time (TBUT) is normally greater than 10 sec for healthy tears. Pathologies of this film, or its production, are typically responsible for dry eye syndrome which possesses many features that are encompassed by the fluid mechanical and associated solute transport processes of the tear film, and is still far from a complete understanding.

In the past years, there are studies of tear film models [Barbero 2006, Heryudono et al.2007, and Wang 2003]. The optical parameters of tear film from these study results that affect the optical eye modeling include tear film thickness, post-blink tear undulation, tear breakup pattern, eyelid-produced bumps and ridges, bubbles, and rough pre-contact lens tear surfaces. These tear film characteristics in spatial and temporal domains are possible to be included in the schematic eye models. The predictive modeling and simulation could yield insightful information regarding the dry eye vision and promote the diagnostics technology for the disease.

4.3.2 Stiles Crawford Effect (SCE)

The Stiles-Crawford effect is the wave-guide property of the cone photoreceptors of the human eye. A photoreceptor acts like an optic fiber on retina; it captures light that hits it at a narrow angle from its normal. As a result, rays of light passing through the periphery of the pupil are more oblique to the cone. The acceptance angle of a cone is narrow, approximately 5°, rods have larger acceptance angles. The SCE reduces the disadvantageous effects of aberration and the light scatter on the retina at photopic levels.

A number of different mathematical functions have been used to describe the Stiles-Crawford effect, with the most popular one being a Gaussian distribution as first used by Stiles (1937). This function is usually an excellent fit to experimental data out to 3 mm from the peak of the function, and has the addition virtue of simplicity. This Stiles-Crawford effect function $L_e(r)$ is described as $L_e(r) = \exp(-\beta r^2)$, where r is the distance in the pupil from the peak of the function. The function is normalized to have a value of 1 at the peak. The Stiles-Crawford co-efficient β describes the steepness of the function, and is assumed to reflect the directionality (variation in alignment) of the photoreceptor population being tested. It may not have the same value for measurements in eyes affected by retinal pathology. Measured β coefficients for the large-scale study of Applegate and Lakshminarayanan [Applegate 1993] are given in the following table. Combining the data across many studies gives a mean value of 0.12 [Applegate 1993). Figure 4.4 shows the SCE functions that represent the 5 per cent, 50 per cent and 97.5 per cent population distribution.

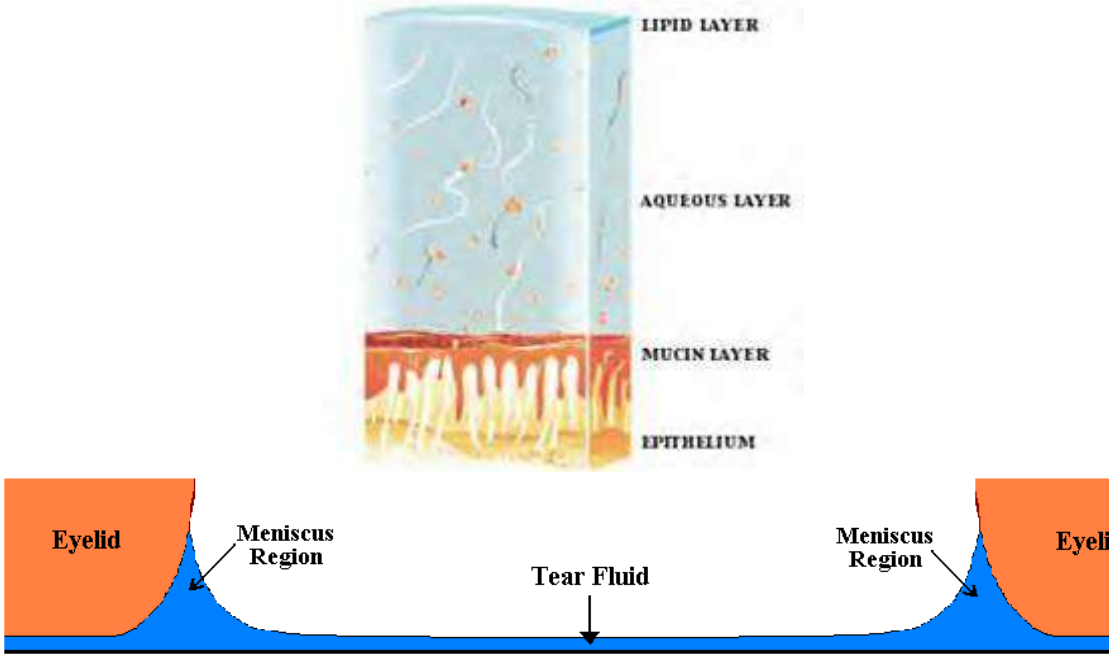

Figure 4.3*Ttear film*

Table 4.2 *Published values of the Stiles-Crawford β parameter and the position of the peak*

Investigation	No. subjects/eyes	β±1 sd (mm^{-2})	peak±1 sd (mm)
Dunnewold (1964)	29/47	-	N: 0.37±0.78 S: 0.29±0.80
Applegate and Lakshminarayanan (1993)	49/49	0.116±0.029	N: 0.47±0.68 S: 0.20±0.64

N: nasal; S: superior

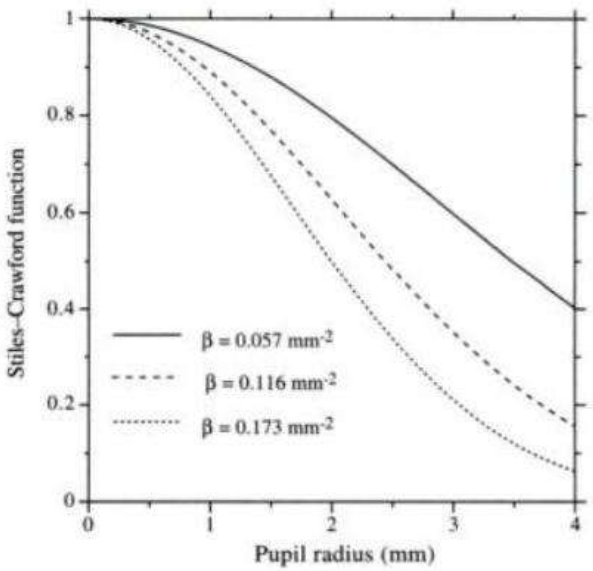

Figure 4.4 *The Stiles-Crawford function for β values of 0.057, 0.116 and 0.173, which are 2.5 per cent, 50 per cent and 97.5 per cent population limits, respectively [Applegate 1993]. [p124, Atchison and Smith, Optics of the human eye]*

The Stiles-Crawford effect can be included easily in optical modeling of the eye as an apodization effect, which means that it can be treated as an optical filter of variable density attenuation placed at the pupil. The apodization filter can be simply added into our model by entering a user defined surface and load a dll file to define this surface, which represents the equation of SCE. The C^{++} code for creating this dll file can be found in appendix.

4.3.3 Multiple Reflection and Scattering on the Retina

In some applications of eye modeling, especially the simulation of ophthalmic measurement that will be discussed in the next chapter, the reflection and scattering properties of retina need to be addressed. Because the human retina is not self-luminous, an external light source is necessary to make the retina visible and the light reflected from the retina will bring the information behind the cornea to the instrument. Thus, the multiple reflection and scattering properties of the retina is reviewed in this section.

Although most layers in the retina are virtually transparent, there are small refractive index variations between cells. Such disturbs give rise to scattering and reflections. A proper model of any ophthalmic or optometric instrument measurement that uses the double pass reflection must consider the uniqueness and complexity of this retinal reflection. Even if simplifications of any model are used, the implications of such simplifications must be understood. Reviewed by Roorda [Roorda Ph.D. dissertation 1996] and adopted in Appendix C are eight properties of the retina: A. spectral dependence of retinal reflection, B. position of reflectance, C. reflection of polarized light from the retina, D. scattering of light at the retina, E. peripheral reflections, F. coherence properties of the reflection, G. contribution of the retina to optical aberration, and H. directionality of the retinal reflection; i.e. SCE. Here I will address the considerations of these properties in eye modeling.

So far, I have been using only **sequential design** for eye modeling. It means that rays are always traced from the object surface to the assigned surface numbers in a strict sequential order. Each ray "hits" each surface once and only once in this predetermined sequence. The sequential model is straight

forward, numerically fast, and extremely useful and complete for many important cases. However, there are times when a **non-sequential ray tracing** is required. Non-sequential means the rays trace are traced in the actual physical order that they encounter the various objects or surfaces, and not necessarily in the order the objects are listed in the software user interface. Note that rays in a non-sequential trace may hit the same object repeatedly, and entirely miss other objects. Generally, the order in which objects are hit by rays depends upon the object geometry and the angle and position of the input ray. Objects which require or at least benefit from non-sequential ray tracing include prisms, light pipes, lens arrays, reflectors, and Fresnel lenses. Certain types of analysis, such as stray or scattered light effects, are only practical in a completely non-sequential environment. In the ophthalmic simulation including the back scattering from retina, non-sequential system may as well the only solution in ZEMAX to mimic the multiple reflection and scattering from the retina.

The Stiles-Crawford effect that has been discussed in 4.3.2 can be managed on the pupil plane for both forward and backward ray tracings. The **spectral property** of retina can be easily handled by assigning the wavelength and weight at the beginning of each of the double paths simulation. A birefringent **retinal surface** can be modeled using the birefringent in/out surface types, described in "Birefringent In and Birefringent Out" in ZEMAX. As to the position-dependent reflectance, a retina component with schematic layers, using the non-sequential component in ZEMAX and setting the scattering type and parameters of each layer, can be constructed. However, by using this multiple-retina-layer model to make any simulation, the computation time could be significantly increased while the result may not be appreciably different from the calculation based on single-layer retina model. To simulate the **scattering** rays, the combination of specular and diffusive reflection can be modeled by defining "fraction to scatter" at surface properties setting. After set a fraction value between 0 and 1, we need to set "ray splitting" on or off. If ray splitting is off, the decision to scatter or not to scatter is made by the generation of a single random number between 0.0 and 1.0. If this random number is larger than the fraction-to-scatter, the ray will not scatter, otherwise, the ray will scatter. For example, if the fraction to scatter is 1.0, the ray always scatters. If the fraction to scatter is 0.0, the ray will never scatter. If the fraction to scatter is 0.25, then on average 25% rays will scatter. All of the energy of the ray follows the randomly generated scatter path. The number of scatter rays has no affect if ray splitting is off. If ray splitting is on, then ZEMAX will split the specular ray into one or more scattered rays, while still possibly tracing the specular ray. The specular ray will receive a fraction of the original energy equal to (1.0 - f) where f is the fraction to scatter. The remaining energy will be divided equally among the one or more scattered rays. The number of scatter rays determines how many scatter rays will be generated. For example, if the fraction to scatter is 1.0, then the specular ray will receive zero energy and will no longer be traced; and all the energy will be divided equally among the scattered rays. If the fraction to scatter is 0.0, no scattered rays will be traced, and the specular ray retains all the original energy. If the fraction to scatter is 0.25 and the number of scatter rays is 5, then the specular ray will receive a relative energy of 0.75, and each of the 5 scattered rays will have a relative energy of 0.05. If the number of scatter rays is set to zero, then the fraction to scatter is ignored and no scattering occurs. The reflection and scattering can be modeled by using non-sequential retina surface with defining the scattering and reflection properties. However, the use of non-sequential ray tracing increases the computation time dramatically. A second and very significant concern is the loss of ray intensity in the process. In my eye modeling work in this dissertation, I use two sequential ray tracings instead of one non-sequential ray tracing. In another word, I export the resulting retinal image from the inward eye model and run the 2nd sequential ray tracing in a backward eye model with input light source of the 1st result assuming a totally diffused retinal scattering. Since the retinal image in my ophthalmic simulation is very small and close to the optical axis, this 2-step method is sufficient in describing the retinal property. Because I can increase an order or two on the ray numbers of light source in the 2nd step, it produces the much higher image intensity resolution and more realistic and satisfactory simulation results.

4.4 CONSIDERATIONS IN MODELING DISEASED EYES

The personalized eye modeling technique that is discussed in section 4.2 should be able to apply to the normal healthy and ametropic eyes. The diseased eye conditions may require additional cares in the modeling process. This section considers a few special eye diseases that include optical opacities such as cataracts and floaters, eyes with extremely irregular corneal surface such as keratoconus and **Pellucid Marginal** Degeneration (PMD), and tear film disruption such as dry eye syndromes.

4.4.1 Optical Opacity

The only published cataract eye model I found is that proposed by Donnelly in his dissertation and his advances human eye modeling. In his study, Scheimpflug cameras characterize the anterior segment and backscatter from cataract. The author discussed how to measure and model intraocular light scatter with SH wavefront sensing data. [Donnelly 2004]

A cataract is a clouding that develops in the crystalline lens of the eye or in its envelope, varying in degree from slight to complete opacity, that obstructs the passage of light. Early in the development of age-related cataract the power of the lens may be increased, causing near-sightedness (myopia), and the gradual yellowing and opacification of the lens may reduce the perception of blue colors. Cataracts typically progress slowly to cause vision loss and are potentially blinding if untreated. The following is a classification of the various types of cataracts. This is not comprehensive and other unusual types may be noted.

Age-related cataract

Immature Senile Cataract (IMSC) - partially opaque lens, disc view hazy

Mature Senile Cataract (MSC) - Completely opaque lens, no disc view

Hypermature Senile Cataract (HMSC) - Liquefied cortical matter: Morgagnian Cataract

Congenital cataract

Sutural cataract

Lamellar cataract

Zonular cataract

Total cataract

Secondary cataract

Drug-induced cataract (e.g. Corticosteroids)

Traumatic cataract

Blunt trauma (capsule usually intact)

Penetrating trauma (capsular rupture & leakage of lens material - calls for an emergency surgery for extraction of lens and leaked material to minimize further damage)

As a cataract becomes more opaque, clear vision is compromised. A loss of visual acuity is noted. Contrast sensitivity is also reduced, so that contours, shadows and color vision are less vivid. Veiling glare can be a problem as light is scattered by the cataract into the eye.

Thus the key to simulate the cataract based our personalized eye models is to simulate surface and volumetric scattered light in the eye, both of which contribute to contrast reduction of the image at the retina. The scattering theory we will apply is Rayleigh-Mie scattering since cataracts basically are volumes composed of small scattering particles [Donnelly 2004, and Gilliland 2004]. The scattering of cataracts can be simulated with a Bi-directional Scatter Distribution Function (BSDF) in non-sequential component in ZEMAX.

The Bi-Directional Scatter Distribution Function (BSDF) is defined as the scattered radiance per unit incident irradiance. Note BSDF has units of inverse steradians. In general, the BSDF is a function of the incident angle and wavelength. The term BSDF can refer to two separate functions, the BRDF and BTDF, for reflective and transmitted distributions, respectively. The integral of the BSDF over all possible scatter

angles (a hemisphere) is called the Total Integrated Scatter (TIS). For all scatter models other than ABg, the BSDF is normalized to yield a TIS equal to the "fraction to scatter" parameter. For the ABg model, the TIS must be less than 1.0, and the TIS indicates the total fraction of energy that scatters. All remaining energy is assumed to be specular.

4.4.2 Excessive Irregularity of Corneal Elevation:

We have described one type of cornea dystrophy, keratoconus, and its' general modeling. Keratoconus and **Pellucid Marginal Degeneration** (PMD) are abnormalities with irregular corneal surfaces. Modeling such cases are not particularly considering how to adopt the corneal topography into eye modeling and construct personalized KC model (sections 4.1 and 4.2 and Appendix B). However, there is some caution to be taken in the simulation calculations. First, unlike the industrial optical elements, excessive irregular optical surface from diseases produce high levels of aberration from cornea, which usually furnish two primary effects of pupil aberration: the shift in location of the pupil with field angle, and the anamorphic scaling of the edges of the pupil. When this occurs, ZEMAX can be instructed manually to account for aberrations of the pupil using ray aiming. With ray aiming, every ray trace is performed iteratively, with the program adjusting the ray coordinates or cosines in object space so that the ray crosses the correct location on the stop surface. To determine the correct location on the stop surface, the stop surface radius must be computed. The stop surface radius is computed by tracing a marginal ray from the center of the object to the stop surface at the primary wavelength. Either paraxial or real rays may be used in this trace to determine the stop radius. Paraxial rays are well behaved and paraxial definitions are commonly used for most first-order system properties such as focal length, F/#, and magnification, and so paraxial rays may also be used to determine the stop size. However, for systems that have significantly aberrated pupils, there will be a difference between the paraxial and real ray stop radius. These systems will exhibit a difference between the real and paraxial ray system aperture. For example, the paraxial object space numerical aperture may be defined as 0.4, but the actual numerical aperture of real rays may be a different value. For real rays to have the object space properties defined by the system aperture, use real rays instead of paraxial rays to determine the stop radius. Note that real ray based ray aiming will not work in systems where the stop lies in a caustic or where the real rays cannot be traced at the full entrance pupil diameter or numerical aperture. If real ray aiming causes any of these problems, set the ray aiming to paraxial rather than real. Note that once the stop radius is determined all rays are aimed to the correct location on the stop, regardless of whether paraxial or real rays were used to determine the stop radius.

To eliminate any ambiguity in the calculation of the actual stop size, set ray aiming to paraxial or real, and then set the system aperture type to "float by stop size". This eliminates the need for any ray tracing at all to determine the stop size, and both real and paraxial rays will be aimed to the real stop exactly. The trade back is the significant increase of calculation time consumption.

For systems with virtual stops, such as some eyepieces, the effective stop location and size may be a function of wavelength. For these systems, use the multi-configuration capability to treat each wavelength and system aperture definition separately.

Although ray aiming is more accurate than paraxial entrance pupil aiming, most ray traces will take from two to eight times as long to perform. Therefore, ray aiming should only be used when required. To determine the amount of entrance pupil aberration in your system, select ray aiming off, and then look at the pupil aberration plot. Pupil aberration of less than a few percent is generally insignificant. If the eye model has significant pupil aberration, select ray aiming ON and repeat the calculation. The aberration will decrease to zero, or very nearly so. Ray aiming does not, of course, actually eliminate pupil aberration, it merely accounts for it.

When using ray aiming, two settings are needed to be checked carefully, "Ray Aiming Cache" and "Robust Ray Aiming (slow)". If "Ray Aiming Cache" is checked, ZEMAX caches ray aiming coordinates so that new ray traces take advantage of previous iterations of the ray tracing algorithm. Using the cache

can speed up ray tracing dramatically. However, use of the cache does require that the chief ray can be traced accurately. For some systems, the chief ray cannot be traced, and for these systems, the cache should be turned off. If “Robust Ray Aiming (slow)” is checked, ZEMAX uses a more reliable, but slower algorithm for aiming rays. This switch should only be set if the ray aiming algorithm is failing even with the cache turned on. This switch has no affect unless the ray aiming cache is checked on. Robust mode goes through an additional check to make sure that if multiple ray paths to the same stop surface location exist, only the correct one is chosen. This is typically a problem in very fast, very wide angle systems where off axis fields may find a virtual path to the stop that confuses the ray aiming iteration.

For some very wide angle or highly tilted or decentered systems, the ray aiming feature will fail if unassisted. The problem is that the paraxial entrance pupil is used as a first guess to trace the ray. If the pupil aberration is severe, it is possible that even this first guess cannot be traced, which prevents the algorithm from taking a second, more refined guess.

The solution is to provide a rough guess as to how much the pupil has been shifted and compressed with respect to the paraxial pupil. There are three shift components; x, y, and z; all measured in lens units. There are two compress components; x and y, and these are dimensionless scaling factors. The default value of zero for all five may be modified to assist the algorithm in finding a successful first guess for the ray aiming.

The shifts move the center of the aim point on the paraxial entrance pupil. Positive values for the z shift indicate that the aim point is to the right of the paraxial pupil; negative values indicate the pupil is shifted to the left. Most wide angle systems have left-shifted pupils. The z pupil shift value provided is scaled linearly with the field angle of the ray being traced, so the pupil shift refers to the offset of the pupil at full field. If "Scale pupil shift factors by field" is selected, the x and y pupil shift values are also scaled with field, otherwise, the x and y shift values are used for all fields without any scaling. All shifts are in lens units.

The x and y compress values are used to change the relative coordinates on the paraxial entrance pupil to start the iteration. The pupil coordinates used to start the ray aiming interation are given by: $P'_x = P_x(1-C_x)$ and $P'_y = P_y(1-C_y)$, where C_x and C_y are the ray aiming compress values and the P values are the normalized pupil coordinates. The P values are the modified pupil coordinates used to launch the first ray; thereafter, the rays are aimed to the actual pupil coordinates defined by P. By defining the compress values this way, a value of zero means no compress, while a value of 0.1 indicates the pupil is compressed 10%. The compress values are particularly useful when the real pupil is smaller than the paraxial pupil, and rays traced at the full paraxial pupil size are difficult or impossible to trace.

It is important to understand that the exact values of the pupil shift and compress values are unimportant. Once the first guess ray can be traced, the algorithm will robustly find the exact pupil location. The pupil shift and compress values are just to get the ray aiming started. Neither the shift nor the compress values actually change the size of the entrance pupil. Generally, guessing at the pupil shift and compress values is an acceptable way of determining a suitable value.

Another thing we should note is to set the “semi-diameter” equal to the aperture radius for the aperture surface, especially the stop surface. We can set semi-diameter as “automatic” or “maximum” for other non-aperture surfaces.

4.4.3 Tear Film Break-Up

There is no technical difficulty to include the tear film and even the tear film disruption into eye models with known thickness of tear film upon the cornea surface. What we need is to add the tear layer in front of the anterior corneal surface. Hence the curvature of this layer is determined mostly by the anterior corneal surface shape and the thickness of this layer. The major problem in tear film modeling is the information regarding the description of film thickness patterns and variations for different tear qualities.

For the tear film, a number of possible definitions of thickness are possible, as indicated in Figure 4.13. The height of human microplicae is 0.5 to 0.75mm [Ehlers 1965] and the height of the glycocalyx (in guinea pigs) is 0.3mm, [Nichols 1983] so that the thickness difference between B and F in Figure 4.5 is about 1mm. Additionally, an appropriate measure for the thickness of the tear film might depend on the intended use for the thickness value. For example, assuming that a separate mucus layer exists (as in Figure 4.5) and that it behaves as a gel, then an appropriate measure to use in calculating tear fluid flow might be the thickness of the aqueous layer (A in Fig. 4.5). For the same tear film, an optical measurement of tear film thickness might correspond to the total thickness from air surface to the bases of the microplicae (F in Figure 4.5). Which thickness is measured optically depends on the relative amplitudes reflected from the various interfaces in Figure 4.13; the reflectance at any interface, in turn, depends on the step change in refractive index across that interface. [Jenkins 1976.]

Benedetto et al. [Benedetto 1984] have provided evidence that tear film thickness is dependent on both the time after a blink and the position on the cornea. Using fluorophotometry, they showed that the superior tear film thickens for about 1 sec after a blink, whereas the inferior tear film thins over a comparable time. When the fluorescence reached a steady state, it was greater over the superior cornea than over the inferior cornea, implying that tear film thickness was also greater over superior cornea; further evidence supporting this idea has recently been presented. [Shimmura 1998, and King-Smith 2003] Over the central cornea, thinning of about 1mm typically occurs in this time period, [Ehlers 1965, King-Smith 2000, and King-Smith 2002] as shown in Figure 4.6A; this shows a 20-s recording of PCTF thickness, replotted from King-Smith et al., [King-Smith 2002] with the subject blinking about 1 s after the start of the recording and then keeping his eye open for the remaining 19 s. Figure 4.6B shows upward movement, after a blink, of a particle on the surface of the cornea, that is re-plotted on the same time scale from Berger and Corrsin [Berger 1974]. The initial thinning after a blink is seen to have a similar time course to this upward movement, implying that the thinning is probably caused by this movement. At later times, there is a slower thinning of about 1.2mm/min21 (dashed line in Figure 4.6A), which has been ascribed to evaporation [King-Smith 2002]. However, this may give an underestimate of evaporation rate if there is a significant fluid flow across the epithelial surface caused by the osmotic gradient between epithelium and the hyperosmotic tears. The spatial and temporal variations in tear film thickness will be discussed more fully later.

With regard to suitable temporal conditions for general measurement of tear film thickness, about 2 s after a blink is probably satisfactory. By this time, the rapid changes occurring just after a blink have normally been completed [Benedetto 1984, and King-Smith 2002] (Figure 4.6A). Additionally, for most subjects, this time is well within the inter-blink interval of about 5 s. [Carney 1982] The center of the cornea would seem to be the most suitable area for measurements, as this is the region of greatest optical interest (and also is easiest to study by some methods).

The methods of measuring the human tear film thickness and the results are shown in table 4.3. From this table we can have a basic idea about the range of tear film thickness.

Most authors assume that the wavelength variation of refractive index (dispersion) of tears, n_1, equals that for water. Thus we have spatial and temporal variation of the shape (determined by the anterior cornea shape), the thickness (determined by experimental data), and the refractive index of the tear film. The simulation tear film breakup in our personalized model will be achievable next step.

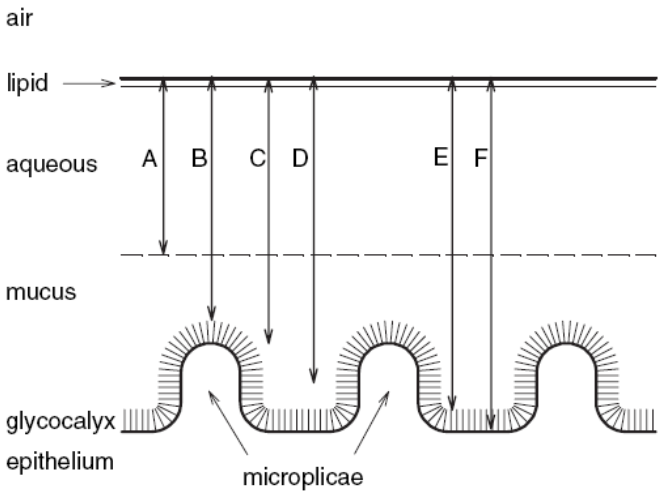

Figure 4.5 *Possible measures of the tear film. Most measures are self-explanatory. D is some sort of average thickness. [King-Smith 2004]*

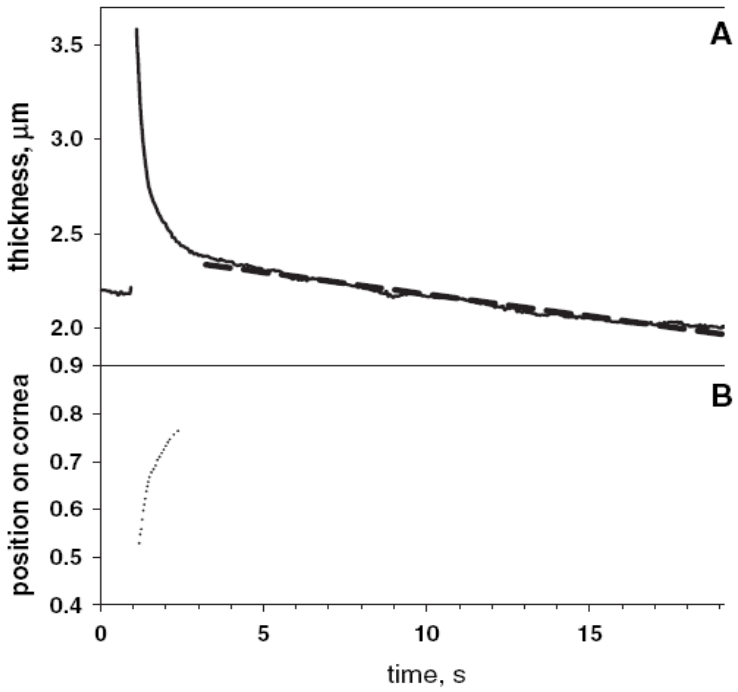

Figure 4.6 *(A) Thinning of the PCTF after a blink (discontinuity near time 1 s). Replotted from King-Smith et al.21 Dashed line is regression line fitted from 2 to 19 s after the blink. (B) Upward movement of a particle in the superficial tear film after a blink, replotted from Berger and Corrsin.14 Time scale has been aligned so that blink occurred at the same time as in A. Position on the cornea is given as fraction of interpalpebral aperture (lower lid = 0, upper lid = 1). [King-Smith 2004]*

Table 4.3 *Human tear film thickness [King-Smith 2004].*

Source	Layer	Method	Invasive?	Measurements	Thickness
Ehlers 1965[13]	PCTF	Absorbent disks	Yes	1	7 µm
Benedetto *et al.* 1975[17]	PCTF	Fluorometric	Yes	(1)	4 µm
Green *et al.* 1975[25]	PCTF	ADF	?	1	<10 µm
Wilson *et al.* 1980[21]	PCTF	Optical pachometry	No	1	<<40 µm
Prydal *et al.* 1992[20]	PCTF	ADF	No	1	34–45 µm
Prydal *et al.* 1992[20]	PCTF	Confocal microscopy	No	1	41–46 µm
Danjo *et al.* 1994[33]	PCTF	WDF	No	1	11 µm
Wong *et al.* 1996[10]	PCTF	Theory	–	–	8 µm
Creech *et al.* 1998[24]	PCTF	Theory	–	–	10.4 µm
King-Smith *et al.* 2000[20]	PCTF	WDF	No	1	2.7 µm
Wang *et al.* 2003[26]	PCTF	OCT	Yes	2	3.3 µm
Norn 1966[35]	Conj.	Aspiration	Yes	1	×2 = 7.8 µm
Guillon 1986[55]	PLTF	TDF	No	1	Up to 5.5 µm
Doane and Gleason 1994[66]	PLTF	TDF	No	1	1.5–2 µm
Fogt *et al.* 1998[23]	PLTF	WDF	No	1	2.7 µm up to 4.9 µm
Nichols and King-Smith 2003[8]	PLTF	WDF	No	1	2.3 µm
Wang *et al.* 2003[26]	PLTF	OCT	No	2	3.8 µm
Lin *et al.* 1999[28]	PoLTF	Optical pachometry	Yes	3	11.5 µm
Nichols and King-Smith 2003[8]	PoLTF	WDF	No	1	2.3 µm
Wang *et al.* 2003[26]	PoLTF	OCT	Yes	2	4.6 µm
Petroll *et al.* 2003[67]	PoLTF	Confocal microscopy	Yes	1	<9 µm
Olsen 1985[41]	Lipid	Two wavelengths	No	1	40 nm
Korb 2002[42]	Lipid	Color	No	1	87 nm
Goto and Tseng 2003[68]	Lipid	Color LUT	No	1	74 nm

4.5 VALIDATION OF THE PERSONALIZED EYE MODELS

As mentioned in the previous sections, validation of eye modeling with the patient vision and/or the clinically obtained low and high-order aberration is required to confirm the modeling success. The validation with refractive errors and the wavefront aberration are guaranteed as described in the sections 4.1 and 4.2. Here I will address the validation with patient vision.

4.5.1 Visual Acuity vs. PSF

The size and shape of the Point Spread Function (PSF) provide the indication of visual acuity (*VA*). PSF is the image of a point source. In general, the real image of an object on retina can be calculated by the spatial convolution of the PSF with the object in the object space. Knowing the PSF of one eye model, we can estimate the subject's VA by how concentrated the PSF is. The dimension and the profile of the PSF can be compared with the clinical VA report to evaluate the success of our modeling. PSF can be directly obtained in the ZAMAX analysis. Notice that the PSF depends on the object distance and the field angle that are assigned in the lens editor.

Figure 4.7 shows the PSF of one personalized KC eye model with and without its best refraction correction of (S-1.875C-1.250X68). As mentioned in Chap 3, a 5μm spot on the retina corresponds to about 1 min of arc of filed angle. We also know that the spatial resolution of the 20/20 vision on a Snellen Letter chart corresponds to 5 arc min of field angle, which thus corresponds to about 25 μm of spatial resolution on the retina surface. Since the retinal PSF image size in Figure 4.7 is 128 μm, we can estimate the width of PSF is about 50-100 μm, which corresponds to 20/40-20/80 line on the chart. From figure 4.7b, we can estimate the width of PSF is smaller than 25-35 μm, which corresponds to 20/20-20/30 vision after correction.

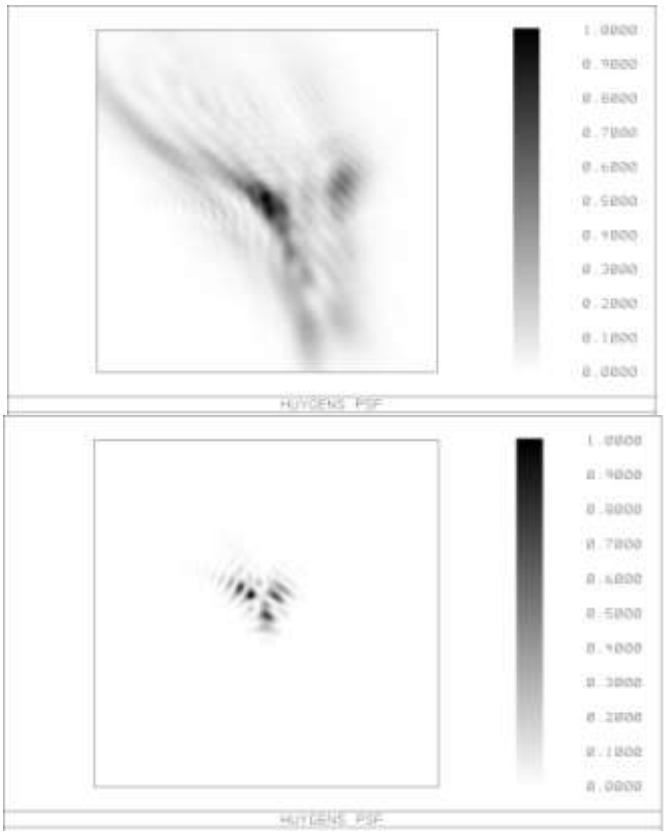

Figure 4.7 *a) PSF without correction; b) PSF with correction (The image filed size is 128* μm *in both sides.)*

4.5.2 Letter Chart

The PSF can be used to infer how well the subject can see a point source but using the parameter alone is neither straightforward nor reliable to describe the subjective vision alone. Before calculating the PSF, we have to set a pupil sampling number of ray tracing (i.e. the size of the grid of rays to trace to perform the computation). Higher sampling densities yield more accurate results at the cost of longer computation times. Secondly, PSF depends on the location of the point source in the field of view. When the subject looks at an object, especially a large object, calculation of PSF over a large field angle range is required for accurateness. Third, and also the most importantly, PSF is a two-dimensional function, which is difficult to direct quantify or correspond to VA. A single index that is derived from PSF such as the FWHM or STR, do not directly correspond to VA as well, especially when PSF profile is far from a Gaussian or Lambertian types of symmetric shapes. For these reasons, the best way to validate the personalized eye models is to simulate the subject's vision of an extended object, using, for example, a Snellen letter chart. ZEMAX Geometric Image Analysis (GIA) is used to provide such vision simulation instead of using PSF convolution. GIA is based strictly upon geometrical ray tracing. It can be used to model extended (light) sources, analyze useful resolution, represent the appearance of imaged objects, and provide intuition as to image rotation. A perfect letters E for example is assigned as the object image (or the light source) at the desired distance. Each letter in the letter chart is simulated individually with its corresponding resolution.

The following figure is an example of the vision simulation result. We can compare the vision simulation result of an eye model with the VA test result in the patient's clinical file. As the figure shows, the patient may be able to identify a few letter in the 20/30 line with some uneasiness and even possible to 'guess' one or two letters in the 20/20 line from experience.

KC patients' vision can also be simulated by the same technique. At the SESAPS conference in 2007, I presented the vision simulation of KC patients as the KC cone progresses. I produced a series of KC models, using the method described in section 4.1.4. The KC cones were located in three location, on axis, mean location, and far location based on the population statistics. The height and size of KC cone were increased to represent the degree of severity. Subsequently, three-dimensional ray-tracing with ZEMAX on KC eye models was performed to determine the consequential optical imaging quality. The simulation results showed how KC progression influences the vision. Figure 4.9 just show 3 frames from all the images. The significant coma aberration in severe cases of KC results in significant double images and image shifting consequences as shown in Figure 4.9 c.

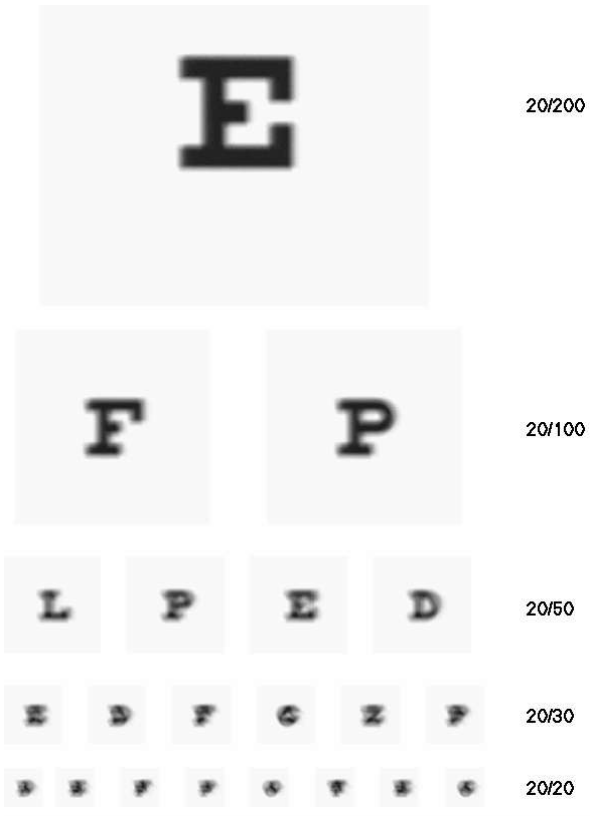

Figure 4.8 *Snellen chart simulation (with correction) of the same subject in figure 4.7*

On axis On average location On far location

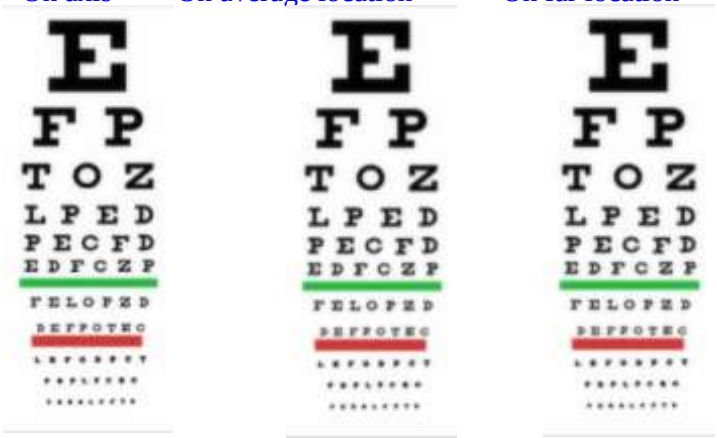

a) 2 µm KC cone height

On axis On average location On far location

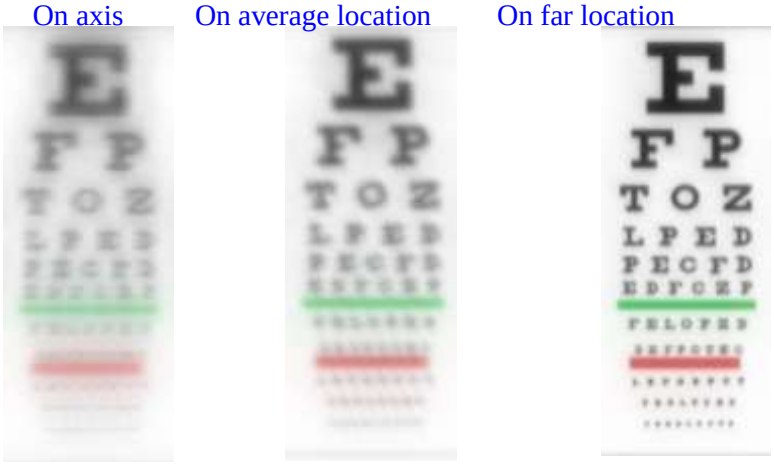

b) 10 µm KC cone height

On axis On average location On far location

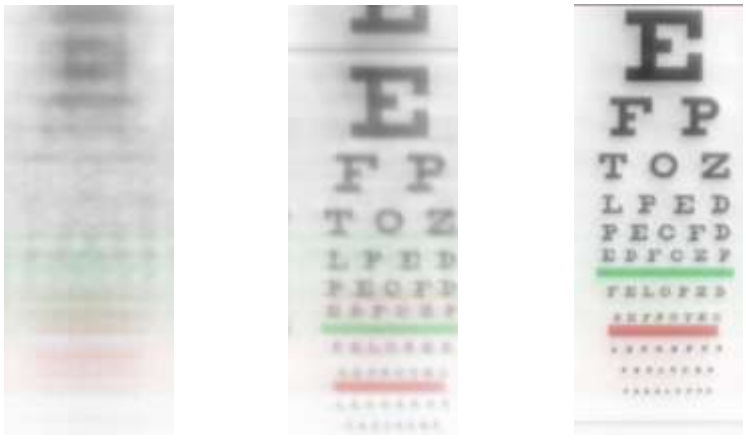

c) 20 µm KC cone height

Figure 4.9 *KC Vision Without Correction*

4.5.3 Night Vision Simulation

The human visions in daylight and night environments are very different because of the change of pupil size. In the darkness, the pupil is naturally dilated to include more light signal. In nature, the human visual procedure and correction are designed and adapted for daytime vision. However, since the human activities extend long into the night fall, the performance of night vision becomes important and requires more concern. The night vision problems have been the reason for most complaints from LASIK patients. Here I will demonstrate the ability of eye modeling in predicting patients' night vision. The object image, such as the street view, can be entered in ZEMAX at the assigned object distance. The retinal image of the street view can then be obtained by running the image analysis procedure through the desired eye model. Pupil size and accommodation level should be assigned adequately. The following figure (Figure 4.10) compares the vision of a normal subject and a KC subject at night. The object is a car running towards the subject. The simulation was done by importing a picture of car as the object and running image analysis on the retina surface. The final images will be the simulated patients' vision at night. The object distance was set at 3 values, 25, 20, and 15m. 100 million rays were used for image simulation. The day and night visions prediction can be served as a way for eye modeling validation.

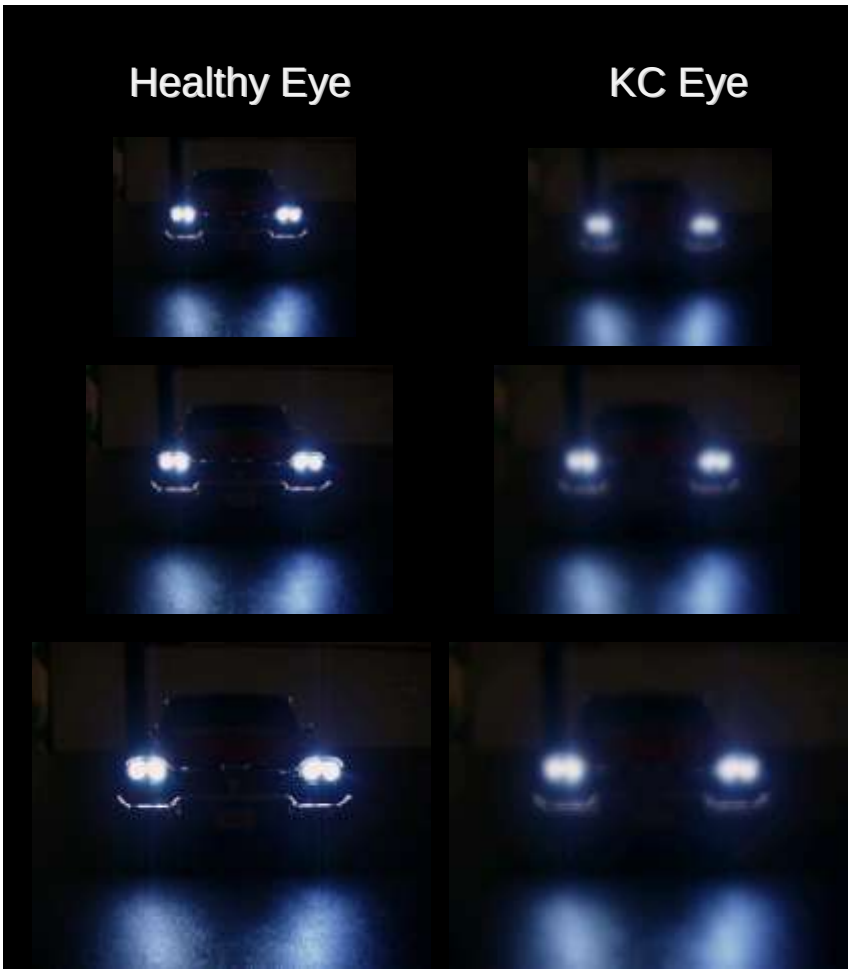

Figure 4.10 *Night vision simulation under 6mm pupil. (The object locations are 25, 20, and 15 meters from the subjects.)*

Chapter 5 Ophthalmic Simulation Using Eye Modeling

The general and population based eye modeling are significant in gaining the knowledge of visual optics and the disease development study. The personalized eye modeling, on the other hand, provide promising features in assisting ocular surgery and in designing customized spectacle-, contact-, or intraocular lens. With supplementary adaptations, both type of modeling could apply to predict visual changes under specified environmental or physical conditions. Furthermore, the computer simulation of ophthalmic measurements that utilize eye modeling technique offers a comprehensible tool for medical training. In this chapter, the ophthalmic simulation application is demonstrated on two ophthalmic devices, the retinoscope and the photorefraction devices. The computation results and detailed discussions of retinoscopy in section 5.1 were published on the online journal, Optics Express [Tan 2007] and the conference [ARVO 2009]. Most of the results of photorefraction in section 5.2 were published in 2 papers in Optics Express [Chen 2003, and Chen 2006]. I will introduce the 2 devices, and review and summarize the research methods and results in this chapter.

5.1 RETINOSCOPY: SPOT AND STREAK RETINOSCOPES

5.1.1 Retinoscope & Retinoscopy

Retinoscopy has been introduced for over 100 years to detect refractive errors of an eye. It is still a standard method to objectively measure defocus in small children. Rosengren was one of the first to describe the method of retinoscopy. The device has a small light source and the optics is aligned to the observer's eye and then manually moved the illuminating light beam across the examinee's eye [Rosengren, 1935]. A traditional "spot retinoscope" or a contemporary "streak retinoscope" (left of Figure 5.1) projects a spot light or a straight-filament image respectively onto a patient's eye at a distance of 0.5-1.0 meter (middle of Figure 5.1). The size of the spot or streak projection is adjustable by moving a condenser lens that is located above the light source (or filament) in the handle of the device. The retinal reflex is observed by the examiner through a peephole on the scope. When moving the streak projection across the patient's pupil, the reflex of a myopic or hyperopic eye appears to move with or against the projection motion. The moving speed and direction of reflex depend on the position of the condenser lens. Subsequently the examiner uses a phoropter (right of Figure 5.1) or manually places trial lenses (middle of Figure 5.1) over the examinee's eye to "neutralize" the reflex movement. When the refraction is neutralized, the pupil will suddenly appear bright as the light projection aligns to the center of pupil and turn dark with a slight misalignment toward either side. No movement should be seen under neutralization condition. The compensation lens indicates the required defocus correction.

Retinoscopy is objective and, therefore, especially useful in prescribing corrective lenses for patients who are unable to undergo a subjective refraction test that requires a response and judgment from the patient (such as mentally handicapped or non-verbal people or animals). It is also used to evaluate accommodative ability of the eye and detect latent hyperopia. Static retinoscopy is performed when patient was asked to fixate on a distant object or attempt to relax accommodation completely. Dynamic retinoscopy is when the patient is asked to fixate and focus with both eyes (binocularly) on a near object. As accommodation is in demand, the refraction power increases and the reflex shape, intensity, and movement change accordingly.

Figure 5.1 *Retinoscope (left) in use with trial lens (middle) or phorotpter (right).*

Although the optical setup of retinoscopy is simple, the thorough analysis is difficult because of the utilization of low cost imprecise elements. Because of the absence and difficulty of detailed analysis, medical text books illustrate retinoscopy with over-simplified portraits and results. Ambiguous observations occur when the ocular aberration is more significant and when the multiple aperture stops in the light path overlap. These indefinite situations discourage the clinical practices.

In our paper of 2007 [Tan 2007], we simulate the streak retinoscopic observation using both general and personalized eye models. Instead of simple geometric analysis, high density ray tracing is applied through the optical path of both the device and the ocular elements. Typically 100 million rays are traced in each of the double path simulation. Both plane- and concave-mirror practices of retinoscopy are presented. Observation of the typical ammetropia reflex movements and the so-called "anomalous with-motion" of the high myopia condition are produced in this paper. Further, the famous scissors reflex of a keratoconus eye is simulated and published for the first time. Also included at the end of section 5.1.3 is the hour-glass retinal reflex observation that was reported by Dr. Guyton in Johns Hopkins in 2002. This simulation result was presented in ARVO conference 2009.

5.1.2 Retinoscopy Simulation

For both general and personalized eye modeling, parameters of the Navarro wide-angle eye model were used and then modified in portions for the needs of this work. The personalized keratoconus and ametropic models are described in a previous chapter where patients' topographies are adopted and the two-step iteration procedures were performed. Although the posterior corneal surface is also affected in KC patients, the posterior irregularity was omitted in the modeling. The optical influence of irregular posterior surface was estimated to be no more than 10 to 20% of the anterior influence due to the smaller refractive index difference. The general ametropic eye models were approached in a similar manner for the desired refractions without replacing the corneal topographies. A three-mm aperture stop (3.4 mm entrance pupil) was used in the refraction approach. Since the pupil is typically not large for non-mydriatic visible illumination from the retinoscope, the directional retinal reflection of Stiles-Crawford effect was omitted in the modeling.

Figure 5.2 illustrates the computation elements with corresponding retinoscope parameters. The simulation includes 2 parts of calculation. The first part is the streak projection from the light source, through the aperture, lens, and beam splitter to the face surface of the examinee. The 2nd part is the simulation of the pupil reflex image, which comprises procedure of 2 steps of forward and reverse path respectively. The forward path is traced by millions of rays from the light source, through the optics of retinoscope and the entire eye model, and reach the retinal surface. The retina image is exported and used as the light source and redistributed with millions of rays in the 2nd step. The second path starts at the retina, through the model eye and enter the peephole of the scope. A simple 1-lens, 1-aperture eye model is used as the examiner's eye to form the final image of reflex. From the light source, the elements

include a filament light source (0.03 mm X 3 mm), a rectangular aperture (2 mm X 4 mm), a condenser lens (20 mm focal length), a beam splitter with window aperture (10 mm X 14 mm), and a circular peephole (3 mm diameter). The distances between each element are specified in the figure. A movable sleeve was included that allows the examiner to vertically move the lens and change the convergence of the streak projection. The wavelength was set at 555 nm and 0.5 or 0.67 meter working distance was assumed. Coordinate breaks (including coordinate shifts and rotations) were used to move or rotate the streak beam across the entrance pupil of the model eye. Double-pass image analysis through the model eye was performed under the assumption of perfect diffusive retinal reflection/scattering. Multiple reflections and scattering were omitted. An aberration-free imaging system was used to simulate the examiner's eye behind the peephole. The focus plane of the examiner's eye was set on the corneal surface of the model eye.

As in the real condition, four effective apertures were involved in this retinoscopic simulation. These apertures were the small aperture in front of the filament, the window on the beam splitter (along both paths), the pupil of the eye (along both paths), and the peephole of the observation. Ray aiming was applied to ensure that all of the vignetting or cut-off effects were encountered when using coordinate breaks.

Zemax setting and macros for the projection movement are given in Appendix E.

5.1.3 Results

Clinical operation conditions of plan-mirror and concave-mirror are simulated as well as the detections of different eye conditions. They are described below.

A. *Sleeve position: Plane mirror & concave mirror operations*

The retinoscope sleeve position defines the location of the lens and therefore the width of the streak projection on the examinee's cornea plane. Plane- and concave-mirror operations indicate the conditions of a diverged and a converged beams. Figure 5.3 shows the simulation result when the retinoscope sleeve moves vertically across a fifteen mm distance. The corresponding streak projections on the center of patient's eye are illustrated on the very left column. The illustrated eye in each image has a 3.4 mm pupil and an 11 mm iris. Each image is scaled 10 cm by 10 cm. The false colors represent the relative intensity distribution. As the sleeve moves upward, the convergence of projection increases. Because the condenser lens has a focal-length of 20-mm, the filament image is sharply focused at a sleeve height of h=21 mm. The sleeve-down position (h<21mm) corresponds to the "plane mirror" position, and sleeve-up, the "concave mirror" position. When the sleeve moves all the way up, the projection shape tends to reveal the rectangular filament window.

The measurement simulation was performed for five refractive conditions of hyperopia of +2, and myopia of -1, -2, -4, and -6 D, as indicated at the top of each column. The pupil is 3.4 mm diameter. Since the observing distance is d_{ob} = 0.5 meter, the retina surface of the -2D eye is conjugate to the window of retinoscope. Neutralization occurs at any sleeve location for this refractive condition.

Notice that the pupil strip-reflex is often in poor contrast and hard to observe if the images are in gray-level instead of the false-color illustration. It is especially so for a refractive condition that is close to neutralization and when the sleeve location is away from h=21 mm. Streak reflex is more easily observed under concave-mirror operation for high myopia and under plane-mirror operation for hyperopia.

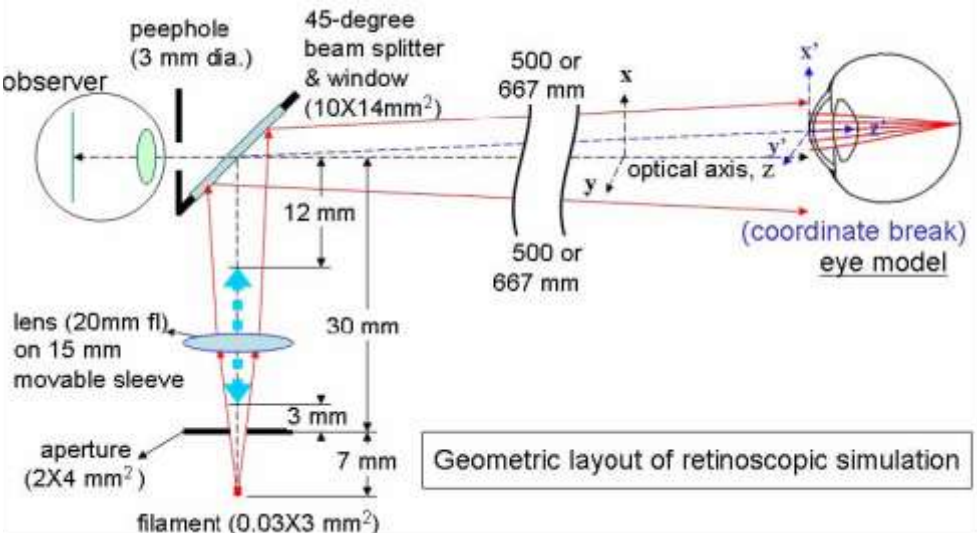

Figure 5.2 *Optical layout in the simulation of retinoscopic measurement. Wavelength of filament is set at 555 nm. The observation behind the peephole is simulated with a Gaussian lens that focuses on the cornea plane.*

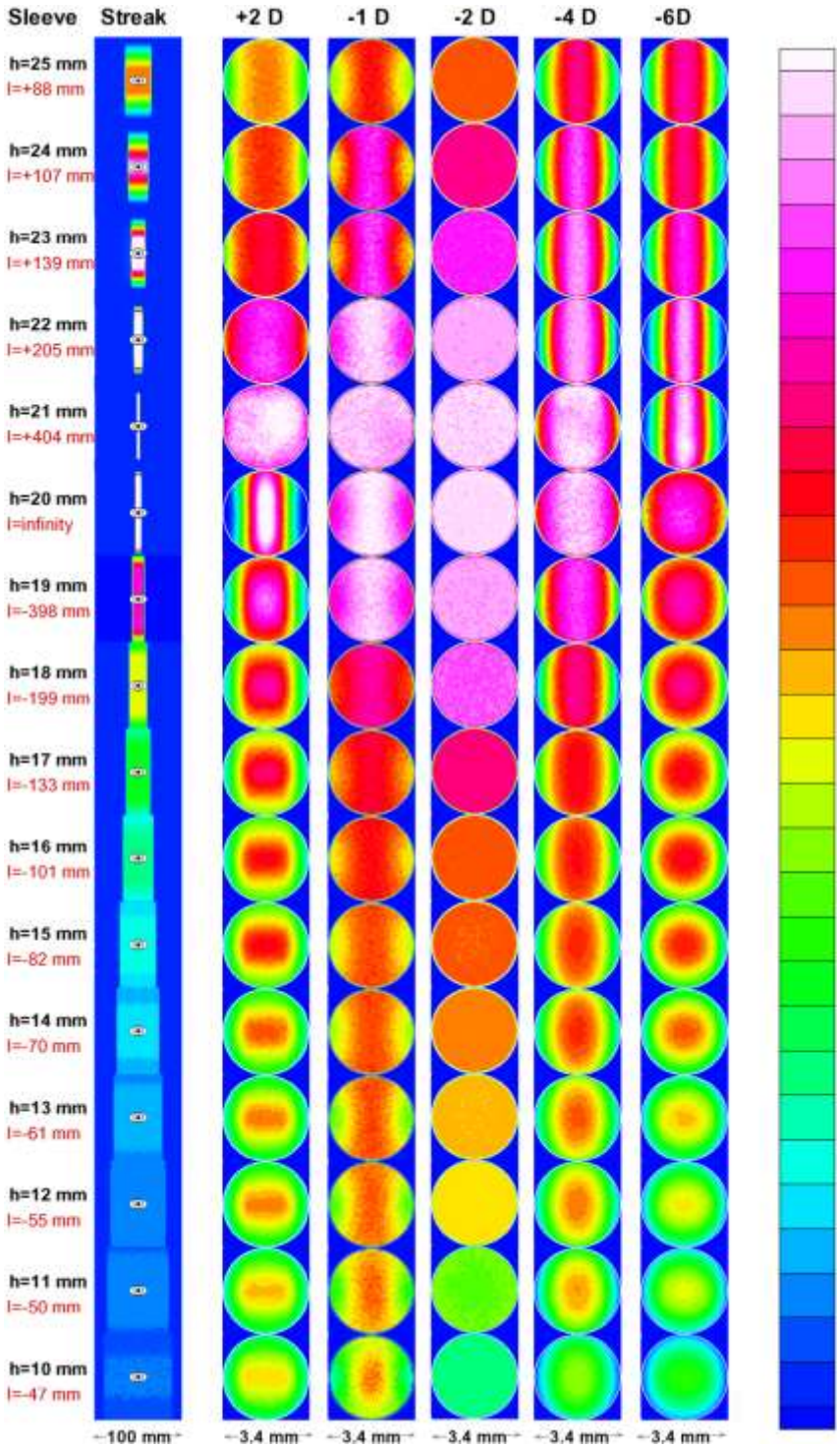

Figure 5.3. *Simulation results of the retinoscopic observation as the condenser lens moves from a height of 10 mm (indicated as h=10 mm) to 25 mm above the filament. The left most column shows the streak projections on the surface of the examinee's eye. The 5 columns on the right illustrate the appearances of retinal reflex of 5 eyes with +2, -1, -2, -4, and -6 diopter of refractive errors.*

In the streak retinocope, the filament is imaged by a condenser lens. The location of the filament image, l, has an important effect and is indicated beside the figure. From the patient's viewpoint, the light source (filament image) changes with the sleeve position. When the lens is located at the lowest position, about 10-mm above the filament, the image of the filament is about 47 mm behind the peephole. As the sleeve moves upward, the light source image rapidly moves farther away from the patient. The light source approaches to infinity as the sleeve glides into the 20-mm height position. When the sleeve moves above the 20-mm position, i.e. into the concave-mirror condition, the filament image appears to be on the patient side of the peephole. At h=21 mm, the filament image is at about 10 cm in front of the patient's eye. When the sleeve is pushed farther upward, the light source image moves toward back to the retinoscope. This light source location, in relation to the peep-hole position, determines the reflex motion, the direction, and speed of the reflex movement.

B *Streak rotation: the detection of cylindrical refractive error*

In retinoscopy, astigmatism is often observed by rotating the streak projection. When rotating the streak, two distinctive astigmatic appearances are the variation in reflex brightness and strip thickness. When the streak projection is aligned with one of the two major meridians, the thickness and the brightness appear to be either optimized or minimized. Illustrated in gray scale and, more clearly, in false color, Figure 5.4 shows the retinal reflex of an eye with the prescription of (S+1.00, C+2.00, X90). The dotted arrow line in each image indicates the orientation of the projection. The sleeve location was set at 18 mm. The reflex thickness and intensity variations are obtained. A third astigmatic appearance is the skew or break phenomenon, which shows the misaligned motions between the projection and reflex streak. This is also clearly shown in the simulated images where the beams are not aligned with meridians at either 180 or 90 degrees. The streak reflex appears to be misaligned to the streak projection.

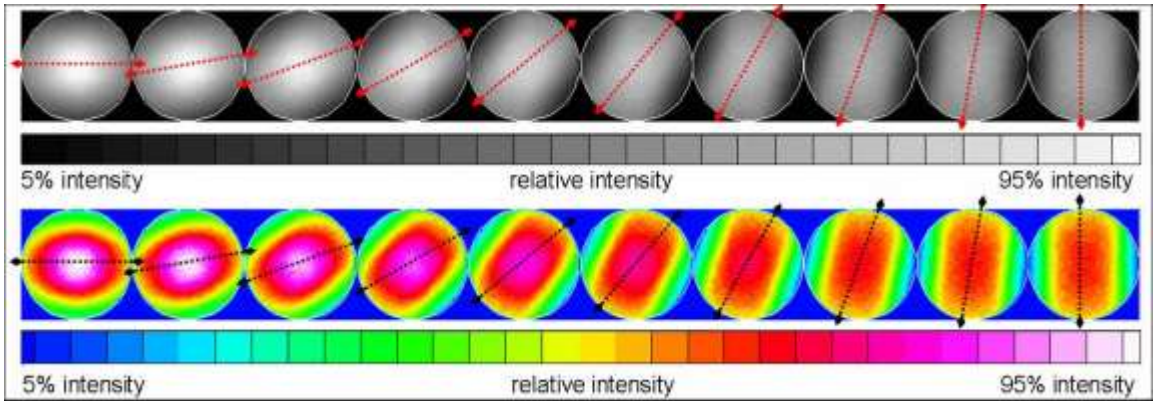

Figure 5.4*. Streak retinoscopic reflex of an astigmatic eye, (S+1.00, C+2.00, X90). Both gray level and false color illustrations are scaled from 5% to 95% of the maximum intensity. Theorientations of streak projections are indicated by dotted arrow lines.*

***C** With and against motion in ametropia*

Figures 5.5 and 5.6 show the retinal reflex motion under the plane mirror (sleeve located at h=19 mm) and the concave mirror (h=21 mm) operations, respectively. The upper row in each simulation illustrates the projection that moves across the pupil along one major meridian of the eye. Three personalized eye models are used in the simulation. In upper Figure 5.5 is presented the reflex of a mild myopic eye, MY1 with prescription of (S–1.50D, C+0.25D, X180) and a best-correction RMS wavefront aberration (WA) of 0.111 μm in the 3.4 mm pupil. The streak projection moves along the –1.5D meridian at a working distance of 667 mm. The neutralization or reversal appearance is clearly seen. The intensity variation shows the larger high-order aberration of this eye.

In middle Figure 5.5 and upper Figure 5.6 are illustrated measurements of an hyperopic eye, HY2, of (S+2.55D, C+0.5D, X10) and best-correction RMS WF of 0.079 μm. The streak projection moves along the 10-degree meridian. The characteristics of with-motion in the plane-mirror setting and against -motion in concave-mirror operation are clearly shown. Similarly, in lower Figures 5.5 and 5.6, the observations of a myopic eye model, MY3, with prescription of (S–6.0D, C+0.75D, X70) and best-correction RMS WF of 0.117 μm are predicted and the against-motion and with-motion behaviors, respectively, in plane- and concave-mirror operations are clearly demonstrated. One observation to be noticed is the so-called "cut-off" phenomenon that occurs when the edge of projection falls inside the pupil. This effect is present in the against-motion cases in lower Figure 5.5 and upper Figure 5.6. In these two sets of images, the appearance of the edge doesn't affect the judgment on reflex movement. However, at certain conditions, anomalous reflex motions occur.

The anomalous motion is often observed at high myopic or accommodative conditions in infants or patients with large pupils. This phenomena was first reported by Borish in 1970 [Borish 1970] and named the cut-off phenomena. Later, Howland in 1978 [Howland 1978] and Mutti in 2004 [Mutti 2004] investigated the geometric causes of this anomalous motion. Figure 5.7 shows the simulation of such observation in the myopic eye, MY3, with 5.65 mm pupil. Under plane-mirror operation, the myopic eye should be against-motion, but because of the edge-effect that occurs at sideways, 5, 7, and 9 mm, the reflex motion appears as with-motion. If one looks carefully at the center images without edge influence, the movement of reflex, although not clear, is against-motion as it should be. This is more evident from the false-color images (shown in Figure 5.7).

***D** Scissors reflex in the keratoconus patient*

The simulation results using a personalized keratoconus (KC) eye model are shown in Figure 5.8. This KC eye has a protruding cone of about 60 μm in the lower left quadrant in its topography. The manifest refraction is (S–6.00D, C+6.00D, X135), and the best-correction RMS WA is 1.994 μm. The upper set of images in Figure 5.8 shows the result of rotating the retinoscope projection at a distance of 0.5 meter. Although the refraction of –6.00D is significant, the strip-shaped reflex is not observed. Instead, a typical keratoconus "shadow" appears in the retinoscopic reflex. The irregular intensity distribution shows the significant high-order aberration and especially the coma of this eye. The lower set of images shows the so-called scissors reflex of KC eye as the projection moves along the meridian of 135 degree. The opening and closing movements of a pair of scissors is clearly shown.

***E** Hourglass shape streak reflex with high SA:*

In the recent years, case observations suggested that inadvertently induced spherical aberration from surgical procedures such as the Schachar's sclera band procedure and the use of intraocular lens produce "pseudoaccommodation" in presbyopia patient vision. One of such cases was reported by Dr. Guyton in Johns Hopkins in 2002 [Guyton 2002]. He had the opportunity to examine a patient after surgery for presbyopia. The patient had relied on the reading glasses for near vision and had undergone Schachar's scleral band procedures for presbyopia. 2 to 3 months later, she went without glasses entirely, with 20/20 uncorrected visual acuity at both distance and near. However, in the dynamic retinoscopic reflex examine,

Dr. Guyton observed the static hourglass shape of reflex, instead of streak reflex, for both near and distant visions, demonstrating the absence of actual accommodation. He suspected that the hourglass reflex indicates a condition of high degree of spherical aberration, which provides an effect of long focal depth, or the so-call "pseudoaccommodatrion".

Guyton's observation has been reproduced with our retinoscopy simulation using eye models. We examine the effect of spherical aberration on the near and far visions of presbyopia patients. The Navarro eye model is used as the base model, and a ZERNIKE phase plate is utilized on the surfaces of either the anterior cornea or the lens to produce spherical aberration of the desired magnitude. The previously described setup of the retinoscpy was applied. Then we reproduced the hourglass shape reflex (shown in figure 5.9). The entrance pupil diatmeter is 5mm; the sleeve position of the retinoscope is 20mm (plain-mirror position); the working distance is 500mm. Figure 5.9a corresponds to the case of putting the phase plate on the anterior lens surface while Figure 5.9b is showing the result when the phase plate was put on the anterior cornea surface. In these two setting, the total SA are same. Thus we can conclude that the original positions of SA have effect on the final reflex appearance. The variation of streak width is smaller when SA appears on the anterior lens surface than on the anterior cornea surface. The visions of letter chart at near and far are also examined and published in the conference ARVO 2009 [Tan 2009]. These results faithfully reproduce the clinical condition in the 2002 case.

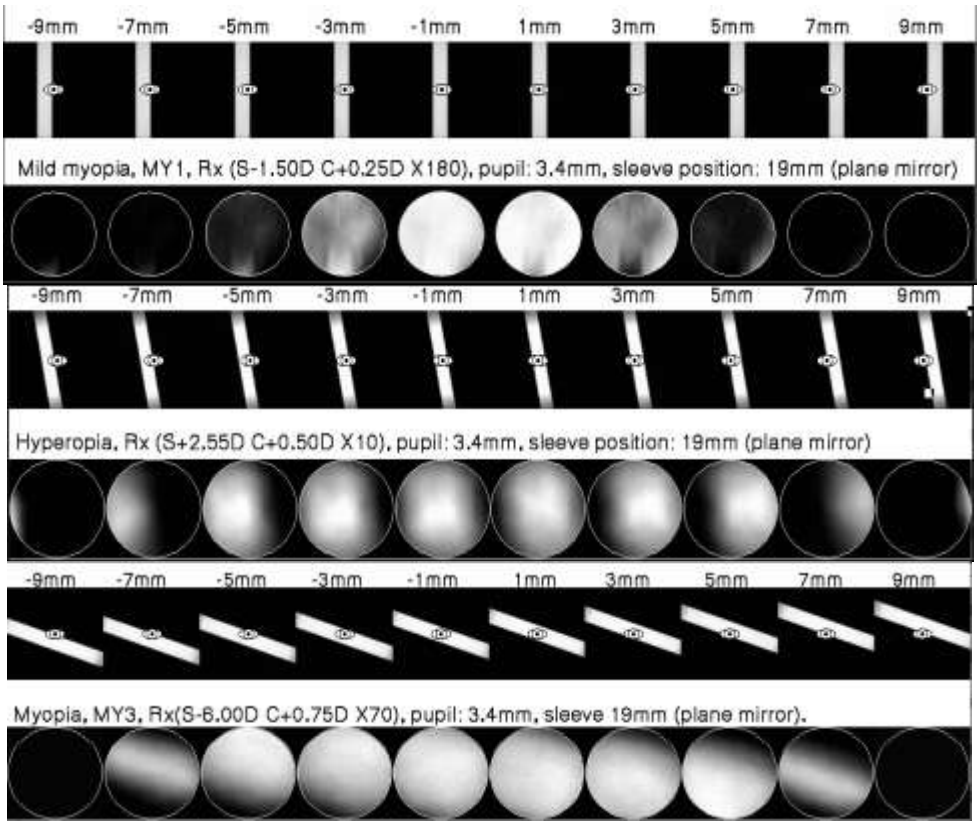

Figure 5.5 *Predicted retinal reflex motion of neutralization (top), with motion (middle), and against motion (bottom). Sleeve of retinoscope is located at 19 mm above the filament (plane-mirror).*

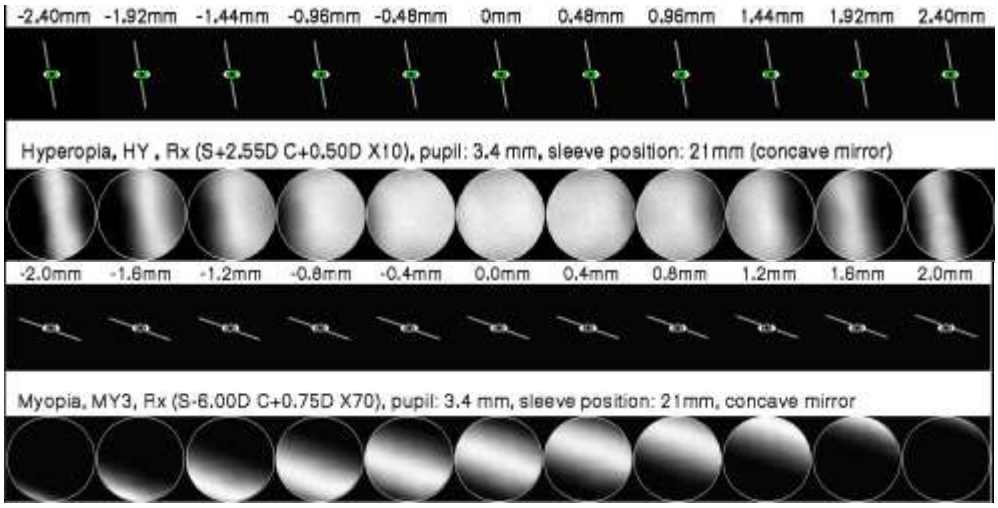

Figure 5.6 *Predicted retinal reflex motion of with motion and against motion under concave-mirror operation. Sleeve of retinoscope is located at 21 mm above the filament.*

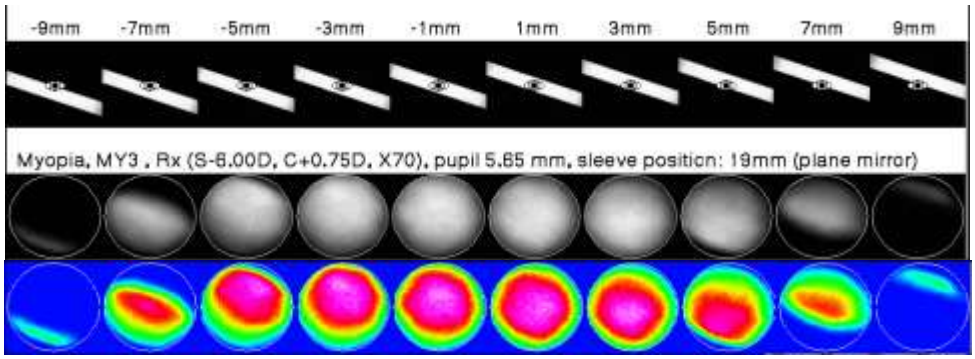

Figure 5.7 *Anomalous retinal reflex of a myopic eye from a streak retinoscope. The top row shows the streak beam swiping from the left to the center of pupil. Sleeve position of retinoscope is 19 mm above the filament (plane mirror).*

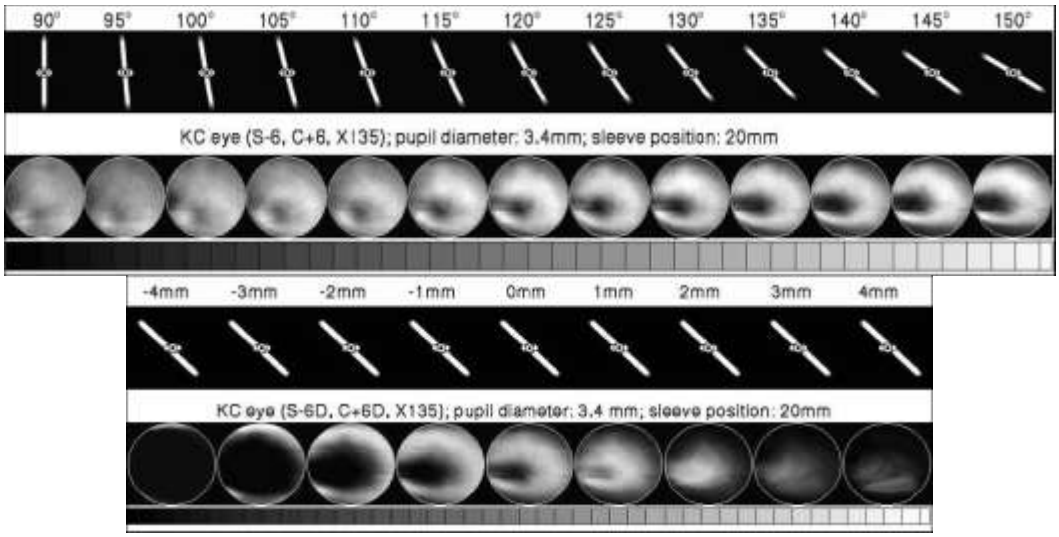

Figure 5.8 *Simulated retinoscopic observation of a keratoconus eye. The upper images show the observation when the streak rotates along the pupillary axis. The lower images show the observation when streak swipes across the pupil in 135 degree angle. The scissors reflex that indicates the irregular cornea surface is clearly shown.*

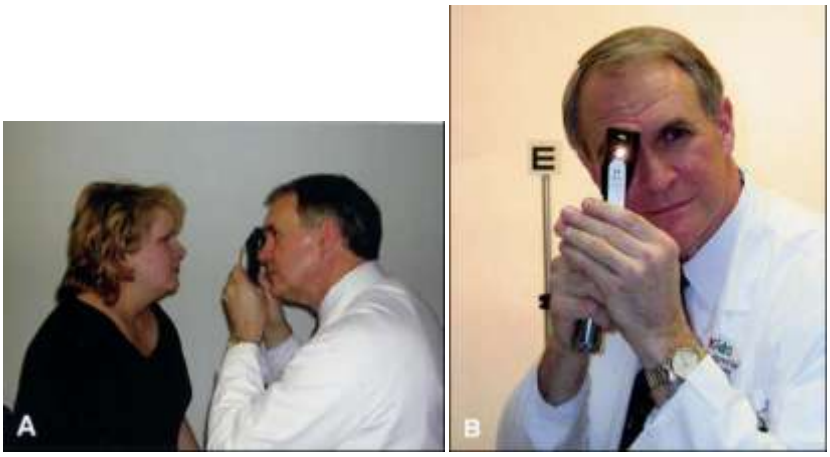

Figure 5.8 *Dynamic retinoscopy without lenses. The patient (A), wearing refractive correction if any, looks alternately between a distant target and a near accommodative target that the examiner holds just beneath the retinoscope peephole (B). Accommodation is observed objectively by neutralization of the "with" retinoscopic reflex when the patient accommodates to the plane of the near target.*

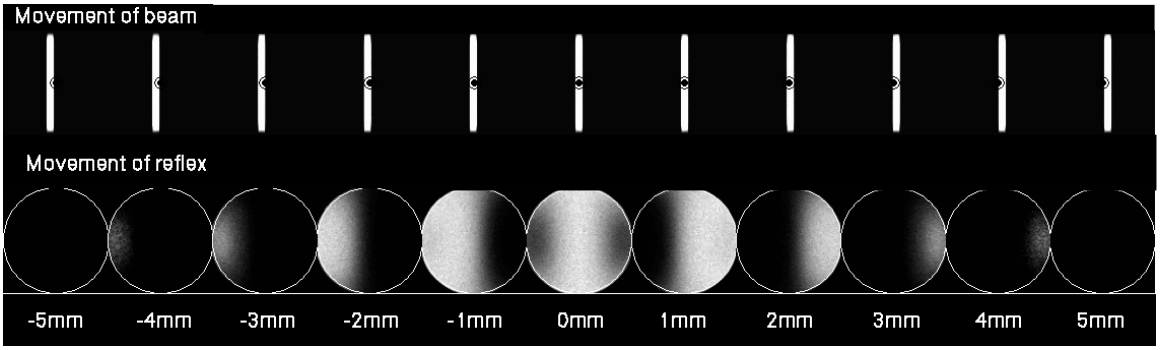

a. SA is added on the lens surface

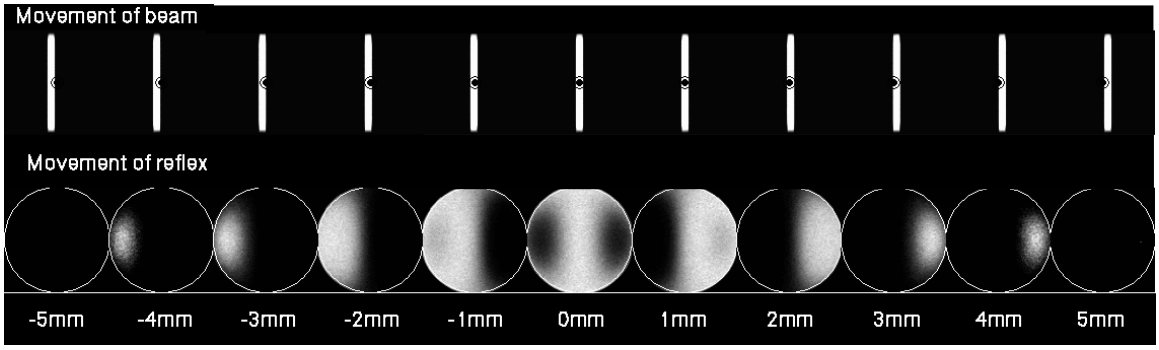

b. SA is added on the cornea surface

Figure 5.9 *Hourglass shaped retinoscope reflex*

5.2 Simulation of photorefraction (PR) measurement

5.2.1 Photorefraction (PR)

Stationary photorefraction (PR) was introduced during the 1970s and 1980s by replacing the observer's eye with a camera [Kaakinen 1979, Howland 1985, and Bobier 1985]. The stationary PR is classed into two types: the coaxial photorefraction (CPR) and the eccentric photorefraction (EPR). The CPR method has the light source rested in front and at the center of the camera lens [Howland 1974, and Howland, 1983]. The light coming out from the eye to the camera is defocused into a blur pattern, which changes with the eye's defocus. CPR bases the estimation of the state of refractive error on the extent of the defocused retinal reflex. In contrast, EPR places a light source eccentric from the camera lens aperture and the camera is focused right on the examined eye to form a sharp pupil image as shown in the Figure 5.10 [Kaakinen 1979, Howland 1985, and Bobier 1985]. EPR includes only one small light source beside a camera that is away from the patient. When the light illuminates the eye the retina reflex return to the camera and a photograph is taken. For a normal eye that is focused on the camera and light source plane, the returning reflex will propagate toward the exact position of the light source. Therefore, all the rays will not get into the camera. The entire pupil will appear to be dark as a result. However, if the eye is near-sighted (i.e. focused at near location), the returning rays are converged between the camera and the eye. As illustrated in the figure, only the rays through the lower part of the pupil can get into the camera. The bright crescent will appear to be at lower part (i.e. the same side of the light source related to camera). For far-sighted eyes, the pupil will only be bright at the opposite corner of the light source. EPR calculates the state of refractive error from the size of bright crescent that appears in the focused pupil image. EPR is currently the most used PR method to screen for binocular refractive errors in children and for detection of accommodation in animals in the research labs. The commercial PR instruments for pediatric vision screening include at least the iScreen Photoscreener [iScreen, Inc., Memphis, TN], the MTI Photoscreener [Medical Technology, Inc., Cedar Falls, Iowa], and the Power Refractor II [Plusoptix, Nuremburg, Germany].

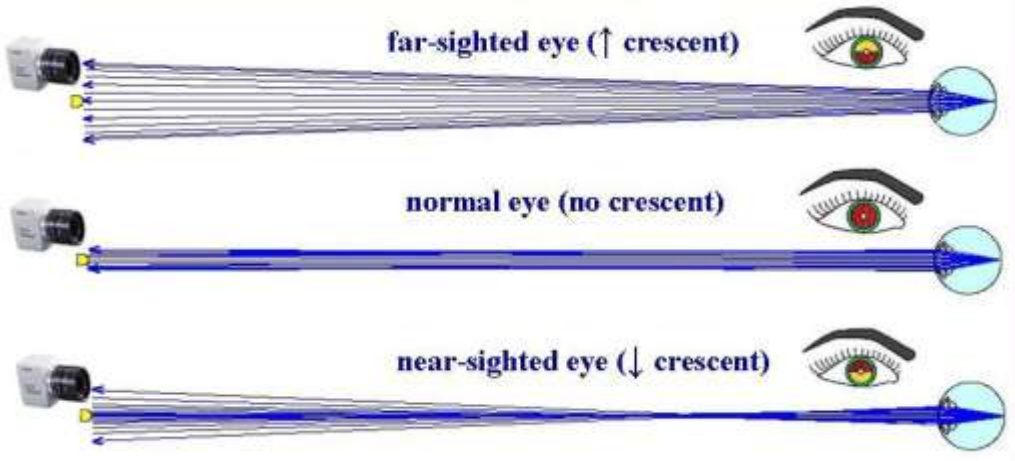

Figure 5.10 *Photorefraction diagram*

5.2.2 Method

The simulation of eccentric photorefraction measurement is even more straightforward than the retinoscopy. As Figure 5.11 shows, the double path calculation includes: the step 1 of only one light source and a forward eye model, and the step 2 of plainly a backward eye model and one camera system. The simple optics of photorefraction is actually more advantageous compared to retinoscopy. As mentioned earlier, retinoscopy encounters multiple optical stops that are restricted by the components' mounts in a retinoscope and the pupil stop in the human eye. When moving the scope, the misalignment of these stops result to significant and complicated vignetting effects and lead to ambiguous results. Another benefit of EPR over retinoscope is the ability of using the narrow band infrared light source, which controls the chromatic aberration problem and reduce the intensive stimulation to the pupil response. Devices that use infrared light sources are the PowerRefractor and the CLA prototype device. The UTSI CLA device further include an optical beam splitter and a 2-dimentional multiple LED light source panel that comprises a coaxial source as well as multi-meridian and eccentricity sources as shown in Figure 5.11. In the PR simulation I performed, retinal surface is assumed to be totally diffusive. Stiles Crawford Effect is ignored. Further computation detail is described in the 2003 and 2007 publications [Chen 2003, and Tan 2007].

5.2.3 Results

A. Commercial EPR device measurement of normal eyes with refractive error:

In our 2003 paper [Chen 2003], EPR simulation was performed using the optical parameters of the commercial device, iScreen Photoscreener [iScreen, Inc., Memphis, TN]. Three generic eye models, the Navarro model [Navarro 1985], Arizona model [Greivenkamp 1995], and Liou model [Liou 1997], were tested with induced refractive errors as described in Chap3. The measurement simulation results of the 3 models are compared. The influence of ocular chromatic aberration as well as the monochromatic spherical aberration upon the EPR measurement was concluded with a formula. The pupil size effect on the PR measurement was also investigated. Shown in Figure 5.12 is the measurement of my eyes in comparison to the simulation results. As indicated in the figure, by wearing contact lenses, my right eye was +4 diopter far-sighted and left eye is -4 diopter near-sighted. The lower portion of the figure shows the simulation prediction of eyes with refractive error from +10 to -10 diopters. Figure 5.13 is the investigation performed to compare the racial difference due to the pigment associated retinal discrepancy. Figure 14 is a simulation result that has never been published. It investigates the influence of gazing angle on the EPR measurement. As the picture shows, the crescent size and shape are altered by the gazing condition. The tilting of the crescent, which is interpreted as the presence of astigmatism by iScreen and MTI readers, can be clearly seen in both experimental data in Figures 5.12 and 5.13.

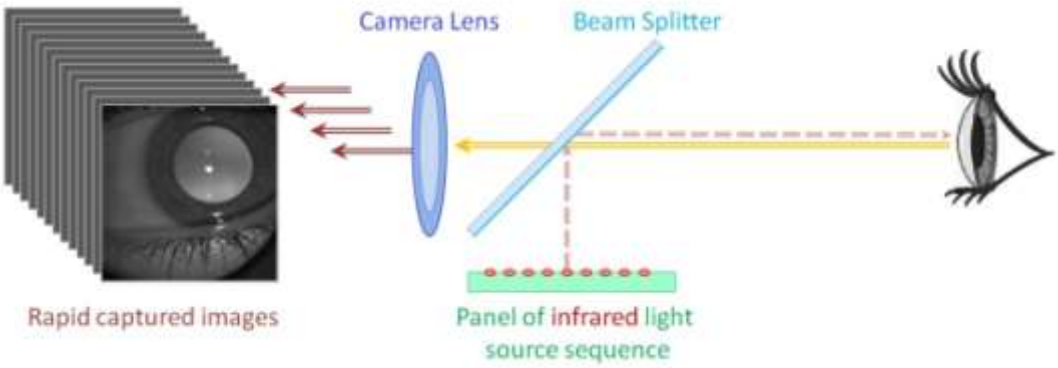

Figure 5.11 *The optical setup of photorefraction prototype.*

Experiment PR Image

+4 diopter (far-sighted) -4 diopter (near sighted)

Computer Simulation PR Reflex of Refractive Eyes

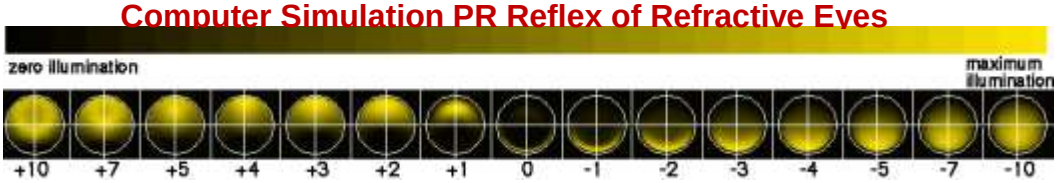

Figure 5.12 *PR images of refractive eyes. (upper): image acquired with my eyes (with contact lenses) (lower): simulation results of +10 to -10 diopter refractive errors.*

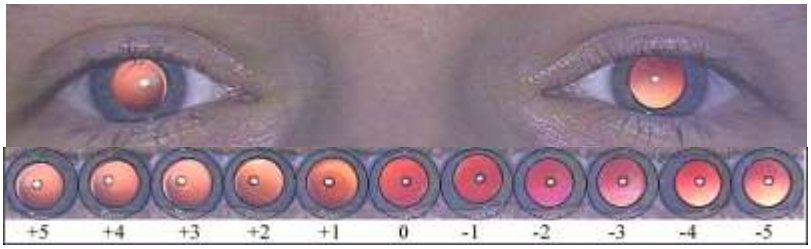

Figure 5.13 *EPR image of a Caucasian using iScreen photoretinoscope. Lower area is portions cropped from the original photographs. The iris, pupil, and the 1st Purkinje image in each photograph are circled using a target-finding program. The corresponding refractive error (in diopter) is indicated.*

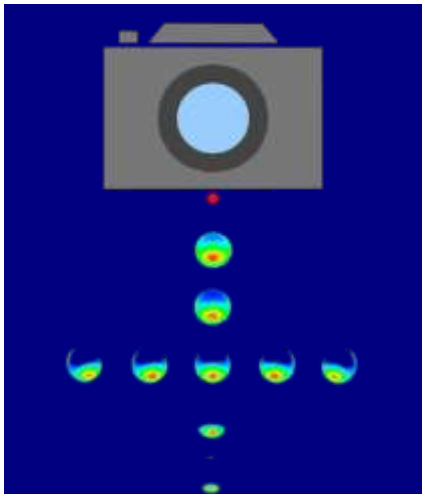

Figure 5.14 *Investigation of gazing angle effect on the EPR measurement. The night reflex images in the lower portion are results corresponding to the measurement of a -5 diopter- near-sighted eye with gaze of zero (centered reflex), 10 prism diopters, and 20 prism dioptes in 4 directions.*

B. CLA prototype measurement of eyes with monochromatic aberration:

Unlike the traditional single-frame iScreen and MTI devices that use visible flash lamp as light source, CLA prototype acquires multi-meridian, multi-eccentricity PR image with near infrared LEDs. The optical setting is as shown in the Figure 5.11. In our 2006 Optics Express paper [Chen 2006], I simulated the measurements using optical parameters of CLA prototype and the customized eye models of KC patients and normal ammetropic eyes. With clinical trial performed in Wang Vision Institute (UTK Institution Review Board Approval IRB # 7024B), the patient data of the prototype were obtained for comparison. In the study, 5 normal myopic personalized eye models and 5 personalized KC eye models were constructed with their clinical topography data and refractive error data. Shown in Figure 5.15 is the comparison between simulated results (on the left) and the images acquired from the prototype (on the right) of a myopic eye. The refractive error condition and the RMS WF error are as specified in the figure. The color maps in the middle are the clinically acquired topography of the patient (upper) and the numerically extrapolated topography that is used for the personalized eye modeling. The clinical data with missing data points near the eye lids areas is typical since the eye lids and eye lashes are often get in the way of the measurement. The 5 circular images are the PR reflex images. The center one is the coaxial and the 4 outside are the eccentric PR images. On the very right is the infrared raw image before process. The EPR images of the myopic eye show the brightness distribution toward outward.

Similar to Figure 5.15, Figure 5.16 shows the case of a keratoconus eye. The high-order aberration of thus eye is much larger compared to the myopic eye as indicated by the RMS WF error. Both the measured images on the right and the simulated images show no symmetricity reflex as in the Figure 5.15. The comparison between the simulation and the experiment data validates the faithfulness of personalized eye modeling technique.

Further shown in Figure 5.17 is the simulation result that has not yet been published. This simulation used personalized eye modeling with not only the topographic patient data, but also the wavefront aberration data of the patient. The simulation is executed using the optical setting of more recent version of CLA prototype. The experiment data of the same patient is shown on the right for comparison. The predicting capability of personalized modeling technique offers a promising future for extensive applications.

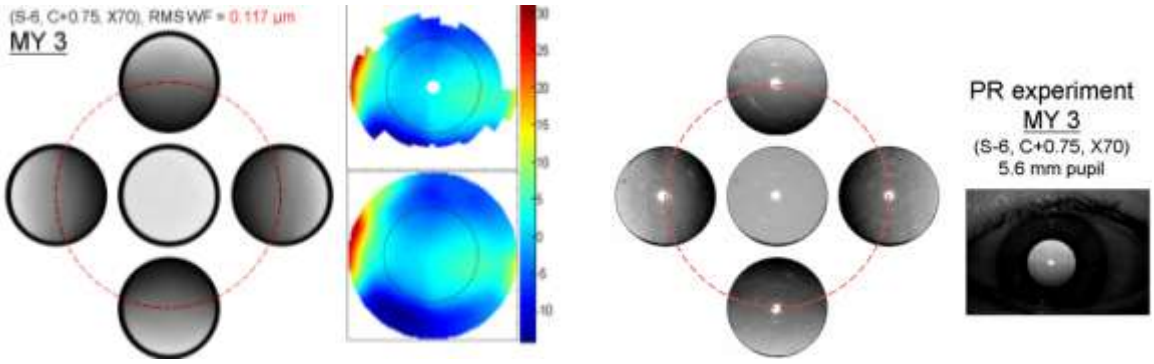

Figure 5.15 (*Left): Simulated prediction of CLA prototype measurement using personalized eye model of a myopic eye. The 2 color pictures are the clinical data of topography (upper) and the computer-extrapolated data for eye modeling. (Right): Experimental data from the real eye. Picture on the very right is the raw infrared photograph.*

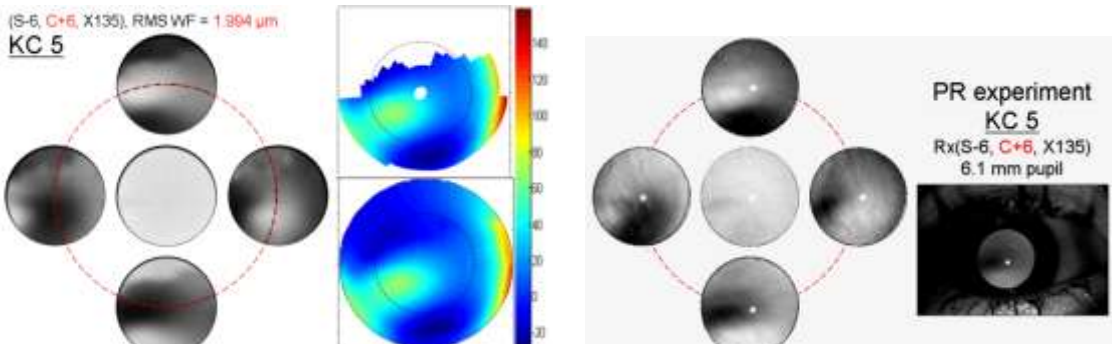

Figure 5.16 *(Left): Simulated prediction of CLA prototype measurement using personalized eye model of a keratoconus eye. The 2 color pictures are the clinical data of topography (upper) and the computer-extrapolated data for eye modeling. (Right): Experimental data from the real eye. Picture on the very right is the raw infrared photograph.*

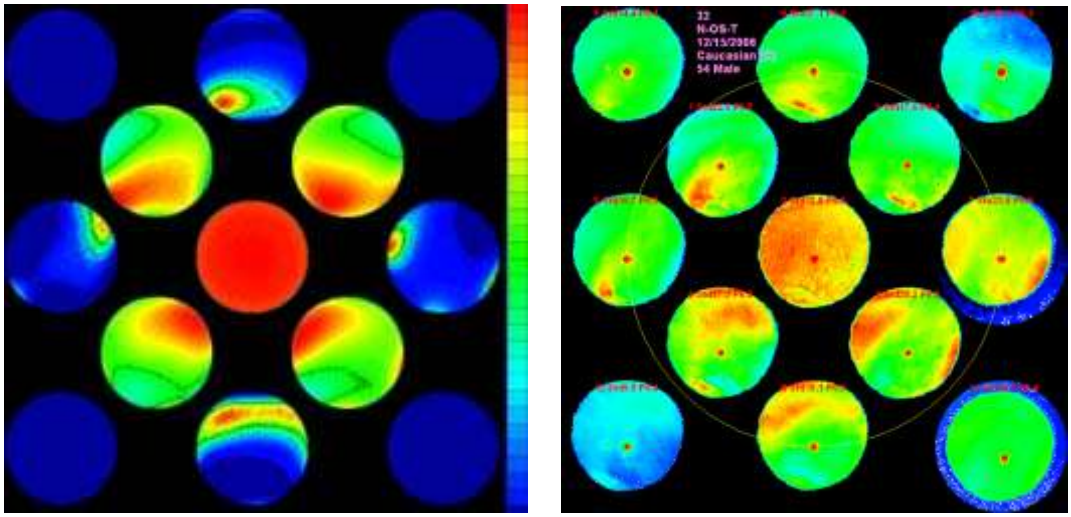

Figure 5.17 *(Left) Simulated prediction of CLA prototype measurement using personalized eye model with corneal topography and WFA measurement result. (Right): Experimental data from the real eye.*

Chapter 6 Conclusion

The capability to provide accurate predictions of vision performance and ophthalmic diagnostics of healthy and diseased eyes is desired. If such a computational capability existed, it would serve as a needed stepping stone for dramatic changes that could result in ocular instrument design and development, ophthalmic medical education, and ocular telemedicine. Physics and mathematical models of the eye would then be used with computational methods to simulate and predict accurately ocular characteristics and responses to varied stimuli. The paradigm of instrument development and testing can be adapted to achieve faster deployment of diagnostic instrumentation if demographically representative ocular responses were confidently known at the outset of the development. Similar advances are possible in medical training if realistic diagnostic device behavior could be demonstrated for students using computed images of disease and conditions. Finally, opportunities in telemedicine and expert system-based diagnostic and referral decisions become possible and practical. The major obstacles to this capability have been two-fold: 1) the absence of demographically specific characteristics of the ocular model of health and diseased eyes and 2) the verification that such a data-base of ocular characteristics can be used in computations to provide accurate predictions. This research is the initial step in addressing and solving these problems.

Traditional eye models are typically based on average ocular biometry in limited population groups. This dissertation concentrated on pioneer developments in two specific areas: first, the broad and general population-based general eye modeling that describes the statistics in more specified population and second, the personal-tailored, microscopic eye modeling that illustrates individual detailed characteristics. Chapters 2 to 5 cover the technical considerations of optical eye modeling using the most recent ocular biometry and clinical data. In Chapter 2, I collected hundreds of journal papers that report ocular biometry measurements. I reviewed the contemporary techniques of measuring the ocular biometry and updated the literature review for the required parameters for general population-based eye modeling. This thorough analysis is essential to understand the variation of parameters, accuracies, and precisions among different measurement approaches and to gain the knowledge of the statistical distributions and discrepancies among different generic or geographic groups. The published results are plotted in figures and summarized in tables for clearer comparisons and ease of update.

In Chapters 3 and 4, the techniques of eye modeling are detailed with the commonly used optical software ZEMAX. Based on my experience in the past a few years, the selection of appropriate merit functions and optimization procedures were determined and are given in Chapter 3, with the deliberations in both visual science and optical computation aspects. Following the construction of a reasonably accurate initial model, optical optimization is the key procedure to achieve a more specific eye model through assigning the appropriate free variables and defining the suitable merit functions. The choice of different merit functions leads to different optimization results. Therefore, a detailed discussion about the different optical merit functions is given. The conclusions provide a knowledge base on how to select the right merit function according to different optimization goals. In summary, the merit function of RMS WFA reference to centroid ray is sufficient to construct a general ametropic eye model with clinical prescription. The merit function of Strehl ratio in space domain (SRX), in addition to the initial default optimization, is sufficient to construct a personalized eye model that is described by the clinical refraction prescription and ocular dimension measurement(s). Finally, merit functions assigned to approach all Zernike coefficients are adequate to create the wavefront-corrected personalized eye model.

Following the technical conclusions of Chapter 3, the step-by-step procedures of the population-based eye modeling and the personalized eye modeling are addressed in the first two sections of Chapter 4. Considerations of population-based eye modeling are given with examples of the ametropic eyes that describe any assigned refractive error status, accommodative eye that illustrate arbitrary focusing extent, age-dependent eye, and general KC eyes that express the disease in various progressing stages. This type

of models is established upon the prior knowledgebase of statistics and characteristic descriptions of particular population. In contrast, personalized optical eye modeling relies on the clinical measurements of individual human eye. The procedure is similar to that of general eye modeling with an initial generic schematic eye. Substitution of the ocular parameters of patient's clinical data, optimization(s) was performed to obtain and to validate the optical quality and performance of the same eye. Certain conditions including optical opacities, irregular optical surfaces, multiple reflection, scattering, and spectral properties of the ocular media are discussed. The technical difficulties and possible solutions are provided in the discussion. Additional validation tools for eye modeling are also addressed at the end of this chapter.

Optical eye modeling has a variety of applications. In this chapter is presented an example in the population-based eye modeling section that is one of the most significant contributions of this work: the pioneering investigation on how the diseased eye of keratoconus influences the visions [Tan 2008]. As the irregular cone develops, the patient vision degeneration is mathematically illustrated in the forms of refractive error, astigmatism, and high-order aberrations. The computational investigation was performed for the isolated geometric factors of the abnormal corneal shape: the cone dimension, location, and irregularity of cone shape. A second application example is given in the last section of Chapter4: the validation of personalized eye models. The realistic patient vision simulation can be used use for medical training, patient education, and consultation.

In Chapter 5, applications in the predicting ophthalmic measurements are presented as the further demonstration. In addition to the published journal papers that I summarize in this chapter, I include a few more recent unpublished simulation results. In summary, the major research contribution includes the construction of the ground-breaking keratoconus eye modeling (Chapter 4), the realistic measurement simulation for instrumentation (Chapter 5) [Chen 2006], and the first demonstration of contemporary ophthalmic measurement simulation [Tan 2007] for medical training application (Chapter 5).

References

Reference

- Allouch, C., Touzeau, O., Kopito, R., Borderie, V., and Laroche, L. (2005) Crystalline lens biometry using A-scan ultrasound and the Orbscan device. J Fr Ophtalmol. 28(9), 925-32.
- Alpern, M, and Campbell, F. W. (1962) The spectral sensitivity of the consensual light reflex. J Physiol. 164, 478-507.
- Alsbirk, P. H. (1978) Corneal thickness. 1. Age variation, sex difference and oculometric correlations. Acta Ophthalmol Scand 56, 95-104.
- Alsbirk, P. H. (1977) Variation and heritability of ocular dimensions. A population study among adult Greenland Eskimos. Acta Ophthalmol (Copenh). 55(3), 443-56.
- Altinok, A., Sen, E., Yazici, A., Aksakal, F. N., Oncul, H., and Koklu, G. (2007) Factors influencing central corneal thickness in a Turkish population. Current Eye Research, 32, 413-19.
- American National Standards Institute (2004) Methods for reporting optical aberrations of eyes. ANSI Z80.28-2004
- Applegate, R. A., and Lakshminarayanan, V. (1993) Parametric representation of Stiles-Crawford functions: normal variation of peak location and directionality. J Opt Soc Am A. 10(7), 1611-23.
- Artal, P., and Navarro, R. (1992) Simultaneous measurement of two-point-spread functions at different locations across the human fovea. Applied Optics, 31(19), 3646-56.
- Atchison, D. A., Markwell, E. L., Kasthurirangan, S., Pope, J. M., Smith, G., and Swann, P. G. (2008) Age-related changes in optical and biometric characteristics of emmetropic eyes. J. Vis. 8(4):29, 1-20.
- Atchison, D. A. (2006) Optical models for human myopic eyes. Vision Research 4614), 2236-50.
- Atchison, D. A., & Charman, W. N. (2005). The influences of reference plane and direction of measurement on eye aberration measurement. Journal of the Optical Society of America A. Optics and Image Science, 22, 2589-97.
- Atchison, D. A., Jones, C. E., Schmid, K. L., Pritchard, N., Pope, J. M., Strugnell, W. E., and Riley, R. A. (2004) Eye shape in emmetropia and myopia. Invest Ophthalmol Vis Sci. 45(10), 3380-6.
- Atchison, D. A., and Smith, G. (2000) Optics of the Human Eye. By Elsevier Health.
- Avila, M. T., Sherr, J. D., Hong, E., Myers, C. S, and Thaker, G. K. (2003) Effects of nicotine on leading saccades during smooth pursuit eye movements in smokers and nonsmokers with schizophrenia. Neuropsychopharmacology. 28 (12), 2184-91.
- Barbero, S. (2006) Refractive power of a multilayer rotationally symmetric model of the human cornea and tear film. J Opt Soc Am A Opt Image Sci Vis. 23(7), 1578-85.
- Baumgartner, A., Möller, B., Hitzenberger, C. K., Drexler, W., and Fercher, A. F. (1997) Measurements of the posterior structures of the human eye in vivo by partial coherence interferometry using diffractive optics. Proc SPIE 2981, 85-91.
- Beckmann, P. (1967) Scattering of light by rough surfaces. In: Wolf, E. (Ed.) Progress in Optics: Vol VI, 53-69. Amsterdam: North-Holland Publishing Company.
- Benedetto, D. A, Clinch, T. E., and Laibson P. R. (1984) In vivo observation of tear dynamics using fluorophotometry. Arch Ophthalmol. 102, 410–412.
- Berger, R. E., and Corrsin, S. (1974) A surface tension gradient mechanism for driving the pre-corneal tear film after a blink. J Biomech. 7, 225-38.
- Bestelmeyer, P. E., Tatler, B. W., Phillips, L. H., Fraser, G., Benson, P. J., and St Clair, D. (2006) Global visual scanning abnormalities in schizophrenia and bipolar disorder. Schizophr Res. 87(1-3):212-22. Epub 2006 Jul 24.

- Blix, M. (1880) Oftalmometriska studier. Upsala Läkareförenings Förhandlingar 15, 349.
- Bobier, W. R., and Braddick, O. J. (1985) Eccentric photorefraction: optical analysis and empirical measures. Am J Optom Physiol Opt. 62(9), 614-20.
- Borish, I. M. (1970) Clinical refraction, 3rd ed. Professional press, Chicago, IL.
- Born, M., and Wolf, E. (1980) Principles of optics, Pergamon Press, UK.
- Brown, N. P. (1974). The change in lens curvature with age. Experimental Eye Research, 19, 175–183.
- Bruckner, V. R. (1962) Exacte strabismusdiagnostic bei 1/2 – 3 jahrigen Kindern mit einem einfachen Verfahren, dem "Derchleuchtungstest". Ophthalmologica 144, 184-98.
- Cameron, B. D., and Anumula, H. (2006) Development of a real-time corneal birefringence compensated glucose sensing polarimeter. Diabetes Technol Ther. 8(2):156-64.
- Cardascia, N., Tommasi, R., Vetrugno, M., Sborgia, G., Lugara, P. M., and Sborgia, C. (2006) Indocyanine green laser retinal oximetry: preliminary report. Adv Exp Med Biol. 578, 143-8.
- Carney, L. G., Mainstone, J. C., and Henderson, B. A. (1997) Corneal topography and myopia. A cross-sectional study. Invest Ophthalmol Vis Sci. 38(2), 311-20.
- Carney, L. G., and Hill, R. M. (1982) The nature of normal blinking patterns. Acta Ophthalmol (Copenh). 60.
- Chang, S. W., Tsai, I. L., Hu, F. R., Lin, L. L., and Shih, Y. F. (2001) The cornea in young myopic adults. Br J Ophthalmol. 85(8), 916-20.
- Charman, W. N. (1980) Reflection of plane-polarized light by the retina. Br J Physiol Opt. 34, 34-49.
- Chau, A., Fung, K., Pak, K., and Yap, M. (2004) Is eye size related to orbit size in human subjects? Ophthalmic Physiol Opt. 24(1), 35-40.
- Chen Y.-L., Tan, B., Baker, K., Lewis, J. W. L., Swartz, T., Jiang, Y., and Wang, M. (2006) Simulation of keratoconus observation in Photorefraction. Optics Express 14(23), 11477-85.
- Chen, Y.-L., Tan, B., and Lewis, J. W. L. (2003) Simulation of eccentric photorefraction images 11(14) Optics Express 1628-42.
- Cheng, H. M., Singh, O. S., Kwong, K. K., Xiong, J., Woods, B. T., and Brady, T. J. (1992) Shape of the myopic eye as seen with high-resolution magnetic resonance imaging. Optom Vis Sci. 69(9), 698-701.
- Cho, P., and Lam, C. (1999) Factors affecting the central corneal thickness of Hong Kong Chinese. Curr Eye Res 18, 368-74.
- Chui, T. Y., Yap, M. K., Chan, H. H., and Thibos, L. N. (2005) Retinal stretching limits peripheral visual acuity in myopia. Vision Res. 45(5), 593-605.
- Cook, A., White, S., Batterbury, M., and Clark, D. (2003) Ocular growth and refractive error development in premature infants without retinopathy of prematurity. Invest Ophthalmol Vis Sci. 244(3), 953-60.
- Cosar, C. B., and Sener, A. B. (2003) Orbscan corneal topography system in evaluating the anterior structures of the human eye. Cornea, 22, 118-21.
- Davis, W. R., Raasch, T. W., Mitchell, G. L., Mutti, D. O., and Zadnik K. (2005) Corneal asphericity and apical curvature in children: a cross-sectional and longitudinal evaluation. Invest Ophthalmol Vis Sci. 2005 46(6), 1899-906.
- Delori, F. C., and Pflibsen, K. P. (1989) Spectral reflectance of the human ocular fundus. Applied Optics, 28(6), 1061-77.
- Denninghoff, K. R., Smith, M. H. Lompado, A., and Hillman, L. W. (2003) Retinal venous oxygen saturation and cardiac output during controlled hemorrhage and resuscitation, J. Appl Physiol 94(3), 891-6.

- Dohadwala, A. A., Munger, R., and Damji, K. F. (1998) Positive correlation between Tono-Pen intraocular pressure and central corneal thickness. Ophthalmology 105, 1849–54.
- Donnelly, W. J. 3rd, Pesudovs, K., Marsack, J. D., Sarver, E. J., and Applegate, R. A. (2004) Quantifying scatter in Shack-Hartmann images to evaluate nuclear cataract. J Refract Surg. 20(5), S515-22.
- Dorsch, R. G., Haimerl, W. A., and Esser, G. K. (1998) Accurate computation of mean power and astigmatism by means of Zernike polynominals. JOSA A, 15(6), 1686-8.
- Doughty, M., and Zaman, M. (2000) Human Corneal Thickness and Its Impact on Intraocular Pressure Measures1, 2A Review and Meta-analysis Approach Survey of Ophthalmology, 44(5), 367-408.
- Drexler, W., Findl, O., Menapace, R., Rainer, G., Vass, C., Hitzenberger, C. K., and Fercher, A. F. (1998a) Partial coherence interferometry: a novel approach to biometry in cataract surgery. Am. J. Ophthalmol. 126(4), 524-34.
- Drexler, W., Findl, O., and Menapace, R., et al. (1998b) Dual beam optical coherence tomography: signal identification for ophthalmologic diagnosis. J. Biomed. Opt. 3, 55– 65.
- Drexler, W., Findl, O., Schmetterer, L., Hitzenberger, C. K., and Fercher, A. F. (1998c) Eye elongation during accommodation in humans—differences between emmetropes and myopes. Invest. Ophthalmol. Vis. Sci. 39, 2140-7.
- Drexler, W., Baumgartner, A., Findl, O., Hitzenberger, C. K., Sattmann, H., and Fercher, A. F. (1997a) (Sub)micrometer precision biometry of the anterior segment of the human eye. Invest. Ophthalmol. Vis. Sci. 38, 1304-13.
- Drexler, W., Findl, O., and Menapace, R., et al. (1997b) Clinical feasibility of dual beam optical coherence topography and tomography for ophthalmologic diagnosis. ARVO Abstracts. Invest. Ophthalmol. Vis. Sci. 31(4, suppl), 217.
- Drexler, W., Hitzenberger, C. K., Sattmann, H., and Fercher, A. F. (1995) Measurement of the thickness of fundus layers by partial coherence tomography. Opt Eng 34, 701-10.
- Dubbelman, M., Sicam, V., and Van der Heijde, G. L. (2006) The shape of the anterior and posterior surface of the aging human cornea. Vision Research, 46(6-7), 993-1001
- Dubbelman, M., Van der Heijde, G. L., and Weeber, H. A. (2005) Change in shape of the aging human crystalline lens with accommodation. Vision Res. 45(1), 117-32.
- Dubbelman, M., Weeber, H. A., van der Heijde, R. G., and Völker-Dieben, H. J. (2002) Radius and asphericity of the posterior corneal surface determined by corrected Scheimpflug photography. Acta Ophthalmol Scand. 80(4):379-83.
- Dubbelman, M., and Van der Heijde, G. L. (2001) The shape of the aging human lens: curvature, equivalent refractive index and the lens paradox. Vision Res. 41(14), 1867-77.
- Dunne, M. C., Royston, J. M., Barnes, D. A. (1992) Normal variations of the posterior corneal surface. Acta Ophthalmol (Copenh). 70(2), 255-61.
- Edmund, C., and Sjøntoft, E. (1985) The central-peripheral radius of the normal corneal curvature. A photokeratoscopic study. Acta Ophthalmol (Copenh). 63(6), 670-7.
- Ehlers, N., and Hansen, F. K. (1976) Further data on biometric correlations of central corneal thickness. Acta Ophthalmol Scand 54, 774-8.
- Ehlers, N. (1965) The thickness of the precorneal tear film. Acta Ophthalmol (Copenh). 81, 92–100.
- Emsley, H. H. (1952) Visual optics. London, Butterworth.
- Escudero-Sanz, I., and Navarro, R. (1999) Off-axis aberrations of a wide-angle schematic eye model. JOSA A, 16(8), 1881-91

- Eysteinsson, T., Jonasson, F., Sasaki, H., Arnarsson, A., Sverrisson, T., Sasaki, K., et al. (2002) Central corneal thickness, radius of the corneal curvature and intraocular pressure in normal subjects using noncontact techniques: Reykjavik Eye Study. Acta Ophthalmologica Scandinavica, 80, 11-15.
- Fercher, A. F. (1996) Optical coherence tomography. J. Biomed. Opt. 1, 157-73.
- Fercher, A. F., Hitzenberger, C. K., Drexler, W., Kamp, G., and Sattmann, H. (1993) In vivo optical coherence tomography. Am. J. Ophthalmol. 116, 113-4.
- Findl, O., Drexler, W., Menapace, R., Hitzenberger, C. K., and Fercher, A. F. (1998a) High precision biometry of pseudophakic eyes using partial coherence interferometry. J. Cataract. Refract. Surg. 24, 1087-93.
- Findl, O., Drexler, W., and Menapace, R., et al. (1998b) Accurate determination of intraocualar lens position and lens-capsule distance using partial coherence interferometry. J. Cataract Refract. Surg. 24, 1094-8.
- Flower, R. W., McLeod, D. S., and Pitts, S.M. (1977) Reflection of light by small areas of the ocular fundus. Invest Ophthalmol Vis Sci. 16(10), 981-5.
- Forbes, G. W. (1988) Optical system assessment for design: numerical ray tracing in the Gaussian pupil. J. Opt. Soc. Am. A, 5(11), 1943-56.
- Foster, P. J., Baasanhu, J., Alsbirk, P. H., et al (1998) Central corneal thickness and intraocular pressure in a Mongolian population. Ophthalmology 105, 969–73.
- Gao, L., Zhuo, X., Kwok, A. K., Yu, N., Ma, L., and Wang, J. (2002) The change in ocular refractive components after cycloplegia in children. Jpn J Ophthalmol. 46(3), 293-8.
- Garner, L. F., Stewart, A. W., Kinnear, R. F., and Frith, M. J. (2004) The Nepal longitudinal study: predicting myopia from the rate of increase in vitreous chamber depth. Optom Vis Sci. 81(1), 44-8.
- Garner, L. F. (1997a) Calculation of the radii of curvature of the crystalline lens surfaces. Ophthalmic Physiol Opt. 17(1), 75-80.
- Garner, L. F., and Yap, M. K. (1997b) Changes in ocular dimensions and refraction with accommodation. Ophthalmic Physiol Opt. 17(1), 12-7.
- Garner, L. F., Yap, M., and Scott, R. (1992) Crystalline lens power in myopia Optom Vis Sci. 69(11):863-5.
- Gilliland, K. O., Freel, C. D., Johnsen, S., Craig Fowler, W., and Costello, M. J. (2004) Distribution, spherical structure and predicted Mie scattering of multilamellar bodies in human age-related nuclear cataracts. Exp Eye Res 79(4), 563-76.
- Glickstein, M., and Millodot, M. (1970) Retinoscopy and eye size. Science. 168(931), 605-6.
- Goh, W. S. H., and Lam, C. S. Y. (1994) Changes in refractive trends and optical components of Hong Kong Chinese aged 19–39 years. Ophthalmic and Physiological Optics 14(4), 378-82.
- Goldsmith, J. A., Li, Y., Chalita, M. R., Westphal, V., Patil, C. A., Rollins, A. M., Izatt, J. A., and Huang, D. (2005) Anterior chamber width measurement by high-speed optical coherence tomography. Ophthalmology. 112(2), 238-44.
- Gorrand, J. M. (1989) Reflection characteristics of the human fovea assessed by reflecto-modulometry. Ophthalmic Physiol Opt. 9(1), 53-60.
- Gorrand, J. M., and Bacin, F. (1989) Use of reflecto-modulometry to study the optical quality of the inner retina. Ophthalmic Physiol Opt. 9(2), 198-204.
- Gorrand, J. M. (1979) Diffusion of the human retina and quality of the optics of the eye on the fovea and the peripheral retina. Vision Res. 19(8), 907-12.

- Goss, D. A., Van Veen, H. G., Rainey, B. B., and Feng, B. (1997) Ocular components measured by keratometry, phakometry, and ultrasonography in emmetropic and myopic optometry students. Optom Vis Sci. 74(7), 489-95.
- Greivenkamp, J. E., Schwiegerling, J., Miller, J. M., and Mellinger, M. D. (1995) Visual Acuity Modeling Using Optical Raytracing of Schematic Eyes. American Journal of Ophthalmology 120, 227-240
- Gullstrand, A. (1909) The optical system of the eye. Appendix 11.3. In Helmholtz, H. Von, Physiological Optics. 3rd ed. Vols 1. (Hamburg, Voss, 1909) 350-358.
- Guyton, D. L. (2002) Accommodative Amplitude Measurements After Surgery for Presbyopia. In "Hyperopia and Presbyopia" by Kazuo Tsubota, Brian S. Boxer Wachler, Dimitri T. Azar by Informa Health Care.
- Gwiazda, J., Marsh-Tootle, W. L., Hyman, L., Hussein, M., Norton, T. T., and COMET Study Group (2002) Baseline refractive and ocular component measures of children enrolled in the correction of myopia evaluation trial (COMET). Invest Ophthalmol Vis Sci. 43(2), 314-21.
- Ham, W. T. Jr. (1975) Remarks on fundus reflectance. Vision Res. 15, 1167-8.
- Hansen, F. K. (1971) Clinical study of normal human central corneal thickness. Acta Ophthalmol Scand 49, 82-9.
- Hartnegg, K., and Fischer, B. B. (2002) A turn-key transportable eye-tracking instrument for clinical assessment. Res Methods Instrum Comput. 34 (4), 625-9.
- Hashemi, H., Yazdani, K., Mehravaran, S., and Fotouhi, A. Anterior chamber depth measurement with a-scan ultrasonography, Orbscan II, and IOLMaster. Optom Vis Sci. 82(10), 900-4.
- Hemenger, R. P., Garner, L. F., and Ooi, C. S. (1995) Change with age of the refractive index gradient of the human ocular lens Invest Ophthalmol Vis Sci. 36(3), 703-7.
- Heryudono, A., Braun, R. J., Driscoll, T. A., Maki, K. L., Cook, L. P., King-Smith, P. E. (2007) Single-equation models for the tear film in a blink cycle: realistic lid motion. Math Med Biol. 24(4), 347-77. Epub 2007 Oct 17.
- Hitzenberger, C. K., Baumgartner, A., Drexler, W., and Fercher, A. F. (1994) Interferometric measurement of corneal thickness with micrometer precision. Am. J. Ophthalmol. 118, 468-76.
- Hitzenberger, C. K., Drexler, W., and Dolezal, C., et al. (1993) Measurement of the axial length of cataract eyes by laser Doppler interferometry. Invest. Ophthalmol. Vis. Sci. 34:1886-93.
- Hitzenberger, C. K., Drexler, W., and Fercher, A. F. (1992) Measurement of corneal thickness by laser Doppler interferometry. Invest. Ophthalmol. Vis. Sci. 33, 98-103.
- Hitzenberger, C. K. (1991) Optical measurement of the axial eye length by laser Doppler interferometer. Invest. Ophthalmol. Vis. Sci. 32, 616-24.
- Hodgkinson, I. J., Greer, P. B., and Molteno, A. C. (1994) Point-spread function for light scattered in the human ocular fundus. J Opt Soc Am A Opt Image Sci Vis. 11(2), 479-86.
- Hodgkinson, I. J., Khoo, B. C., Lunt, B. J., and Molteno, A. C. (1990) Pupillary irradiance distributions for light backscattered in the human eye. Australas Phys Eng Sci Med. 13(2), 51-8.
- Horner, D. G., Soni, P. S., Vyas, N., and Himebaugh, N. L. (2000) Longitudinal changes in corneal asphericity in myopia. Optom Vis Sci. 77(4), 198-203.
- Hosny, M., Alio, J. L., Claramonte, P., Attia, W. H., and Perez-Santonja, J. J. (2000) Relationship between anterior chamber depth, refractive state, corneal diameter, and axial length. J Refract Surg. 16(3), 336-40.
- Howland, H. C. (1985) Optics of photoretinoscopy: results from ray tracing. Am J Optom Physiol Opt. 62(9), 621-5.
- Howland, H. C., Braddick, O., Atkinson, J., and Howland, B. (1983) Optics of photorefraction: orthogonal and isotropic methods. Journal of the Optical Society of America. 73(12), 1701-8.

- Howland, H. C. (1978) Retinoscopy of infants at a distance: limits of normal and anomalous reflexes. Vision Res. 18, 597-9.
- Howland, H. C., and Howland, B. (1974) Photorefraction: a technique for study of refractive state at a distance. J Opt Soc Am. 64(2), 240-9.
- Hu, C. Y., Jian, J. H., Cheng, Y. P., and Hsu, H. K. Analysis of crystalline lens position. J Cataract Refract Surg. 32(4), 599-603.
- Huang, D., Swanson, E. A., and Lin, C. P., et al. (1991a) Optical coherence tomography. Science 254, 1178-81.
- Huang, D., Wang, J., Lin, C. P., Puliafito, C. A., Fujimoto, J. G. (1991b) Micron-resolution ranging of cornea anterior chamber by optical reflectometry. Lasers Surg. Med. 11, 419-25.
- Hung, G. K. (2001) Models of Oculomotor Control, by World Scientific Publishing Co. Pte. Ltd., River Edge, NJ.
- Jansson, F. (1963). Measurements of intraocular distances by ultrasound. Acta Ophthalmologica. Supplementum, 74, 1-49.
- Jenkins, F. A., and White H. E. (1976) Fundamentals of Optics, 4th ed. McGraw-Hill, New York, NY.
- Jones, L. A., Mitchell, G. L., Mutti, D. O., Hayes, J. R., Moeschberger, M. L., and Zadnik, K. (2005) Comparison of ocular component growth curves among refractive error groups in children. Invest Ophthalmol Vis Sci. 46(7), 2317-27.
- Kaakinen K. (1979) A simple method for screening of children with strabismus, anisometropia or ametropia by simultaneous photography of the corneal and the fundus reflexes. Acta Ophthalmol (Copenh). 57(2), 161-71.
- Kaur, C., Foulds, W. S., and Ling, E. A. (2008) Blood-retinal barrier in hypoxic ischaemic conditions: Basic concepts, clinical features and management. Prog. Retin. Eye Res. 2008 Oct 4.
- Khoramnia, R., Rabsilber, T. M., and Auffarth, G. U. (2007) Central and peripheral pachymetry measurements according to age using the Pentacam rotating Scheimpflug camera. Journal of Cataract and Refractive Surgery, 33, 830-6.
- Kiely, P. M., Smith, G., and Carney, L. G. (1984) Meridional variations of corneal shape Am J Optom Physiol. 61(10), 619-26.
- King-Smith, P. E., Fink, B.A., Hill, R. M., Koelling, K. W., and Tiffany, J. M. (2004) The thickness of the tear film. Curr Eye Res. 29(4-5), 357-68.
- King-Smith, P., Nichols, K. K., and Wood, E. J. (2003) Is Inferior Tear Film Thinner than Superior Tear film? Invest Ophthalmol Vis Sci 44, E-Abstract 2476.
- King-Smith, P. E., Fink, B. A., and Hill, R. M. (2002) Evaporation from the human tear film studied by interferometry. Adv Exp Med Biol. 506(Pt A), 425-9.
- King-Smith, P. E., Fink, B. A., Fogt, N., Nichols, K. K., Hill, R. M., and Wilson, G. S. (2000) The thickness of the human precorneal tear film: evidence from reflection spectra. Invest Ophthalmol Vis Sci. 41(11), 3348-59.
- Kirschkamp, T., Dunne, M., and Barry, J.-C. (2004) Phakometric measurement of ocular surface radii of curvature, axial separations and alignment in relaxed and accommodated human eyes. Ophthalmic & Physiological Optics. 24(2), 65-73.
- Koretz, J. F., Cook, C. A., and Kaufman, P. L. (2001) Aging of the human lens: changes in lens shape at zero-diopter accommodation. J Opt Soc Am A Opt Image Sci Vis. 18(2):265-72.
- Koretz, J. F., Kaufman, P. L., Neider, M. W., and Goeckner, P. A. (1989) Accommodation and presbyopia in the human eye--aging of the anterior segment. Vision Res. 29(12), 1685-92.

- Kunert, K. S., Bhartiya, P., Tandon, R., Dada, T., Christian, H., and Vajpayee, R. B. (2003) Central corneal thickness in Indian patients undergoing LASIK for myopia. J Refract Surg 19, 378-9.
- Lam, C. S., Edwards, M., Millodot, M., and Goh, W. S. (1999) A 2-year longitudinal study of myopia progression and optical component changes among Hong Kong schoolchildren. Optom Vis Sci. 76(6), 370-80.
- Lam, A. K., and Douthwaite, W. A. (1996) Application of a modified keratometer in the study of corneal topography on Chinese subjects. Ophthalmic Physiol Opt. 16(2), 130-4.
- Lam, A. K. C., and Douthwaite, W. A. (1994) Three month study of changes in the cornea after computer-determined and conventionally-determined contact lens fitting. Ophthalmic and Physiological Optics 14(1), 59-63.
- Lam, C. S. Y., Goh, W. S. H., Tang, Y. K., Tsui, K. K., Wong, W. C., and Man, T. C. (1994) Changes in refractive trends and optical components of Hong Kong Chinese aged over 40 years. Ophthalmic Physiol Opt. 14(4), 383-8.
- Landers, J. A., Billing, K. R., Mills, R. A., Henderson, T. R., and Craig, J. E. (2007) Central corneal thickness of indigenous Australians within Central Australia. American Journal of Ophthalmology, 143, 360-2.
- Le Grand, Y., and El Hage, S. G. (1980) Physiological optics. Springer Series in Optical Sciences, Springer, Berlin.
- Le Grand, Y. (1956) Optique Physiologique, Tome I, La dioptrique de l'oeil et sa correction (Masson, Paris, 1956). Revised edition translated to English: Y. Le Grand and S. G. El Hage, Physiological Optics, (Springer-Verlag, Berlin, 1980).
- Lekskul, M., Aimpun, P., Nawanopparatskul, B., Bumrungsawat, S., Trakulmungkijkarn, T., Charoenvanichvisit, J., et al. (2005) The correlations between central corneal thickness and age, gender, intraocular pressure and refractive error of aged 12–60 years old in rural Thai community. Journal of the Medical Association of Thailand, 88, S175-S179.
- Li, P., Hu, Y., Xu, Q., Zhang, G., and Mai, C. (2006) Central corneal thickness in adult Chinese [English abstract]. Journal of Huazhong University of Science and Technology. Medical Science, 26, 141-4.
- Liou, H.-L., and Noel, A. (1997) Brennan Anatomically accurate, finite model eye for optical modeling. J. Opt. Soc. Am. A 14(8), 1684-95.
- Liu, Z., and Pflugfelder, S. C. (2000) The effects of longterm contact lens wear on corneal thickness, curvature and surface regularity. Ophthalmology 107, 105-111.
- Llorente, L., Barbero, S., Cano, D., Dorronsoro, C., and Marcos, S. (2004) Myopic versus hyperopic eyes: axial length, corneal shape and optical aberrations. J Vis. 4(4), 288-98.
- Logan, N. S., Gilmartin, B., Wildsoet, C. F., and Dunne, M. C. (2005) Posterior retinal contour in adult human anisomyopia. Invest Ophthalmol Vis Sci. 45(7), 2152-62.
- Mainstone, J. C., Carney, L. G., Anderson, C. R., Clem, P. M., Stephensen, A. L., and Wilson, M. D. (1998) Corneal shape in hyperopia. Clin Exp Optom. 81(3):131-137.
- Mallen, E. A., Gammoh, Y., Al-Bdour, M., and Sayegh, F. N. (2005) Refractive error and ocular biometry in Jordanian adults. Ophthalmic Physiol Opt. 25(4), 302-9.
- Martola, E. L., and Baum, J. L. (1968) Central and peripheral corneal thickness-a clinical study. Arch Ophthalmol 79, 28.
- McBrien, N. A., and Adams, D. W. (1997) A longitudinal investigation of adult-onset and adult-progression of myopia in an occupational group. Refractive and biometric findings. Invest Ophthalmol Vis Sci. 38(2), 321-33.

- McBrien, N. A., and Millodot, M. (1987) A biometric investigation of late onset myopic eyes. Acta Ophthalmol (Copenh). 65(4), 461-8.
- Millodot, M., and O'Leary, D. J. (1980) On the artifact of retinoscopy and chromatic aberration. Am J Optom Physiol Opt. 57(11), 822-4.
- Millodot, M. (1972) Reflection from the fundus of the eye and its relevance to retinoscopy. Atti. Fond. Giorgio Ronchi, 27, 31-50.
- Murphy, J. (1999) Our Myopic View of Children's Vision and the Rx for it. Review of Optometry, Sept. 1999, 94-99
- Mutti, D. O., Mitchell, G. L., Jones, L. A., Friedman, N. E., Frane, S. L., Lin, W. K., Moeschberger, M. L., and Zadnik, K. (2005) Axial growth and changes in lenticular and corneal power during emmetropization in infants. Invest Ophthalmol Vis Sci. 46(9), 3074-80.
- Mutti, D. O. (2004) Sources of normal and anomalous motion in retinoscopy. Opotom. Vision. Sci. 81, 663-72.
- Mutti, D. O., Zadnik, K., Fusaro, R. E., Friedman, N. E., Sholtz, R. I., and Adams, A. J. (1998) Optical and structural development of the crystalline lens in childhood. Invest Ophthalmol Vis Sci. 39(1), 120-33.
- Navarro, R., González, L., Hernández-Matamoros, J. L. (2006) On the prediction of optical aberrations by personalized eye models. Optom Vis Sci. 83(6), 371-81.
- Navarro, R., González, L., and Hernández, J. L. (2004) On the prediction of optical aberrations by personalized eye models. II Physiological Optics Topical Meeting of the European Optical Society; Granada, Spain; September 2004.
- Navarro, R., Santamaria, J., and Bescós, J. (1985) Accommodation-dependent model of the human eye with Aspherics. J. Opt. Soc. Am. A 2(8), 1273-81.
- Neumann, D., Spezio, M. L., Piven, J., and Adolphs, R. (2006) Looking you in the mouth: abnormal gaze in autism resulting from impaired top-down modulation of visual attention. Soc. Cogn. Affect Neurosci. 1(3), 194-202.
- Nichols, B., Dawson, C. R., and Togni, B. (1983) Surface features of the conjunctiva and cornea. Invest Ophthalmol Vis Sci. 24(5), 570-6.
- Nomura, H., Ando, F., Niino, N., Shimokata, H., and Miyake, Y. (2002) The relationship between age and intraocular pressure in a Japanese population: The influence of central corneal thickness. Current Eye Research, 24, 81-5.
- Numerical Recipes (1989) Cambridge University Press.
- Ojaimi, E., Rose, K. A., Morgan, I. G., Smith, W., Martin, F. J., Kifley, A., Robaei, D., and Mitchell, P. (2005) Distribution of ocular biometric parameters and refraction in a population-based study of Australian children. Invest Ophthalmol Vis Sci. 46(8), 2748-54.
- O'Leary, D., and Millodot, M. (1978) The discrepancy between retinoscopic and subjective refraction: effect of light polarization. Am J Optom Physiol Opt. 55(8), 553-6.
- Patel, S., Marshall, J., and Fitzke, F. W. (1993) Shape and radius of posterior corneal surface Refract Corneal Surg. 9(3), 173-81.
- Pease, P. L., Adams, A. J., and Nuccio, E. (1973) Optical density of human macular pigment. Vision Res. 27(5), 705-10.
- Pedersen, L., Hjortdal, J., and Ehlers, N. (2005) Central corneal thickness in high Myopia. Acta Ophthalmol Scand. 83(5), 539-42.
- Pennie, F. C., Wood, I. C., Olsen, C., White, S., and Charman, W. N. (2001) A longitudinal study of the biometric and refractive changes in full-term infants during the first year of life. Vision Res. 41(21), 2799-810.

- Porter, J., Queener, H., Lin, J., Thorn, K., and Awwal, A. A. S. (2006) Strategies for High-Resolution Retinal Imaging (by Austin Roorda, Donald T. Miller, and Julian Chrsutou) in "Adaptive Optics for Vision Science" (Wiley-Interscience, 2006), Chap. 10, P273.
- Price, F. W., Jr, Koller, D. L., and Price, M. O. (1999) Central corneal pachymetry in patients undergoing laser in situ keratomileusis. Ophthalmology 106, 2216-20.
- Rabbetts, R. B. (2007) Bennett & Rabbettss' clinical visual optics (chapter 20), by Butterworth-Heinemann.
- Rabsilber, T. M., Becker, K. A., Frisch, I. B., and Auffarth, G. U. (2003) Anterior chamber depth in relation to refractive status measured with the Orbscan II Topography System. J Cataract Refract Surg. 29(11), 2115-21.
- Rommelse, N. N., Van der Stigchel, S., and Sergeant, J. A. (2008) A review on eye movement studies in childhood and adolescent psychiatry. Brain Cogn. 2008 Oct 1.
- Roorda, A. (1996) Double Pass Reflections in the Human Eye. Ph.D. dissertation, University of Waterloo, Waterloo, Canada.
- Rosengren, B. (1935) A method of skiascopy with the electric ophthalmoscope. Acta Ophtalmol (Kbl) 15, 501-11.
- Rüfer, F., Schroder, A., Arvani, M. K., and Erb, C. (2005) Central and peripheral corneal pachymetry-standard evaluation with the Pentacam system [English abstract]. Klinische Monatsblätter für Augenheilkunde, 222, 117-22.
- Salyer, D. A., Beaudry, N., Basavanthappa, S., Twietmeyer, K., Eskandari, M., Denninghoff, K. R., Chipman, R. A., and Park, R. I. (2006) Retinal oximetry using intravitreal illumination. Curr Eye Res. 31 (7-8), 617-27.
- Sanchis-Gimeno, J. A., Lleo-Perez, A., Alonso, L., and Rahhal, M. S. (2004) Caucasian emmetropic aged subjects have reduced corneal thickness values: Emmetropia, CCT and age. International Ophthalmology, 25, 243–246.
- Saw, S. M., Chua, W. H., Hong, C. Y., Wu, H. M., Chia, K. S., Stone, R. A., Tan, D. (2002a) Height and its relationship to refraction and biometry parameters in Singapore Chinese children. Invest. Ophthalmol. Vis. Sci. 43(5), 1408-13.
- Saw, S. M., Carkeet, A., Chia, K. S., Stone, R. A., and Tan, D. T. (2002b) Component dependent risk factors for ocular parameters in Singapore Chinese children. Ophthalmology. 109(11), 2065-71.
- Schwartz, S. H. (2004) Visual Perception: a clinical orientation, third edition, by McGraw-Hill, New York.
- Schwiegerling, J. (1997) Cone dimensions in keratoconus using Zernike polynomials. Optometry and Vision Science, 74, 963-69.
- Schwiegerling, J., Greivenkamp, J. E., and Miller, J. M. (1995) Representation of videokeratoscopic height data with Zernike polynomials. J Opt Soc Am A Opt Image Sci. Vis. 12(10), 2105-13.
- Scott, R., and Grosvenor, T. (1993) Structural model for emmetropic and myopic eyes. Ophthalmic Physiol Opt. 13(1), 41-7.
- Selović, A., Juresa, V., Ivankovic, D., Malcic, D., and Selović Bobonj, G. (2005) Relationship between axial length of the emmetropic eye and the age, body height, and body weight of schoolchildren. Am J Hum Biol. 17(2), 173-7.
- Sheppard, C. J. R., and Gu, M. (1991) Aberration compensation in confocal microscopy Applied Optics, 30(25), 3563-8.
- Shimmura, S., Goto, E., Shimazaki, J., and Tsubota, K. (1998) Viscositydependent fluid dynamics of eyedrops on the ocular surface. Am J Ophthalmol. 125, 386-8.

- Shimmyo, M., Ross, A. J., Moy, A., and Mostafavi, R. (2003) Intraocular pressure, Goldmann applanation tension, corneal thickness, and corneal curvature in Caucasians, Asians, Hispanics, and African Americans. American Journal of Ophthalmology, 136, 603-13.
- Shufelt, C., Fraser-Bell, S., Ying-Lai, M., Torres, M., Varma, R.; Los Angeles Latino Eye Study Group. (2005) Refractive error, ocular biometry, and lens opalescence in an adult population: the Los Angeles Latino Eye Study. Invest Ophthalmol Vis Sci. 46(12), 4450-60.
- Singh, K. D., Logan, N. S., and Gilmartin, B. (2006) Three-dimensional modeling of the human eye based on magnetic resonance imaging. Invest Ophthalmol Vis Sci. 47(6), 2272-9.
- Smith, G. (2003) The optical properties of the crystalline lens and their significance. Clin Exp Optom. 86(1), 3-18.
- Stenstrom, S. (1948) Investigation of the variation and the correlation of the optical elements of human eyes. Part V—Chapter III (D. Woolf, Trans.). American Journal of Optometry and Archives of American Academy of Optometry, 25, 438–449.
- Strang, N. C. Schmid, K. L., and Carney, L. G. (1998a) Hyperopia is predominantly axial in nature. Curr. Eye Res. 17(4), 380-3.
- Strang, N. C., Winn, B., and Bradley, A. (1998b) The role of neural and optical factors in limiting visual resolution in myopia. Vis. Res. 38(11), 1713-21.
- Strenk, S., Semmlow, J., Strenk, L., Munoz, P., Gronlund-Jacob, J., and DeMarco, J. (1999) Age-related changes in human ciliary muscle and lens: a magnetic resonance imaging study. Investigative Ophthalmology and Visual Science, 40, 1162-9.
- Srivannaboon, S. (2002) Relationship between corneal thickness and level of myopia. J Med Assoc Thai 85, 162-66.
- Suzuki, S. Suzuki, Y., Iwase, A., and Araie, M. (2005) Corneal thickness in an ophthalmologically normal Japanese population. Ophthalmology. 112(8), 1327-36.
- Tan, B., Shi, L., Chen, Y.-L., Lewis, J. W. L., and Wang, M. (2009) Spherical Aberration in the Enhancement of Presbyopia Vision. Invest. Ophthalmol. Vis. Sci. 50, E-Abstract 1122.
- Tan, B., Baker, K., Chen, Y.-L., Lewis, J. W., Shi, L., Swartz, T., and Wang, M. (2008) How keratoconus influences optical performance of the eye. J Vis. 8(2), 13, 1-10.
- Tan, B., Chen, Y.-L., Baker, K., Lewis, J. W., Swartz, T., Jiang, Y., and Wang, M. (2007) Simulation of realistic retinoscopic measurement. Optics Express, 15(5), 2753-61.
- Tan, B. (2005) Ametropic eye modeling, Master thesis, University of Tennessee.
- Tanaka, H. M., Mori, E. S., Maia, N., Freitas, D., Campos, M., and Chamon, W. (1996) Corneal thickness in high myopes. Invest Ophthalmol Vis Sci 37, 2566.
- Thibos, L. N., Hong, X., Bradley, A., and Applegate, R. A. (2004) Accuracy and precision of objective refraction from wavefront aberrations. J Vis. 4(4), 329-51.
- Thibos, L. N., Applegate, R. A., Schwiegerling, J. T., Webb, R.; VSIA Standards Taskforce Members. (2002) Vision science and its applications. Standards for reporting the optical aberrations of eyes. J Refract Surg. 18(5), S652-60.
- Tocci, M. (2007) How to Model the Human Eye in ZEMAX. ZeMax knowledge base http://www.zemax.com/kb/articles/186/1/How-to-Model-the-Human-Eye-in-ZEMAX/Page1.html
- Tong, L., Saw, S. M., Siak, J. K., Gazzard, G., and Tan, D. (2004) Corneal thickness determination and correlates in Singaporean schoolchildren. Invest Ophthalmol Vis Sci. 45(11), 4004-9.
- Tong, L., Saw, S. M., Tan, D., Chia, K. S., Chan, W. Y., Carkeet, A., Chua, W. H., and Hong, C. Y. (2002) Sensitivity and specificity of visual acuity screening for refractive errors in school children. Optom Vis Sci. 79(10), 650-7.

- Touzeau, O., Allouch, C., Borderie, V., Kopito, R., and Laroche, L. (2003) Corrélation entre laréfraction et la biométrie oculaire. J Fr Ophtalmol 26, 355-63.
- Trillenberg, P., Lencer, R., and Heide, W. (2004) Eye movements and psychiatric disease. Curr. Opin. Neurol. 17 (1), 43-7. Review.
- van Blokland, G. J. (1986) Directionality and alignment of the foveal receptors, assessed with light scattered from the human fundus in vivo. Vision Res. 26(3), 495-500.
- van Norren, D., and van der Kraats, J. (1981) A continuously recording retinal densitometer. Vision Res. 21(6), 897-905.
- Varri, A., Hirvonen, K., Hakkinen, V., Hasan, J., and Loula, P. (1996) Nonlinear eye movement detection method for drowsiness studies. Int J. Biomed Comput. 43 (3), 227-42.
- Villegas, E. R., Carretero L., and Fimia A. (1996) Le Grand eye for the study of ocular chromatic aberration. Ophthalmic Physiol Opt 16(6), 528-31.
- von Bahr, G. (1956) Corneal thickness: its measurement and changes. Am J Ophthalmol 42, 251-66.
- Vos, J. J., Munnik, A. A., and Boogaard, J. (1965) Absolute Spectral Reflectance of the Fundus Oculi. JOSA, 55(5), 573-4.
- Wan, Q., Cote, G. L., and Dixon, J. B. (2005) Dual-wavelength polarimetry for monitoring glucose in the presence of varying birefringence. J. Biomed. Opt. 10 (2), 024029.
- Wang, M. (2006) Corneal Topography in the Wavefront Era: A Guide for Clinical Application. Page 33 by SLACK incorporated.
- Wang, J., Fonn, D., Simpson, T. L., and Jones, L. (2003) Precorneal and Pre- and Postlens Tear Film Thickness Measured Indirectly with Optical Coherence Tomography. Invest Ophthalmol Vis Sci. 44(6), 2524-8.
- Watkins, R. (2007) ZEMAX Models of the Human Eye. ZeMax knowledge base http://www.zemax.com/kb/articles/193/1/ZEMAX-Models-of-the-Human-Eye/Page1.html
- Weale, R. A.(1966) Polarized light and the human fundus oculi. J Physiol. 186(1), 175-86.
- Wickremasinghe, S., Foster, P. J., Uranchimeg, D., Lee, P. S., Devereux, J. G., Alsbirk, P. H., Machin, D., Johnson, G. J., and Baasanhu, J. (2004) Ocular biometry and refraction in Mongolian adults. Invest Ophthalmol Vis Sci. 45(3), 776-83.
- Wojciechowski, R., Congdon, N., Anninger, W., and Teo Broman, A. (2003) Age, gender, biometry, refractive error, and the anterior chamber angle among Alaskan Eskimos. Ophthalmology, 110, 365-75.
- Wolffsohn, J. S., and Peterson, R. C. (2006) Anterior ophthalmic imaging. Clinical and Experimental Optometry, 89(4), 205-14
- Wong, T. Y., Foster, P. J., Johnson, G. J., Klein, B. E., and Seah, S. K. (2001) The relationship between ocular dimensions and refraction with adult stature: the Tanjong Pagar Survey. Invest. Ophthalmol. Vis. Sci. 42(6), 1237-42.
- Zadnik, K., Manny, R. E., Yu, J. A., Mitchell, G. L., Cotter, S. A., Quiralte, J. C., Shipp, M., Friedman, N. E., Kleinstein, R. N., Walker, T. W., Jones, L. A., Moeschberger, M. L., Mutti, D. O., Collaborative Longitudinal Evaluation of Ethnicity and Refractive Error (CLEERE) Study Group (2003) Ocular component data in schoolchildren as a function of age and gender. Optom Vis Sci. 80(3), 226-36.
- Zadnik, K., Mutti, D. O., Friedman, N. E., Qualley, P. A., Jones, L. A., Qui, P., Kim, H. S., Hsu, J. C., and Moeschberger, M. L. (1999) Ocular predictors of the onset of juvenile myopia. Invest Ophthalmol Vis Sci. 40(9), 1936-43.
- Ziylan, S., Serin, D., and Karslioglu, S. (2006) Myopia in preterm children at 12 to 24 months of age. J Pediatr Ophthalmol Strabismus. 43(3), 152-6.

Appendices

Appendix A: Step-by-step general eye modeling procedure in ZEMAX [Tocci 2007]

Introduction

In this study, we will create model of a human eye in ZEMAX using the Navarro eye model. This is a fairly up-to-date and comprehensive model of the eye, which has been validated by checking optical performance, like chromatic and monochromatic aberrations [Navarro 1985, and Escudero-Sanz 1999].

The prescription for this eye model (along with a wealth of other extremely important and interesting information) can be found in the book titled "Optics of the Human Eye," by David A. Atchison and George Smith [Atchison 2000].

Human Eye Model

We'll begin by setting up the human eye model. You will want to first put ZEMAX into Sequential Mode, and then set the System|General|Units Lens Units to "Millimeters". Next you'll want to set the Wavelengths (found in the System section) to "F, d, C (Visible)" as shown in Figure A.1.

Next, go to System|General|Aperture and set the Aperture Type to "Float By Stop Size" and then go to System|General|Glass Catalogs and add the catalog "MISC" to your Glass Catalogs. Set just one Field, of Type "Angle(Deg)" with an X-Field value of 5 (shown in Figure A.2).

Now insert 3 surfaces before the STOP and insert another 3 surfaces after the STOP. Below is a step-by-step guide to setting up all the surfaces, one at a time.

Surface 0

This surface is not actually labeled Surface 0 in the ZEMAX Lens Data Editor, it's labeled "OBJ" and it's the object surface. Below are the settings for Surface 0 (note that any settings not mentioned here should be left with their default values):

Surf: Type = Standard
Comment = Object
Radius = Infinity
Thickness = 1.00E+009

Surface 1

The first surface (after the Object) is just a dummy plane, and we use it to make our layout drawings easier to understand. Below are the settings for Surface 1:

Surf: Type = Standard
Comment = Input Beam
Radius = Infinity
Thickness = 50.0

(Note that the actual value of the thickness of this surface is not important: feel free to change it as necessary to make your layout drawings look just right) Since we're not actually interested in seeing this surface in the layout drawings (we only want to see the rays after they pass through the surface), let's right click the Surf: Type cell for this surface, then click the Draw tab, and then check the Do Not Draw This Surface box.

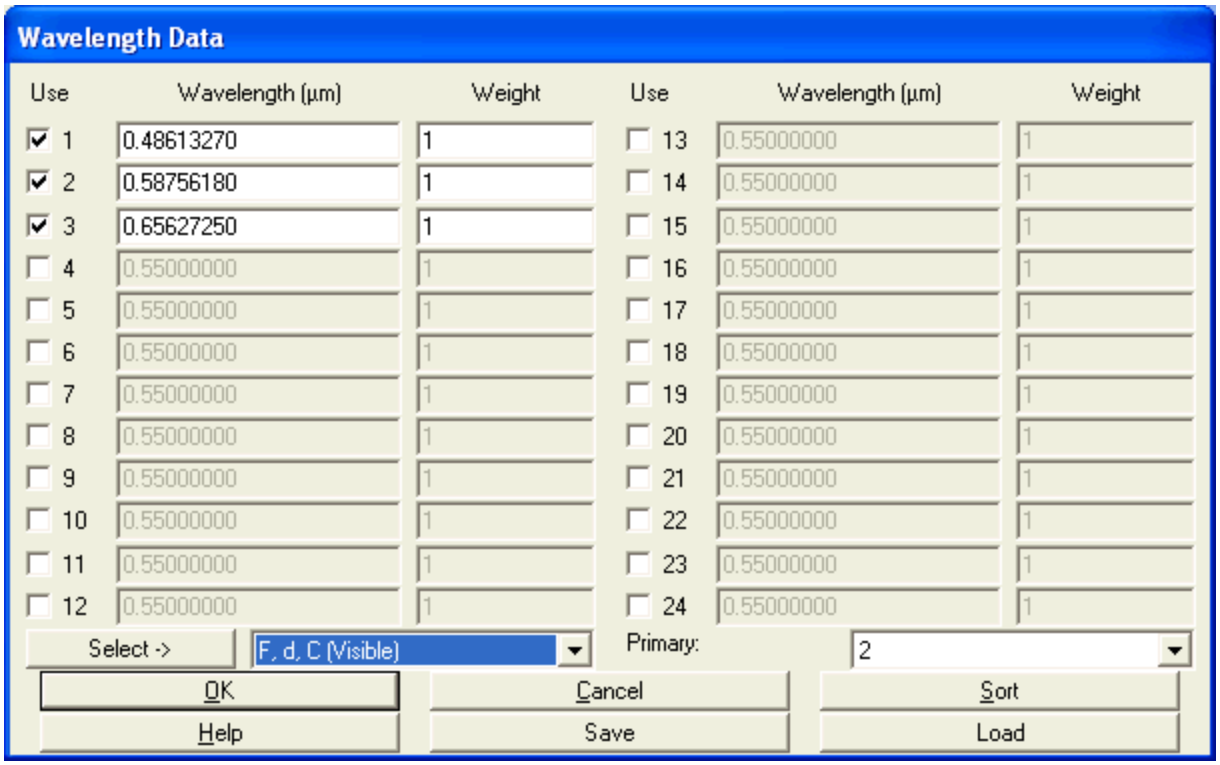

Figure A.1 *Wavelength data editor in ZEMAX*

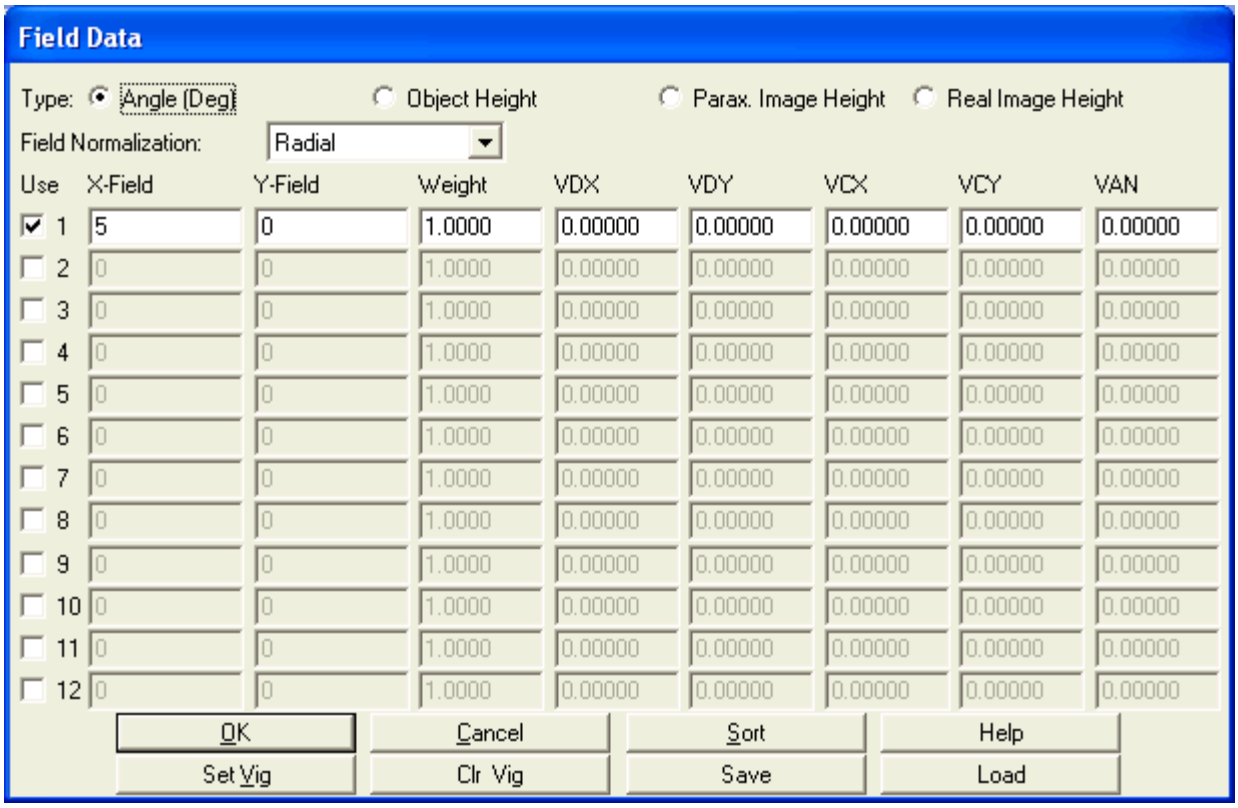

Figure A.2 *Field data editor in ZEMAX*

Surface 2
This is the outer cornea surface. Below are the settings for Surface 2:

Surf: Type = Standard
Comment = Anterior cornea
Radius = 7.72
Thickness = 0.55
Glass = Fixed; Cornea_Navarro
Semi-Diameter = 5.00
Conic = -0.26

Note: to set these glass parameters you will need to right-click the Glass cell, select “fixed” as the Solve Type from the drop down list, and then go to Tools|Catalogs|Glass catalogs: To edit or review data in an existing glass catalog, select Tools, Glass Catalogs. Select the catalog name from those listed in the drop-down list on the dialog box. Once the catalog is selected, you may insert, cut, copy, paste, or modify data in the catalog. You can save the newly modified catalog to either the same name or a new name. When editing the glass catalogs supplied with ZEMAX, be sure to save the modified data to a new name using the "Save Catalog As" button. This is important because future releases of ZEMAX may include an updated catalog which will be installed over the existing catalog, and any changes that had been made to the existing catalog will be lost. All types of glasses, like “cornea_Navarro”, “aqueous_Navarro”, “lens_Navarro”, and “vitreous_Navarro”, are defined by fitting refractive index at four wavelengths, 365nm, 486.1nm, 656.3nm, and 1014nm.

Surface 3

This is the interface between the cornea and the aqueous humor. Below are the settings for Surface 3:

Surf: Type = Standard
Comment = Posterior cornea
Radius = 6.5
Thickness = 3.05
Glass = Fixed; Aqueous_Navarro
Semi-Diameter = 5.00
Conic = 0

Surface 4

This surface is not actually labeled Surface 4 in the ZEMAX Lens Data Editor, it’s labeled “STO” and it’s the aperture stop of the system. This is our eye model’s pupil plane. Below are the settings for Surface 4:

Surf: Type = Standard
Comment = Pupil
Radius = Infinity
Thickness = 0.00
Glass = Model; Aqueous_Navarro
Semi-Diameter = 3
Aperture type = circular aperture; Minimum radius = 0; Maximum radius = 3

Surface 5

This is the anterior surface of our model's crystalline lens. Below are the settings for Surface 5:

Surf: Type = Standard
Comment = Anterior lens
Radius = 10.20
Thickness = 4
Semi-Diameter = 5.00
Conic = -3.1316

Surface 6

This is the posterior surface of our model's crystalline lens. Below are the settings for Surface 6:

Surf: Type = Standard
Comment = Posterior lens
Radius = -6.00
Thickness = 16.3203
Semi-Diameter = 5.00
Conic = -1.0

Surface 7

This surface is not actually labeled Surface 8 in the ZEMAX Lens Data Editor, it's labeled "IMA" and it's the image surface. This is the retina of our model. Below are the settings for Surface 8:

Surf: Type = Standard
Comment = Retina
Radius = -12.0
Semi-Diameter = 5.00

Therefore, we used ZEMAX to model a human eye using realistic parameters.

Appendix B: The exporting Humphrey topography data and the importing user defined surface to ZEMAX

The information of the KC's anterior corneal surface includes the typical values and distribution ranges of the sizes, shapes, and positions of the conical structures. With the advent of the photokeratoscope the height map of the cornea surface can be measured. Corneal topographic technique has been addressed in Chapter 2. In this dissertation, corneal topographic data from Humphrey Atlas Corneal Topography Systems (Carl Zeiss Meditec, Inc., Dublin, CA) was used. The Humphrey Atlas utilizes placido disk technology to acquire images of the corneal surface and calculate the corneal surface curvature. It reports corneal elevation maps, which we will use for our eye modeling. First, let us look at the procedure how to extract corneal elevation maps from Humphrey-Zeiss Mastervue Atlas Corneal Topography system.

Here's a description on how to get raw corneal topographic data out of the Humphrey system. This module has been called "External Data Interface" (EDI). The purpose of EDI is to provide access to the internal data structures of the Mastervue corneal topography maps on the one hand, and to allow for external programs to modify and then display topography data. This is achieved by adding a separate view ("External Interface") to the MasterVue control, which is capable of feeding the data through an external program before it displays it. Whenever an exam is viewed using this option the current exam data is written to an ASCII file. If so desired, a user-supplied DLL is then called which may read the just created ASCII file, perform calculations and create another ASCII file, which is then read and displayed by EDI. EDI may either display the curvature data from the file immediately, or read the height information from the file and convert it to curvature data before display. All filenames and locations are adjustable through an INI file. Figure A.3 demonstrates the flow of the above task.

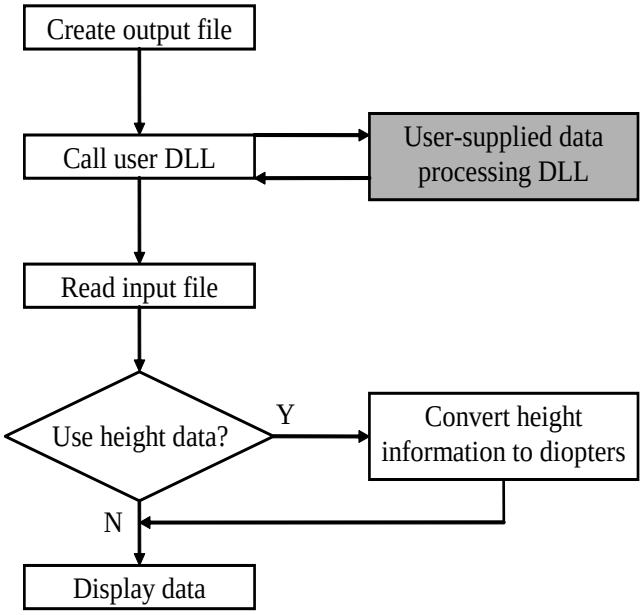

Figure A.3 *procedure to export raw corneal topographic data out from the Hunphrey system*

EDI is a part of the A10.1 or higher software release. We, however, have to enable it in the software by modifying one file as outlined below (the External Interface is normally hidden as only a fraction of Humphrey customers use it). First, turn on the corneal topographer. The MasterVue software should come up automatically. Then we could exit the software by double-clicking on the words "Main Menu" in the upper right hand corner, which takes us back to Windows. Bring up the file manager, or windows explorer, or whatever people normally use to copy and modify files under Windows. We now have to make changes to one file on the system, C:\CTS\CTS.INI. Then we make a copy of this file prior to changing it so that we can go back to the original version later in case something doesn't quite work. The following outlines illustrate what changes we make:

1. Use an editor (e.g. notepad) to open the file c:\cts\cts.ini
2. Search for the section called "[Views]"
3. In this section, change the line reading "#=None" (where # stands for any number) to "#=XMAP" (if an entry "#=XMAP" already exists, don't make any changes and go to step 7)
4. Add a new line, reading "#+1=None". Note: "#+1" means increase the number from the previous line by one and put it in here.

Example:

Before:

```
...
6=KVIEW
7=None
```

After:

```
...
6=KVIEW
7=XMAP
8=None
```

5. Add a new section as follows (it may already be there - you may want to check first):

```
[XMAP]
Title=External Interface
    Library=VIEWXMAP.DLL
Flags=&H8CF
ViewFlags=&H1
Setup=VSETUP.EXE
Path=CTSDIR
ScaleType=DIOPSCALE
```

6. Save the changes.
7. Exit the editor
8. Reboot the system.

After the system has started up again, select "Review", and look at the list of views: Under "Select View:" the last entry should now be "External Interface". Select that and click on OK. We get an axial power map of the selected exam; the screen title (upper right hand corner) should be "External Interface". If an error message jumps up, a General Protection fault, a blank screen, or one that says "View not properly installed", then we have to use the copy of CTS.INI we made previously to revert the system to its original state, but it should work. Seeing the map, we can check if it created an ASCII file with the exam data. Exit the MasterVue software as described above, (double click on Main Menu), and look for a file C:\OUT.MVA. Open it using Notepad and take a look. If we need to create MVA files by exam ID, the following lines describe how to do that (attached is a compiled DLL (MVU2ASC.DLL containing the SaveByID example code in section 8) which have to be copied into C:\CTS directory and we make the changes to C:\CTS\EXTERNAL.INI outlined in EXTDLLA10.DOC section 7.2).

```
[EDI]
OutputFile=c:\out.mva
InputFile=c:\out.mva
Library=mvu2asc.dll
Function=SaveByID
UseHeightData=0
```

EDI writes data to c:\out.mva, calls the external function SaveByID() in the DLL mvu2asc.dll and reads curvature data back from c:\out.mva for display. The purpose of SaveByID() would be to use the ExamID passed to it to construct a new filename containing the ExamID (e.g. E0000815.mva) and to copy the export file to this location. A code example for such a function is shown in the following piece of code.
This shows how a user defined DLL could be written to copy the generated ASCII file to a new location, based on the exam ID. The external.ini file would look like this (assuming the compiled code is named "mvu2asc.dll"):

```
[EDI]
OutputFile=c:\out.mva
InputFile=c:\out.mva
Library=mvu2asc.dll
Function=SaveByID
UseHeightData=0
```

Here is the code for a quick and rough user defined DLL to be used with EDI:

```
#include <windows.h>
#include <stdio.h>

int FAR PASCAL LibMain (HANDLE, WORD, WORD wHeapSize, LPSTR)
{
   if (wHeapSize > 0)
      UnlockData (0);

   return 1;
}

extern "C" int _far _pascal _export SaveByID(char _far *outfile,
                                 char _far *infile,
                                 unsigned long EID)
{
  char filename[256];
  FILE *fpin=NULL, *fpout=NULL;
  unsigned char buf[1024];
  int numread;

  // Create filename to copy the outfile to
  sprintf(filename, "c:\\e%07d.mva", EID);

  // Open outfile for reading
  if((fpin=fopen(outfile, "r"))==NULL)
  {
```

```
  return NULL;
 }

 // Open the new file for writing
 if((fpout=fopen(filename, "w"))==NULL)
 {
  fclose(fpin);
  return NULL;
 }

 // Copy the outfile to the new location
 do
 {
  numread=fread(buf, 1, 1024, fpin);
  fwrite(buf, 1, numread, fpout);
 } while(numread==1024);

 // Close files
 fclose(fpin);
 fclose(fpout);

 return 1;
}
```

Up to this point, we get a corneal elevation map out of the Hunphrey system. What can we do with a corneal elevation map? Corneal irregularities can only be seen after a reference surface is mathematically removed from the original corneal elevation map. Changes in the reference surface can dramatically affect the perceived topography of the corneal landscape, while its true topography (z as function of x and y) remains unchanged. The true elevation, also know as topographic elevation, is the perpendicular distance z of a point on the cornea from the system reference plane.

The KC cone height is the elevation above a reference spherical surface or the healthy cornea surface. To reveal the cone's morphology the normal corneal surface should be determined and subtracted from the height map. This can be done by decomposing the analytical corneal surface into Zernike polynomials {Znm} and then eliminating the low-order polynomials that represent the defocus (near- and farsightedness) and cylindrical power (astigmatism). Then we obtain the elevation difference map. This calculation was executed by MatLab. The code can be found in Appendix D (All programming codes).

The corneal maps are usually not complete, as shown in Figure B2a, because of the eyelid, eyelash, and other obstruction in front of the cornea. Additionally, there is a "hole" or missing data at the central corneal region because the design of the light source and the camera. As a result, we have to interpolate and extrapolate the elevation difference map (the result after interpolation and extrapolation is shown in Figure B2b.). The calculation is described in Appendix D (All programming codes).

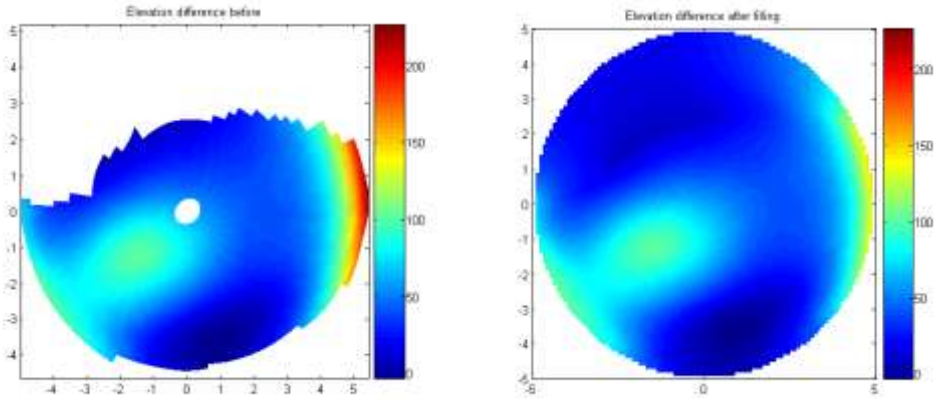

Figure A.4 *a. cornea elevation difference map before processing; b. cornea elevation map after interpolation and extrapolation*

Then the complete elevation difference map will be added on the top of the reference sphere. Therefore, we can use this cornea elevation map to replace the original anterior corneal surface of the base model. Since we use ZeMax as the simulation tool, we need to convert the map to the format that can be imported into ZeMax. This conversion is executed with the help of C++. (See Appendix D All programming codes)

Appendix C: Scattering and reflection properties of retina (Summarized from Roorda Dissertation)

A. Spectral dependence of retinal reflection:

In general, the total reflection of the retina is roughly 1% for deep blue increasing to 10% reflectance at the end of the spectrum. The tenfold increase for the red wavelengths explains the reddish reflex seen in any fundus photograph or in retinal reflections when a white light source is used.

"Absolute reflectance" was claimed by Vos et al. [Vos et al. 1965] although that paper did state that the accuracy of their conversions to absolute reflectance was not great. All subsequent papers, although using similar methods, did not claim absolute reflectance. The difficulty lies in the comparison with the model eye. The overall length of the human eye was not well known for each subject so assumptions were made that all subjects had the same dimensions as the model eye. This factor is important because only a portion of the reflected light exits the pupil and that amount is proportional to the square of the distance from the exit pupil to the retina. The directional effects of the reflected light, the polarization-retaining portion of the reflected light and different surfaces of reflection were also not taken into account in the comparison with the model eye. Also, the optical absorption of the ocular media was often ignored. The results from the above references therefore cannot be considered as absolute reflectance but as relative reflectance. Vos et al. commented, however, that these effects are sufficiently small such that the order of magnitude of the relative and the absolute reflectance will be the same.

Nearly all spectral reflectance measurements have indicated substantial differences in reflections from different locations on the retina. Foveal sites show decreased reflection due to the absorption of the macular pigment, which is not present at the other sites. Optical density measurements of the macular pigment have been performed by calculating the difference spectrum between foveal and nonfoveal sites [Pease et al. 1973].

The accuracy of the measurement can be defined by either the spot size or the number of spectral lines analyzed. The method of Flower et al. [Flower 1977] archived the smallest spot size by measuring the reflectance from a high density photograph. Using this method, they could pinpoint the locations where the reflectance was measured and could avoid averaging effects from retinal blood vessels etc. Delori and Pflibsen [Delori 1989] used a monochromator to analyze the broad band reflectance at 1nm intervals. This enabled them to easily resolve effects such as the absorption bands for hemoglobin at about 560 nm.

van Norren and van de Kraats [van Norren 1981] have described the feasibility of using a scanning laser ophthalmoscope (SLO) to do retinal densitometric measurements on the retina. The measurements are fast and results are easy to manipulate. They measured the reflectances at various stages of pigment regeneration from dark to light adapted conditions. Application of the confocal SLO to a full spectral range is limited by the available wavelengths since the light source is usually a laser.

B. Position of reflectance:

The retina is composed of many complex inhomogeneous layers. Although it is commonly agreed that all parts of the retina have some degree of reflectance (or else they would not be visible), it is not agreed as to the surface of maximal reflectance, as well as the sources of spectral and diffuse reflections. This has important implications to measurements involving reflections from the retina, such as retinoscopy.

The direct retinoscopic measurements [O'Leary 1978] and spectral characteristics [Charman 1980] of the reflections give good evidence of a reflection from the interior limiting membrane, particularly for the young eye. van Blokland and van Norren's [van Blokland 1986] model would agree with this hypothesis if the reflection from this layer as a third origin of the wide-angled component was included. This reflection would also not affected by bleaching. The analysis of the densitometric measurements indicate a large portion of light reflected from the choroid and sclera [Delori 1989, and van Norren, 1986]. This

agrees with Charman's [Charman 1980] analysis of the diffuse reflected light. It must be noted that the Delori and Pflibsen [Delori 1989] model was not used primarily to determine the source of the reflections but rather the optical density of the layers. The reflection from the retinal pigment epithelium is supported by most authors [van Blokland 1986, O'Learry 1978, Delori 1989, Gorrand, 1989, and Artal 1992]. Charman [Charman 1980] prefers the scleral origin of the reflection but the uncertainty of the spectral characteristics of the reflection may just as well allow for some RPE reflectance.

The double-pass spread measurements all found that reflections from the retina are made up of two components. When in proper a focus, a sharp peak was observed and attributed to a diffuse reflection from the photoreceptor layer and a much broader contribution originated from the other retinal layers. The amount of energy scattered from other layers was not determined but it was noted that the amount of background scatter increased for infrared wavelengths.

C. Reflection of polarized light from the retina:

Polarized light reflections have been studied for a variety of reasons. Mueller matrix ellipsometry (MME) as described by Hauge [Hauge 1978] and other psychophysical methods have been used to reveal a birefringent structure for many of the components of the eye, namely the cornea, the lens and the retina. The MME technique has an advantage over the common polarizer-analyzer combination and the psychophysical methods in that it can objectively measure the degree of ellipticity of the reflected beam. In double-pass reflectometry experiments using polarized light, the effect of all of these components must be considered. Aspects of polarization for each of the authors' methods will be described here.

The use of MME indicates that about 90% of the polarization is retained in the eye after a double pass reflection. The preservation of linear polarization is less, about 60%, but this was only a measurement of the linear component of the elliptically polarized light. Some authors attributed the non-linear portion of the reflection to depolarized light. It is understandable that there will be some change in the polarization of light as it is reflected from deeper layers in the retina, since there are known dichroic and birefringent structures in the retina. This would explain the apparent loss of polarization from the posterior layers measured using the traditional polarizer-analyzer combination. If the incident light is coherent, the polarization of the reflected light will be the resultant of the polarization of all the individual scattering elements [Born and Wolf, 1980]. In specular reflection, the polarization of the reflected will be unchanged, whereas in a more complex reflection from birefringent and dichroic structure, the resultant polarization will not likely be linear and will have an angular dependence.

D. Scattering of light at the retina:

Light that scatters from the retina can be separated into several components, including directional, specular and wide-angled reflections. We can step through the various layers of the retina and reference different articles referring to the type of reflections expected to originate from each.

Inner limiting membrane: This is the interface between the retina and the vitreous. The difference in the index of refraction, particularly for young eyes causes a specular reflection at this layer. It is also found that the shorter wavelengths tend to reflect more from this surface. This wavelength dependence is likely due to the fact that for longer wavelengths, the reflectance from deeper layers is greater, thus reducing the relative contribution of the reflection from the inner limiting membrane. A reflection at this layer is supported by O'Leary and Millodot [O'Leary 1978], Charman [Charman 1980] and Delori & Pflibsen [Delori 1989]. The relative amount of light returning from this layer is also wavelength dependent [Charman 1980]. The retinal reflection was investigated in a photorefraction experiment by Hodgkinson et al. [Hodgkinson 1990] to decide whether it was primarily specular or diffuse. Expected reflexes were modeled for a specular reflection but it was found that the experimentally observed reflexes could only be due to a diffuse reflection. The retinoscopy artifact was attributed to a specular reflection from this surface [Glickstein 1970]. Millodot [Millodot 1972] later investigated the effect of a diffuse versus a specular reflecting surface in a model eye for retinoscopy and found little dependence of the

retinoscopic response on the type of reflection. In order to explain the artifact of retinoscopy, he adopted the opinion that there is a high degree of specular reflectance from the inner limiting membrane.

Macular pigment: This layer is located in the foveal region of the retina. It appears yellowish in color but is primarily a light absorbing layer. Its absorption spectrum is centered about 460 nm in the blue. The spectrum of the macular pigment was obtained by comparing the spectral reflection from the fundus on and outside the macula [Pease et al. 1973].

Retinal pigment Epithelium: This layer is immediately posterior to the outer segments of the photoreceptors. Several authors agree that this layer is responsible for a portion of the reflected light [Delori 1989, Millodot 1980, O'Leary 1978, van Blokland 1986, and van Norren 1986] but the polarization of the light from the layer is not agreed upon. Caharman [Charman 1980] and Millodot and O'Leary [Millodot 1980] agreed that this is the layer for the unpolarized reflection while van Blokland proposed a model where all light is reflected from the RPE but the light reaches the RPE and reflects by several different means to account for the different types of reflection. Ham [Ham 1975] suggests that the size of the melanin granules in this layer is suited for Mie scattering model. The scattering in this layer is primarily with or against the direction of propagation with minimum scattering at 90° to the direction of propagation. This scattering causes some reflection from the RPE but, more importantly, the narrow angle of reflectance reduces the amount of scattered light or widening of the image in the retina as it penetrates to deeper parts of the retina.

Bruch's membrane: Weale [Weale 1966] attributed the source of polarization-retaining reflections to this layer.

Choroid: Ham [Ham 1975] also suggested scattering effects in the choroid due to the melanin granules. Delori and Pflibsen [Delori 1989] calculated light reflectance using the Kubelka-Monk equations to account for the absorption and scattering in this layer. Hodgkinson et al. [Hodgkinson 1994] proposed that scattered light from the choroid tends to broaden the reflected light from the retina up to 100μm.

Sclera: This layer is generally considered as a diffuse reflecting surface [Alpern 1962, Charman 1980 and Weale 1966].

E. Peripheral reflections:

Several factors make the reflection from the fovea different from its immediate peripheral region:
The anterior retinal layers at the fovea become very thin to allow minimal inference for the incident light.
The photoreceptors in the fovea are primarily cones and these are predominantly green and red sensitive.
The macula, which lies in a region about the fovea, tends to absorb light at the blue end of the spectrum.
In fundus examinations it has been noted that a specular reflection can be observed in the immediate foveal pit area.

Finally, the Bruchner test examines differences in retinal reflections to indicate whether or not there is foveal fixation [Bruchner 1962].

Artal and Navarro [Artal 1992] performed simultaneous double-pass point spread measurements on and away from the fovea. The eccentricity of the peripheral point was small enough so that differences in the point spread properties would only be due to differences in the retinal surfaces between these two points and not due to off-axis aberrations. They noticed only a small optical degradation of the double pass point spread for reflections at 1 degree from the fovea even though the retina is considerably thicker at that point. The point spread was projected with 632.8 nm He-Ne light. They concluded that in the peripheral retina (at 1 degree extrafoveal) there was no important contribution of retinal scattering to the double pass point spread.

Gorrand [Gorrand 1989 & 1979] and Gorrand and Bacin [1989] measured the demodulation of interference fringes reflected from the retina at an angle of 10° and beyond this in two other papers. There was a reduction in modulation of 10% at 10° and up to 20% at 40°. The light used was at 550 nm for the

10° measurement and 514 nm for the second set. In addition to the expected loss in modulation due to an increase in off-axis aberrations, decreases in modulation were proposed to originate for three reasons:
In the periphery, the absorption by melanin is weaker and therefore deeper layer like the choroid and sclera will contribute more to the aerial image.

Light makes a double pass through anterior layers which are thicker in the periphery and not present at fovea.

The specular reflection of the interior limiting membrane will not contribute to the demodulation at the fovea because the foveal pit is at such a pronounced curvature that the reflection will be in a wide enough angle that it can be ignored. This is not the case for the peripheral retina.

F. Coherence properties of the reflection:

The topic about coherent properties of light reflected from the retina is confusing with respect to the literature. The authors use different definitions for coherent and incoherent reflection and the conclusions are left open for interpretation. This discussion will establish the conventions to be used in this dissertation with respect to the coherence of the scattered light.

Two scattering points are spatially coherent if they radiate with the same frequency and have a fixed phase difference between them. This is generally the case when the illumination is from a point source or a quasi-monochromatic source [Born and Wolf 1980]. The degree of spatial coherence can be measured by the ability of two scattering points to produce interference fringes. The degree of coherence of the scattered light from the retina, therefore, is governed by the nature of the illumination source. It should be noted that there will be no spatial coherence for fluorescent scattered light in which each particle radiates independently.

The appearance of a scattering surface illuminated by coherent light depends on nature of the scattering surface. If the scattering pints are randomly arranged (rough surface) then the surface will have a speckle appearance and light will be scattered in all directions (diffuse). The modulation of this speckle pattern varies with the coherence of the illuminating source in a similar manner as the interference fringes described above. If the surface is smooth with respect to the wavelength of the incident light, no speckle will be observed but instead the incident wavefront is reversed after the reflection. This is called a specular or mirror reflection. In the limits between a smooth and a rough surface, the reflected has both a diffuse and a specular component [Beckmann 1967].

In a pure monochromatic beam, the polarization also has a fixed value. After scattering, the polarization may change but each scattering point will have a predicable polarization as a function of the scattering angle and the nature of the scatterer. The polarization of the light scattered from the whole surface is a superposition of all the individual polarization vectors and a function of scattering angle [Born and Wolf 1980]. In this sense, the polarization and coherence of scattered light are related. The preservation of polarization of reflected light from the retina was measured by van Blokland and van Norren [van Blokland 1986] to be about 90%. It follows from this result that if the polarization is preserved, then the scattered light from the retina is spatially coherent. The 10% of unpolarized light may be due to fluorescence or from the partial coherence of the illuminating source.

Coherent reflections include diffuse, specular, and directional reflections from the retina, and are governed by the coherence of the illuminating source.

G. Contribution of the retina to optical aberrations:

The anterior layers of the retina are quite transparent. This is evident in measurements done by Artal and Navarro [Artal 1992] and Gorrand and Bascin [Gorrand 1989] who measured only small decreases in double-pass image quality after reflection from the peripheral retina where the anterior layer is thickest. The anterior layer will induce aberrations into the incident wavefront. This is of most importance for an application in which light is focused to a point on the retina, such as confocal ophthalmoscopy. In the simplest case, if the anterior layers form a flat plate over the layer to be studied, the layer will induce some spherical aberration into the converging beam [Sheppard 1991, and Artal 1992]. Spherical

aberration has profound effects on the axial resolution for confocal ophthalmoscopy. At the fovea, the anterior layers become very thin and form a curved retinal surface at the foveal pit. The aberrations induced by this surface will be very position dependent and will involve asymmetric terms such as coma. These aberration may cause a slightly distorted view of the retina for the part of the fundus image at the edge of the foveal region.

Appendix D Programming codes

C++ code for converting corneal topography map into grid sag ZEMAX can import

```
#include <stdio.h>
#include <stdlib.h>
#include <string.h>
#include <math.h>



/*
This simple program generates a 4 column file
suitable for importing to the grid surface types.
This generates data for an aspherical surface on a grid
*/


/* these numbers must be odd */
#define NUM_X_PIXELS 101
#define NUM_Y_PIXELS 101

/* define aperture of lens */

#define DIAMETER 10

void main(void)
{
int i, j;
double delx, dely;
double z[NUM_Y_PIXELS+1][NUM_X_PIXELS+1],tz[NUM_Y_PIXELS][NUM_X_PIXELS];
char disp[120];
void GetSag(double x, double y, double *fp);
FILE *out;
FILE *fp;

/* STEP 1. Input the data */

if((fp=fopen("82271_od.mvaZ4.dat","r"))==NULL) printf("error\n");
for (j = 100; j >= 0; j--)
{
        for (i = 100;  i >= 0; i--)
        {
                fscanf (fp, "%lf ", &tz[j][i]);
        }
        fscanf(fp,"\n");
}
fclose(fp);
```

```
for (j = 0; j < NUM_Y_PIXELS; j++)
{
        for (i = 0; i < NUM_X_PIXELS; i++)
        {
                z[j][i] = tz[j][i] - tz[50][50];
        }
}
/* STEP 2. First write the file */
out = fopen("82271_OD_outward.dat", "wt");

/* STEP 3. Write four numbers for the header line */
delx = (double) DIAMETER / (NUM_X_PIXELS-1);
dely = (double) DIAMETER / (NUM_Y_PIXELS-1);

sprintf(disp, "%i %i %.9E %.9E 0 0 0\n", NUM_X_PIXELS, NUM_Y_PIXELS, delx, dely);
fputs(disp, out);

/* STEP 4. Write the rows and columns */


for (j = 0; j < NUM_Y_PIXELS; j++)
        {
        for (i = 0;  i < NUM_X_PIXELS; i++)
                {

                sprintf(disp, "%.9E 0 0 0\n",z[j][i]);
                fputs(disp, out);
                }
        }

/* STEP 5. Close the file */
fclose(out);
}
```

Example matlab code for processing raw cornea topography map to get the elevation difference maps, and interpolating and extrapolating these cornea elevation difference maps

```
% function ShowMVA_generic5
%function ShowMVA
%
% Read in *.MVA ascii file generated by Atlas
%
```

```
global MPath;

d=cd;
if exist(MPath)
  cd(MPath);
end

[fn,p]=uigetfile('*.mva','Select MVA file');
cd(d);

f=fopen(fullfile(p,fn));

if (f<0)
  return
end

MPath = p;

s=fgets(f);

[Data,n]=sscanf(s,' # %d %d'); % read number of rings and steps (per ring)

if (n ~= 2)
  return
end

X1=-5:.1:5;
Y1=-5:.1:5;
[X1,Y1] = meshgrid(X1,Y1);%X and Y values to interperolate over to create a griddata

NRings=Data(1);
NSteps=Data(2);

k=1;
for Rings=1:NRings
  for Steps=1:NSteps
    s=fgets(f);
    [Data,n]=sscanf(s,'%f %f %f %f %f');
    R(Rings,Steps)=Data(3);  % Radius
    a=Data(2)*pi/180;  % Angle
    X(Rings,Steps)=R(Rings,Steps)*cos(a);
    Y(Rings,Steps)=R(Rings,Steps)*sin(a);
    if (n == 5)  % local data available
      Height(Rings,Steps)=Data(5);
      Curvature(Rings,Steps)=Data(4);
      C(k)=Data(4);
      r(k)=(.3375/C(k))*1000;
      x(k)=R(Rings,Steps)*cos(a);
      y(k)=R(Rings,Steps)*sin(a);
```

```
      z(k)=Data(5);
      k=k+1;

    else % sorry, no values could be calculated for this point
      Height(Rings,Steps)=NaN;
      Curvature(Rings,Steps)=NaN;
    end
  end
end

fclose(f);

% P=41.5;%finding best sphere radius from .bmp file
% d_sphere=(.3375/P)*1000;
x=x';
y=y';
z=z';

B=x.*x+y.*y+z.*z;%setting up matrices for least square to calculate best sphere
A(:,1)=-2*x;
A(:,2)=-2*y;
A(:,3)=-2*z;
A(:,4)=1;

P=lsqr(A,B);%(x0,y0,z0,rho) rho=(x0^2+y0^2+z0^2)-r^2
d_sphere=sqrt(abs(P(1)^2+P(2)^2+P(3)^2-P(4)));
P_sphere=(.3375/d_sphere)*1000;

for Rings=1:NRings
  for Steps=1:NSteps
      Z_sphere(Rings,Steps)=sqrt(d_sphere*d_sphere-
((X(Rings,Steps)+P(1))*(X(Rings,Steps)+P(1))+(Y(Rings,Steps)+P(2))*(Y(Rings,Steps)+P(2))));
  end
end

Z_sphere=Z_sphere-P(3);%take away the z0 that was obtained from calculating best sphere

%%%% All data is read. Now display the data.
%%%% Note: Displaying the height alone makes not really sense, because
%%%%       instead the difference between reference surface and
%%%%       measured surface should be displayed.
%%%%       Just display it anyways to make sure that we got the
%%%%       data.

% Close all lines to the 0 deg. vertexes.
Height=[Height,Height(:,1)];
R=[R,R(:,1)];
Curvature=[Curvature,Curvature(:,1)];
Z_sphere=[Z_sphere,Z_sphere(:,1)];
```

```
X=[X,X(:,1)];
Y=[Y,Y(:,1)];
X2=X;
Y2=Y;

a=ones(1,181);
a=a*mean(Curvature(1,:));
Curvature=[a;Curvature];%incrasing curvature to include center
b=zeros(1,181);
X=[b;X];
Y=[b;Y];
R=[b;R];

% c=ones(1,181);
% c=c*d_sphere;
% Z_sphere=[c;Z_sphere];
% e=ones(1,181);
% e=e*(.3375/mean(Curvature(1,:)))*1000;
% Height=[e;Height];

X0=ones(101,101);
Y0=ones(101,101);
X0=X0*P(1);
Y0=Y0*P(2);

D_sphere=ones(23,181);
D_sphere=D_sphere*d_sphere;
D_sphere4=ones(101,101);
D_sphere4=D_sphere4*d_sphere;
Z_sphere4=sqrt(D_sphere4.*D_sphere4-((X1+X0).*(X1+X0)+(Y1+Y0).*(Y1+Y0)))-P(3);

Zdiff=Height-Z_sphere;

% k=1;%trying to subtract off const to get .bmp measured elevation diff.
% for Rings=1:22
%    for Steps=1:181
%       if (isfinite(Zdiff(Rings,Steps)))
%         Zd(k)=Zdiff(Rings,Steps);
%         k=k+1;
%       end
%    end
% end

Zdiff3=griddata(X2,Y2,Zdiff,X1,Y1);
Zdiff4=inpaint_nans(Zdiff3,4);%method 3 or 4
Z4=Z_sphere4+Zdiff4;


Rad=sqrt(X1.*X1+Y1.*Y1);
```

```
Zdiff5=Zdiff4;
for i=1:101
   for j=1:101
      if Rad(i,j)>5
         Zdiff5(i,j)=NaN;
      end
   end
end

figure, pcolor(X2,Y2,Zdiff*1000)
shading interp
caxis([min(Zdiff(:))*1000 max(Zdiff(:))*1000])
colorbar
title('Elevation difference before')
saveas(gcf,strcat(fn, 'test_elevdiff_before.jpg'))

figure, pcolor(X1,Y1,Zdiff5*1000)
shading interp
caxis([min(Zdiff(:))*1000 max(Zdiff(:))*1000])
colorbar
title('Elevation difference after filling')
saveas(gcf,strcat(fn, 'test_elevdiff_after.jpg'))

% D=(.3375./Curvature)*1000;
% S=R./(sqrt(D.*D-R.*R));
% S_sphere=R./(sqrt(D_sphere.*D_sphere-R.*R));
%
% Sdiff=S-S_sphere;
%
% H_remain=zeros(23,181);%integrating slopes
% for i=1:NSteps
%     H_remain(:,i) = cumsimpson(R(:,i),Sdiff(:,i));
% end
%
% % H=H_remain+Z_sphere;
%
% H_remain3=griddata(X,Y,H_remain,X1,Y1);
% H_remain4=inpaint_nans(H_remain3,3);%try methods 2 or 3
% H4=Z_sphere4+H_remain4;
%
% Sdiff2=inpaint_nans(Sdiff,3);%filling in slopes before integration
% H_remain2=zeros(23,181);
% for i=1:NSteps
%     H_remain2(:,i) = cumsimpson(R(:,i),Sdiff2(:,i));
% end
%
% H_remain5=griddata(X,Y,H_remain2,X1,Y1);
% H_remain6=inpaint_nans(H_remain5,3);
```

```
% H6=H_remain6+Z_sphere4;

% outputting data file

% ss=sprintf('%s',fn,'H4.dat');
% disp(ss);
% fid=fopen(ss,'w');
% for i=1:101
%     for j=1:101
%         if (isnan(H4(i,j))==1)
%             H4(i,j)=0.0;
%         end
%
%         fprintf(fid,'%f ',H4(i,j));
%     end
%     fprintf(fid,'\n');
% end
% fclose(fid);
%
% ss=sprintf('%s',fn,'H6.dat');
% disp(ss);
% fid=fopen(ss,'w');
% for i=1:101
%     for j=1:101
%         if (isnan(H6(i,j))==1)
%             H6(i,j)=0.0;
%         end
%
%         fprintf(fid,'%f ',H6(i,j));
%     end
%     fprintf(fid,'\n');
% end
% fclose(fid);

ss=sprintf('%s',fn,'Z4.dat');
disp(ss);
fid=fopen(ss,'w');
for i=1:101
   for j=1:101
      if (isnan(Z4(i,j))==1)
         Z4(i,j)=0.0;
      end

      fprintf(fid,'%f ',Z4(i,j));
   end
   fprintf(fid,'\n');
end
fclose(fid);
clear, close all
```

Vita

Bo Tan was born in Tianjin, China on June 30th, 1979. He was raised and studied in Tianjin until he graduated from Tianjin Yaohua High School in 1997. He then entered University of Science and technology of China, in Hefei, Anhui Province. Many of his relatives are teachers. Growing in this environment, he has been interested in nature and science since childhood. He became more interested in science during his first physics course in middle school. This strong interest carried through middle school period and precipitated his decision to major in Physics at his undergraduate university. After graduating with a Bachelor of Science degree in 2002, Bo accepted a Graduate Research Assistantship at the University of Tennessee Space Institute (UTSI) in Tullahoma, Tennessee. At UTSI, he concentrated on bio-physics, specializing in vision science. His research interests include human eye modeling, pediatric vision screening and telemedicine, and ophthalmic instruments development. He is currently working as a research specialist in Department of Ophthalmology at University of Illinois at Chicago, focusing on retina imaging with adaptive optics.